Probing the Pyrolysis and Ion Chemistry of a Selection of Formates and Chloroformates

Bethany Lowe

Thesis submitted in partial fulfilment of the requirements

for the Doctorate in Philosophy degree in Chemistry

Department of Chemistry and Biomolecular Sciences

Faculty of Science

University of Ottawa

“What God wants to give you in your life is not a healing, what God wants to give you is not a job, what God wants to give you is not money. What God wants to give you is the Word of God in your spirit. Because the Word created the world. And if He can put his Word in your spirit, you can get anything, you can go anywhere, you can be anything.”

Rev Chris Oyakhilome, DSc, DSc, DD

Abstract

This research explores the ion chemistry and pyrolysis of a selection of formates. Alternative fuels have become increasingly popular over the past decade, one of particular interest is biofuels. Biofuels contain a variety of oxygenated compounds that are not present in traditional crude-oil fuels such as formates. Therefore, knowing the pyrolysis and ion chemistry of a selection of formates is of particular interest in being able to determine the environmental implications of switching to biofuels. The pyrolysis in particular for these formates have largely been studied using shock-tube experiments where both unimolecular and bimolecular reactions occur. This study employs the use of a micro-reactor coupled to imaging photoelectron photoion coincidence spectroscopy (iPEPICO) using synchrotron vacuum ultra-violet (VUV) radiation at the Swiss Light Source (SLS). The sample is introduced in the dilute-gas phase to optimise for unimolecular reactions. This thesis therefore presents the unimolecular pyrolysis chemistry of methyl formate, ethyl formate and methyl chloroformate and the ion chemistry of methyl chloroformate, phenyl formate and phenyl chloroformate.

In chapter 3, the thermal dissociation of the atmospheric constituent methyl formate was probed by coupling pyrolysis with iPEPICO. The pyrolysis products of dilute methyl formate, $CH_3OC(O)H$, were elucidated to be CH_3OH^+, CO, 2 CH_2O and CH_4 + CO_2 as in part distinct from the dissociation of the radical cation ($CH_3OH^{+\bullet}$ + CO and CH_2OH^+ + HCO). Density functional theory, CCSD(T), and CBS-QB3 calculations were used to describe the experimentally observed reaction mechanisms, and the thermal decomposition kinetics and the competition between the reaction channels are addressed in a statistical model. One result of the theoretical model is that CH_2O formation was predicted to come directly from methyl formate

at temperatures below 1200 K, while above 1800 K, it is formed primarily from the thermal decomposition of methanol.

Chapter 4 utilises the same techniques but expands on it by taking advantage of threshold photoionization and ion imaging, parent ions of neutral pyrolysis products and dissociative photoionization products could be distinguished, and multiple spectral carriers could be identified in several ms-TPES. The TPES and mass-selected TPES for ethyl formate are reported for the first time and appear to correspond to ionization of the lowest energy conformation having a cis configuration of the O=C(H)–O–C(H_2)–CH_3 and trans configuration of the O=C(H)–O–C(H_2)–CH_3 dihedral angles. We observed the following ethyl formate pyrolysis products: CH_3CH_2OH, CH_3CHO, C_2H_6, C_2H_4, HC(O)OH, CH_2O, CO_2, and CO, with HC(O)OH and C_2H_4 pyrolyzing further, forming CO + H_2O and C_2H_2 + H_2.

The reaction paths and energetics leading to these products, together with the products of two homolytic bond cleavage reactions, $CH_3CH_2O^{\cdot}$ + $^{\cdot}CHO$ and $CH_3CH_2^{\cdot}$ + $HC(O)O^{\cdot}$, were studied computationally at the M06-2X-GD3/aug-cc-pVTZ and SVECV-f12 levels of theory, complemented by further theoretical methods for comparison. The calculated reaction pathways were used to derive Arrhenius rate parameters for each reaction. The reaction rate constants and branching ratios are discussed in terms of the residence time and suggest carbon monoxide as a competitive primary fragmentation product at high temperatures.

Chapter 5 explores the pyrolysis chemistry of methyl chloroformate (MCF) in a similar manner but also introduces the study of the ion chemistry. The TPES for MCF was acquired for the first time; the geometry change upon ionization of MCF results in a broad, poorly defined TPES. Franck-Condon simulations are consistent with an ionisation energy (IE) of 10.90 ± 0.05 eV. Ionized MCF dissociated by the expected loss of Cl with a measured appearance energy

(AE) of 11.30 ± 0.01 eV. Together with the above IE, this AE suggests a reaction barrier of 0.40 eV, consistent with that found from SVECV-f12 calculations (0.41 eV). At higher internal energies, the loss of $CH_3O^{\bullet}$ becomes competitive due to its more favourable entropy of activation.

Pyrolysis of neutral MCF formed the anticipated major products of $CH_3Cl + CO_2$ (R1) and the minor products $HCl + CO + CH_2O$ (R2), all species being confirmed by their mass-selected TPES. Several possible reactions were computationally explored but these two were confirmed to be the dominant reaction channels. R1 proceeds by a concerted Cl atom migration via a 4-membered transition state in agreement with that proposed in the literature. R2 is a two-step reaction proceeding first by loss of HCl to make 2-oxiranone which then decomposes to CH_2O and CO. Kinetic modelling of the neutral decomposition could be made to simulate the observed reactions only if the vibrational temperature of the MCF was assumed not to cool during the expansion.

Chapter 6 further expands on the ion chemistry study by exploring the ion dissociation of phenyl formate (PF) and phenyl chloroformate (PCF). Imaging photoelectron photoion coincidence (iPEPICO) spectroscopy and tandem mass spectrometry were employed to explore the ionisation and dissociative ionisation of phenyl formate (PF) and phenyl chloroformate (PCF). The threshold photoelectron spectra of both compounds are featureless and lack a definitive origin transition, owing to the internal rotation of the formate functional group relative to the benzene ring, active upon ionisation. CBS-QB3 calculations yield ionisation energies of 8.88 and 9.03 eV for PF and PCF, respectively. Ionised PF dissociates by the loss of CO via a transition state composed of a phenoxy cation and a HCO moieties. The dissociation of PCF ions involves the competing losses of CO (*m*/*z* 128/130), Cl (*m*/*z* 121), and

CO_2 (*m*/*z* 112/114), with Cl loss also shown to occur from the second excited state in a non-statistical process. The primary CO- and Cl-loss fragment ions undergo sequential reactions leading to fragment ions at *m*/*z* 98 and 77. The mass-analysed ion kinetic energy (MIKE) spectrum of PCF^+ showed that the loss of CO_2 occurs with a large reverse energy barrier, which is consistent with the computationally derived minimum energy reaction pathway.

Chapter 7 highlights the conclusions drawn from across the chapters 3-6 and brings chapter 1 back into focus with how these findings can help to inform future studies on pyrolysis. Furthermore, chapter 7 discusses how future technologies for biofuels can be shaped with the understanding of the pyrolysis products of these biofuel related compounds.

Acknowledgements

Seeing my PhD through to fruition was mainly fuelled by 3 things.

1) Honouring God by showing excellence in all that I do

It was God who called me to cross the pond and start a degree I wasn't sure I was cut out for, but His plans are far beyond a PhD, it is for a life full of purpose and truth, both now and forever. Throughout the PhD He has shown Himself faithful time and time again, I've never lacked for anything; the right people, the right information or simply the ability to comprehend the material, but mostly knowing my identity in Christ created an anxiety-free environment. I'd therefore like to especially thank my family at Christ Embassy Ottawa and particularly Pastor Joseph and Pastor Isaac for supporting me in the most important way, through prayer and encouragement in the Word of God.

2) Honouring people that have invested in me

There are so many people that have invested heavily into my life. The bible says, 'train a child in the way they should go and when they're old they shall not depart from it,' without my family and particularly my parents continuing to lead, guide and support me I would not be in a different country about to finish a whole PhD, I'm incredibly grateful.

Secondly to all those that have invested in me academically. The whole Mayer Group have taught me so much, a special thank you to Dr. Sharon for continuously being a great joy, Dr. Sander for your years of expertise that you impart into those in the lab, Malick for being ever so helpful and Nick for being a great euchre partner. The great environment in the Mayer Group is truly a reflection of the kindness and generosity of Prof Paul Mayer. It's rare to find such humble, genuinely loving and likeable people in the world but Paul is definitely one of them. I'd like to also thank my collaborators in Argentina, Prof Maxi Burgos-Paci, Dr Alejandro

and Dr Juana, thank you for your input and bringing out different sides to this project that have enhanced the work greatly. Also thank you to Dr Andras Bodi for all your contributions.

3) To be called Dr Chukwu and have people looking confused

While my name may officially still be Lowe, to all those close to me it's Bethany Chukwu, a change that happened during the completion of my PhD. Thank you so much Mitchell for being a rock, you always know what to say, whether I want to hear it or not. Thank you for your love, support and encouragement in all aspects but especially my faith. You are amazing and I love you.

Table of Contents

List of Tables

List of Figures

List of Abbreviations

$\Delta S^{\ddagger}$	Activation Entropy	iPEPICO	Imaging Photoelectron Photoion Coincidence Spectroscopy
AE	Appearance Energy	KE_{e-}	Kinetic Energy of txhe Electron
AO	Atomic Orbital	LCAO	Linear Combination of Atomic Orbitals
BD	Breakdown Diagrams	MIKES	Mass-Analysed Ion Kinetic Energy Spectrometry
TST	Canonical Transition State Theory	ms-TPES	Mass-Selected TPES
CVTST	Canonical Variational Transition State Theory	MCF	Methyl Chloroformate
DFT	Density Functional Theory	MF	Methyl Formate
ESA	Electrostatic Analyser	MW	Multiwell Program Suite
ECF	Ethyl Chloroformate	NO_x	Nitrous Oxides
EF	Ethyl Formate	PCF	Phenyl Chloroformate
FAEEs	Fatty Acid Ethyl Esters	PF	Phenyl Formate
FAMEs	Fatty Acid Methyl Esters	PSC	Polar Stratospheric Clouds
FFR	Field-Free Region	RRKM	Rice-Ramsperger-Kassel-Marcus
FC	Franck–Condon	SOA	Secondary Organic Aerosols
GTO	Gaussian-Type Orbitals	SLS	Swiss Light Source
GD3	Grimme's Empirical Dispersion Correction	TPES	Threshold Photoelectron Spectra
HPL	High-Pressure Limit	TOF	Time-of-Flight
IRC	Intrinsic Reaction Coordinate	VOC	Volatile Organic Compounds
IE	Ionisation Energy	ZPE	Zero-Point Energy

Chapter 1. Formates in the Atmosphere

1.1. Background

1.1.1. Structure of the atmosphere

Earth's atmosphere is composed of several layers, each of which possesses different properties with different chemical environments, and it is therefore important to understand the structure of the atmosphere to understand the chemical processes that can be expected. The layer closest to the Earth is the troposphere. From the Greek word 'tropos' meaning 'change', the troposphere is characterised by its changing weather systems and varying temperature, with a turnover timescale on the order of days. This variation enables varied chemical reactions as there is increased mixing of gases, which can be affected by the weather.

The troposphere is between 8 and 16 km in altitude, depending on where it is measured from Earth.[1] Although there is great variation in the temperature within the troposphere, the temperature is generally warmer closer to the Earth and decreases with increasing altitude, as depicted in Figure 1-1. This is due to the Sun's radiation warming the Earth, which then warms the air closest to the Earth's surface. Heat is then distributed throughout the troposphere through convection currents and vertical mixing.

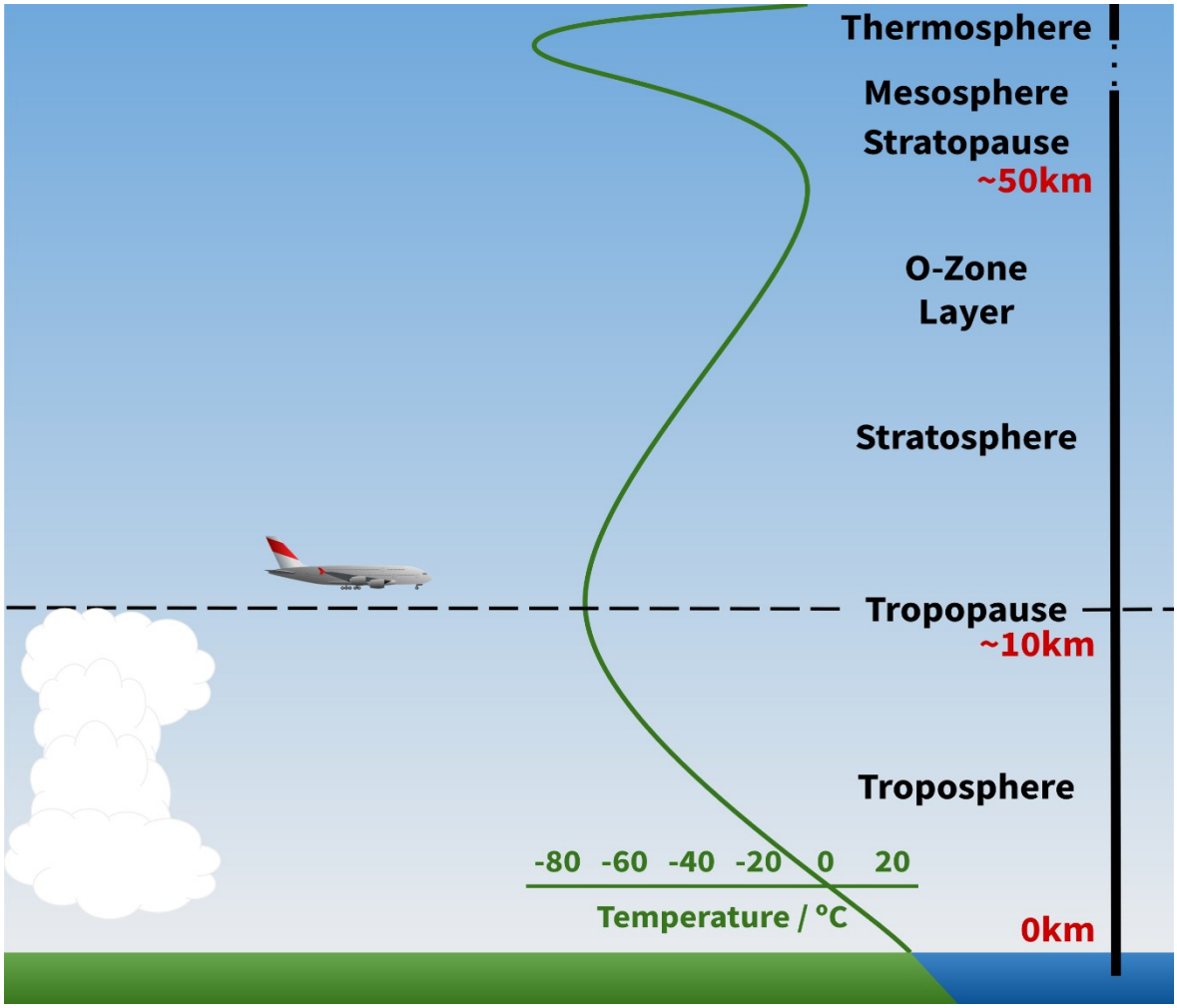

Figure 1-1: Diagram demonstrating the layers of the atmosphere and the change of temperature with increasing altitude.

Despite being the smallest of the layers, it accounts for ~80% of the total mass of the atmosphere;[2] this is largely due to the effect of gravity in combination with the compressibility of air. This causes the density to decrease exponentially with increasing altitude.[3] These factors combined with the large content of water vapour are largely responsible for clouds and stormy weather, which provide different environments for chemical reactions to occur.

The stratosphere is the layer next to the troposphere and extends upward from the Earth's surface to an altitude of ~50 km. Where the troposphere and stratosphere meet is known as the tropopause. Unlike the troposphere, which is well-mixed, the stratosphere is composed of stable (stratified) layers. This means that with increasing altitude, the temperature increases as the main source of

heating is no longer from the Earth and subsequent convection, but is directly from the Sun's radiation.[1] The distribution of molecules within the stratosphere is largely based on size, with heavier molecules closer to the Earth, owing to the greater effect of gravity on them. Mixing in the stratosphere is very slow, on a timescale of years, which leads to reduced chemical interactions with increasing altitude. The stratosphere contains the Ozone layer, which will be described in greater detail later.

The mesosphere and thermosphere are two more layers that extend from the stratosphere respectively. These layers are largely decoupled from the lower layers and thus have little influence on the Earth's weather or pollutant transport processes, and also experience little effect from these processes. [4]

1.1.2. Radiation Exposure

The Sun provides a wide range of wavelengths, spanning from the near-IR to soft X-ray regions of the electromagnetic spectra with a maximum intensity at ~500 nm, corresponding to the blue portion of the visible spectrum,[5] depicted by the blue line in Figure 1-2. As radiation passes through the atmosphere, it is filtered according to the chemical environment.

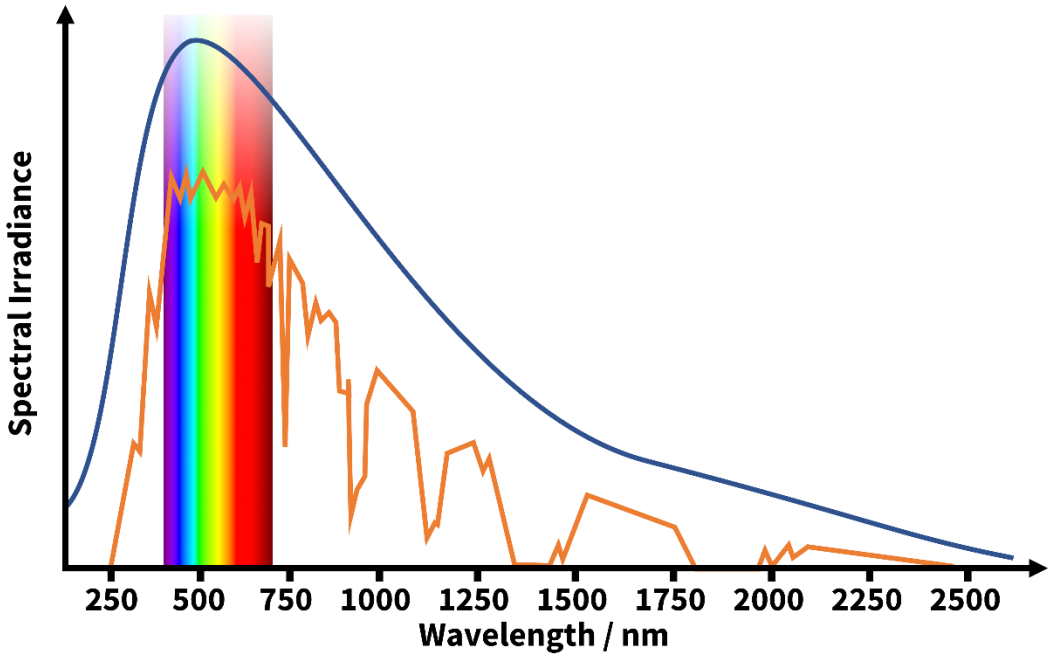

Figure 1-2: Adaptation of a solar irradiance spectrum (blue) and the spectra of radiation reaching Earth's surface (orange) with the visible region highlighted by its respective colours.

When the radiation reaches the thermosphere, almost all the extreme ultraviolet radiation (below 170 nm) is absorbed, as shown by the orange line in Figure 1-2.[6] Absorption by O_2 and N_2 accounts for most of the absorption in the wavelength region of 91.2 – 79.6 nm, while below 79.6 nm atomic O absorption dominates.[6] This accounts for the increase in temperature in the thermosphere shown in Figure 1-1, and this leads to the ionisation of the gases in this region, known as the ionosphere. The gases here are above the turbopause and are no longer mixed but are separated according to molecular mass with heavier molecules at lower altitudes. The visible portion of the solar irradiance remains almost constant, unlike XUV radiation, which experiences large fluxes depending on solar activity, such as solar flares.

Similar processes occur throughout the mesosphere; however, they lie beneath the turbopause, such that the gases undergo mixing. The mesosphere has very low gas density; therefore, bimolecular

reactions are rare. The presence of polar mesospheric clouds contributes to the reflection of radiation back into space, as shown in Figure 1-3.

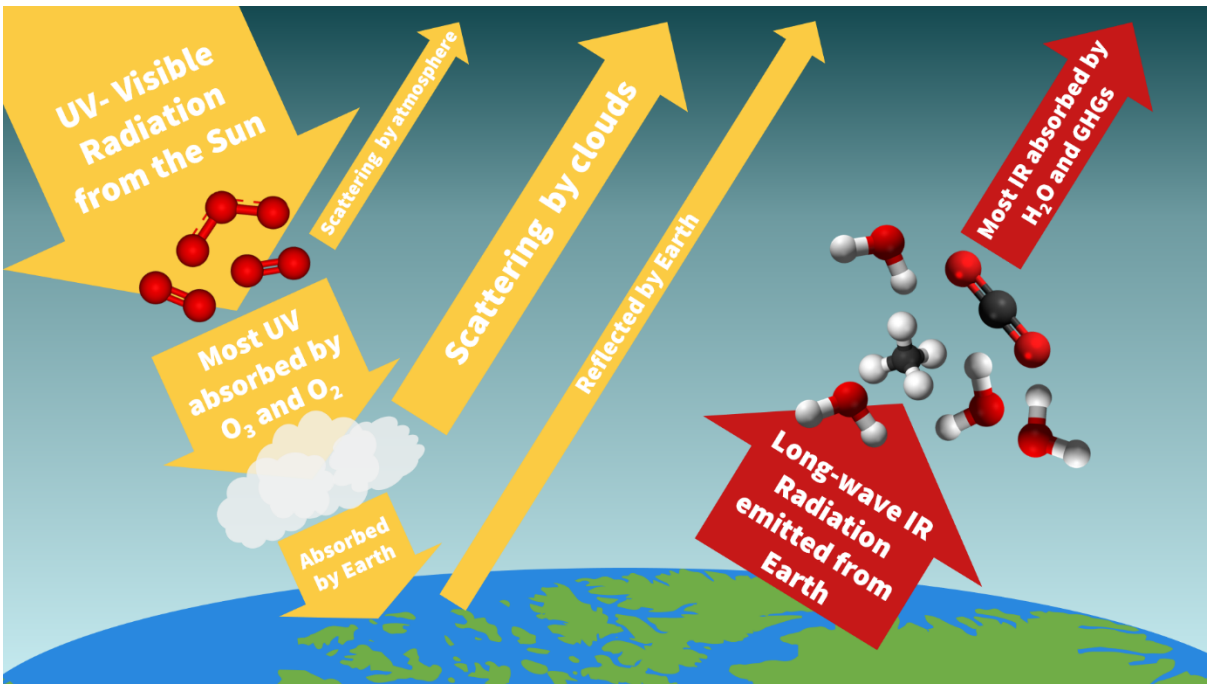

Figure 1-3: Figure of the way that radiation is absorbed and emitted from the Earth through the atmosphere.

As the radiation continues further down the Earth's atmosphere it encounters the stratosphere, where there is a notable reduction in the intensity of the high energy UV. Absorption from O_3, O_2, and O in what is known as the Ozone layer is largely responsible for this, as shown in Figure 1-3. The absorption region for O_3 is complicated and spans across the region of ~950-100 nm with varying degrees of absorption cross section. The UV-Vis region of this spectrum is shown in Figure 1-4. [7,8] All the absorption bands are dissociative, leading to the production of O and O_2, shown in equation (1-3). The strongest absorption band is known as the Hartley band and covers the region of ~300-200 nm, which covers the UV-C region. The bands at longer wavelengths, known as the Chappuis and Wulf bands are weak and don't account for much intensity loss of radiation entering the atmosphere.[9]

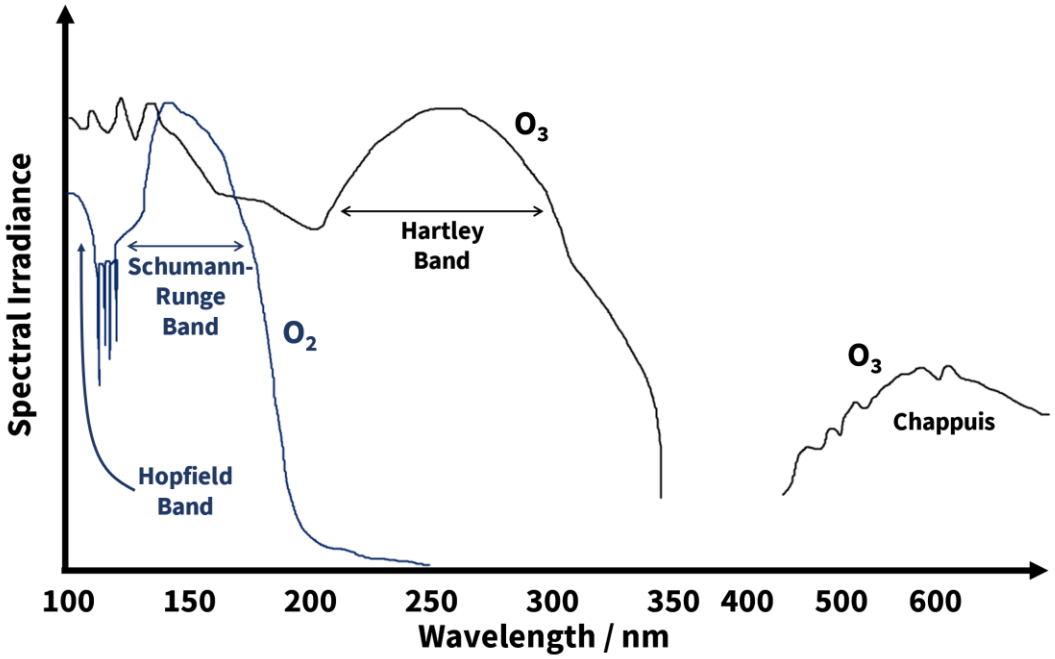

Figure 1-4: Absorption Spectra of O_2 (blue) and O_3 (black) in the UV-Vis region, including band labels. Based on the image from International Geophysics.[8]

O_2 absorbs at a higher frequency than O_3 due to the stronger bonds that comprise it. There are two sets of very intense absorption bands in the ultraviolet region: the Hopfield bands, which extend the wavelengths of 67 and 100 nm [10], and the Schumann–Runge continuum between 135 and 176 nm, [11] with diffuse bands connecting them. At a slightly longer wavelength, the Herzberg continuum extends to the region of 240-260 nm with a lower absorption cross-section. These bands are dissociative (Equation 1-1) and have been proposed as the first step in the Chapman cycle,[12] a series of reactions to describe O_3 creation. Longer wavelength bands, including those in the visible and infrared regions responsible for the ionisation of O_2 to O_2^+ and vibrations, respectively, are also present but have a greater effect on tropospheric warming, as described later.[13] Because of the absorption regions of O_3 and O_2, only low-energy UV (UVA & UVB) passes through the atmosphere to Earth, thus preventing harmful high-energy radiation from damaging biological organisms. This determines the photoinduced chemistry of the troposphere.

$$O_2 \xrightarrow{h\nu\ (\lambda<240\ nm)} 2O \quad (1\text{-}1)$$

Bimolecular reactions can occur in the troposphere because of gas mixing and a higher concentration of gases; because this is still relatively low, the frequency of collisions is also low oxygen radicals are produced in the ground-level triplet state (^3P), are highly reactive given their two unpaired electrons, and combine with O_2 to form O_3, where M is a nonreactive species that absorbs the energy released from the reaction.

$$O+O_2+M \longrightarrow O_3+M \quad (1\text{-}2)$$

Ozone also absorbs these higher-frequency photons, and its bond energy is lower than that of O_2; therefore, O_3 photolyses, but from a longer wavelength than O_2.

$$O_3 \xrightarrow{h\nu\ (\lambda<320\ nm)} O_2+O(\,^1D) \quad (1\text{-}3)$$

$O(^1D)$ is an excited singlet state of oxygen that relaxes to the ^3P state.

$$O(\,^1D)+M \longrightarrow O+M \quad (1\text{-}4)$$

Since O is regenerated, (1-2) can occur again, therefore equations (1-2) – (1-4) are propagation steps. The termination step for the O_3 sink occurs when O_3 reacts with O, given in (1-5).

$$O+O_3 \longrightarrow 2O_2 \quad (1\text{-}5)$$

Halogen radicals and other pollutants such as OH and NO provide alternative sinks for O_3. Halogen radicals are released into the atmosphere by chlorofluorocarbons and other halocarbons that do not break down in the troposphere because of stronger bonds; however, the stratosphere's higher energy radiation will enable dissociation into radicals and undergo a series of reactions of their own that lead to the depletion of O_3.[14] In recent years, this has led to a reduction in Ozone in the stratosphere, which is particularly prominent over the poles because of the extended periods of low

temperatures, leading to the formation of polar stratospheric clouds (PSC).[15] Interactions on the surface of the PSCs allow for an increase in the rate of Ozone depletion, which further increases in the spring when PSCs are still present but increased temperature.[16] Therefore, Ozone holes are formed at the poles. This means that the radiation that was once not reaching Earth in a significant quantity due to Ozone absorption was now extending beyond the stratosphere, enabling higher-energy photochemistry in the troposphere. However, owing to legislation, including the Montreal Protocol, Ozone concentrations have again been increasing, and there has been a significant reduction in Ozone hole sizes.[17]

Once past the stratosphere, tropospheric clouds and the Earth cause a large amount of radiation to be reflected into space. The Earth emits long-wave black-body radiation, depicted in Figure 1-3 by the red outgoing arrows, much of which is absorbed by molecules in the troposphere, such as water, CO_2, and CH_4, which are known as greenhouse gases. Upon absorption, these molecules vibrate. This kinetic motion leads to a temperature increase, thereby keeping the Earth warmer than it would without this absorption. This is essential for life; however, because it is low-frequency radiation, it does not have a significant impact on photolyzed reactions.

1.1.3. Reactive Organic Carbon in the Atmosphere

Volatile organic compounds (VOC) are organic molecules with a high vapour pressure at room temperature. The gas-phase molecules are then able to diffuse into the atmosphere and perform gas-phase chemistry. As previously mentioned, whether this is in the troposphere or stratosphere is determined by the relative bond strength. VOCs are emitted from both natural (biogenic) sources and anthropogenic sources, released from plants, burning of fuels, and are also commonly found in household chemicals such as paint or cleaning solvents.[18,19] VOC concentrations are usually higher

indoors than outdoors, but undergo thorough mixing in the troposphere. These chemicals are often toxic and contribute to tropospheric Ozone generation.

Unlike stratospheric Ozone, tropospheric Ozone is a pollutant that can be detrimental to human health because the troposphere is a part of the atmosphere in which we live and the gases we breathe in. Tropospheric Ozone is generated through a series of chemical reactions involving nitrous oxides (NO_x), carbon monoxide or VOCs, all of which require OH radicals. OH radicals are formed even in 'clean' tropospheric conditions where O_3 is present in low concentrations and is photolyzed to form $O(^1D)$ radicals as described in equation (1-3). These $O(^1D)$ radicals react with water vapour to generate OH radicals, as shown in equation (1-6).[20]

$$O(^1D)+H_2O\longrightarrow 2OH \qquad (1\text{-}6)$$

These hydroxyl radicals then react with NO_x, CO, or VOCs. The scheme for VOC Ozone production is presented, and the schemes for NO_x and CO are similar.[21] The simplest VOC is methane, which is the molecule used in the scheme. [22]

$$OH+CH_4\longrightarrow H_2O+CH_3 \qquad (1\text{-}7)$$

$$CH_3+O_2+M\longrightarrow MCH_3O_2 \qquad (1\text{-}8)$$

$$MCH_3O_2+NO\longrightarrow CH_3O+NO_2 \qquad (1\text{-}9)$$

$$CH_3O+O_2\longrightarrow HCHO+HO_2 \qquad (1\text{-}10)$$

Here, HO_2 is produced because methane is the example; in other systems, it may be RO_2 which undergoes analogous reactions with NO to form RO and NO.

$$HO_2+NO\longrightarrow OH+NO_2 \qquad (1\text{-}11)$$

NO_2 is photolyzed by UV-A radiation and the resulting oxygen radicals can react with molecular oxygen to form Ozone, as in reaction (1-2). The last three steps are the Ozone-forming steps of the cycle and are common, despite the precursor molecule.

$$NO_2 \xrightarrow{h\nu\ (\lambda<400\ nm)} NO+O \qquad (1\text{-}12)$$

Atmospheric aerosols participate in a significant amount of the chemistry occurring in the troposphere. They range in size, from 10^{-9} – 10^{-5} m, and chemical composition, the larger particles are primarily formed from mechanical processes, e.g. sea salt and plant debris, smaller particles are mostly emitted from combustion processes, or formed in the atmosphere.[23] Particles are formed when the gas-phase molecules partition to the particle-phase, both surface and bulk reactions are then possible once in the particle-phase. Secondary organic aerosols (SOA) are formed largely from oxidised VOC reactions, causing changes in volatility and accumulation, as shown in Figure 1-5. Oxidation in the atmosphere has two main pathways, degradation to form higher volatility compounds, or incorporation of functional groups such as carbonyl, hydroxyl, and nitrate into the intact molecule, thus lowering the volatility of the molecule and therefore more likely to contribute to SOA formation.[24]

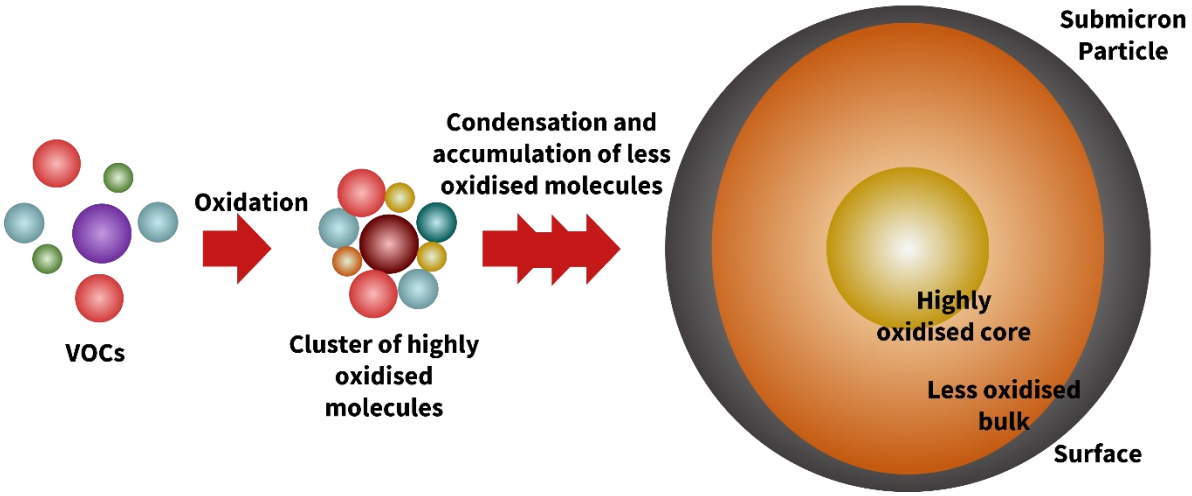

Figure 1-5: Summary of secondary organic aerosol formation.

1.2. Formates

Having looked at the major reactions of carbon in the atmosphere, the aim of the work undertaken in this study is to probe some of the reactions and products resulting from a small subset of molecules in the atmosphere. We will study methyl formate, ethyl formate, phenyl formate, methyl chloroformate, and phenyl chloroformate.

1.2.1. Sources of formates

Formates are largely released anthropogenically, with all non-chlorinated formates in this study being biodiesel components. Methyl formate is used as a drying agent for resins and foam blowing or as a precursor to other molecules in the chemical industry. Ethyl formate is used as a precursor in the chemical industry and used in pest control.[25] All of the formates discussed can be produced in the atmosphere from oxidation of VOCs such as ethyl vinyl ethers with radicals such as OH, NO_3 and O_3.[26,27]

The process by which this occurs for ethyl formate is as follows:

$$OH+C_2H_5OCH=CH_2+(+O_2+NO) \xrightarrow{M} C_2H_5OCH(OH)CH_2O+NO_2 \quad (1\text{-}13)$$

$$OH+C_2H_5OCH=CH_2+(+O_2+NO) \xrightarrow{M} C_2H_5OCH(O)CH_2OH+NO_2 \quad (1\text{-}14)$$

Here, ethyl vinyl ether undergoes OH addition to the carbon-carbon double bond. The resulting hydroxyalcoxyl radicals can react with O_2 to form hydroxycarbonyl compounds; alternatively, they may undergo decomposition to form ethyl formate and formaldehyde. This route tends to dominate.[26]

$$C_2H_5OCH(OH)CH_2O \xrightarrow{M} C_2H_5OCHOH+HCHO \quad (1\text{-}15)$$

$$C_2H_5OCHOH+O_2 \rightarrow C_2H_5OC(O)H+HO_2 \quad (1\text{-}16)$$

$$C_2H_5OCH(O)CH_2OH \xrightarrow{M} C_2H_5OC(O)H+CH_2OH \quad (1\text{-}17)$$

Alternatively, in the absence of NO_x, it has been shown that ethyl formate is formed, from self-reaction of the ethyl vinyl ether that forms these hydroxycarbonyl compounds shown in reactions 1.2-3-5.[26] Phenyl formate is particularly useful in synthesis as a CO surrogate, due to the weak bonding and formation of the stable phenol.[28,29]

Methyl chloroformate has uses in the chemical industry in synthesis of insecticides and formerly as a warfare agent in world war 1.[30,31] Phenyl chloroformate is also primarily used in the chemical industry as a reagent.[32,33]

Chlorine atom-initiated oxidation of unsaturated species can lead to the formation of products such as chloroacetaldehyde and chloroacetone.[34] However, the direct formation of chloroformates from oxidation processes has not yet been reported. Elimination reactions in the atmosphere could lead to the formation of formates, as reported by Chuchani et al., where the elimination of CO led to the formation of methyl chloroformate.[35] Therefore, it is expected that the decomposition of longer-chain chlorinated species will lead to the formation of shorter chloroformates, such as those that are to be investigated in this study.

1.2.2. Pyrolysis

Formates are prevalent in biofuels,[36,37] due to this they are exposed to high heat and pyrolysis conditions. Kinetic modelling experiments and engine experiments have shown that oxygenated hydrocarbons can reduce soot production in diesel engines.[38] Knowledge of the pyrolysis is therefore of importance. Since the formates typically present in biofuels are long chain formates, it is simpler to use surrogates to study the expected chemistry. Previous shock-tube studies have shown the primary loses to be from the functional group to lose CO, CO_2 and methanol among other

products.[36,39–41] Shock-tube studies have their limitations due to the lack of specificity in the type of dissociations occurring and also due to the longer residence time many sequential reactions can take place and not show the full scope of what is occurring in these processes. Previous work using a micro-reactor coupled to imaging photoelectron photoion coincidence (iPEPICO) spectroscopy has enabled study of various molecules while optimising for unimolecular dissociations.[42–44]

1.2.3. Ion Chemistry

One method of VOC abatement is to use nonthermal plasma.[45,46] This process is characterised by low gas temperature, neutrals and radicals, and high electron temperature. These high-energy electrons cause ionisation and excitation of neutrals.[45] This can be utilised to promote oxidative decomposition of VOCs present in the plasma, thus leading to VOC reduction in the plasma. Such systems have been used for air filtration and have potential uses in retroactively adding to vehicles to primarily reduce NO_x emissions, however, VOC emissions would also be reduced.[46,47] Therefore ion-chemistry of these VOCs, particularly those found in automotives is of interest in determining the decomposition products and mechanisms.

1.3. Goals

This thesis will focus on the pyrolysis chemistry of methyl formate, ethyl formate and methyl chloroformate and the ion dissociation of methyl chloroformate, phenyl formate and phenyl chloroformate. A major goal is to compare the results from the micro-reactor coupled to iPEPICO with previous studies that involved higher sample pressures and thus were dominated by bi-molecular reactions. Each of these will be explored using iPEPICO at the Swiss Light Source (SLS) and will highlight the unimolecular reactions in the neutral (pyrolysis only) and ion (ion dissociation).

Chapter 2. Techniques

2.1. Introduction

To study the ion chemistry and pyrolysis of the selected formates we used primarily iPEPICO at the Swiss Light Source (SLS). We used computational techniques to support the findings and to fit the data.

2.2. Imaging Photoelectron Photoion Coincidence Spectroscopy (iPEPICO)

iPEPICO was the primary experimental technique used for the study of both the ion chemistry and pyrolysis of the formates studied. An overall schematic of the iPEPICO apparatus at the SLS is shown in Figure 2-1 and where the left side focuses on sample introduction, the centre is for the study of pyrolysis and the right side is the iPEPICO set-up itself.

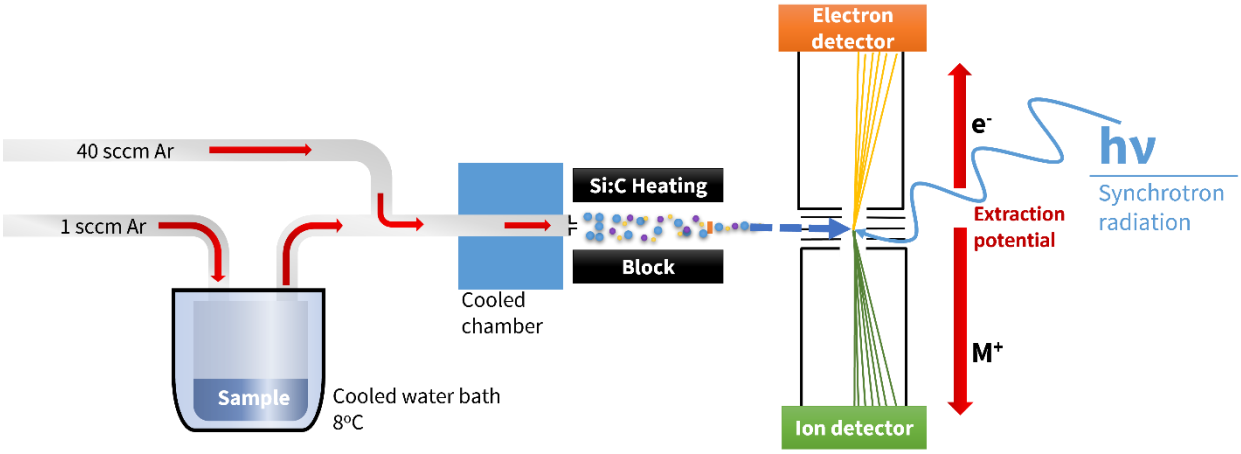

Figure 2-1: Schematic of the pyrolysis set up at the SLS. The left shows the sample introduction by passing argon gas over the liquid sample that is contained in a cooled water bath. The centre shows the sample gas being diluted with more argon gas and passing through the cooled chamber as a molecular beam (blue dashed arrow) and into the microreactor, where circles highlight that pyrolysis occurs here to form different compounds. The right side shows the iPEPICO set up where the sample is ionised by synchrotron radiation (solid blue line), where the extraction potential causes the ions (green lines) and electrons (yellow lines) to be accelerated to their respective detectors.

2.2.1. Sample introduction

Figure 2-2: Sample introduction pictured at the SLS.

All the samples studied are volatile liquids, therefore for sample introduction argon gas is passed over a container filled with the sample. The container is kept inside a cooled water bath at 8°C to maintain a constant vapour pressure. The sample gas and argon then passes out and is diluted by more argon gas to optimise for unimolecular reactions, the argon gas mixture then passes through to the pyrolysis chamber. Figure 2-2 shows the experimental set-up at the SLS, the cooled water bath is not pictured.

2.2.2. Pyrolysis Chamber

Before the gas mixture passes into the Si:C heating tube it passes through a cooled chamber; the purpose of the cooled chamber is to ensure that all the instrument elements prior to the heating element are protected from heat damage. The mixture passes through an orifice to form a molecular beam.

The molecular beam passes into the Si:C heating tube and unimolecular pyrolysis occurs. Here neutral decomposition occurs, so neutrals are formed. The cooled chamber and Si:C microreactor are pictured in Figure 2-3. The molecular beam containing the pyrolysis products and unreacted material passes through to the iPEPICO set up.

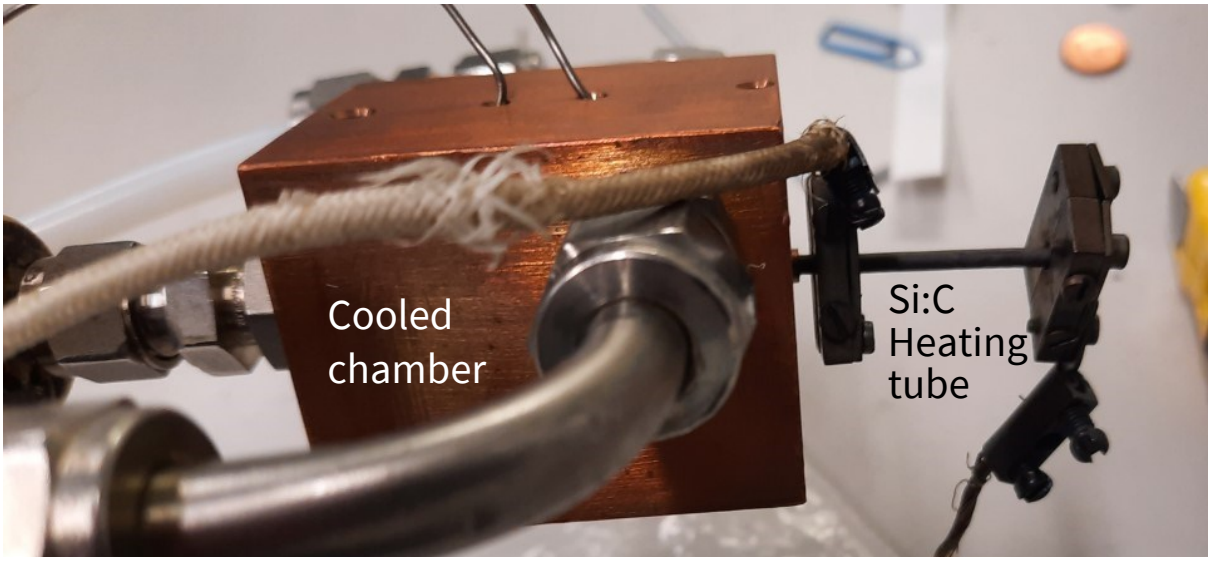

Figure 2-3: Cooling chamber and Si:C heating tube pictured at the SLS.

2.2.3. iPEPICO

The molecular beam is ionised by the synchrotron radiation, leading to the release of an electron and formation of a molecular ion.

$$M \xrightarrow{h\nu} M^+ + e^- \qquad (2\text{-}1)$$

There is an extraction potential across the ionisation region that leads to the electrons and ions being accelerated in opposite directions, toward their respective detectors. Electrons travel 3 orders of magnitude faster than the ions, and upon the electron hitting the detector the time-of-flight timer starts and it ends when the ion hits the ion detector. This is a coincidence event. Equation 2-2 shows the relationship of photon energy (hv) with adiabatic ionisation energy (IE), internal energy of the ion (E_i) and kinetic energy of the electron (KE_{e^-}) upon photoionisation.

$$h\nu = IE + E_i + KE_{e^-} \quad (2\text{-}2)$$

The electrons released may have kinetic energy, known as 'hot' electrons. Hot electrons can travel perpendicular to the detector, so upon acceleration the electron will hit the imaging detector off-centre, shown in Figure 2-4a as route 1. Those with zero kinetic energy will not travel until accelerated by the extraction potential therefore they will hit the centre of the detector, route 2 in Figure 2-4a. Therefore, the centre spot of the electron detector is selected in the i2PEPICO software for data processing (Figure 2-4b), this eliminates the KE_{e^-} term in equation 2-2. However, the hot electrons can also have kinetic energy in the direction towards or away from the electron detector, leading to them hitting the detector in the centre also, shown as route 3 in Figure 2-4a. To account for these, a

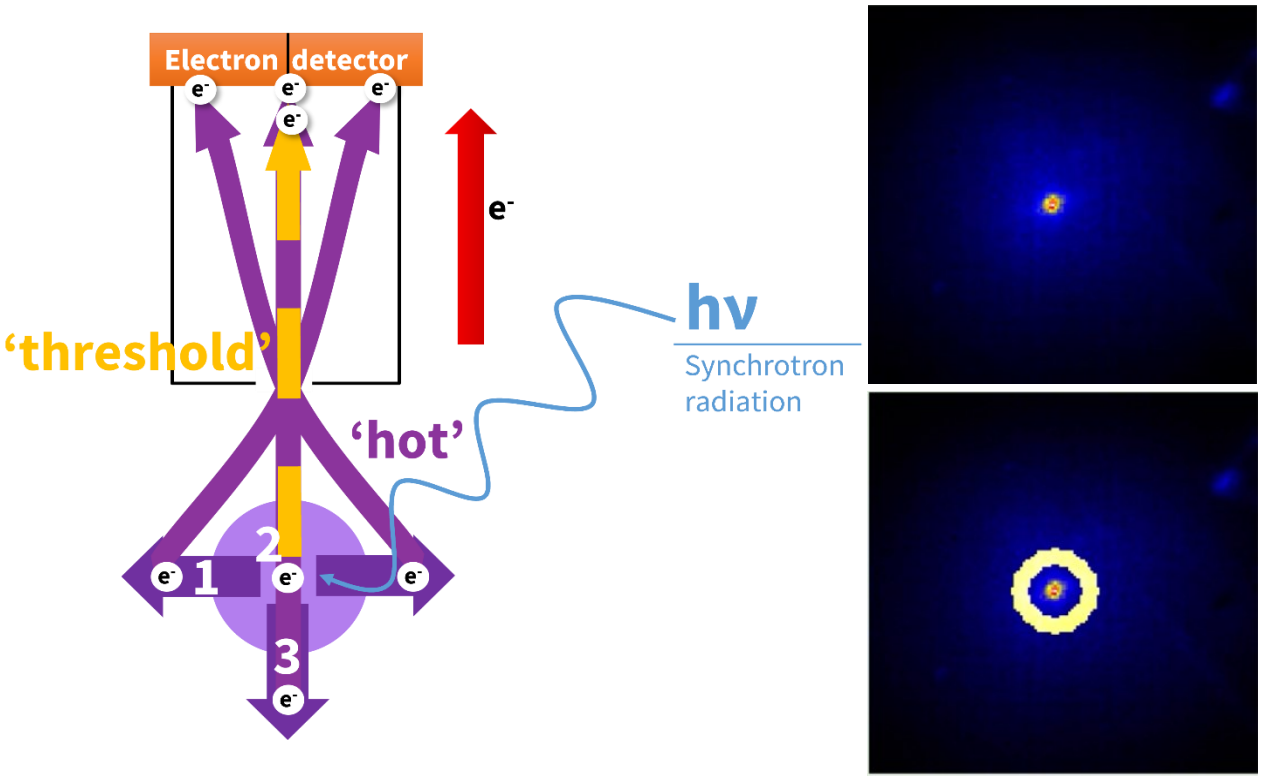

Figure 2-4: (a) [left] Diagram showing how electrons can move upon ionisation of a molecule within the ionisation region of the iPEPICO. If the electron has kinetic energy perpendicular to the electron detector that 'hot' electron will hit the detector off centre (1). If the electron has 0 kinetic energy, a threshold electron, or has kinetic energy in the direction of the detector, it will hit the detector in the centre, 2 and 3 respectively. **(b)** [right] Electron detector images with the top showing the bright centre spot and the bottom showing the same image but with a ring selected for subtracting hot electron contribution to the threshold (centre) electrons.

ring is taken from around the centre spot and subtracted from the total of coincidences inside the ring, Figure 2-4b.

Since the sample is introduced to the ionisation region as a molecular beam, the ions travel fast in the direction perpendicular to the detector with a narrow velocity distribution,[43] this leads to a short intense line on the imaging ion detector. The background signal has a broad and uniform velocity distribution and no average momentum,[43] leading to a broad uniform circular signal on the ion detector. The ions formed from neutrals in the molecular beam are selected by using an oval shape over that portion of the ion detector image, shown in Figure 2-5.

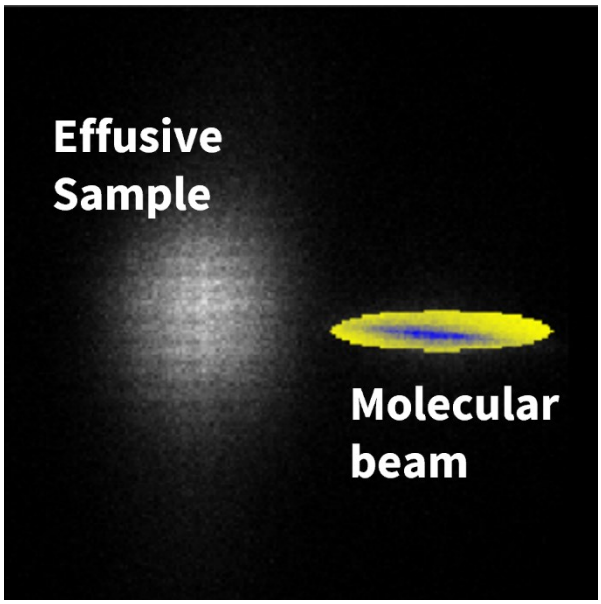

Figure 2-5: Molecular beam selection on an iPEPICO ion detector image. Molecular beam selection depicted by yellow oblong.

2.3. Data processing

2.3.1. iPEPICO Data

The data extracted contains the electron intensity from the “centre” spot and the “ring” correction, integrated ion intensities from coincidences corresponding to electron events from the “centre” spot (circle) and the “ring”, acquisition times and the photon energy. This is used to create threshold photoelectron spectra (TPES), mass-selected TPES (ms-TPES) and breakdown diagrams (BD), the data that composes each of these is compiled in Figure 2-6.

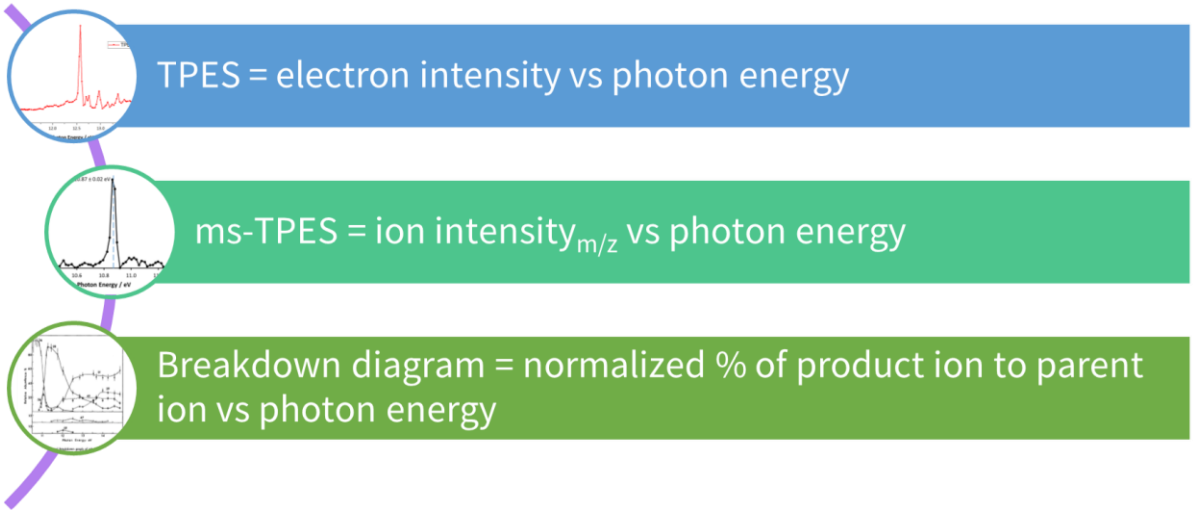

Figure 2-6: Diagram to show what the iPEPICO data can be used to make for data processing, including a small example of each respectively.

The first step in determing any of the above is to make the correction for hot electrons, this is done by multiplying the ring data with a multiplication factor (B) such as 0.6, then subtracting the resultant value from the ‘central circle’ data. If too much of the ring is subtracted from the inner-circle then it can produce negative signals in the data, so B is optimised to account for hot electron contribution while not leading to negative values.

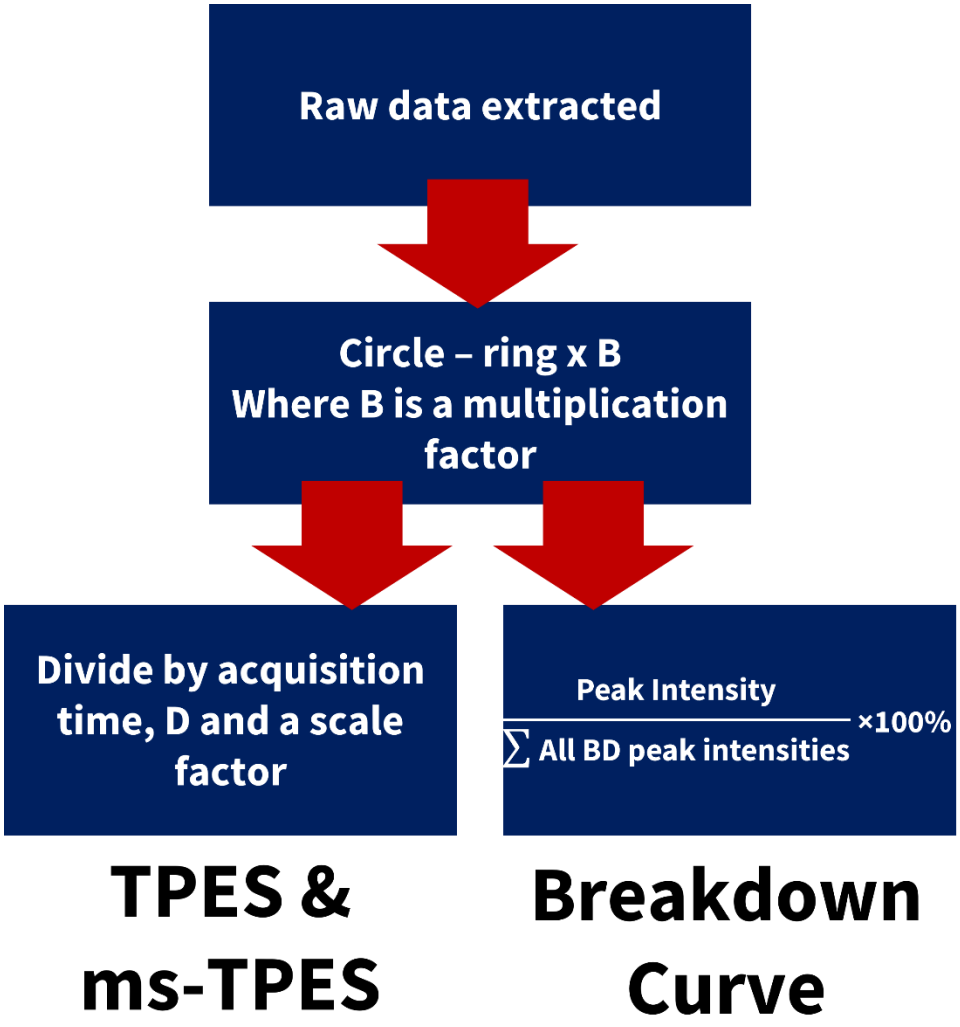

Figure 2-7: Flowchart to depict how the raw iPEPICO data is processed to give the breakdown curves and TPES and ms-TPES.

For breakdown curves the intensity is normalised by summing the individual peaks to be included in the BD curve then to divide the individual peaks by the sum value, equation 2-3. This process is summarised in Figure 2-7.

$$\text{Normalised Peak Intensity} = \frac{\text{Peak intensity}}{\sum \text{All BD peak intensities}} \times 100\% \qquad (2\text{-}3)$$

2.3.2. Vibrational Structure

The ms-TPES can sometimes show vibrational structure, this is due to the Franck-Condon principle. Since the equilibrium structure of the ion is not the same as the neutral equilbrium structure and nuclear displacement (Figure 2-8b) is slower than for electrons, ionisation occurs into the vibrational state with the best nuclear overlap, therefore forming bands of higher intensity according to vibrational states. This is summarised in Figure 2-8. The FC-overlap can be simulated using Gaussian and overlaid on ms-TPES to show the vibrational structure occuring.

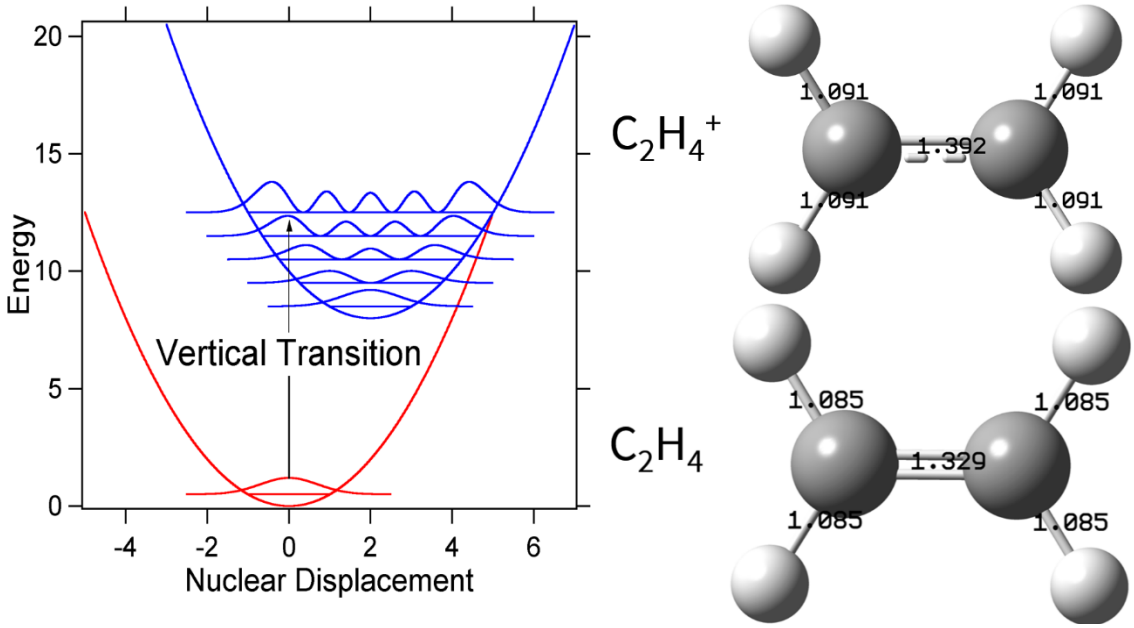

Figure 2-8: (a) [left] Energy level diagram showing vertical ionisation according to nuclear overlap, denoting the Franck-Condon Principle. **(b)** [right] equilibrium structure of the ion and neutral for C_2H_4 with bond lengths (Å) overlaid to highlight the change in structure upon ionisation.

2.3.3. Statistical Modelling

Rice-Ramsperger-Kassel-Marcus (RRKM) theory is a chemical kinetics theory for estimating the rate of unimolecular reactions.[48,49] In RRKM each vibrational mode is treated individually, giving it the advantage of not using a single oscillator to describe the entire system, unlike in the preceding RRK

theory.[49,50] In RRKM it is assumed that the rate is related to the number of ways that energy can be distributed among the internal degrees of freedom of the reactant and transition state (unimolecular process), where the critical energy is located in one particular degree of freedom known as the critical oscillator.[51]

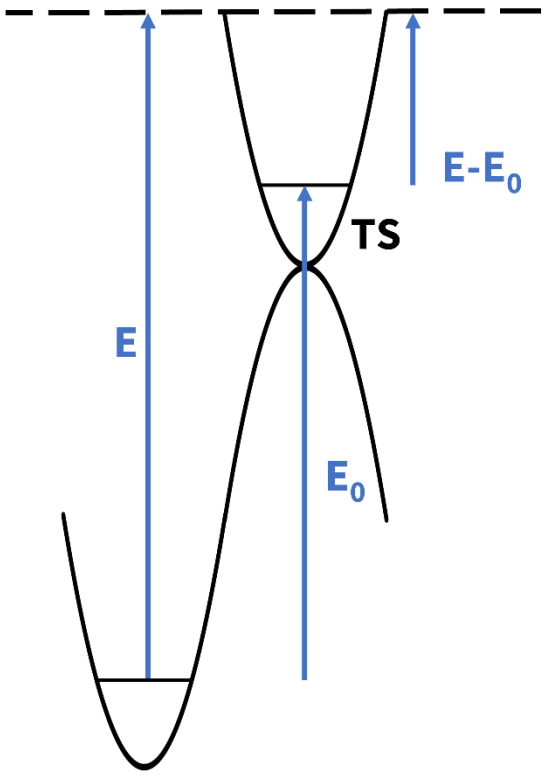

Figure 2-9: Energy level diagram to show the relationship between E and E_0.

The equation that defines the microcanonical rate constant (k(E)) is given in equation 2-4 where σ is the reaction degeneracy, the number of ways that the given reaction can proceed from the reactant molecule; h is Planck's constant, $N^{\ddagger}(E\text{-}E_0)$ is the 'sum of states' for the transition state at an internal energy of $E\text{-}E_0$; ρ(E) is 'density of states' of the reacting ion at an internal energy of E. The relationship of E and E_0 is given in Figure 2-9.[51]

$$k(E)= \frac{\sigma}{h}\frac{N^{\ddagger}(E\text{-}E_0)}{\rho(E)} \qquad (2\text{-}4)$$

$N^{\ddagger}$ represents the number of ways the energy can be distributed among the 's' number of oscillators. Giving equal weighting to each of the configurations, they are all summed.[51] Therefore, $N^{\ddagger}(E\text{-}E_0)$ reflects the number of ways to pass through the TS that has total energy $E\text{-}E_0$ (Figure 2-9), thus the number of ways the reaction can proceed to products. The more ways to proceed to products, the higher the rate constant k(E). ρ represents the number of ways the energy, E, can be distributed

amongst the rotational-vibrational states of the reacting molecule.[51] The more ways the energy is distributed, the more ways it cannot find its way into the critical oscillator.

An important part of the statistical processing is the determination of the activation entropy ($\Delta S^{\ddagger}$) and how this can affect how fast or slow the reaction proceeds.[52] Transition states that are less constrained than the reactant ion have a positive $\Delta S^{\ddagger}$ value, a typical example are bond-cleavage reactions, as the atoms are simply pulling away from each other. Where the transition state is more constrained than the reactant ion the $\Delta S^{\ddagger}$ value is negative, for example rearrangement processes.

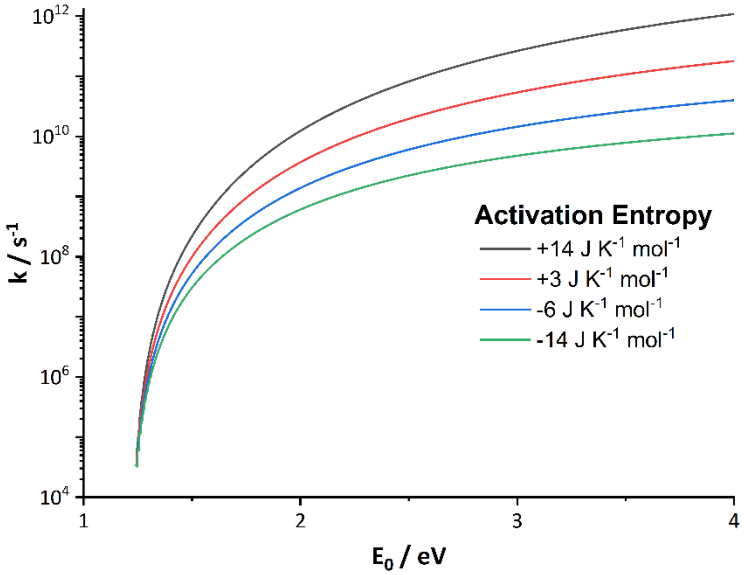

Figure 2-10: How the rate of reaction changes in RRKM according to the activation entropy using methyl chloroformate ion dissociation of a Cl neutral as an example.

Since the value of the $\Delta S^{\ddagger}$ is determined by the geometry of the transition state compared to the reactant ion, ab initio vibrational frequency values can be used to determine $\Delta S^{\ddagger}$ directly. If the TS geometry is not known, for example for a barrierless bond cleavage reaction then the $\Delta S^{\ddagger}$ can be estimated and changed according to the BD or TOF RRKM fitting.

A positive $\Delta S^{\ddagger}$ causes the rate to increase rapidly with increasing photon energy and will therefore dominate particularly at higher energies, shown in Figure 2-10. The opposite is true for a negative $\Delta S^{\ddagger}$ this allows channels that have a higher activation energy to dominate at higher energies, despite being energetically less favourable.

The process by which the computer program that is used (minimal-pepico) operates by is summarised in Figure 2-11.[53] The program includes the physical parameters of the ion optics in the iPEPICO experiment, the internal energy distribution of the parent ion (obtained based on the neutral temperature, shifted up by the photon energy less the adiabatic ionization energy) and the statistical rate constant for each reaction to calculate theoretical branching ratios and TOF distributions, which are then compared to the experimental data. Adjusting the various k(E) curves for the observed reactions is done manually and the results visually and mathematically compared to the experimental data to achieve the best fit possible.

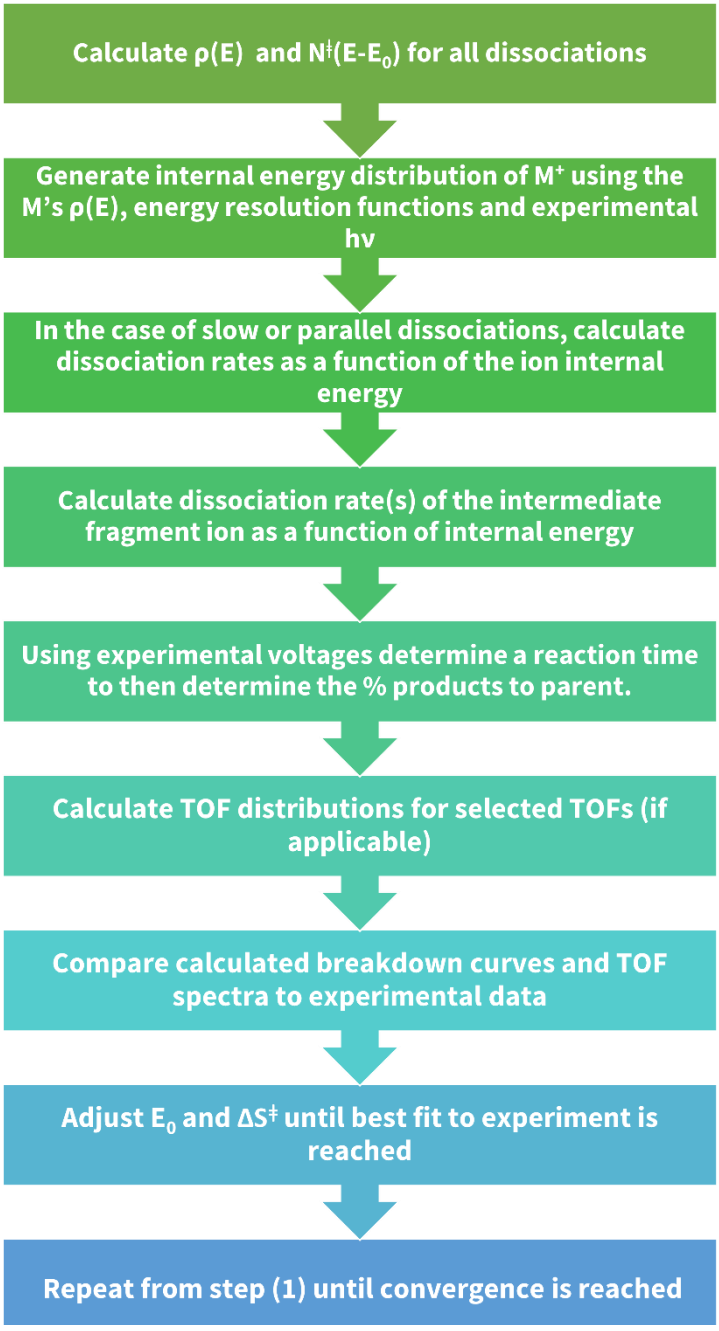

Figure 2-11: Flow diagram depicted the process by which minimalpepico determines the fitting of a breakdown curve or TOFs from iPEPICO data and RRKM.

RRKM theory is used to calculate k(E) according to equation 2-4.[51,54] Rovibrational densities and sums of states are calculated using M06-2X/aug-cc-pVTZ rotational constants and harmonic vibrational frequencies by the direct count algorithm of Beyer and Swinehart.[55] The DFT-calculated rate-limiting transition states combined with the CBS-QB3-computed activation energies

serve as a starting point for the fitting procedure. The fit is optimised to reproduce the measurement within its signal-to-noise ratio by scaling the lowest five transition state vibrational frequencies, to adjust the entropy of activation $\Delta^{\ddagger}S$, and barrier heights. Frequency multiplication factors less than one increase, while values greater than one decrease, $\Delta^{\ddagger}S$.[54] The agreement between the experimental and theoretical breakdown curves was thus achieved by varying only $\Delta^{\ddagger}S$ to minimize the error function:

$$\text{Error}=1-\frac{\sum_i e_i m_i}{\sqrt{\sum_i e_i^2 \sum_i m_i^2}} \tag{2-5}$$

Where e_i and m_i refer to experimental and modelled fractional ion abundances in the breakdown diagram as well as TOF channel counts, weighted so that breakdown diagram and TOF modelling errors influence the fit in a balanced way.

2.4. Mass-analysed Ion Kinetic Energy Spectroscopy

2.4.1. Experimental Set-up

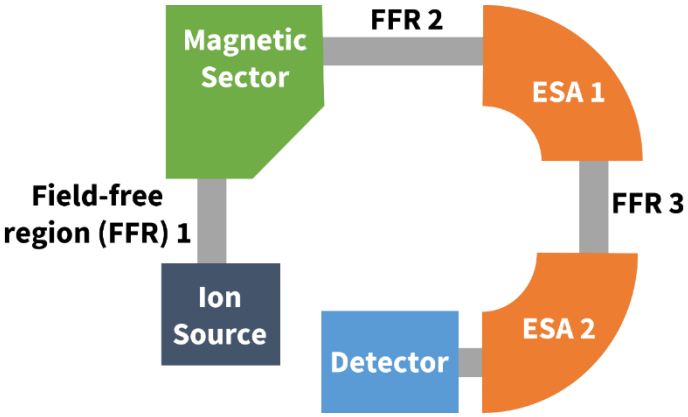

Figure 2-12: Schematic of the modified VG-ZAB instrument.

For the ion chemistry of phenyl chloroformate in chapter 6 MIKES was performed. This is completed at the University of Ottawa using a modified VG-ZAB mass spectrometer. The outline for the mode of operation is given in Figure 2-12. The sample is introduced as vapour into the ion source through a heated septum using a syringe, where it is ionised using electron ionisation. The ions are then accelerated to the magnetic sector where the ions are separated according to mass and the ion of choice can be selected.[56] The selected ions then pass through to the second field-free region (FFR). The metastable ions undergo dissociation, those with sufficient internal energy to dissociate within the FFR, with no collisions. The resulting ions are detected in the first electrostatic analyser (ESA) according to their kinetic energy.[57]

2.5. Computational Methods

2.5.1. Basis Sets

Basis sets are linear combinations of basis functions to create molecular orbital approximations. Basis functions are comprised of a linear combination of wavefunctions, each are solutions to the Schrödinger equation. The variational method is applied to optimise the coefficients for the basis functions, with the criteria being to find the lowest energy. A typical basis set is made up of a linear

combination of atomic orbitals (LCAO), where each atomic orbital (AO) function is centred on its respective nuclei. The AOs can be Slater-type orbitals (exact hydrogenic orbitals) which are computationally heavy or Gaussian-type orbitals (GTO), where a Gaussian approximation is used. To better account for the molecular orbital shape in GTOs multiple basis functions are used for each AO. The number of basis functions applied to each AO is defined in the notation as shown in Figure 2-13 using a double zeta basis set as an example. Triple zeta basis sets can be applied which instead of 2 sets of basis functions adds 3 sets of basis functions to the valence orbitals.

Polarisation functions are added throughout the studies to improve the accuracy by accounting for

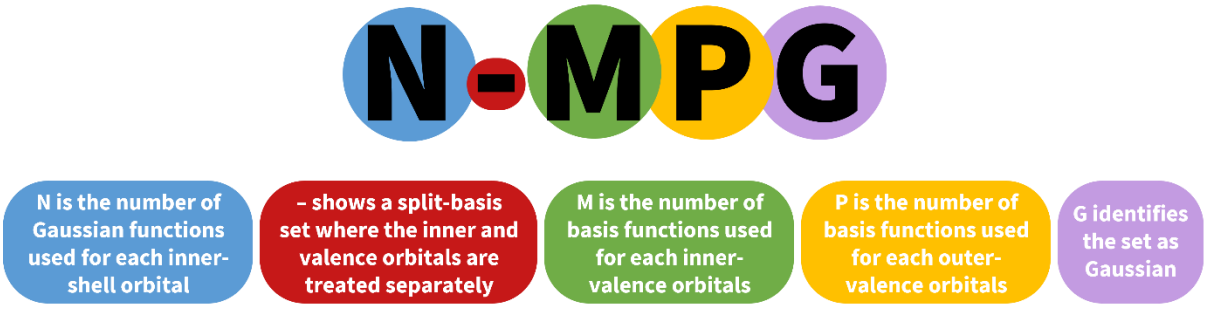

Figure 2-13: Gaussian basis set notation summarised.

the polarizability of the molecules, it does this by adding these functions to the atoms defined in the basis set. Throughout the forthcoming chapters d,p polarisation is specified which adds the polarisation function d to second row atoms only and p polarisation function to hydrogen atoms.

Diffuse functions are also added to the basis set to help describe the electronic structure of the outermost electrons and account for the long-range electron density. This is useful for systems that have weak intermolecular interactions, such as Van-der-Waals, therefore particularly helping in transition state determination. These are denoted by + or ++ depending on the number and application of the diffuse functions.

2.5.2. Correlation methods

Density functional theory (DFT) calculations were performed. DFT methods were adapted from Hartree-Fock methods that assume electrons move in an average potential generated by all of the other electrons without accounting for the interactions between them, known as electron correlation. However, DFT treats electron correlation differently by using Kohn-Sham equations, which includes contributions from both exchange (the repulsion between identical electrons) and correlation (the tendency of electrons to avoid each other), known as the exchange-correlation functional. Hybrid functionals between Hartree-Fock exchange and DFT-exchange correlation can improve the accuracy of the calculations.

B3LYP is used in this study which includes local (short-range) and non-local (long-range) exchange contributions, while staying less computationally intensive for the geometry optimisations. The commonly used B3LYP methods used in the chapters is B3LYP/6-311++G(d,p) which is a triple zeta, split valence basis set with the inclusion of diffuse and polarisation functions. This provides a good balance between a complete basis set and computational efficiency and is used for geometry optimisations as a result.

Similarly, M06-2X-GD3/aug-cc-pVTZ is used throughout the chapters which is also a DFT method used for geometry optimisations. Zhao's and Truhlar's M06-2X functional is specified including Grimme's empirical dispersion correction (GD3) and the cc-pVTZ and aug-cc-pVTZ basis sets of Dunning.[58–60] The 'aug' specifies diffuse functions applied to 'augment' the basis set, 'cc-p' stands for 'correlation-consistent polarised', 'V' shows they are valence-only basis sets and 'TZ' stands for triple zeta.

CCSD(T)[61,62] is also specified in the chapters to refine the energetics by completing a single-point energy calculation. CC specifies a coupled-cluster method that takes the basic Hartree-Fock

molecular orbital method and to account for electron correlation uses multi-electron wavefunctions that use the exponential cluster operator. SD(T) allows for the number of excitations, single, double and triple respectively for S D and T. It is a much more computationally heavy method; however, it produces some of the most accurate energetics for small molecules.

2.5.3. Composite Methods

For more accurate energy determinations, single point composite calculations were implemented. These are more computationally intensive so were chosen to be energy calculations from the already determined geometries from the previously discussed B3LYP or M06 DFT methods. Composite methods apply more complete basis sets and then extrapolate to obtain the best energy approximation. The composite methods applied are CBS-QB3[63] and the more recently developed SVECV-f12 method of Ventura et al.[64] The former delivers reasonably accurate energetics at a moderate computational cost.[63] The latter is specially developed to give more accurate approximations for reaction barriers in particular.[64] The basis sets that are applied before complete basis set extrapolation are shown in Figure 2-14.

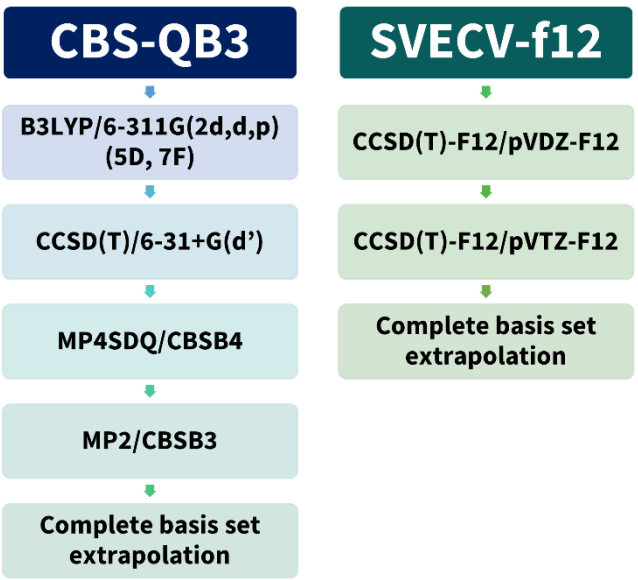

Figure 2-14: Flow chart showing the basis sets applied in the composite methods, CBS-QB3 (left) and SVECV-f12 (right).

Chapter 3. Probing the Pyrolysis of Methyl Formate in the Dilute Gas Phase by Synchrotron Radiation and Theory

3.1. Published Contributions

B. Lowe, A. L. Cardona, J. Salas, A. Bodi, M. A. Burgos Paci and P. M. Mayer, *J. Mass Spectrom.*, 2022, **57**, e4868.

B. Lowe, with supervision from P. M. Mayer, completed experimental data processing for the iPEPICO data and wrote the accompanying sections along with the introduction.

A. L. Cardona along with assistance from J. Salas and supervised by M. A. Burgos Paci completed the computational side including the Gaussian calculations and statistical modelling, writing the methods and findings in the accompanying sections.

A. Bodi assisted with work completed at the Swiss Light Source.

3.2. Introduction

The need for oxygenated fuel additives, designed to decrease particulate matter emissions, has led to the increased release of formates into the atmosphere. These formates are also produced in the atmosphere through reactions involving volatile organic compounds (VOCs).[65,66] Understanding the role that these molecules play in atmospheric chemical processes is therefore of importance. Methyl formate (MF) is a colourless liquid with a high vapour pressure which is commonly used as a quick-dry finishing solvent in resins, a cooling agent, and a precursor to other molecules in the chemical industry.[67] It is also produced in the atmosphere from oxidation of VOCs, such as ethyl vinyl ethers, with $^{\bullet}OH$, NO_3 and O_3.[26,27] In addition, methyl formate is a good model compound to understand the

chemistry of more complex esters used in the production of and found in biodiesel.[65,66,68] When such esters experience high-temperature combustion environments, they may also decompose to smaller molecules or ions, such as $CH_3OCO^{\bullet}$, CH_3OH, and CO.[69] The combination of the atmospheric presence of these molecules and the high engine temperatures that these formates are exposed to make the pyrolysis pathways significant in the determination of the atmospheric fate of these molecules.

The increasing interest in biofuel development has inspired several studies on methyl formate combustion chemistry. The generally accepted mechanism was developed by Dooley et al.[40] from shock tube experiments. They showed the major MF decomposition pathways to be hydrogen abstraction, with reactions (3-1) and (3-2) contributing 31% and 17%, respectively. The remaining MF is decomposed in unimolecular processes outlined in reactions (3-3) and (3-4), which contribute to 38% and 3% to the total methyl formate decomposition.[68]

$$CH_3OCHO+O \rightarrow CH_3OCO + OH \quad (3\text{-}1)$$

$$CH_3OCHO+OH \rightarrow CH_3OCO + H_2O \quad (3\text{-}2)$$

$$CH_3OCHO \rightarrow CH_3OH + CO \quad (3\text{-}3)$$

$$CH_3OCHO \rightarrow CH_4+CO_2 \quad (3\text{-}4)$$

Dooley also saw CH_2O as a product, however, attributed it to the sequential thermal decomposition of methanol (3-5).

$$CH_3OH \rightarrow CH_2O+H_2 \quad (3\text{-}5)$$

This is in contrast to computational studies by Francisco[70] suggesting the direct decomposition of CH_2O from MF (3-6).

$$CH_3OCHO \rightarrow CH_2O+CH_2O \quad (3\text{-}6)$$

Dooley disregarded this option because the activation energy calculated by Francisco, when inserted into his kinetic model, did not match his experimental results.[40] In this study, we employ low-pressure pyrolysis to study primarily unimolecular decomposition processes as a function of temperature, identifying the products by photoion mass-selected threshold photoelectron spectroscopy (ms-TPES). To distinguish neutral decomposition from dissociative ionization conclusively, it is important to know the chemistry and fragmentation paths of the MF radical cation. $MF^{+\bullet}$ decompose to $CH_3OH^{+\bullet}$ + CO at low internal energies,[71] then the fragments CH_2OH^+ + $HCO^\bullet$ dominate above 11.8 eV.

3.3. Experimental Procedures

The experiments were carried out at the Swiss Light Source (SLS, Paul Scherrer Institut, Villigen, Switzerland) using imaging photoelectron photoion coincidence (iPEPICO) spectroscopy at the VUV beamline, the details of which have been described thoroughly elsewhere.[72,73] Pyrolysis was carried out using the high-temperature pyrolysis microreactor previously described for this endstation.[44,74] Synchrotron radiation with 3 meV energy resolution was dispersed using a 600 grooves/mm grating, the higher harmonics filtered out using a differentially pumped gas filter filled with 9 mbar of a Ne:Ar mixture over 10 cm optical length. The resulting monochromatic VUV radiation photoionises molecules in a 2×2 mm^2 interaction region. Both photoions and photoelectrons were velocity-mapped on imaging RoentDek delay line detectors. The electrons are time- and position-stamped at the detector, and the delayed, coincident photoion signal is evaluated to obtain the time-of-flight mass spectrum. Threshold photoelectrons are detected at the centre of the electron detector, whereas non-zero-kinetic energy ("hot") electrons are detected according to their off-axis momentum. Hot electrons without an initial lateral momentum component also have a trajectory to hit the centre spot. The mass spectrum based on electrons detected in a ring around the centre spot

is used to subtract the hot electron contamination from the centre signal to obtain the threshold photoionisation mass spectrum.[75] Plotting the normalized intensity of a peak with a particular *m*/*z* ratio from these mass spectra as a function of photon energy yields the photoion mass-selected TPES, ms-TPES.[76]

Pyrolysis experiments were performed by passing argon, at a pressure of 1.8 bar and a flow rate of 1 sccm, over a vial cooled to 8 ^{o}C and containing the sample. At this temperature, the methyl formate vapor pressure is ca. 380 mbar.[77] This mixture was further diluted with argon to a flow of 41 sccm, resulting in about 0.5% sample in argon, which expanded through a 100 μm pinhole into the 3 cm long, 1 mm internal diameter, resistively heated SiC pyrolysis microreactor. Reactor surface temperatures had been measured in an identical pyrolysis setup by a type C thermocouple, and the reactor temperatures herein have been derived based on the previously observed power dependence (3-7):

$$T/°C = P/W \times 14.27 + 303 \qquad (3\text{-}7)$$

Where *T* is the reactor temperature and *P* is the heating power. The reactor temperature is considered to represent the gas temperature inside the reactor to within 100 ^{o}C.[78] The pressure and residence time in the reactor has been estimated to be 10–40 mbar and up to 100 μs, respectively.[78,79] The reactor is placed in the source vacuum chamber, where the pressure was ~ 5 × 10^{-5} mbar during measurements. The molecular beam exiting the pyrolysis reactor passed through a 2 mm diameter skimmer into the detection chamber, kept at a pressure of 10^{-6} mbar during measurements. Cation velocity map imaging means we could select only ion signals from the molecular beam portion of the ion image (Figure A1-1 of appendix 1), disregarding the scattered, re-thermalized background signal (Figure A1-2), thereby selecting unambiguously pyrolysis products

exiting the furnace. Temperatures between 200 and 1000 °C can be explored as a function of photon energy to probe the distribution of pyrolysis products as a function of temperature.

3.4. Computational Details

3.4.1. Electronic Structure Calculations

The optimized structures and thermochemical properties for stationary points in the calculated reaction pathways were obtained using density functional theory (DFT) with Zhao´s and Truhlar´s M06-2X[58] functional including Grimme´s empirical dispersion correction (GD3)[59] and the cc-pVTZ basis set of Dunning.[60] For transition states, intrinsic reaction coordinate (IRC) calculations were carried out to confirm that they connect the proposed reactants and products. Single-point energy calculations with coupled cluster singles and doubles including perturbative triples correction CCSD(T)[61,62] were performed at the DFT-optimized geometries. In addition, the CBS-QB3 composite method was also used, which delivers reasonably accurate energetics at a moderate computational cost.[63] The Franck–Condon simulation of the MF TPES was carried out at the B3LYP/6-311++G(d,p) level of theory. All electronic structure calculations were carried out using Gaussian 16.[80]

3.4.2. Kinetics

The kinetics calculations were carried out using the *thermo* and *ktools* programs of the MultiWell suite[81–83] over the temperature range of 300–2500 K. The molecular channels were calculated using canonical transition state theory (TST) with Eckart asymmetric tunnelling correction.[84] For dissociation channels, canonical variational transition state theory (CVTST) was used to locate the transition state assuming that the path corresponded to a bond being broken, *i.e.,* a barrierless reverse association channel. Constrained geometry optimizations were carried out at fixed C–O and O–C bond distances depending on the case (Figures A1-4 and A1-5), starting with 30 points with a step size of 0.03 Å. The optimized geometries at each point were used to obtain the rotational

constants, the vibrational zero-point energy (ZPE) corrections and frequencies orthogonal to the reaction path. The CVTST rate constant for a given temperature is identified as the minimum "trial" CVST rate constant as a function of distance along the reaction coordinate.[85–87] Using the simulated kinetics constants, a sensitivity analysis was performed using the KINTECUS[88] program to determine the weight of the proposed dissociation pathways at different pyrolysis temperatures.

3.5. Results and Discussion

MF pyrolysis mass spectra recorded at a photon energy of 14 eV and at varying pyrolysis temperatures are presented in Figure 3-1. The mass spectrum at 474 °C shows peaks at *m/z* 60 (MF^+ = methyl formate radical cation), 32 (CH_3OH^+), 31 (CH_2OH^+) and 28 (CO^+) with the assignment given in brackets. The *m/z* 18 peak corresponds to water, present in the chamber as background.

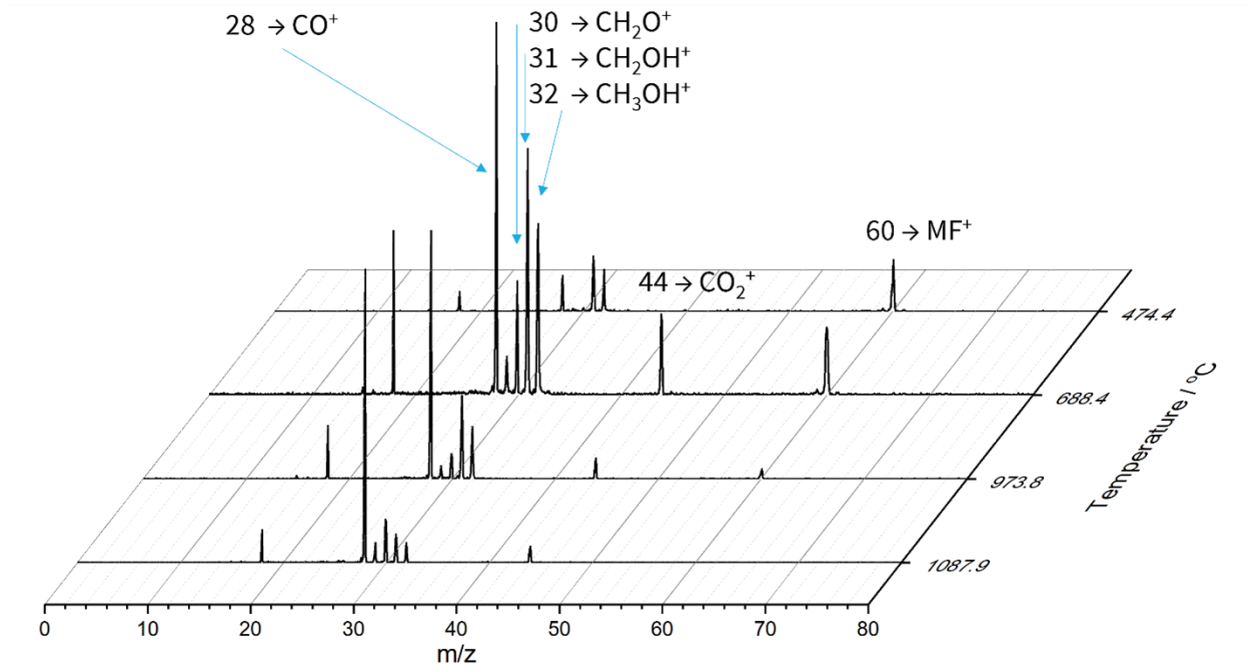

Figure 3-1: Mass spectra over varying pyrolysis temperatures recorded at 14 eV photon energy.

When the pyrolysis temperature is increased to 688 °C and beyond, new peaks appear in the mass spectrum at *m/z* 44 (CO_2^+), 30 (CH_2O^+), and 29 (CHO^+). It is also observed that the intensity of the *m/z*

60 peak decreases when the temperature increases. The most abundant peaks are in accordance with previous studies.[40,68,84]

To confirm the isomeric identity of the spectral carriers of the *m*/*z* peaks, the corresponding ms-TPES were extracted and compared with the literature. Figure 3-2 shows the TPES for *m*/*z* 60, ionized MF, at 688 °C.

The origin band at 10.83 ± 0.01 eV agrees with the ionization energy reported by Waterstradt et al. using threshold electron detection[89] and a recent He(I) photoelectron spectrum by Nunes et al.[90] The peaks following show the presence of vibrational structure: the spacing of 832 cm^{-1} corresponds primarily to a stretching vibration of the methyl carbon and the adjacent oxygen and that of 1485 cm^{-1} corresponding to a methyl group deformation, which were confirmed by Franck–Condon simulation of the spectrum, shown in red in Figure 3-2.

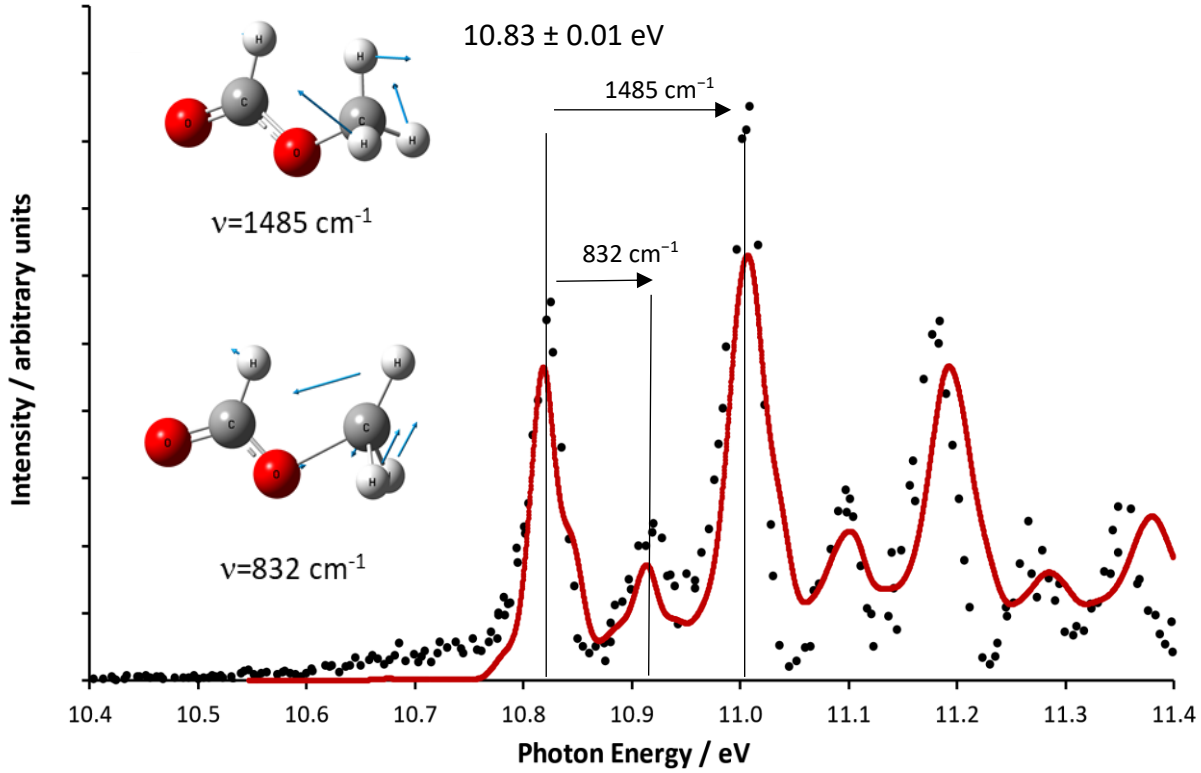

Figure 3-2: ms-TPES for m/z 60 (black markers), methyl formate, obtained at a pyrolysis temperature of 688 °C with a FC-simulation overlaid (solid red curve).

Figure 3-3 shows the ms-TPES for *m/z* 30 (CH_2O). This TPES exhibits a single peak at 10.88 ± 0.01 eV, which corresponds to the ionization energy of formaldehyde, 10.889 eV.[91] This is also in agreement with the PEPICO studies completed by Nishimura et al.[71]

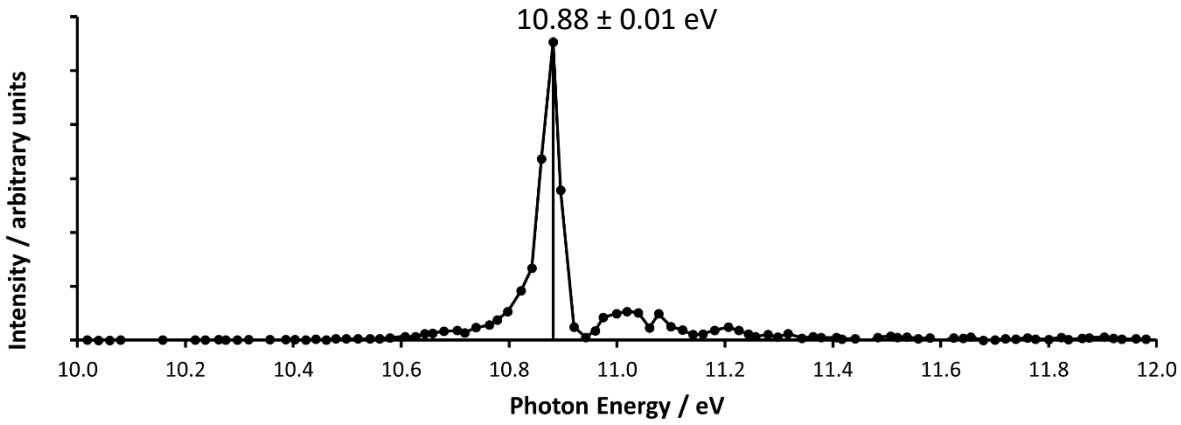

Figure 3-3: ms-TPES for CH_2O, m/z 30, obtained at a pyrolysis temperature of 974 °C.

The ms-TPES for *m/z* 31 is shown in Figure 3-4. The peak indicated in red (10.88 eV) in the figure is the residual $^{13}CH_2O$ signal after correction based on the *m/z* 30 ms-TPES (Figure 3-3) and is likely an artefact. Dooley et al. showed that $CH_3O^{\bullet}$ is produced when the $CH_3OCO^{\bullet}$ radical (formed by hydrogen abstraction from methyl formate) itself decomposes by reaction (3-8).[68]

$$CH_3OCO \rightarrow CH_3O + CO \qquad (3\text{-}8)$$

However, the spectrum in Figure 3-4 exhibits a gradual onset starting from 10.72 eV and the profile is similar to that obtained by Yu et. al.[92] for CH_2OH^+ produced from the dissociative photoionization of methanol. The authors complemented the TPES spectrum with theoretical modelling and assigned m/z 31 to CH_2OH^+. In addition, this TPES was completed at 974 °C where neutral MF (and thus the radical cation) is in very low abundance (see Figure 3-1), so producing this amount of CH_2OH^+ from $MF^{+\bullet}$ dissociation is unlikely. Furthermore, if neutral $^{\bullet}CH_2OH$ were made by pyrolysis, it would be observed at much lower photon energy than its onset in Figure 3-4 because of its low ionization energy of IE(CH_2OH) = 7.56 eV.[93] Finally, the recently measured TPES of $CH_3O^{\bullet}$ by Tang et al.[94] shows a discrete band at 10.72 eV, which is not observed in the present study, confirming that the peak corresponds to CH_2OH^+ from the dissociative photoionization of methanol.

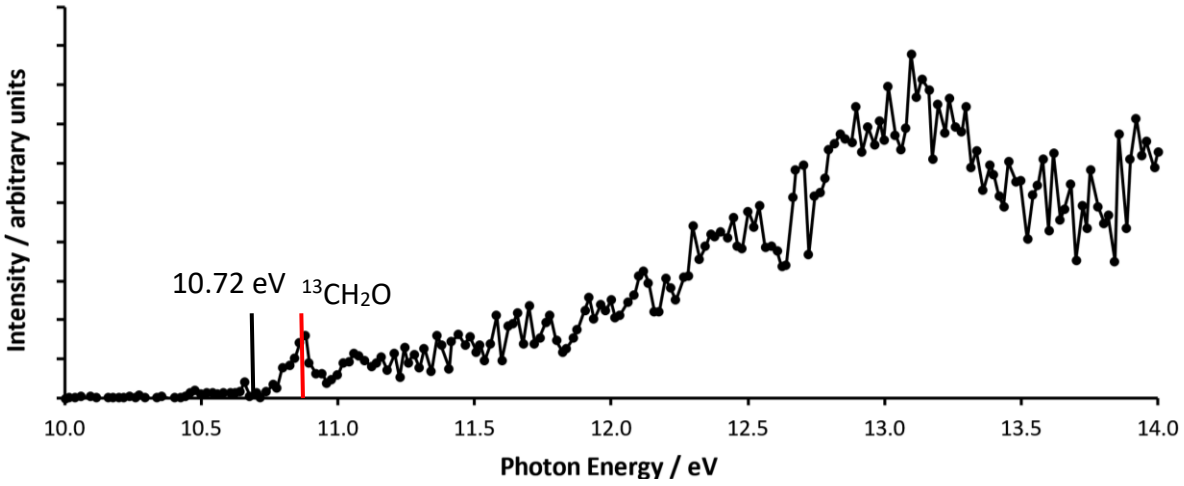

Figure 3-4: ms-TPES for m/z 31 obtained at a pyrolysis temperature of 974 °C.

Methanol radical cations are known to be a product of the dissociative photoionization of methyl formate, but the appearance energy for this process is 11.58 eV,[95] higher than that shown in Figure 3-5, indicating that neutral methanol is also being formed by pyrolysis and then ionized. However, at lower temperatures (and thus higher methyl formate radical cation abundance), we also observed a contribution to *m*/*z* 32 from the dissociative ionization of MF.

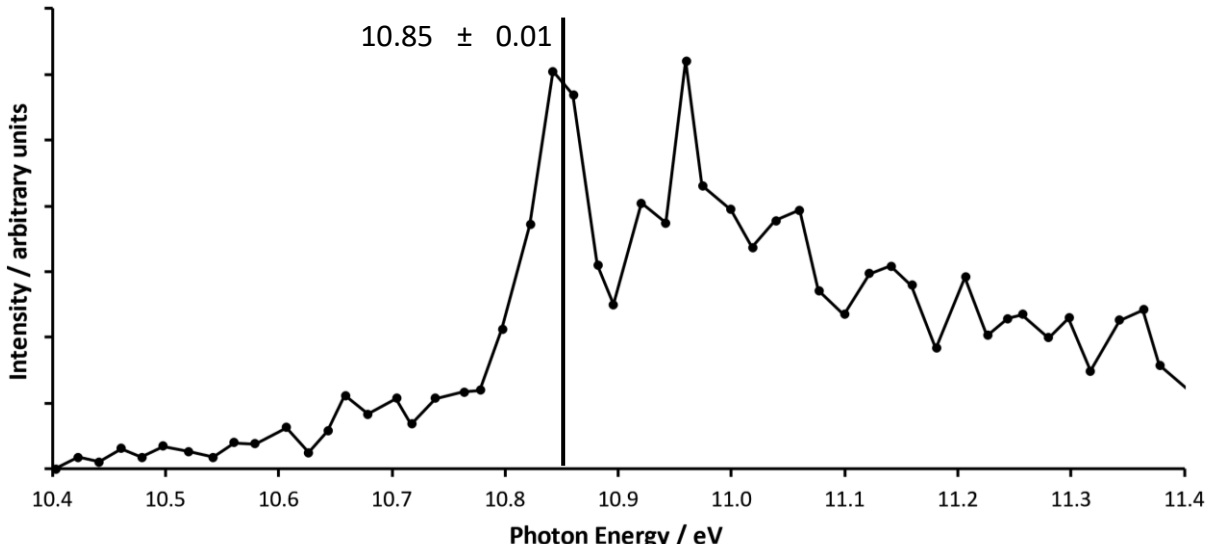

Figure 3-5: ms-TPES for CH_3OH, m/z 32, obtained at a pyrolysis temperature of 974 °C.

3.5.1. Reaction Pathways and Kinetics

Ground state reaction mechanisms for the thermal decomposition of methyl formate were evaluated using ab initio calculations. Six channels were postulated (Figure 3-6), which explain the final products found by experiment, plus two homolytic bond cleavages to form $CH_3O^{\bullet}$ + $HCO^{\bullet}$ (D_{O-C}) and $CH_3^{\bullet}$ + $HCO_2^{\bullet}$ (D_{C-O}). The formyl hydrogen atom is presented in red in the figure.

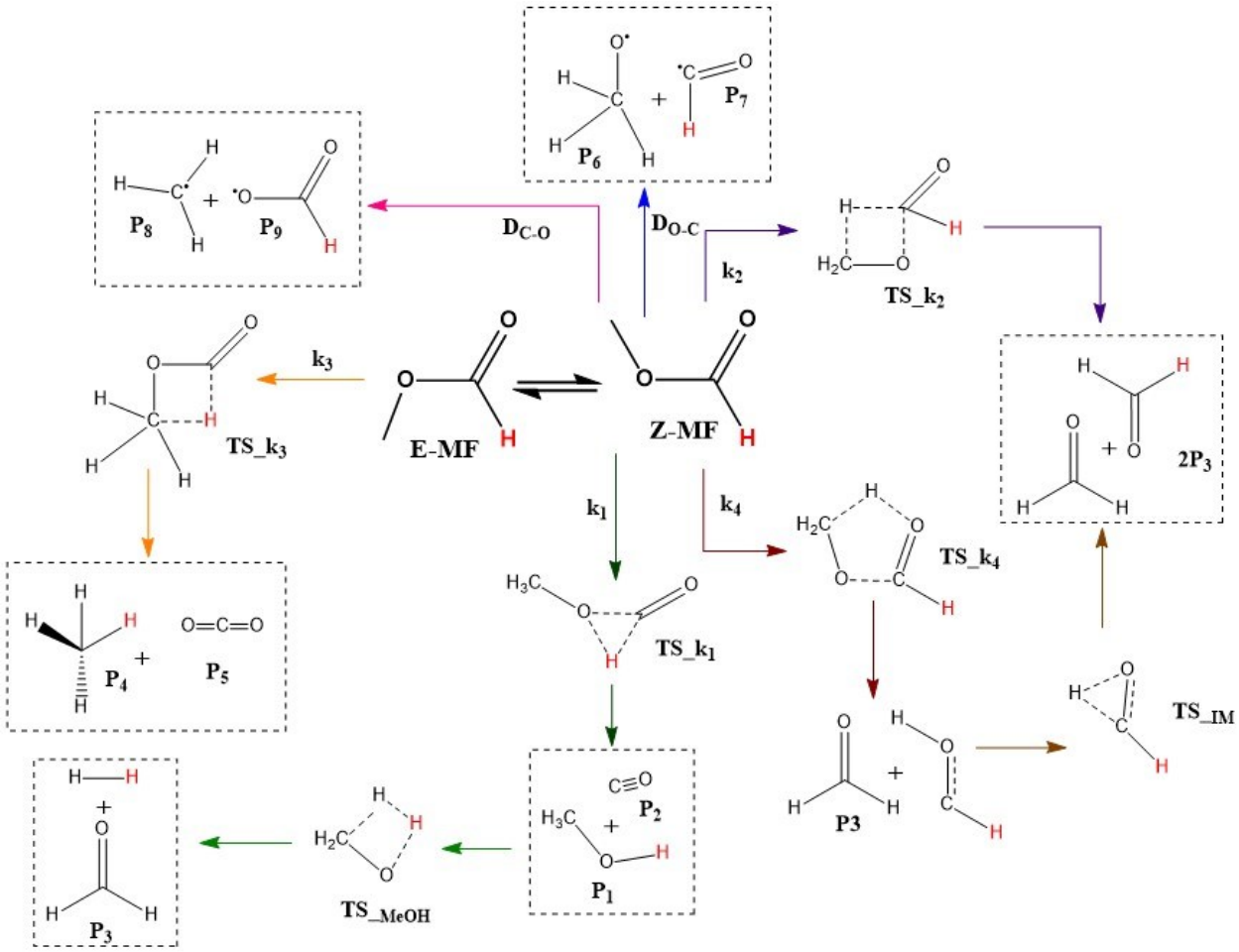

Figure 3-6: Unimolecular dissociation mechanisms for MF. To highlight hydrogen migration, the formyl hydrogen atom is shown in red.

Five channels start from the most stable conformer *Z*-methyl formate (Z-MF). $D_{O–C}$ and $D_{C–O}$ correspond to direct homolytic fission and are barrierless paths with loose transition states. The first one corresponds to the homolytic dissociation of the O–C bond to give $HCO^{\bullet}$ and $CH_3O^{\bullet}$ radicals and channel $D_{C–O}$ yields $CH_3^{\bullet}$ + $HCO_2^{\bullet}$. The other channels give rise to closed-shell products. Channel 1 yields CO and CH_3OH involving a three-centre transition state, TS (TS_k_1). In this case, the hydrogen from the formyl group is part of the TS and interacts with the central O to form the O–H bond of CH_3OH. The second channel involves a four-centre TS (TS_k_2) that dissociates to give two CH_2O molecules. In this case, one H from the CH_3 fragment is involved in the TS and migrates from the CH_3

to the CH=O moiety. In the third channel, isomerization from the *Z* to the *E* conformer takes place first, followed by a four-centre TS, TS_k_3, which dissociates to give CH_4 and CO_2 as final products. In this four-centre TS, the formyl H interacts with the methyl carbon to form CH_4. Channel 4 gives, through a five centre TS (TS_k_4), CH_2O and hydroxy methylene fragment HOCH that further isomerizes to CH_2O (TS_k_{IM}). Molecular structures for these TS's are presented in Figure 3-7, and the optimized structures for MF conformers and reaction products are included in appendix 1.

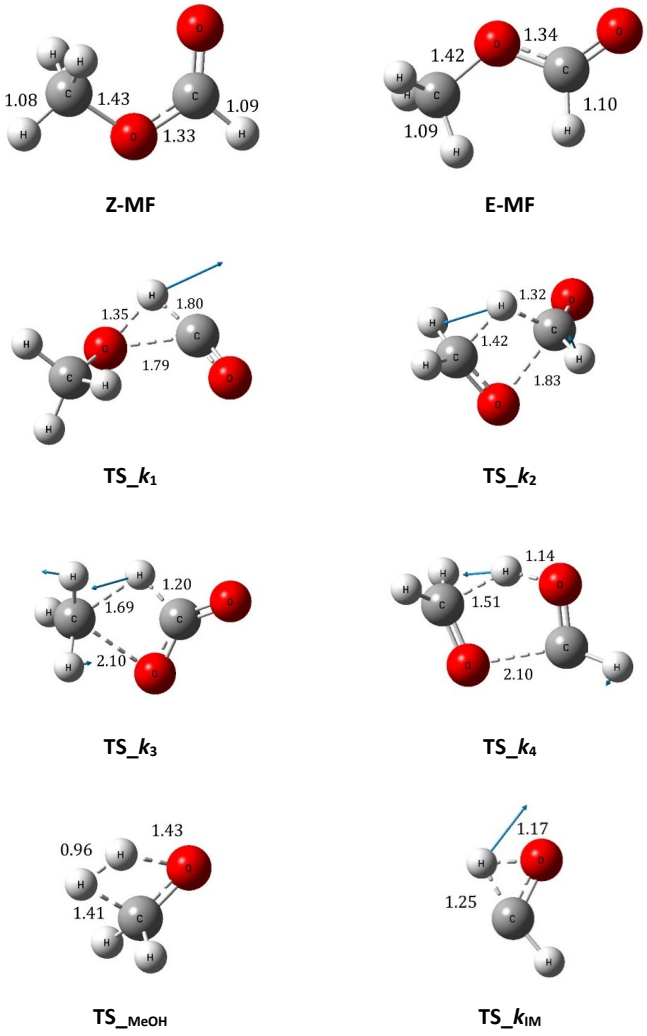

Figure 3-7: Optimized geometries at the M06-2X-GD3/cc-pVTZ level of theory of the MF conformers and transition states for decomposition (bond lengths in Å). Blue arrows illustrate the normal mode with the imaginary frequency, corresponding to the reaction coordinate, in each TS.

The minimum energy reaction surface for the thermal decomposition of MF is depicted in Figure 3-8 and the calculated energies are presented in Table A1-1. The difference in the activation energy

values between the three methods is less than 12 kJ mol^{-1} (ca. 4%). For the final product energies, the three methods give more of a spread with deviations of 25% for route 1 and 12 % for the other routes. Inspection of Figure 3-7 and Table A1-1 indicate that the first step of channel 1 has the lowest activation energy (TS_k1), followed by TS_k2. The next TS is TS_k3 that is close in energy with the homolytic D_{O-C} and D_{C-O} paths. TS_k4 has the highest energy from reagent and TS_k_{IM} corresponds with the highest energy TS of the PES and corresponds to the isomerization of the HC=OH intermediate. The second step of channel 1, which is the dissociation of CH_3OH to CH_2O and H_2 (TS_$_{MeOH}$) is also a high energy path.

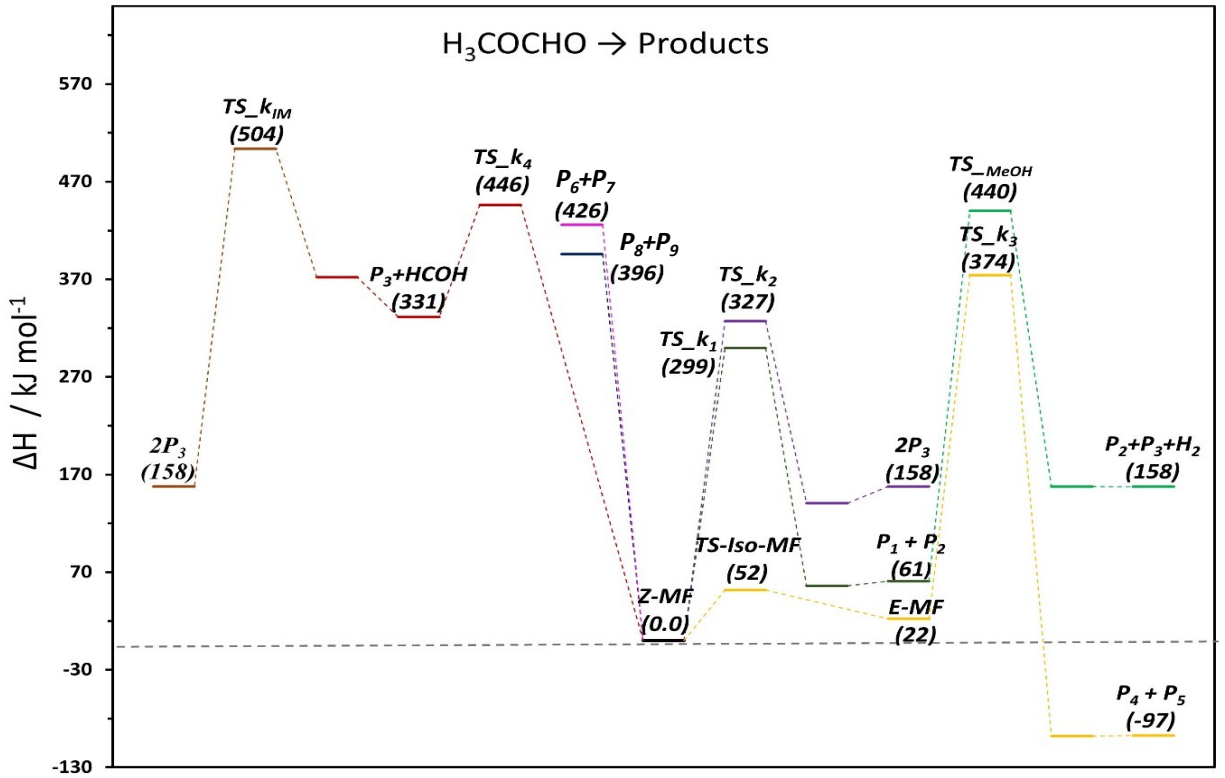

Figure 3-8: Minimum energy reaction pathways for the thermal decomposition of MF at the M06-2X-GD3/cc-pVTZ level of theory.

3.5.2. Kinetic Analysis

Theoretical rate constants for the decay channels discussed in the previous section are tabulated in Tables A1-1 and A1-3 in appendix 1. They correspond to two bond fission channels with loose TS

($k_{D\_C–O}$ and $k_{D\_O–C}$) and four isomerization channels over tight TS (k_1 to k_4). Our calculations estimate that the decomposition rate of MF to methanol and carbon monoxide is the dominant channel compared to the other molecular channels. However, when the temperature increases, the fission channel of the O–C bond begins to be more favoured.

From the rate constants calculated for the different channels, a sensitivity analysis for the MF concentration was performed for each temperature. In the sensitivity analysis, coefficients near zero represent reactions with no influence on the concentration of a particular species and positive and negative values indicate sources and sinks, respectively, for that component. The coefficients obtained are presented in Table A1-2.

The coefficients obtained indicate that the prevailing channel is 1. At 474 °C, all the other channels have zero coefficients, so only methanol and CO, the products from this channel are expected to be formed. This result agrees with the species present in the mass spectrum (Figure 3-1) at this temperature: MF^+, CH_3OH^+, CH_2OH^+ (from methanol) and CO^+. Also, when the temperature increases (688 °C, 973 °C and 1087 °C), the other channels are enabled (coefficients are nonzero) so in the mass spectra the signal of MF diminishes, and other products appear (CO_2 and CH_2O).

In general, as the temperature increases, the differences between the computed rate constants decrease, which indicates a broader spectrum of decomposition products, such as formaldehyde, carbon dioxide and methane. This can be observed in Figure 3-9, where the ratio between k_1 and k_2 is depicted as function of temperature with the energies and configurations obtained for the three theoretical methods. As can be seen, the ratio diminishes considerably with temperature, indicating that the rate constants become similar. A similar behaviour is observed for the other channels, shown in appendix 1. It is worth noting that, for the $D_{O–C}$ channel, the rate constant becomes higher than k_1

around 1000 K. The fact that $CH_3O^{\bullet}$ and $HCO^{\bullet}$ are not observed in the experiment indicates that they likely react with surfaces in the furnace, or decompose sequentially.

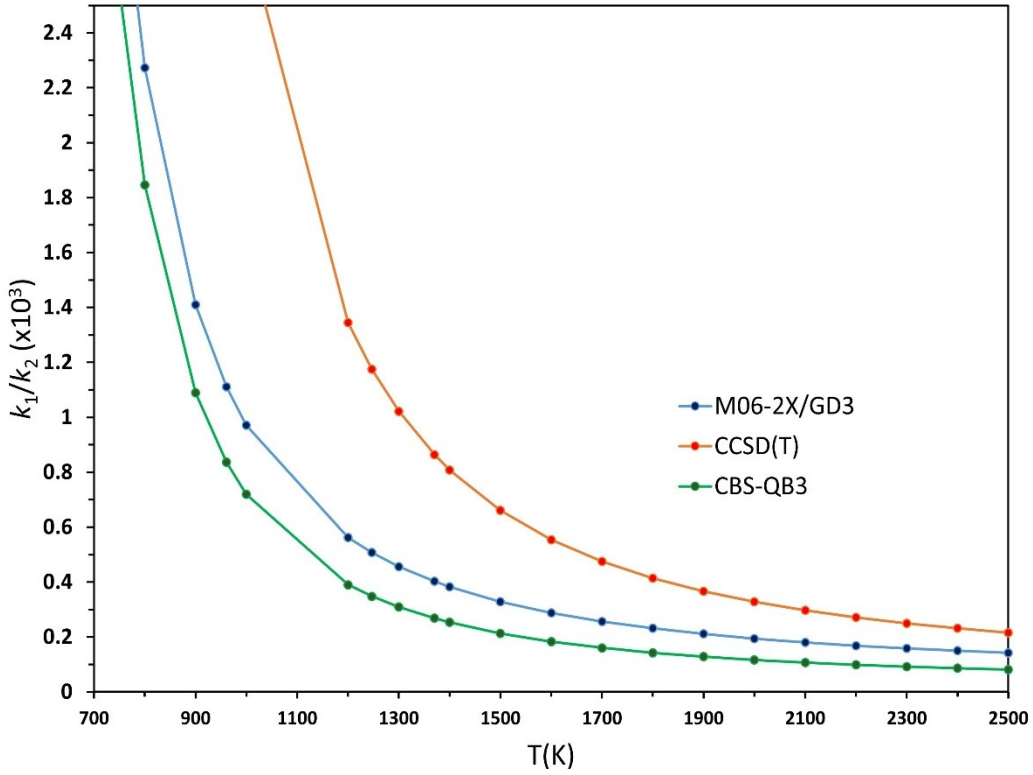

Figure 3-9: Relationship of the theoretical reaction rates k_1 and k_2 as a function of temperature.

In Table A1-3, the Arrhenius parameters calculated from the reaction rate constants are listed at different temperatures. In general, there is good agreement with the values obtained previously[40,96] (Figure 3-10 and Figures A1-16 to A1-20 in appendix 1) but with deviation at low temperatures. Below 1500 K, the partition functions differ by many orders of magnitude making the rate constants very sensitive to the vibrational frequencies from the electronic structure calculations. The CBS-QB3 method presents a non-linear plot due to the known limitations of this method in transition state characterization.[97,98] In addition, it is observed that the trend is similar, especially the increase in the pre-exponential factors of the decomposition channels through bond fission, calculated from loose transition states that are more sensitive to the uncertainty in the kinetic model.

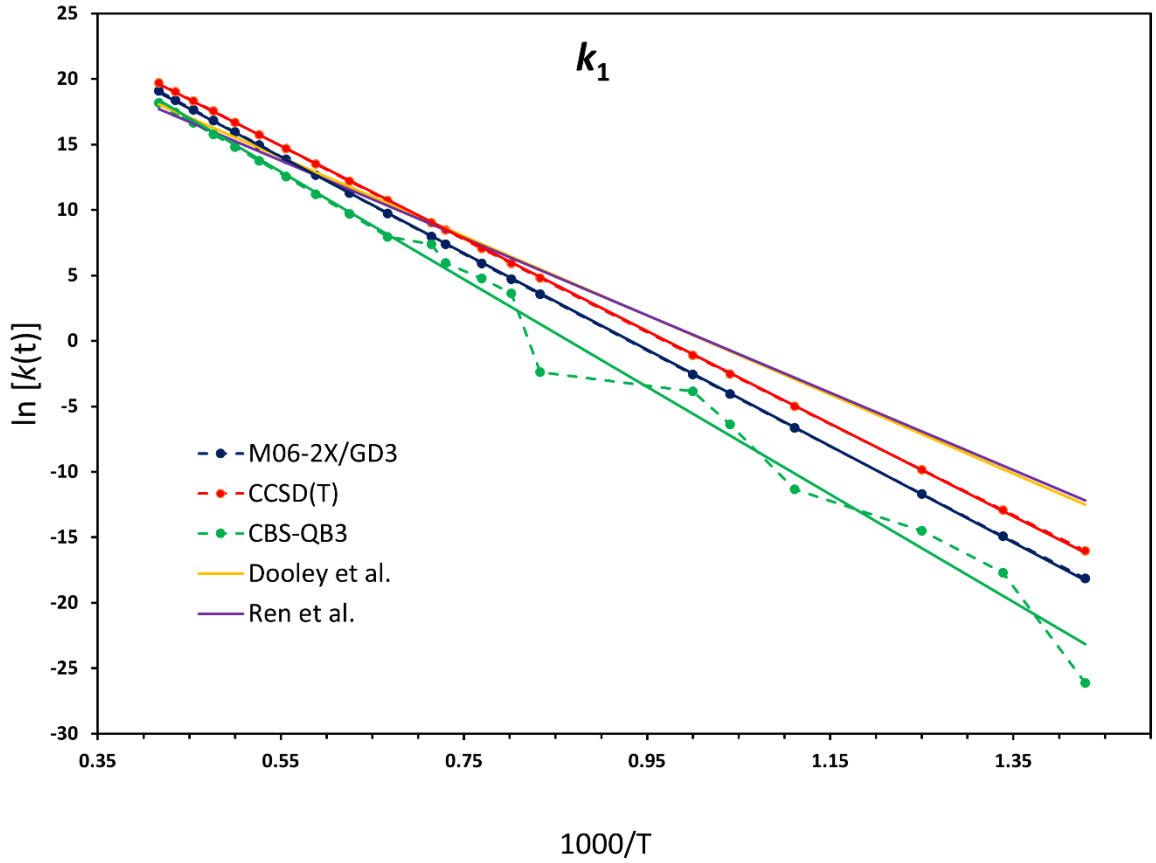

Figure 3-10: Comparison between calculated k_1 with previous experimental values.

3.5.3. Formaldehyde branching ratio

Francisco[70] calculated that CH_2O can come from both the decomposition of MF (our k_2) or from the sequential decomposition of CH_3OH formed in k_1 (via TS_{MeOH}) as deduced by Dooley.[40] The full kinetic model comparing these two pathways is described in appendix 1. Due to the high barrier to methanol decomposition in Figure 3-8, CH_2O formation directly from MF dominates at temperatures below 1200K (Figure 3-11). At 747K, 99.96% of the formed formaldehyde comes directly from MF by path 2. At higher temperatures the proportion of path 1 continues to increase until it reaches levels above 97% at 2500 K. Although the barrier TS_k_1 is lower in energy, at low temperatures the energy of the system is not enough to overcome TS_{MeOH} and the formation of formaldehyde via path 2 is favoured. As the temperature increases, the system has more energy and finally the ratio changes and the reaction goes almost exclusively by path 1.

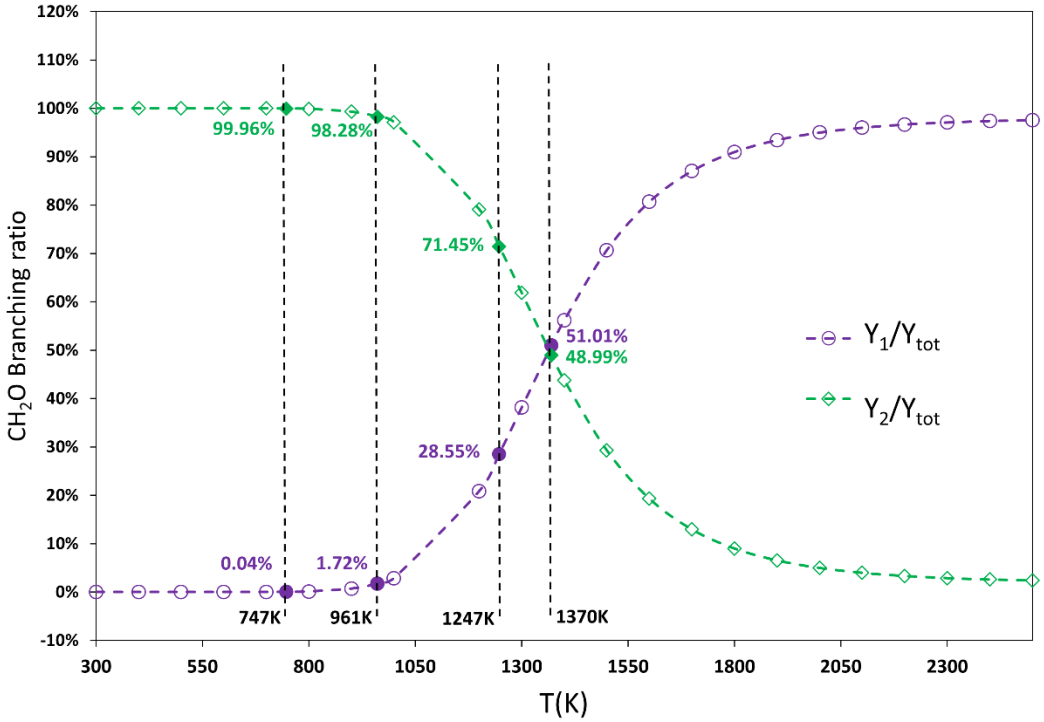

Figure 3-11: Branching ratio for formaldehyde formation by MF → CH_3OH + CO → CH_2O (P3) + H_2 + CO (P2) (Y_1) and MF → 2 CH_2O (P3) (Y_2) as function of temperature in the thermal decomposition of MF. Calculated at M06-2X/GD3/cc-pVTZ level of theory. See appendix 1 for full model details.

3.6. Conclusions

The low-pressure pyrolysis of methyl formate was studied using synchrotron radiation alongside theory to show the main channels to thermal decomposition. To reach the different decomposition channels, molecules were exposed to high temperatures. The thermal decomposition pathways of the neutral were differentiated from dissociative ionization with the help of photoion mass selected TPES and trends of the ion abundance with pyrolysis temperature. We can accurately determine routes of thermal decomposition due to the low-pressure environment where primarily unimolecular processes occur at a quantifiable rate. We were also able to computationally confirm Francisco's prediction of methyl formate thermally decomposing directly to formaldehyde and not just via the initial loss of methanol.[70] The predicted rates suggest this direct path is kinetically more favourable than the path forming CH_2O from sequential methanol decomposition at low temperatures.

The three predominant thermal channels elucidated in this study are:

$$CH_3OCHO \rightarrow CH_3OH + CO$$

$$CH_3OCHO \rightarrow 2\ CH_2O$$

$$CH_3OCHO \rightarrow CH_4 + CO_2$$

These results also validate the methodology for studying larger formates and esters in the future.

Chapter 4. Probing the Pyrolysis of Ethyl Formate in the Dilute Gas Phase by Synchrotron Radiation and Theory

4.1. Published Contributions

B. Lowe, A. L. Cardona, J. Salas, A. Bodi, P. M. Mayer and M. A. B. Paci, *J. Mass Spectrom.*, 2023, e4901.

B. Lowe, with supervision from P. M. Mayer, completed experimental data processing for the iPEPICO data and wrote the accompanying sections along with the introduction.

A. L. Cardona along with assistance from J. Salas and supervised by M. A. Burgos Paci completed the computational side including the Gaussian calculations and statistical modelling, writing the methods and findings in the accompanying sections.

A. Bodi assisted with work completed at the Swiss Light Source.

4.2. Introduction

Biodiesel is a promising alternative to fossil fuels having a lower carbon burden on the atmosphere. It is typically made by the transesterification of vegetable oils to produce fatty acid methyl esters (FAMEs); alternative methods using ethanol can be used to produce fatty acid ethyl esters (FAEEs).[36,99] Although the combustion of FAEEs is considered to be closer to 'carbon neutral,' it is still important to study the products resulting from combustion and thermal decomposition in the engine and their potential for toxic emissions. Ethyl formate (EF) is the smallest of these ethyl esters and can be used to study the breakdown of larger FAEEs. Shock-tube methods by Balla et al. showed that the primary decomposition of ethyl formate is by a unimolecular elimination step to produce ethene

and formic acid.[39] This accounted for up to 95% of the products at 927 °C. Since the lowest pressure employed in the experiment was 0.01 atm, bimolecular reactions made a large contribution to the total decomposition. This includes the production of methane and propane. Carbon monoxide was further predicted to be released in the direct decomposition of EF and from the decomposition of formic acid. However, some products could not be quantified, including H_2, H_2O, and CO. Later shock-wave studies by Ning et al.[41] and Ren et al.[96] also showed the dominance of the decomposition channel leading to ethene and formic acid. CO_2 was proposed to be the minor product of a bimolecular reaction involving ethane rather than originate directly from EF.

Previous theoretical studies explored the mechanism for forming C_2H_4 + HC(O)OH and found a six-membered ring transition state mediating the reaction.[100,101] Hermida-Ramón et al.[102] predicted three local minimum-energy conformations for EF and studied how different levels of theory affect the predicted mechanism. More recent work explored further decay channels predicted to be accessible at high temperatures following kinetic treatment of the results.[39,69,103]

The experiment at the Swiss Light Source ionizes neutral molecules and radicals to form two distinct classes of ions relevant to this study: a) unfragmented parent ions of neutral EF and its pyrolysis products and b) ions resulting from the decomposition of the EF radical cation or of pyrolysis product parent ions themselves by dissociative ionization. It is therefore important to understand the ion chemistry of EF to help identify the products of pyrolysis. Zha et al.[104] studied the unimolecular decomposition of $EF^{+\bullet}$ using photoelectron photoion coincidence (PEPICO) spectroscopy and found that decomposition into $C_2H_4^{+\bullet}$ + HC(O)OH dominated between 11.0 and 12.5 eV, while decomposition to CH_2OH^+ + CO + $^\bullet CH_3$ became the major path above 12.5 eV. Other observed dissociative ionization channels yielded CH_2OCHO^+ + $^\bullet CH_3$; $C_2H_4CO^{+\bullet}$ + H_2O; $HCO_2H_2^+$ + $^\bullet C_2H_3$; $C_2H_5O^+$ + $^\bullet CHO$; $C_2H_5^+$ + $HC(O)O^\bullet$; and HCO^+ + $CH_3CH_2O^\bullet$.

In this study, we use a low-pressure pyrolysis microreactor coupled to imaging photoelectron photoion coincidence (iPEPICO) to determine the pyrolysis products for EF.[44,74,105] Coincidence mass spectra were obtained at different temperatures as a function of photon energy to yield the photoion mass-selected threshold photoelectron spectra (ms-TPES) of thermal degradation products. In addition to experimental results, a computational study was performed to provide a complete mechanism, potential energy surfaces and unimolecular dissociation rate constants of EF. These results were compared with those obtained experimentally and in previous works to confirm and validate the implemented methods.

4.3. Experimental Procedures

Imaging photoelectron photoion coincidence (iPEPICO) spectroscopy experiments were carried out at the Swiss Light Source (SLS, Paul Scherrer Institute, Villigen, Switzerland) on the VUV beamline, which has been described in detail elsewhere.[72,73] The set-up is as described in Chapter 3.3, using ethyl formate here as the sample.

Previous work with these types of reactors have concluded that the role of unimolecular vs. bimolecular reactions is largely molecule dependent, with bimolecular reactions increasing with sample pressure (for obvious reasons). Reactions involving 0.2% propionic acid in argon and 0.3% furfural in helium gave results consistent with primarily unimolecular chemistry,[106,107] while benzaldehyde pyrolysis at similar concentrations evidenced bimolecular chemistry,[106] as well as analogous acetone pyrolysis experiments.[108]

4.4. Computational Details

4.4.1. Electronic structure calculations

Computational methods are as described in Chapter 3.4.1. Comparisons to the other methods can be found in Appendix 2.

4.4.2. Kinetics

Kinetics calculations for the decomposition paths in the high pressure limit were carried out over the 300–2500 K temperature range: unimolecular dissociation rates were calculated using canonical transition state theory (CTST) with Eckart asymmetric tunnelling correction[84] for molecular pathways and canonical variational transition state theory (CVTST) for barrierless pathways assuming that the reaction path corresponded to a homolytic bond dissociation channel.[85–87] Temperature and pressure-dependent rate constants were determined from master equation calculations done with MultiWell program suite.[81–83]

4.5. Results and Discussion

4.5.1. Threshold photoelectron spectra

Mass spectra obtained at 11 eV photon energy show the EF radical cation as a low intensity peak, decreasing in abundance with increasing pyrolysis temperature. At 14 eV, where all the products produced by pyrolysis can be ionised, major peaks were observed at *m*/*z* 44, 28, 26, and 18. The corresponding ms-TPES can be used to identify the spectral carriers of these peaks (Figure 4-1 – Figure 4-5).

Figure 4-1a shows the TPES for ethyl formate obtained without pyrolysis and the mass-selected TPES (ms-TPES) for *m*/*z* 74. The ms-TPES intensity declines above 10.8 eV due to the dissociation of the radical cation.[104] The measured ionisation energy, IE, of 10.60 ± 0.02 eV agrees with that measured

by Zha et al (10.61 ± 0.05 eV).[104] The ms-TPES can be compared to the He(I) photoelectron spectrum obtained by Śmiałek and co-workers.[109,110] They observed vibrational structure due to modes at 1567 and 596 cm^{-1} and assigned an adiabatic IE of 10.588 eV. FC simulations (Figure 4-1a, red curves) compare favourably with the experimental spectrum and highlight vibrational excitation of three main modes, 575 cm^{-1} (scissor bend of the CO_2 group), 703 cm^{-1} (internal rotation of the HC(O)O group relative to ethyl), and 1583 cm^{-1} (stretching of the C–O bond between HCO and the ethoxy group), two of which were identified by Śmiałek et al.[109] Figure 4-1b corresponds to the ms-TPES of m/z 74 with the furnace at 717 ^{o}C (990 K). The low signal in Figure 4-1b is due to the pyrolytic degradation of ethyl formate reducing the amount of *m*/*z* 74 produced by photoionization. With the heater on, only the ms-TPES can be derived as the total electron signal has contributions from the ionization of neutrals formed by the pyrolysis of ethyl formate.

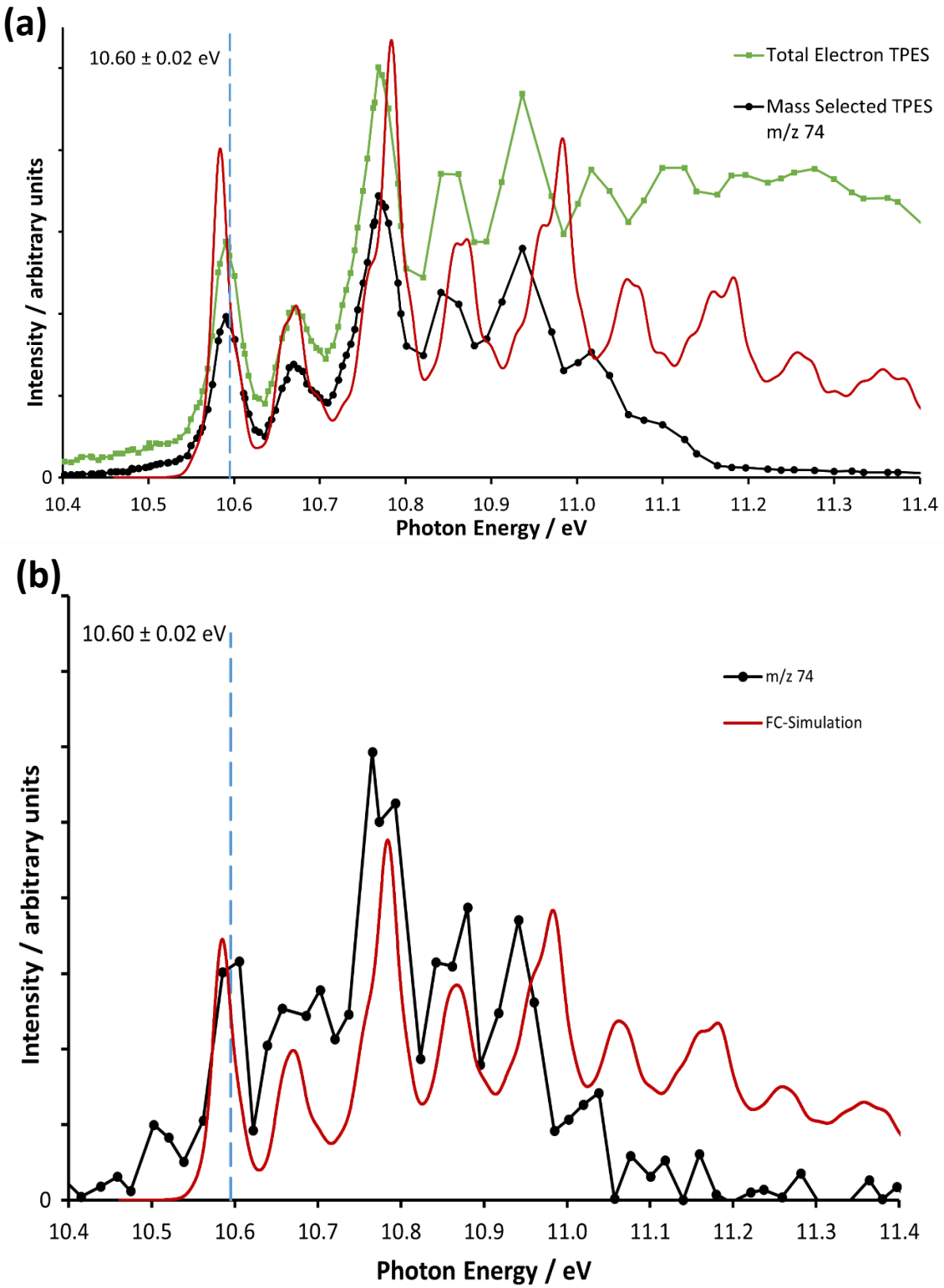

Figure 4-1: (a) TPES and ms-TPES for m/z 74 with 0 W on the furnace along with Franck–Condon simulation (red) corresponding to the most stable C–T isomer (see text) of ethyl formate. (**b)** ms-TPES for *m/z* 74 at 717 °C, with the Franck–Condon simulation overlaid in red.

Figure 4-2 shows the *m*/*z* 30 ms-TPES. The measured IE of 10.87 ± 0.02 eV corresponds to the ionization energy of formaldehyde (CH_2O, 10.88 eV).[91]

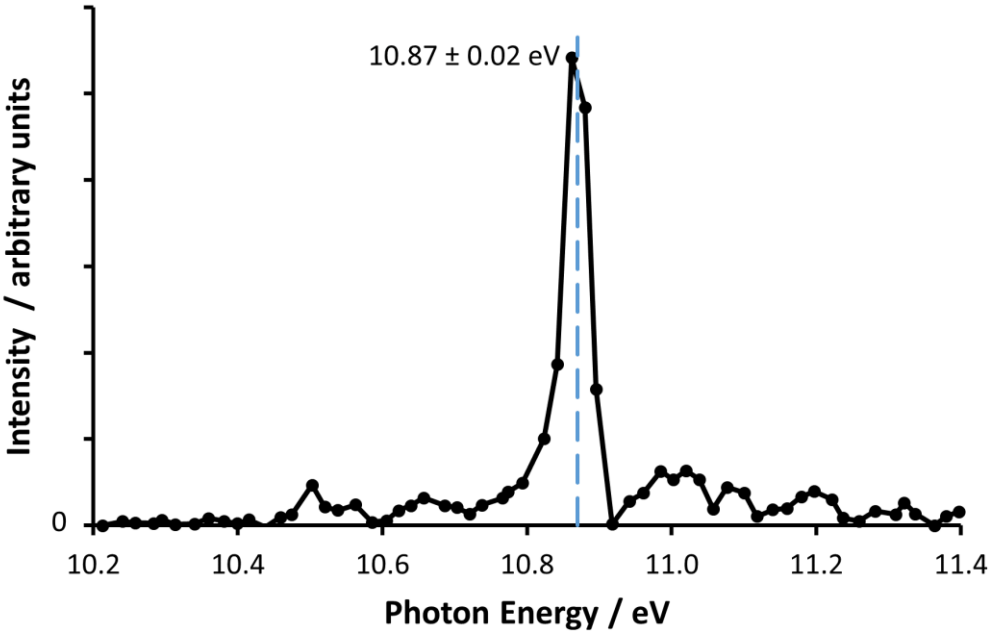

Figure 4-2: ms-TPES for CH_2O, *m*/*z* 30, obtained at 717 °C (990 K). The reported ionization energy of formaldehyde is 10.88 eV.

The ms-TPES for *m*/*z* 44 is shown in Figure 4-3. Observed pyrolysis species are acetaldehyde, IE = 10.21 ± 0.02 eV (compared to the reported 10.24 eV),[111] and CO_2, IE = 13.76 ± 0.02 eV (compared to the known 13.78 eV).[112] The FC simulation of acetaldehyde ionization matches very well with the experimental spectrum and displays a progression in a 1307 cm^{-1} mode corresponding to a hydrogen wagging mode. The *m*/*z* 44 ms-TPES also illustrates a unique analytical advantage of PEPICO detection: at the ionization energy of CO_2, acetaldehyde dissociatively photoionizes. Thus, the pure CO_2 TPES can be recorded and assigned in this energy range, although acetaldehyde is another significant component in the reaction mixture with 44 amu mass.

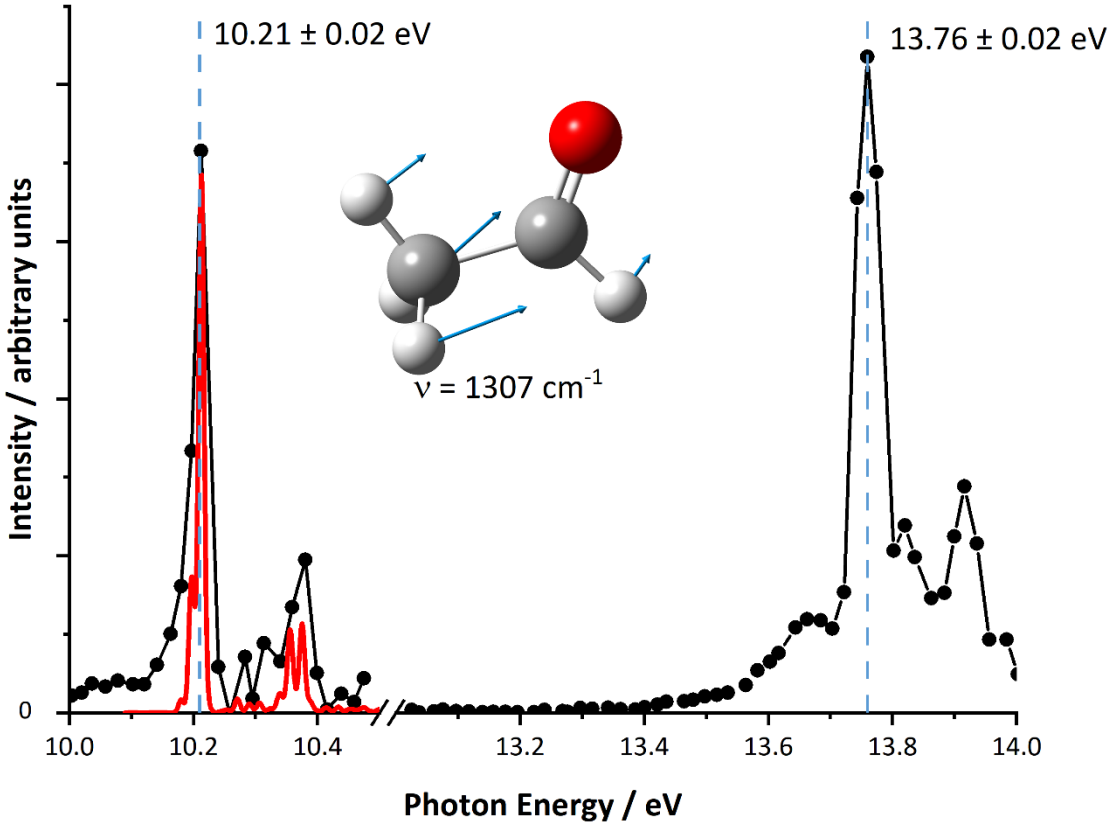

Figure 4-3: ms-TPES of *m/z* 44 indicating the presence of acetaldehyde (CH_3CHO, left peak) and carbon dioxide (CO_2, right peak). An FC simulation is overlaid in red for CH_3CHO.

The ms-TPES for *m/z* 28 exhibits three features in Figure 4-4. The leftmost band is due to C_2H_4 formed by pyrolysis of EF, (IE = 10.50 ± 0.02 eV, corresponding to that obtained by Williams and Cool).[113] FC simulations (shown in red) showed the major vibrational excitation to be 891 cm^{-1} corresponding to a rocking motion of the hydrogens. The broad peak in the centre of Figure 4-4 at ~12.5 eV also corresponds to $C_2H_4^{+\bullet}$; however, the ethylene cation seen in threshold ionization in this photon energy range is due to the dissociative ionization of ethane, C_2H_6. Ethane parent ions yield $C_2H_4^{+\bullet}$ only 0.57 eV (0 K) above the adiabatic ionization energy of 11.8 eV,[114,115] due to the quantum tunnelling of H atoms.[116] Our experiment has ions at much higher temperatures, which shifts the onset lower in energy. We did not observe a TPES signal in coincidence with *m/z* 30 ions corresponding to $C_2H_6^{+\bullet}$ (see Figure 4-2). Since the photoelectron spectrum for ethane is already broad due to Jahn–Teller distortion and vibrational coupling effects,[117] the resulting TPES for ethane in our experiment may be

below the detection limit. The rightmost peak at 13.98 ± 0.02 eV is due to CO, based on its known ionisation energy.[118] Thus, in the *m*/*z* 30 channel, PEPICO is capable of identifying three neutral spectral carriers independently.

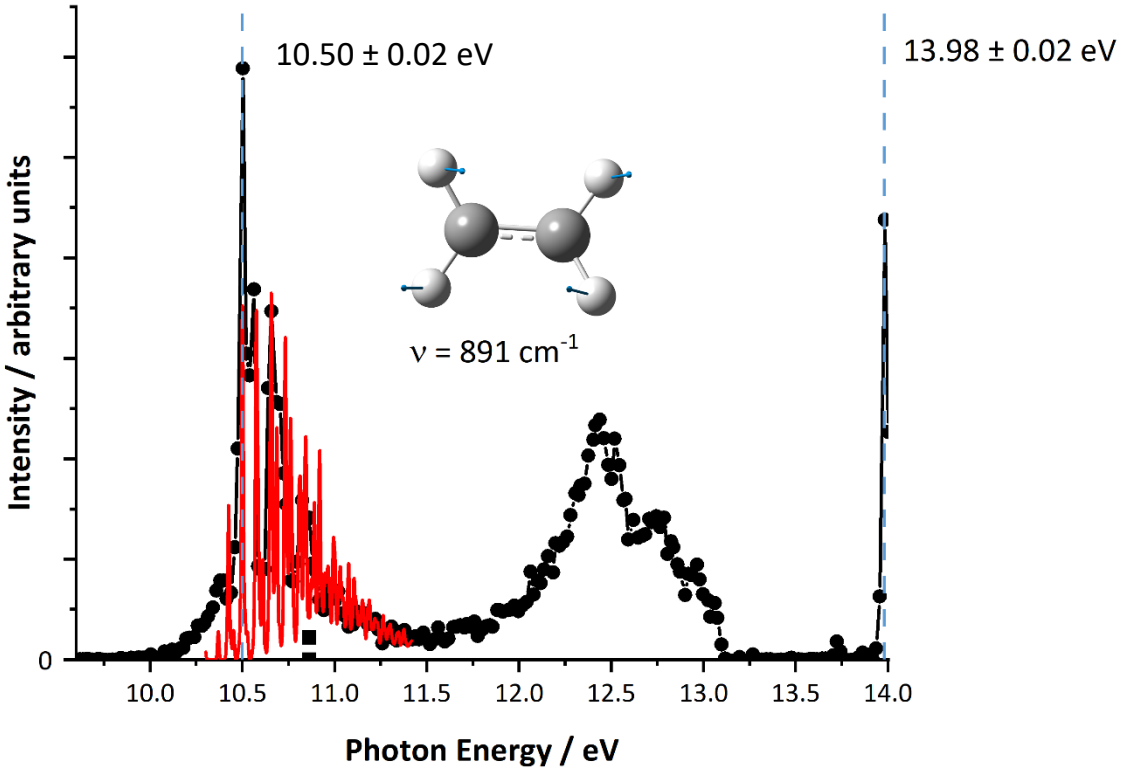

Figure 4-4: ms-TPES of *m*/*z* 28 showing the presence of ionized C_2H_4 from the pyrolysis of EF (left most peak), $C_2H_4^{+\bullet}$ formed from the dissociation of $C_2H_6^{+\bullet}$ (centre peak) and ionized CO from the pyrolysis of EF (right most peak). The FC simulation for C_2H_4 ionization is overlaid in red.

Figure 4-5 shows the ms-TPES for *m*/*z* 46, which contains two sets of bands. The low-energy band with an onset at 10.46 ± 0.02 eV corresponds to ethanol, with a reported ionisation onset of 10.48 eV.[119] Its ionisation energy is ca. 100 meV lower, which indicates large geometry change and explains the broad nature of the peak.[120] The 0 K appearance energy for H loss is 10.81 eV,[120] which explains the disappearance of the ethanol signal above 10.75 eV. The set of peaks to the right are due to the ionization of formic acid (IE = 11.32 eV).[121] The vibrational fine structure is primarily from an asymmetric CO stretch with a frequency of 1536 cm^{-1} as confirmed by the FC simulation. Two neutral spectral carriers are thereby identified.

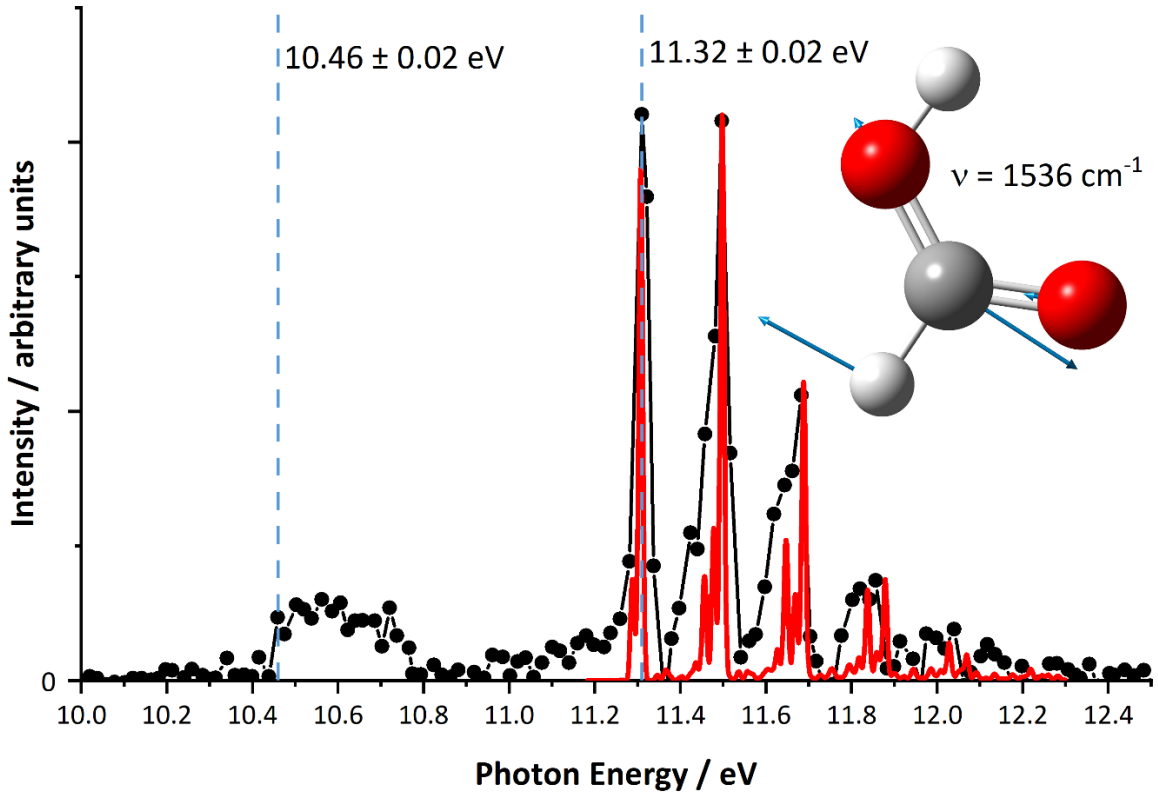

Figure 4-5: ms-TPES of *m*/*z* 46 showing ethanol (low-*E* band) and formic acid (high-*E* band) contributions. An FC simulation is overlaid in red for formic acid.

Finally, the *m*/*z* 26 ms-TPES is shown in Figure 4-6. Acetylene is the carrier of the peak on the left at 11.38 ± 0.02 eV, which is formed in the decomposition of neutral EF (IE = 11.40 eV).[122] The vibrational fine structure is due to the active symmetric stretch at 1889 cm^{-1} as confirmed by the FC simulation. The high-energy band is due to $C_2H_2^{+\bullet}$ formed in the dissociative ionisation of C_2H_4, with an appearance energy of 13.2 eV. The dissociative ionisation onset is skewed to lower photon energies by the high thermal internal energy of the precursor ion.[123] Other hydrocarbon fragments could also produce $C_2H_2^{+\bullet}$ by dissociative ionization. At least two neutrals are, thus, found with the help of the *m*/*z* 26 ms-TPES.

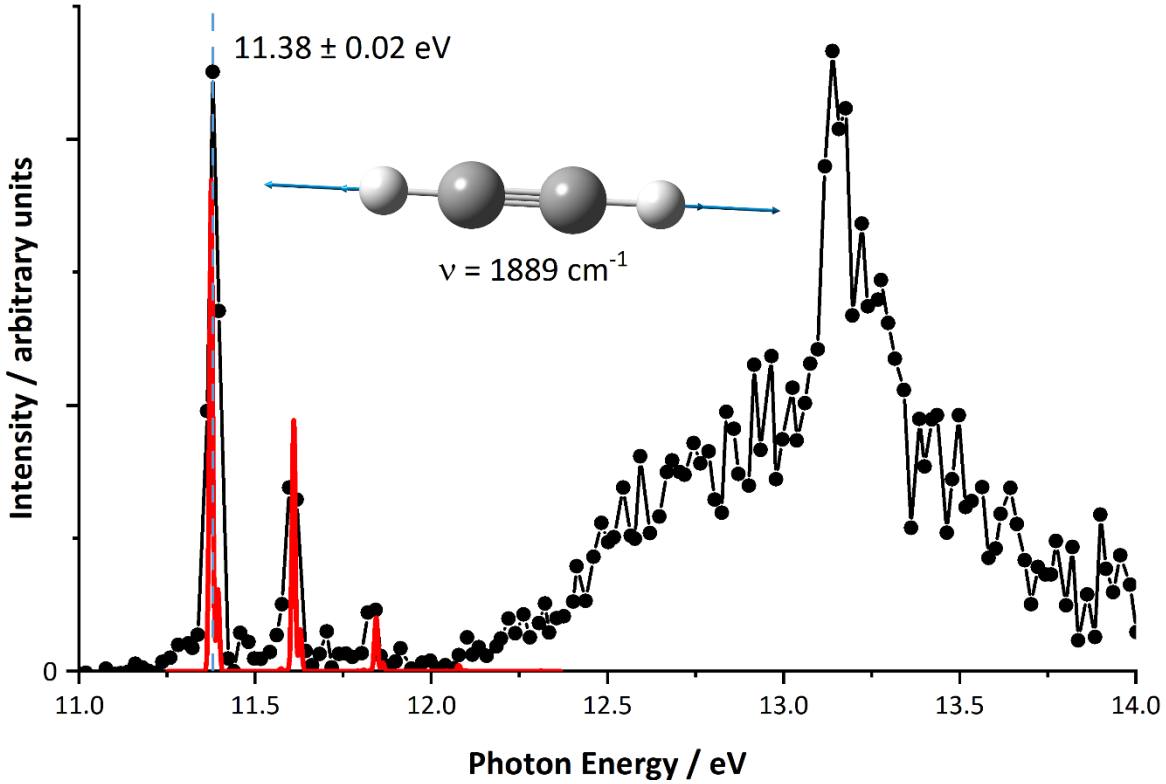

Figure 4-6: ms-TPES of *m/z* 26 showing the ionization of C_2H_2 formed in the thermal decomposition of EF (left) and $C_2H_2^{+\bullet}$ formed from the dissociative ionization of C_2H_4 (right). An FC simulation for C_2H_2 is overlaid in red.

Based on the experimental TPES, the observed pyrolysis reactions of ethyl formate are summarized in Table 4-1.

Table 4-1: Neutral reaction pathways based on products observed in the experiment and where these reactions are found in the literature.

No.	Reaction	ms-TPES assigned of	References
R1	$CH_3CH_2OC(O)H \rightarrow C_2H_4 + HC(O)OH$	C_2H_4, HC(O)OH	39,41,124
R2	$CH_3CH_2OC(O)H \rightarrow CH_3CH_2OH + CO$	C_2H_5OH, CO	39,41,125
R3	$CH_3CH_2OC(O)H \rightarrow CH_3CHO + CH_2O$	CH_3CHO, CH_2O	103,126
R4	$CH_3CH_2OC(O)H \rightarrow C_2H_6 + CO_2$	C_2H_6*, CO_2	96,103,115
R1a	$HC(O)OH \rightarrow CO + H_2O$	CO	39,127
R1b	$C_2H_4 \rightarrow C_2H_2 + H_2$	C_2H_2	126

*Ethane is not directly observed but inferred based on dissociative ionization products (see text).

4.5.2. The ethyl formate molecule

We have labelled the oxygen and carbon atoms in EF as **O1**=**C1**(H)–**O2**–**C2**(H_2)–**C3**H_3. The lower energy conformations of EF according to the cis-trans and cis-gauche dihedral angles O1-C1–O2–C2 and C1–O2–C2–C3 are denoted as **C–G**, **T–G**, **C–T** and **T–T**, respectively (Figure 4-7). These conformations can be compared with previous studies that predicted between three and five equilibrium species.[41,102,103] The C–G and the C–T forms are the most stable conformations of EF with an estimated enthalpy difference of about 1 kJ mol^{-1} with all calculation methods (appendix 2). The results agree with previous experimental observations of the gas phase conformer distribution[128] and calculated energy differences.[102,129] The energy of the **C–T** geometry was predicted to be 1.1 (1.2), 19.6 (19.4), and 20.0 (19.7) kJ mol^{-1} lower than **C–G**, **T–G** and **T–T** geometries, respectively (energies at the M06-2X-GD3/aug-cc-pVTZ and SVECV-f12 levels).

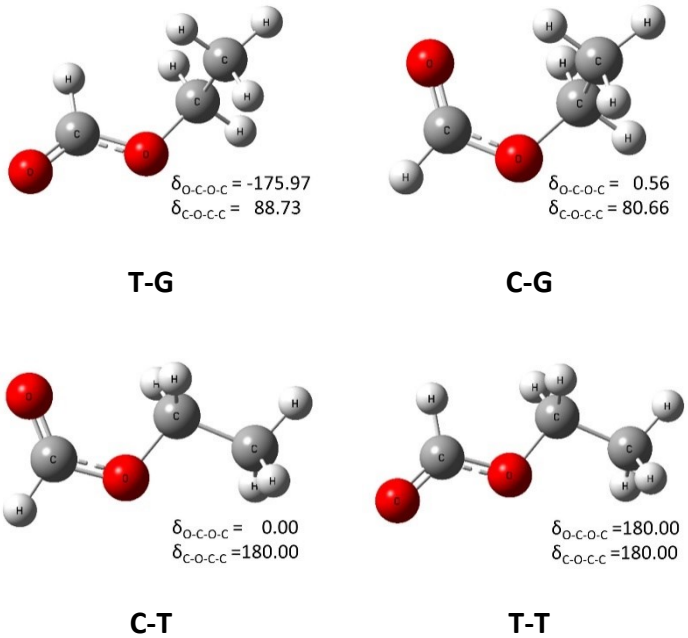

Figure 4-7: Optimized geometry of the EF minima conformation at the M06-2X-GD3/aug-cc-pVTZ level.

The calculated relative energies for the geometries of EF and all transition states between them can be found as supporting material. Of the four minimum EF molecular conformers found in this study, only the **C–T** conformer was found to have significant Franck–Condon factors near the ionization threshold (and is responsible for the FC simulations in Figure 4-1). This is due to the stable **C–T** radical cation conformation, which minimizes electrostatic repulsion between the O atoms and the neighbouring CH_2 group hydrogens, both of which carry small positive charges. The other conformers undergo large geometry change upon ionization, which leads to small FC factors close to the adiabatic ionization energy and, presumably, a slowly rising and featureless photoelectron spectrum for the ground-state cation.

4.5.3. Reaction pathways for the thermal decomposition of EF

We considered eight EF decomposition pathways: six unimolecular rearrangement pathways that account for reactions listed in Table 4-1 through well-defined transition states and two direct homolytic bond fission pathways. A scheme of EF decomposition is shown in Figure 4-8 and the energetics for each path are summarized in Figure 4-9. There is good agreement between the calculation methods employed for the optimized structures and their energies (Table A2-1 in appendix 2). R1 corresponds to an internal elimination mechanism through a concerted six-membered TS in which a hydrogen goes from C3 in the ethyl group to the carbonyl oxygen, while breaking the C1–O2 bond. The relative energy for the TS_1 is 209.4 (208.1) mol^{-1} (listed hereafter at the M06-2X-GD3/aug-cc-pVTZ and (SVECV-f12) levels of theory). This is the path with the lowest barrier and the products formed in this path are favoured in the thermal decomposition process.

Reactions R2-R5 involve hydrogen migration. R5, which forms an isomer of CH_2O, occur by the same hydrogen transfer mechanisms as reported for methyl formate.[68,70,130,131]

$$CH_3CH_2OC(O)H \rightarrow CH_3CHO + HC{=}OH \qquad (R5)$$

The calculated relative energies for **TS_2**, **TS_3**, **TS_4** and **TS_5** are 295.7 (284.7), 301.9 (301.9), 348.6 (335.8) and 439.1 (429.0) kJ mol^{-1}. The hydroxymethylene intermediate (IM) formed in (R5) may finally yield formaldehyde through internal H rearrangement.

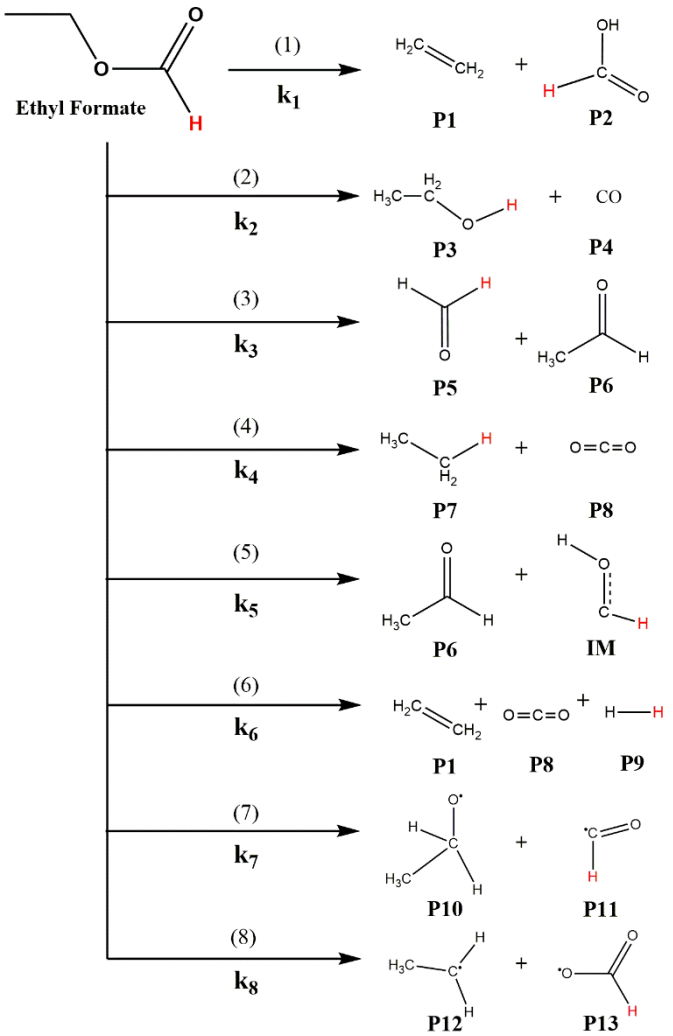

Figure 4-8: Paths in the unimolecular decomposition of EF. The formyl hydrogen is shown in red.

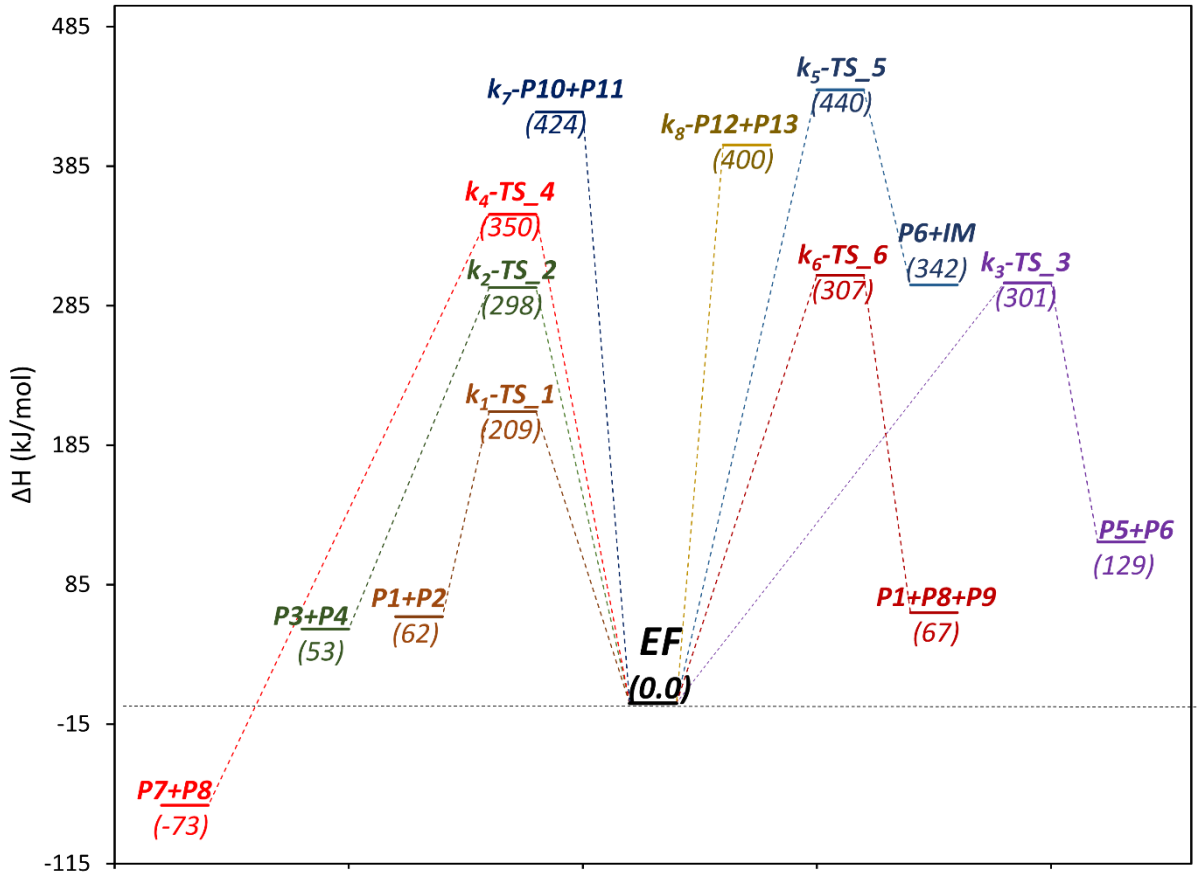

Figure 4-9: Enthalpy diagram (298 K) for the unimolecular decomposition of EF at the M06-2X-GD3/aug-cc-pVTZ level of theory. See Figure 8 for the description of each channel.

Chou et al.[103] proposed a four-membered ring TS for reaction R6, an H_2 elimination yielding $CH_2CHOCHO + H_2$, at an energy of 471 kJ mol^{-1} at the (U)B3LYP/aug-cc-pVQZ//(U)B3LYP/aug-cc-pVTZ level. Instead of this path, we have found a six-membered ring TS at ca. 170 kJ mol^{-1} lower energy, namely 306 kJ mol^{-1} at the M06-2X-GD3/aug-cc-pVTZ level. In **TS_6**, H_2 is formed when the formyl hydrogen bonds to a C3 hydrogen while the C1–H, O2–C2 and C3–H bonds are broken, leading to C_2H_4, CO_2 and H_2. As can be seen in Figure 4-10, the six-membered ring geometry makes the **TS_6** energetically and sterically more feasible.

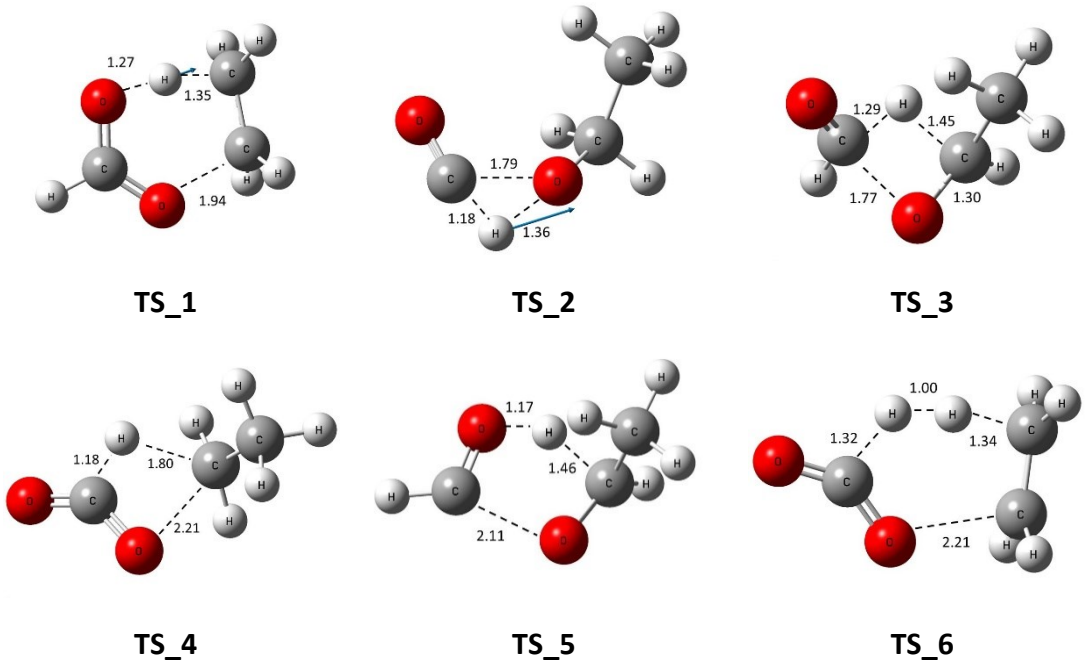

TS_1 **TS_2** **TS_3**

TS_4 **TS_5** **TS_6**

Figure 4-10: Optimized geometries of the EF thermal decomposition TS at the M06-2X-GD3/aug-cc-pVTZ level of theory.

The direct bond fission channels are endothermic with the C2–O2 (R8) channel being 23.5 kJ mol^{-1} lower in energy than the O2–C1 channel (R7). Secondary products as C_2H_2 and CH_3CHO could also be produced from the decomposition of C_2H_4 (R1 and R6) and CH_3CH_2OH (R2) via H_2 elimination. The C_2H_4 decomposition to C_2H_2 is a two-step H_2 elimination through the ethylidene intermediate and two TS with relative energies 362.2 (355.7), and 506.5 (506.6) kJ mol^{-1}. While CH_3CH_2OH decays through a four-centre TS with an energy of 409.8 (402.0) mol^{-1}. HC(O)OH could decay to CO + H_2O via a three-centre TS at 361.9 (345.2) kJ mol^{-1} or CO_2 + H_2 via a four-centre TS 365.0 (355.5) kJ mol^{-1}. The complete EF decomposition mechanism and schematic PES are shown in Figures A2-15 and A2-16 in appendix 2. Reaction products agree with those reported in the experiments performed.

The calculated barrier values for transition states at the SVECV-f12 level agree well with the previous values calculated with the high level methods[41,103,129] with an estimated difference below 1%, suggesting that the SVECV-f12 composite method is a good choice for describing thermal decomposition barriers and mechanism of formates (Table 4-2).

Table 4-2: Relative zero-point corrected energy (E-ZPE) for the unimolecular thermal decomposition of EF. Comparison between methods (kJ mol^{-1}).

	M06-2X-GD3/a-TZ[a]		SVECV-f12		B3LYP/a-QZ[a,b]		CCSD(T)/CBS(T-Q)[c]	
	TS	Products	TS	Products	TS	Products	TS	Products
R1	209.4	71.3	208.5	63.3	188.0	-	210.0	63.2
R2	295.7	51.0	284.7	41.8	274.1	-	285.8	39.8
R3	301.9	123.8	301.9	113.0	284.2	-	301.7	113.0
R4	348.6	-77.2	335.8	-88.5	299.4	-	335.1	-89.1
R5	439.1	336.6	429.0	330.8	405.3	-	429.7	330.1
R6	306.4	56.4	300.0	42.1	-	-	-	-
R7	-	417.2	-	412.0	-	-	-	415.47
R8	-	393.4	-	389.6	-	-	-	379.49

[a] a-TZ stands for aug-cc-pVTZ and a-QZ represents aug-cc-pVQZ
[b] Ref [103]
[c] Ref [41]

4.5.4. Kinetic Modelling

High-pressure limit (HPL) rate constant calculations for all unimolecular decomposition pathways of EF employed harmonic vibrational frequencies also for large-amplitude internal motions. Considering the less than 100 µs residence time of the sample in the heated region of the pyrolysis microreactor, the absolute rate constants are too low to account for the observed conversion of the sample. This is consistent with the findings of Pazdera et al., who calculated dimethoxymethane decomposition rate constants, which also appear to be too low for the reaction to proceed significantly in the heated zone.[132] Photoelectron spectroscopy and dissociative ionization experiments have shown that the rovibrational cooling in the expansion is negligible after the sample leaves the reactor.[43] Therefore, unimolecular reactions may proceed further during the ca. 1 ms collision-free flight time from the reactor exit to the ionization region. Therefore, only relative rate constants are analysed to obtain branching ratios. The calculated rate constants, as well as the relative energies of the TS's (Table A2-1), indicate that the decomposition to HC(O)OH + C_2H_4 is the main reaction path in the temperature range used for calculations (300–2500 K), in agreement with experimental observations. However, it

is observed that when the temperature rises, other decomposition routes become energetically accessible. At 990 K (717 °C), the ratios of k_n/k_1 (n = 2–6) are $1.73\times10^{-3}/6.65\times10^{-6}/1.84\times10^{-6}/6.03\times10^{-12}/3.39\times10^{-5}$; when the temperature rises to 1347 K (1074 °C), the ratios k_n/k_1 increase to 2.11×10^{-2} /$1.35\times10^{-4}/1.22\times10^{-4}/8.29\times10^{-9}/7.71\times10^{-4}$ and, at 2500 K (2227°C) the ratios go to $0.51/6.1\times10^{-3}$ /$2.48\times10^{-2}/8.69\times10^{-5}/4.4\times10^{-2}$. The branching ratios calculated assuming additive rate constants based in the energies at the SCVECV-f12 level for k_{1-6} at 1347 K (the highest experimental temperature) were 97.84 %, 2.06%, 0.01%, 0.01%, 0.0% and 0.8%, respectively (Figure 4-11). Data for all temperatures are depicted in Tables A2-2 to A2-16. It is observed that with increasing temperature the different reaction channels become more important (mainly R2), suggesting that experimental observation of products from the six channels is possible because of the high sensitivity of the technique.

Pressure-dependent rate constants of the main reactions channels (R1 and R2) are given in Tables A2-17 to A2-18. The rates constants were calculated at pressures of 0.01, 0.1, 1.0, 10 and 100 bar for temperatures above 818 K and were used to obtain the fall-off curves and pressure-dependent Arrhenius parameters. As temperature increases the dependence of the unimolecular decomposition rate with pressure becomes stronger, i.e., at temperatures up to 2000 K the relationship is almost linear (Figures A2-31-2-32).

The HPL Arrhenius parameters for the unimolecular decomposition of EF calculated with the M06-2X-GD3/aug-cc-pVTZ and SVECV-f12 levels of theory can be found in Table 4-3 and compared to the other levels described in the computational section in Table A2-21. The Arrhenius form of the rate constants calculated at the SVECV-f12 level for the main paths are (The units of the activation energy are kJ mol^{-1}):

$$k_{1\infty}(T) = 2.55 \times 10^{14}\ e^{-209.5/RT}\ s^{-1},$$

$$k_{2\infty}(T) = 1.89 \times 10^{15}\ e^{-275.7/RT}\ s^{-1},$$

$$k_{3\infty}(T) = 2.34 \times 10^{14}\ e^{-308.4/RT}\ s^{-1},$$

The kinetic values for different temperature and pressure are in good agreement with previous values.[39,41,103] The calculated branching ratios at 1347 K explain only the formation of products by the R1 and R2 pathways.

Acetaldehyde and formaldehyde are proposed to arise from hydrogen abstraction mechanisms and not through unimolecular EF decomposition.[126] The present results in Figure 4-11 and those of Chou et al.[103] suggest the unimolecular paths R3 and R5 are not kinetically competitive with formation of CO + ethanol (R2). However, the required homolytic cleave prior to the hydrogen abstraction reactions proposed by Osswald *et al.*[71] makes this mechanism less competitive than R3. Bimolecular processes have been observed in SiC pyrolysis microreactors primarily when the primary decomposition channel yields reactive species, such as radicals[24-26] or when reactants are supplied in large concentrations.[133] The number density of the reagent in our system (10^{15} cm^{-3}) together with the assumption of a high H abstraction rate constant of 10^{-12} cm^3 s^{-1} predicts a half-life of 600 µs, higher than the residence time in the reactor. The missing primary radical products and the insufficient residence time in the reactor suggest that the unimolecular reaction R3 is the sole source of the acetaldehyde and formaldehyde in the present experiment, likely occurring during transit to the ionization region. CO_2 is also a known minor neutral decomposition path accompanied by ethane loss and is a similar reaction to that seen in the decomposition of methyl formate.[96,103,131] It can also be produced in formic acid decomposition along with H_2; however, formic acid decomposition to CO and water is kinetically preferred.[127,134] C_2H_4 is a product of the major EF decomposition pathway to

formic acid and ethene.[39] CO can be formed directly from ethyl formate producing ethanol (R2) or from formic acid decomposition (R1a).[39,41,135] The latter is the kinetically preferred reaction according to shock tube experiments[39] and comparison of the RRKM rates of the two pathways.[134] However, the barrier leading from formic acid to CO + H_2O is significant (**TS_1a**, 351 kJ mol^{-1}). A comparison of the overall yield of CO from reaction R2 (CO + CH_3CH_2OH) and formic acid (R1 then R1a) reveals that the former is dominant at low temperatures (where **TS_1a** cannot be reached, Tables A2-22-A2-26, Figures A2-33-A2-37). R2 then declines in importance as R1 becomes dominant and returns to compete at high temperatures due to the looseness of the transition state compared to **TS_1** ($\Delta^{\ddagger}S_{600K}$ = 26 J K^{-1} mol^{-1}, Figure 4-11, R2). We are unable to characterise H_2O due to its presence in the background overlapping with the molecular beam signal. C_2H_2 has been studied as a decomposition product from C_2H_4 pyrolysis, which was determined to be through sequential H losses, via a C_2H_3 intermediate.[126]

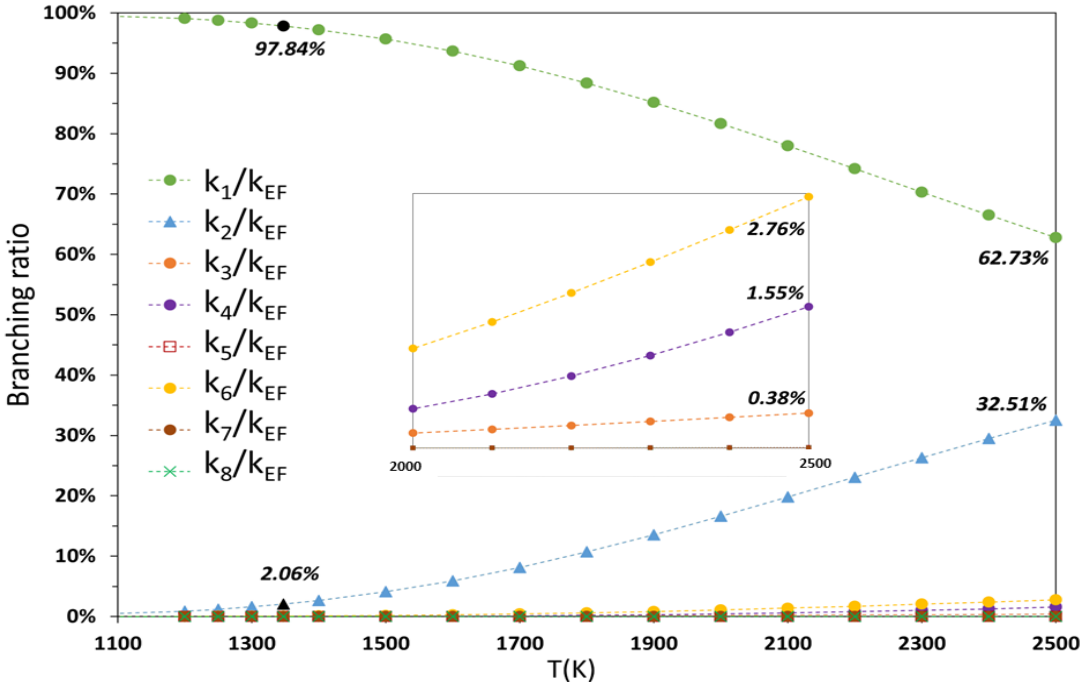

Figure 4-11: Branching ratios for the unimolecular decomposition of EF in the range of 300 to 2500 K at the SVECV-f12 level of theory.

Tables A2-2-A2-16 show the kinetics results obtained using different computational levels of theory. It is worth mentioning that the best results for energies and rates were obtained with the M06-2X-GD3/aug-cc-pVTZ and SVECV-f12 levels of theory, while the CBS-QB3 method give results with the largest deviations from previously reported values (Table A2-21). The explicit correction of the empirical dispersion included in the SVECV-f12 optimisation step better describes the non-covalent attractive forces present in some transition states, improving the performance of this method over CBS-QB3.[97,136] In addition, it has been proposed that the f12 correction improves the convergence of the basis set; i.e. calculations with a TZ basis set are more accurate and faster than the standard CCSD(T)/5Z calculation.[31] The energy values for the transition states at the SVECV-f12 level have a difference of less than 1% with the values calculated at the CCSD(T)/CBS(T-Q)//M06-2X/6-311++G(d,p) level.[41]

Table 4-3: Arrhenius parameters, A (s^{-1}) and E_a (kJ mol^{-1}) for EF thermal decomposition in the range of 300–2500 K.

	M06-2X-GD3/a-TZ [a]		**SVECV-f12**	
	A	**E_a**	**A**	**E_a**
k_1	2.57×10^{14}	210.5	2.55×10^{14}	209.5
k_2	1.83×10^{15}	286.4	1.89×10^{15}	275.7
k_3	2.34×10^{14}	308.4	2.34×10^{14}	308.4
k_4	5.31×10^{15}	357.3	5.31×10^{15}	344.5
k_5	1.32×10^{15}	446.2	1.33×10^{15}	436.2
k_6	1.33×10^{15}	314.4	1.33×10^{15}	307.9
k_7	2.31×10^{14}	401.1	2.12×10^{14}	397.2
k_8	2.76×10^{14}	425.0	2.66×10^{14}	419.6

[a] a-TZ stands for aug-cc-pVTZ

4.6. Conclusions

Pyrolysis imaging photoelectron photoion coincidence spectroscopy was employed to elucidate the products of the thermal degradation of EF by their mass-selected threshold photoelectron spectra (ms-TPES). Thanks to substantial differences in the ionization energies and dissociative photoionization of the lower-IE neutral, single mass channel ms-TPE spectra could be employed to identify multiple neutral spectral carriers unambiguously. The observed pyrolysis products for neutral ethyl formate are CH_3CH_2OH, CH_3CHO, C_2H_6, C_2H_4, HC(O)OH, CH_2O, CO_2, and CO. The TPES of EF was acquired for the first time and confirmed a He(I) ionization energy for EF of 10.60 ± 0.02 eV. Of the four lowest energy EF molecular conformers found in this study, only the lowest energy one (C–T), having a *cis*-configuration of the **O**=**C**(H)-**O**-**C**(H_2)-CH_3 dihedral angle and *trans*-configuration about O=**C**(H)-**O**-**C**(H_2)-**C**H_3 angle, was found to have significant Franck–Condon factors near the ionization threshold.

The energetics and kinetics of the unimolecular thermal decomposition of ethyl formate were calculated. The predicted neutral pyrolysis reactions generally confirmed those in the literature. The calculated absolute rates, however, are too low compared with the residence time of the microreactor, which may be indicative of unimolecular processes taking place in the collision-free environment after expansion. The primary thermal process yields formic acid and ethene, with several other reactions making up the remainder small fraction of the total reactivity. Previous studies suggested CO is primarily formed in the decomposition of the formic acid primary pyrolysis product. However, our kinetic analysis showed that direct CO loss from ethyl formate to yield the ethanol co-product is comparatively fast at high temperatures due to the looseness of the transition state compared to that governing the main decomposition channel R1. We also confirm that the primary steps of ethyl formate decomposition proceed to closed shell products.

Chapter 5. The Unimolecular Chemistry of Methyl Chloroformate Ions and Neutrals: A Story of Near-Threshold Decomposition

5.1. Published Contributions

In preparation.

B. Lowe, with supervision from P. M. Mayer, completed experimental data processing for the iPEPICO data and wrote the accompanying sections along with the introduction.

A. L. Cardona along with assistance from J. Salas and supervised by M. A. Burgos Paci completed the computational side including the Gaussian calculations and statistical modelling, writing the methods and findings in the accompanying sections.

A. Bodi assisted with work completed at the Swiss Light Source.

5.2. Introduction

The pyrolysis of formates such as methyl and ethyl formate has been explored extensively due to their presence in biofuels.[65,66] They are also released into the atmosphere from their use as industrial solvents, drying agents and pest control.[67] Halogenated formates are formed by replacement of the H atoms by halogens and the thermal decomposition of methyl chloroformate (MCF) was explored by Johnson and Stimson in 1977.[137] They showed that in the presence of surface-reaction inhibitors, MCF decomposed into methyl chloride and CO_2 via a homogeneous (gas phase) reaction. This rate is 4000 times slower than the comparable reaction in ethyl chloroformate (ECF),[138] which was attributed to ECF being able to form a 6-membered transition state, while MCF is limited to a more constrained 4-membered transition state in the decomposition mechanism. They also noted that

without surface-reaction inhibitors they detected a 'permanent gas', expected to be H_2, CO and HCl,[137] although they were unable to perform an analysis.

The gas-phase ion chemistry of MCF was previously studied by electron ionization.[139–141] Holmes and Lossing showed that at 11.24 eV ionized MCF loses Cl to form CH_3OCO^+.[140] The dissociation of CH_3OCO^+ then proceeds to form CH_3^+ + CO_2.[142] The ionisation energy (IE) and the photoelectron spectrum for MCF have not been reported.

In this study we use a low-pressure pyrolysis chamber coupled to imaging photoelectron photoion coincidence (iPEPICO) to determine the pyrolysis products for MCF, as we have done previously for methyl and ethyl formate.[131,143] Coincidence mass spectra were obtained at different temperatures as a function of photon energy to yield the mass-selected threshold photoelectron spectra (TPES) of thermal degradation products. The experimental results were modelled with density functional theory to elucidate reaction pathways and kinetic modelling to extract Arrhenius parameters. We have also explored the dissociative photoionization of MCF and report the first threshold photoelectron spectra (TPES), and thus IE. The experimental breakdown of the ions is computationally explored.

5.3. Experimental Procedures

Experimental details for the pyrolysis experiment are outlined in Chapter 3.3. Ion chemistry experiments are completed the same as those outlined in chapter 3 except with the high temperature reactor off.

5.4. Computational Details

5.4.1. Electronic Structure Calculations

Computational methods are as described in Chapter 3.4.1. Comparisons to the other methods can be found in Appendix 2.

5.4.2. Kinetics

The minimalPEPICO program was used to fit the iPEPICO breakdown curve.[53] The procedure for the fitting is outlined in Chapter 2.3.3.

Kinetics for the main thermal decomposition paths of MCF were modelled using the *MultiWell* Program suite (MW).[82,83,144] Low frequency modes of MCF were treated as one dimensional (1D) hindered rotors. Relaxed scan of the corresponding dihedral at the M06-2X/GD3/cc-pVTZ was performed to determine the internal rotation potential energy and moments of inertia using the *lamm* module of MW. Unimolecular dissociation rates were calculated using the canonical transition state theory (CTST) with Eckard asymmetric tunnelling correction.[84] The time concentration profiles and the temperature and pressure-dependent rate constants was modelled employing the RRKM/ME approach on the *multiwell* master equation code. Exponential down model $\langle \Delta E \rangle_{down}$= 250 cm^{-1} was used to describe the collisional energy transfer probability. *DenSum* module implementation of the Beyer-Swinehart direct count algorithm[55] was used for computing the sum and density of states.

5.5. Results and Discussion

5.5.1. Ion Chemistry

The total electron TPES and mass-selected TPES (ms-TPES, m/z 94) for MCF are shown in Figure 5-1. Overlaid in blue is a Franck-Condon (FC) simulation of the molecular ionization employing an IE of 10.90 eV, for which the onset and vibrational pattern in the experimental data is qualitatively reproduced. As a comparison, the adiabatic and vertical IE determined at the CBS-QB3(sp)//B3LYP/6-

311++G(d,p) level of theory are 11.02 eV and 11.43 eV, respectively. The corresponding adiabatic CBS-QB3, G2 and G3 IE values are 10.98, 10.96 and 10.94 eV, respectively. The lack of an obvious onset band in the TPES, and large difference between vertical and adiabatic IEs, is primarily due to the poor FC overlap of the neutral and ion geometries, Figure 5-1b. . Most notable is the CH_3O─C(O)Cl bond, which is longer in the neutral (1.320 Å) than in the ion (1.249 Å). The TPES band at 10.85 eV is missing in the *m*/*z* 94 *ms*-TPES, indicating that this feature does not belong to the MCF spectrum. Indeed, it corresponds to the ionization of formaldehyde (IE 10.88 eV),[44] a decomposition product of neutral MCF.

The experimentally-derived appearance energy (AE) for Cl loss is 11.30 ± 0.02 eV, which agrees with the literature electron ionisation value of 11.24 ± 0.05 eV within the respective error bars. Note that there was no kinetic shift in the data and so the AE could be read directly from the experimental breakdown curve. Combined with the experimental IE determined with the help of the FC simulation, this AE yields an E_0 = 0.40 ± 0.05 eV. Thus, decomposition occurs only a few tenths of an eV above the IE. The optimised minimum energy reaction pathway for the loss of Cl is shown in Figure 5-2b and illustrates the relatively small activation energy of 0.41 eV required for the dissociation which is close to the experimentally determined 0.40 eV. The primary fragment ion CH_3OCO^+ subsequently dissociates to $CH_3^+ + CO_2$.[45] As seen in the potential energy surface in Figure 5-2b, Cl loss is associated with a reverse barrier as the CO_2 moiety becomes quasi-linear upon increasing C–Cl bond length. Once the system passes the transition state, fragmentation is likely to be impulsive with suprastatistical kinetic energy release. This makes statistical analysis of the breakdown curve of consecutive CO_2 loss challenging and superfluous,[46,47] as the experimental energetic is unlikely to be more accurate or precise than the computational results shown in Figure 5-2b.

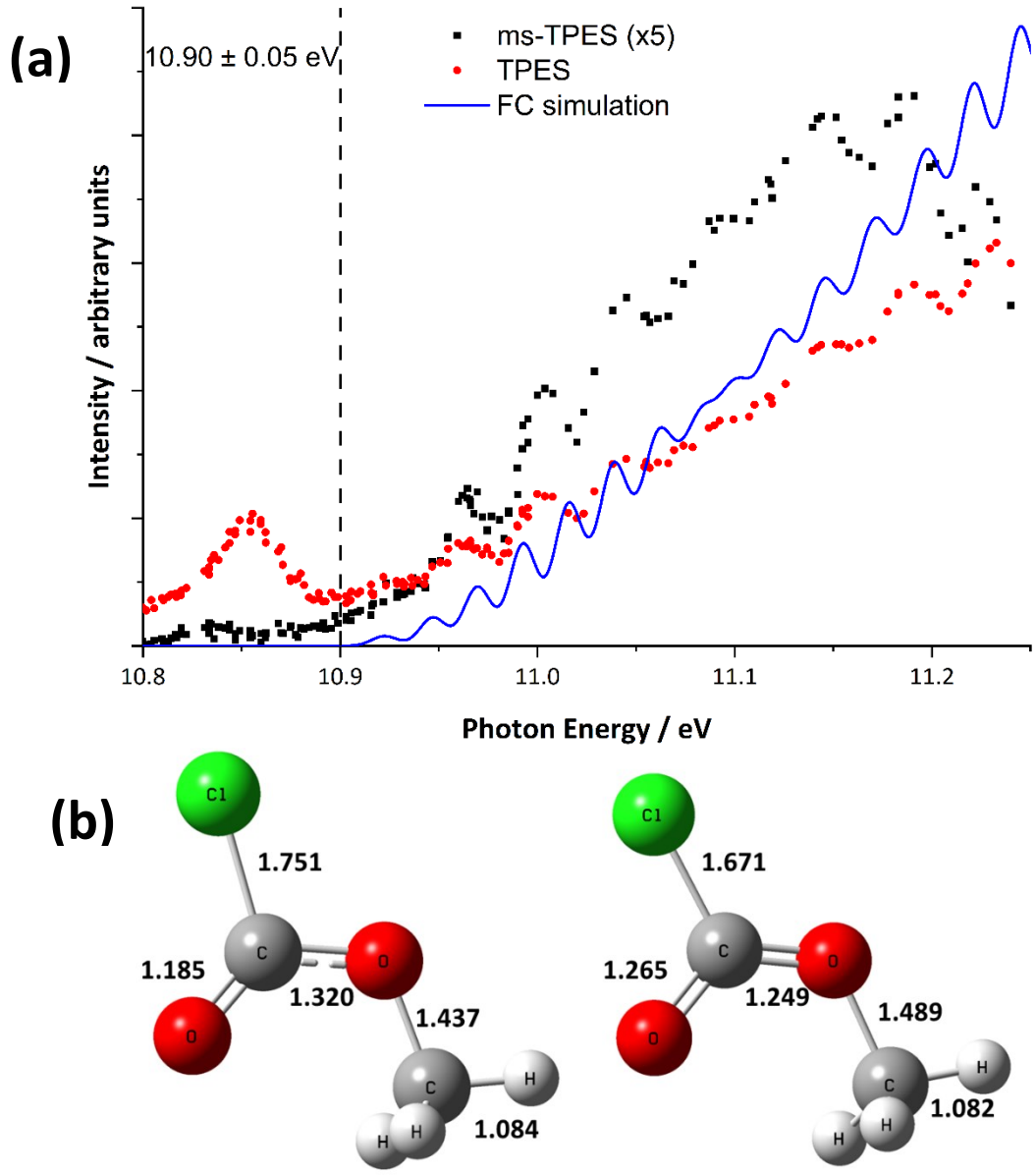

Figure 5-1: (a) TPES of m/z 94, methyl chloroformate with the FC-simulation overlaid in red and the experimental ionisation energy shown. **(b)** M06-2X/aug-cc-pVTZ optimised structures for methyl chloroformate ion (left) and neutral (right).

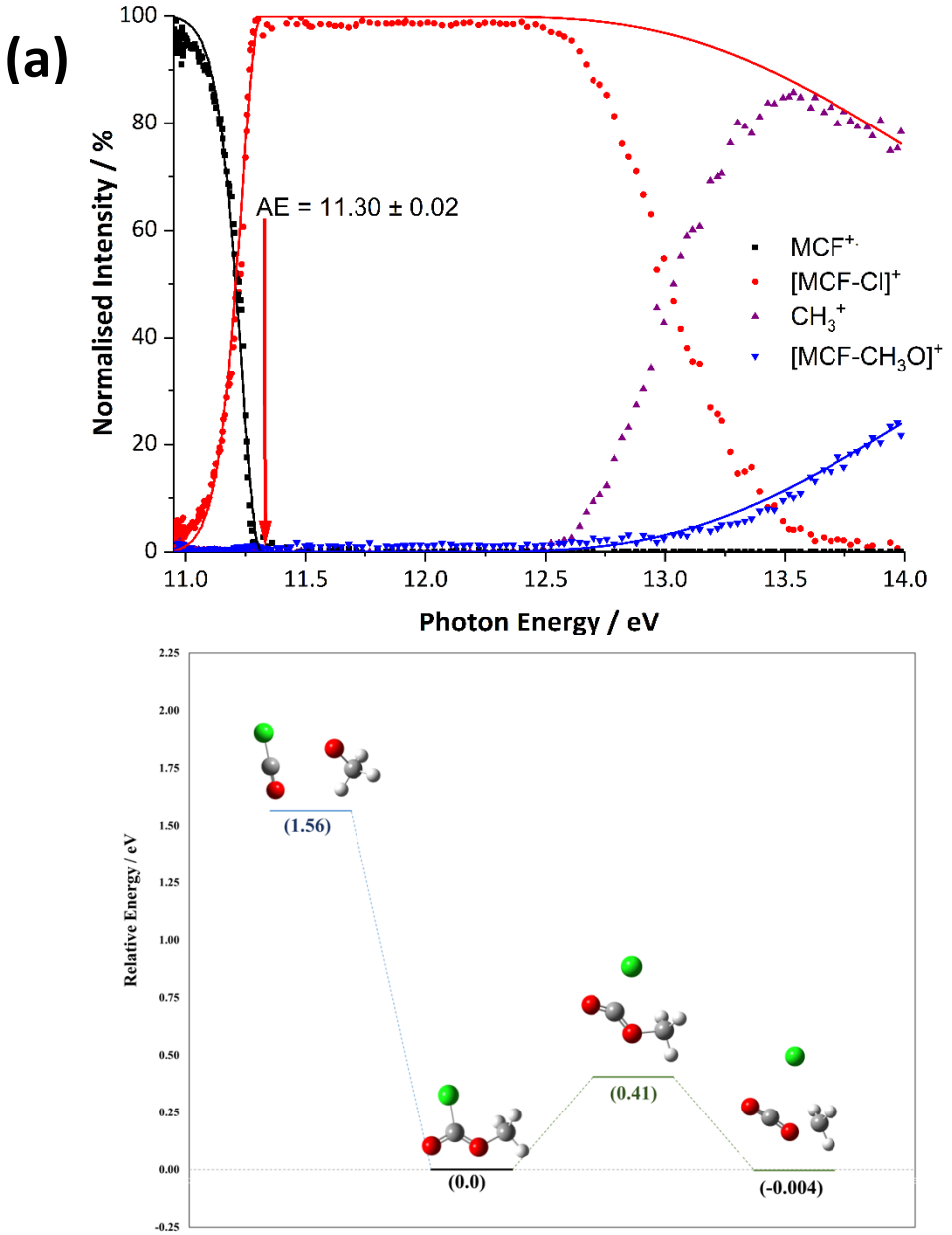

Figure 5-2: (a)[Top] MCF breakdown diagram with RRKM fitting. **(b)** [Bottom] Reaction pathway for the dissociation of methyl formate ions, losing CH_3O to the left and Cl to the right, with the energies relative to the minimum energy conformation of $MCF^{+\bullet}$, calculated at the SVECV-f12 level.

Figure 5-2a also shows the loss of $CH_3O^{\bullet}$ to form $ClCO^+$ which appears at higher photon energy. To compete at higher photon energies, the activation entropy for this channel had to be set ~ 25 J K^{-1} mol^{-1} higher than that for CO_2 loss (+4 J K^{-1} mol^{-1}, as determined from the calculated TS vibrational frequencies). This is consistent with the lack of rearrangement required for $CH_3O^{\bullet}$ loss. Figure 5-3

shows the RRKM *k*(E) vs E. curves for both channels and shows that at higher photon energy the rates converge.

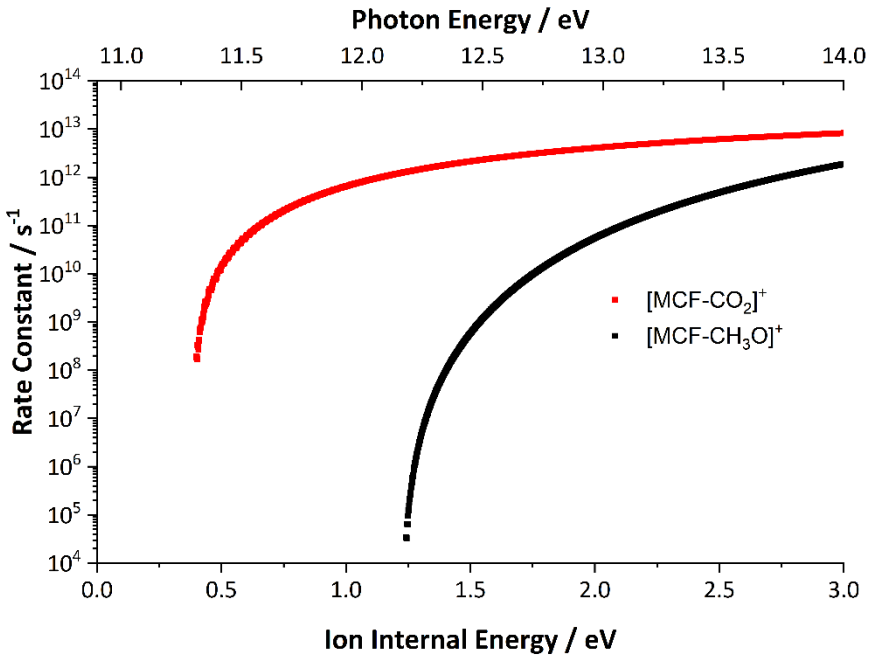

Figure 5-3: RRKM reaction rate constant plot of MCF-CO_2 vs MCF-CH_3CO.

5.5.2. Neutral decomposition

Mass spectra obtained with increasing pyrolysis temperature are shown in Figure A3-1. Figure A3-1a, taken at 11.5 eV photon energy, shows the presence of the MCF radical cation as a low intensity peak, decreasing in abundance with increasing temperature. Figure A3-1b corresponds to 14.0 eV where all the products produced by pyrolysis can be ionised. Some of the major peaks are m/z 59, 50/52, 44, and 36/38. The corresponding ms-TPES can be used to identify the molecular carriers of these peaks. Figure 5-4 shows the ms-TPES for m/z 50 which corresponds to CH_3Cl; the experimental IE is 11.26 ± 0.02 eV which agrees with the previously reported value of 11.29 eV using photoelectron spectroscopy.[145] The FC-simulation shows a similar pattern to the observed ms-TPES for CH_3Cl with the first main transition at 11.34 eV being 0->2^1 which corresponds to the 1032 cm^{-1} vibrational mode, a rocking motion of the methyl group. The second prominent transition at 11.46 eV is due to

the 0->6^1 transition which is from the 3068 cm^{-1} vibrational mode, a C-H stretch. The TPES for m/z 44 (Figure A3-2a) also shows that CO_2 is present, so both products of this decomposition channel are observed.

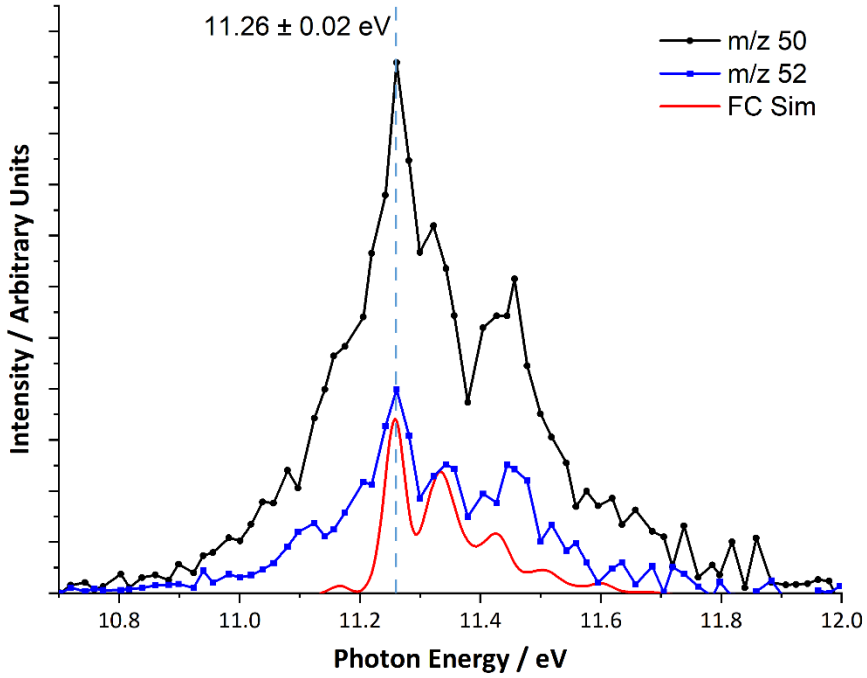

Figure 5-4: ms-TPES for CH_3Cl, m/z 50 with FC-simulation overlaid in red, obtained at 1088 °C.

The TPES for m/z 36 with the furnace at 617°C is shown in Figure 5-5, which corresponds to HCl, with an IE of 12.70 ± 0.02 eV. A photoelectron value of 12.75 eV was derived by Weiss et al.[49] who also observed vibrational structure due to the H–Cl stretching mode at 2570 cm^{-1} in the cation. A threshold PES study by Yencha yielded 12.745 ± 0.002 eV.[50] FC simulations (Figure 5-5, red line) compare favourably with the experimental spectrum and highlight vibrational excitation of 2590 cm^{-1}.

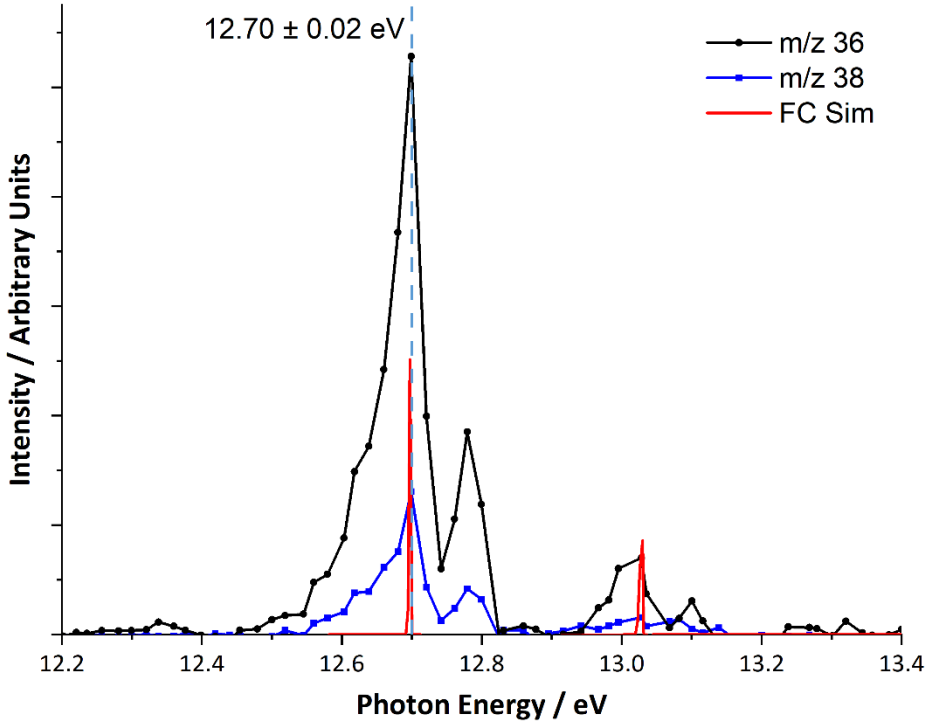

Figure 5-5: ms-TPES for HCl, m/z 36 with FC-simulation overlaid in red, obtained at 617 °C.

The loss of HCl results in $C_2H_2O_2$ which breaks down into CO and CH_2O as seen by their TPES at m/z 28 and 30 respectively (Figures A3-2b,c).

In summary, the ms-TPES results demonstrate two main pyrolysis reactions with MCF decomposing to CH_3Cl + CO_2 and HCl + CO + CH_2O, the first of which was the dominant reaction observed by Johnson and Stimson.[137] We estimated the experimental percentage for dissociation and the branching ratios between R1 and R2. Employing either measured or estimated photoionization cross sections for CH_2O (18.8 Mb),[52] CH_3Cl (30 Mb)[53] and MCF (39 Mb, based on the cross-section for methyl formate, 9 Mb, and the difference between CH_4 and CH_3Cl, 30 Mb)[54] and their respective uncorrelated integrated peak areas at 1000 K, we derived an approximate % dissociation at this temperature of ~ 15% and an R2:R1 ratio of 0.1. Note that the ion peaks for MCF and its main fragment, m/z 59, were summed to represent the total amount of undissociated precursor.

5.5.3. Thermodynamics

Methyl chloroformate has conformations with anti and syn orientation of the methyl group with chlorine depending on the H_3**C-O-C**(O)-**Cl** dihedral angle. The global minimum corresponds to the syn conformer (*syn*-MCF). Six reaction pathways were considered for the thermal decomposition of MCF in order to rationalize the experimentally identified products (Figure 5-6).

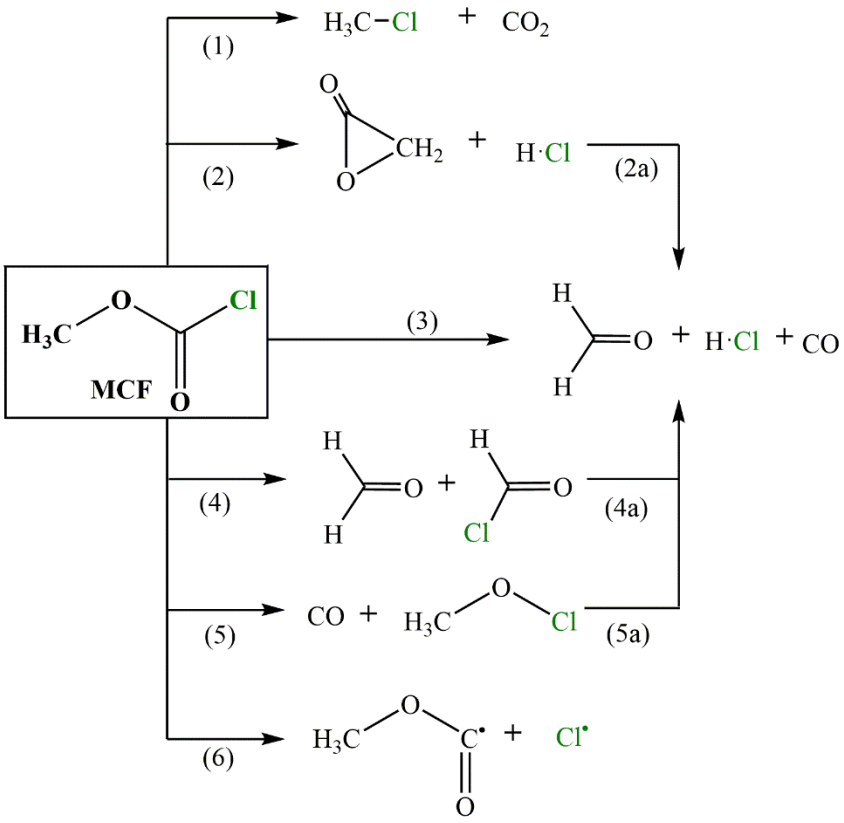

Figure 5-6: Unimolecular thermal decomposition paths for MCF.

The energetics relative to the *syn*-MCF conformation obtained at different level of theory are presented in Table A3-1, and the minimum energy reaction pathways at SVECV-f12 level of theory are shown in Figure 5-7. There is a good agreement between the levels of theory in the prediction of the reactivity trend of the different reaction paths. The main dissociation paths start from the higher energy conformer *anti*-MCF (16.9 kJ mol^{-1} relative to *syn*-MCF) which is separated from the global minimum by an energy barrier of approximately 42 kJ mol^{-1} (Figure 5-7).

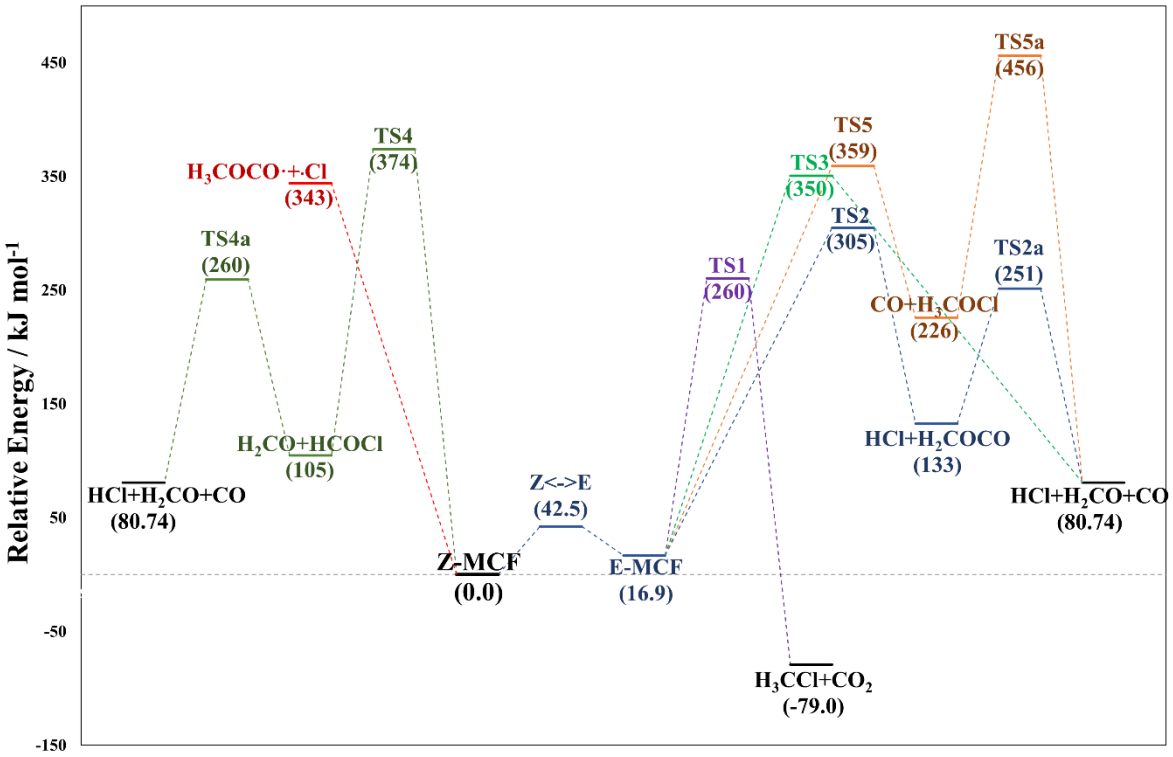

Figure 5-7: Energy diagram (E+ZPE) for the unimolecular decomposition of MCF at SVECV-f12 level of theory

The most energetically favourable decomposition path (R1) proceeds by a concerted Cl atom migration from the formyl to the methyl group to generate CH_3Cl and CO_2 via a 4-membered transition state (**TS1**, 260.4 kJ mol^{-1}), as predicted by Johnson and Stimson.[51] Both decomposition paths (R2) and (R3) lead to CO and H_2CO product formation by HCl loss. Path R2 follows a two-step mechanism, with intramolecular hydrogen abstraction for HCl loss forming the cyclic H_2COCO intermediate (**TS2**, 304.8 kJ mol^{-1}) in the first step, which then promptly decomposes CO + H_2CO with over a submerged transition state at 251.4 kJ mol^{-1} (**TS2a**) in the second one. In R3, these products are formed directly, but the barrier **TS3** is about 45 kJ mol^{-1} above **TS2**. Path R4 occurs by an intramolecular H-shift TS (**TS4**, 374 kJ mol^{-1}), which produces H_2CO and HC(O)Cl, similar to that reported for the decomposition of methyl formate.[13] HC(O)Cl can eventually decompose to HCl and CO. The high relative energy of **TS4** suggests that R4 is not a competitive path to HCl + CO + H_2CO. Path R5 also can yield HCl + CO + H_2CO over even higher-lying transition states (**TS5**, 359.2 kJ mol^{-1}

and **TS5a**, 456.0 kJ mol^{-1}), which makes this reaction pathway unlikely to contribute to the mechanism except at very high temperatures (see below).

Finally, Cl atom loss is highly endothermic (343.9 kJ mol^{-1}), which would make competition with R1 and R2. Based on our results we suppose that the permanent gas that was studied by Johnson and Stimson was likely composed of HCl, CO and CH_2O (or at higher temperatures than in this experiment, H_2).[137]

Bimolecular reactions have been demonstrated in some cases when using SiC microreactors.[23,24] Nevertheless, these were detected between the parent molecule and a primary product. In the present case, the only possibility could be a reaction with atomic chlorine, since the other decomposition products are closed shell molecules. Cl loss has a high activation energy (Figure 7) and if we assume an H abstraction rate constant of 10^{-12} cm^3 $molec^{-1}$ s^{-1} by Cl and a molecular number density of MCF of 10^{15} cm^{-3}, reaction a half-life of 600 µs is obtained which is significantly higher than the residence time in the reactor.

5.5.4. Kinetic Modelling

Kinetic modelling was performed based on the optimized geometries at the M06-2X-GD3/aug-cc-pVTZ level of theory for the main unimolecular decomposition paths (R1 and R2). Calculated rate constants, branching ratios, assuming additive rate constants, and Arrhenius parameters were calculated at the high-pressure limit (HPL) at 790–2500 K. Microcanonical rate constants were computed using RRKM theory, the sums and densities of states were calculated in the harmonic approximation using the vibrational frequencies of the optimized structures. The internal energy is measured relative to the ZPE-corrected energy of *syn*-**MCF**. As both R1 and R2 reactions occur from the *anti*-**MCF** conformer, relative concentrations based on the pseudo-equilibrium between

conformers were considered (Table A3-2 in ESI). The values for rate constants obtained in this work are consistent with our previous works for alkyl formates (Table A3-3). The k_1/k_2 branching ratios at the HPL at 790, 890 and 1361 K were 99.9/0.1, 99.8/0.2 and 99/1 % respectively, the primary channel is Cl atom migration (R1) and dominates the decomposition at all temperatures. With increasing temperature, the branching ratio of R1 decreases from 99.9% at 790 K to 94.9 % at 2500 K. The Arrhenius parameters for thermal unimolecular decompositions calculated at levels of theory described in the computational section are listed in Table S7. The Arrhenius form of the rate constants for R1 and R2 are (E_a in kJ mol^{-1}):

$$k_1 = 5.94 \times 10^{16}\, e^{-285.5/RT}\ s^{-1}$$

$$k_2 = 2.46 \times 10^{16}\, e^{-330.2/RT}\ s^{-1}$$

The dominance presented by the R1 path in the whole temperature range agrees with the assumption that the reaction goes mainly through the R1 and R2 pathways. According to the results, it is expected that there is a low concentration of the products of the R2 reaction at low temperatures. The experimentally derived branching ratio of 0.1 for R2 is consistent with the HPL kinetic model only at temperatures well above 1361 K (there the ratio of 0.01). So as with previous work, we observe more dissociation and product ratios that are consistent with higher temperatures than measured in the experiment.

5.6. Conclusions

The TPES and ms-TPES of MCF and its dissociative ionization fragment ions were recorded for the first time using iPEPICO spectroscopy, and FC simulations used to evaluate the adiabatic IE for MCF as 10.90 ± 0.05 eV. The unimolecular ion chemistry of MCF is characterized by the loss of CO_2 as the most significant reaction occurring just above the ionization threshold (AE = 11.30 ± 0.02 eV). At

higher photon energies, loss of $CH_3O^{\bullet}$ competes due to its more favourable activation entropy (AE = 12.14 ± 0.19 eV). The decomposition of neutral methyl chloroformate, studied by pyrolysis and iPEPICO detection, confirmed that the major decomposition route is formation of $CH_3Cl + CO_2$, while the generation of $HCl + CO + CH_2O$ is able to compete due to the high temperatures in the experiment. This latter reaction could be the source of the "permanent gas" described by Johnson and Stimson.[51] The calculated reaction rate constants could be used to qualitatively predict the decomposition of MCF if the vibrational temperature remained high during the experimental timeframe, suggesting inefficient vibrational cooling after the molecules leave the pyrolysis reactor.

Chapter 6. The Unimolecular Ion Chemistry of Phenyl Formate and Phenyl Chloroformate

6.1. Published Contributions

In preparation.

B. Lowe, with supervision from P. M. Mayer, completed experimental data processing for the iPEPICO data, the computational calculations and the writing up.

A. Bodi assisted with work completed at the Swiss Light Source.

6.2. Introduction

Phenyl formate (PF) is of interest in organic synthesis as a CO surrogate, eliminating the need to work with CO gas, thereby reducing toxicity.[28,29] Being the simplest aromatic ester, it is also a component and a representative model compound of biofuels.[37] Phenyl formate pyrolysis has been studied, and the primary reaction pathways were revealed to occur via an intramolecular hydrogen shift, followed by the release of CO or CO_2, with CO loss being kinetically favourable.[37] However, very little is known about the ion chemistry of phenyl formate. The related phenyl acetate exhibits an ionisation energy (IE) of 8.6 eV, and a dissociative ionisation channel to form CH_2CO plus ionised phenol with an appearance energy, AE, of 10.15 eV.[146]

Phenyl chloroformate (PCF) has been used in the chemical industry as a precursor to form N,N-dialkyl formamidines and as a hydrogen-bond donor catalyst.[32,33] The pyrolysis of phenyl chloroformate has been previously studied, showing the loss of CO or CO_2. In contrast with PF, however, CO_2 loss

dominates in PCF, because it has a larger activation entropy and lower overall $\Delta G^{\ddagger}$ than CO loss.[147] The ion chemistry of phenyl chloroformate has not yet been reported in the literature.

In this study, we explore the relationship between the ion chemistry of these formates and the high-temperature unimolecular chemistry of the neutral employing imaging photoelectron photoion coincidence spectroscopy (iPEPICO) and tandem mass spectrometry. The experimental data were modelled using RRKM theory, while reaction pathways were explored computationally using density functional theory.

6.3. Experimental Procedures

iPEPICO experiments carried out at the Swiss Light Source were completed the same as those outlined in Chapter 3.3 however, the sample was effusively inputted.

The comparatively low draw-out field results in cation residence times in the acceleration region of several μs. If the unimolecular rate constant for fragmentation is in the 10^4–10^7 s^{-1} range, ions will dissociate while still in the acceleration region, resulting in a smaller than nominal kinetic energy and larger than nominal time of flight for the fragment ion. This results in asymmetric time-of-flight (TOF) peaks for product ions, which can be modelled to extract unimolecular decay rate constants as a function of photon energy.

Mass-analysed ion kinetic energy spectrometry (MIKES) experiments were performed on a modified VG-ZAB three sector instrument that has been described in detail previosuly.[57,148] The spectrometer consists of a magnetic sector, followed by two electrostatic analysers (VG Analytical, Manchester, U.K.). Phenyl chloroformate vapour was introduced into the ion source where electron ionisation creates radical cations. Ions were accelerated to 8 kV, and metastable molecular ions were selected with the magnetic sector and transmitted to the second field-free region (2FFR) of the instrument,

where those dissociating at rate constants between 10^4 and 10^6 s^{-1} form fragment ions. The fragment ions are then detected according to their kinetic energies by the first electrostatic analyser (ESA). Spectra were recorded using ZABCAT program, developed by Mommers Technologies (Ottawa, Canada).[149]

6.4. Computational Details

6.4.1. Electronic Structure Calculations

Electronic structure calculations were carried out using the Gaussian 16 software suite.[80.] All structures were optimized with Density Functional Theory (DFT) using B3LYP/6-311++G(d,p). CBS-QB3 single-point energy calculations at these geometries were employed to obtain accurate relative energies for all structures. Transitions states were confirmed by intrinsic reaction coordinates (IRC) calculations. Franck-Condon simulations were carried out in Gaussian 16. Rice-Ramsperger-Kassel-Marcus (RRKM) calculations were performed using the direct count algorithm of Beyer and Swinehart.[55]

6.4.2. Kinetics

The minimalPEPICO program was used to fit the iPEPICO breakdown curve.[54] The procedure for the fitting is outlined in Chapter 2.3.3.

6.5. Results and Discussion

6.5.1. Phenyl Formate

The TPES and ms-TPES for $PF^{+\bullet}$ are shown in Figure 6-1. The TPES exhibits a broad peak, which is due to the large difference in the equilibrium geometry of the neutral and the cation leading to a poor Franck–Condon factor for the origin transition (Figure 6-1b). The formate group is orthogonal to the benzene ring in the neutral, but the system is planar in the cation ground electronic state. There is a

small bump at 8.82 eV in the TPES which doesn't appear in the ms-TPES for PF; it does, however, appear in the *m*/*z* 94 ms-TPES (shown). While this corresponds to the CO-loss dissociative ionisation channel of PF, the signal at this energy is consistent with a band owing to phenol ionisation to a vibrationally excited level.[150] Thus, photoion mass selection helps us identify a minor phenol contamination of the sample. At the same time, the 8.88 eV adiabatic IE calculated at the CBS-QB3 level of theory is close to the experimental ionisation onset.

$PF^{+\bullet}$ only exhibited the loss of CO in dissociative ionisation the current energy range. The breakdown diagram and the statistical fit to it is given in Figure 6-2a with experimental and RRKM TOF distributions in Figure 2b. Figure 6-2c shows the minimum energy CO-loss pathway in PF^+. The DFT determined activation entropy for the dissociation is 10 J K^{-1} mol^{-1} at 1000 K, and the RRKM fitting yielded E_0 = 0.96 ± 0.05 eV, which, together with an IE of 8.88 eV, gives a 0-K appearance energy (AE) of 9.84 ± 0.05 eV. Although the IE of PF and phenyl acetate agree within their uncertainty, the loss of CO, which involves a 1,2-hydrogen shift, has a lower activation energy in PF^+ compared to the 1.55 eV activation energy for 1,3-hydrogen shift, which leads to the loss of CH_2CO in phenyl acetate.[146]

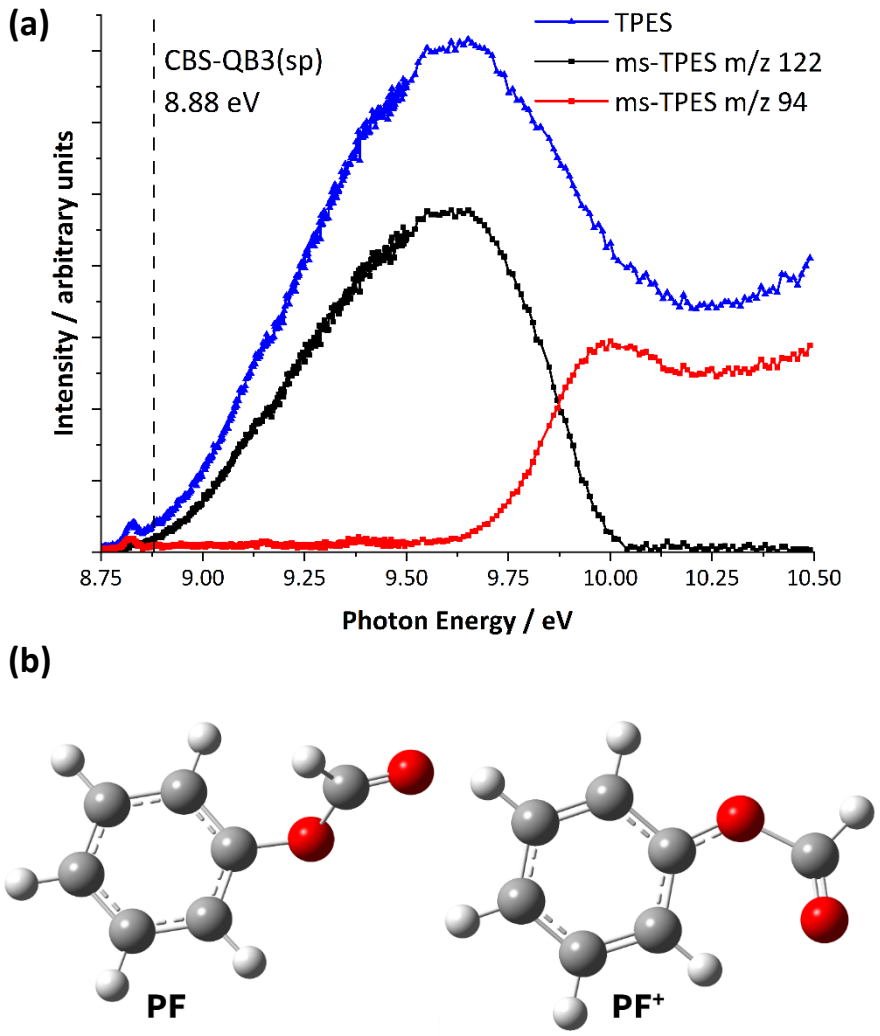

Figure 6-1: (a) TPES and m/z 122 ms-TPES for PF^+ with the CBS-QB3//B3LYP/6-311++G(d,p) calculated IE shown by a dashed line, **(b)** Structures of PF and PF^+ optimised at the B3LYP/6-311++G(d,p) level of theory.

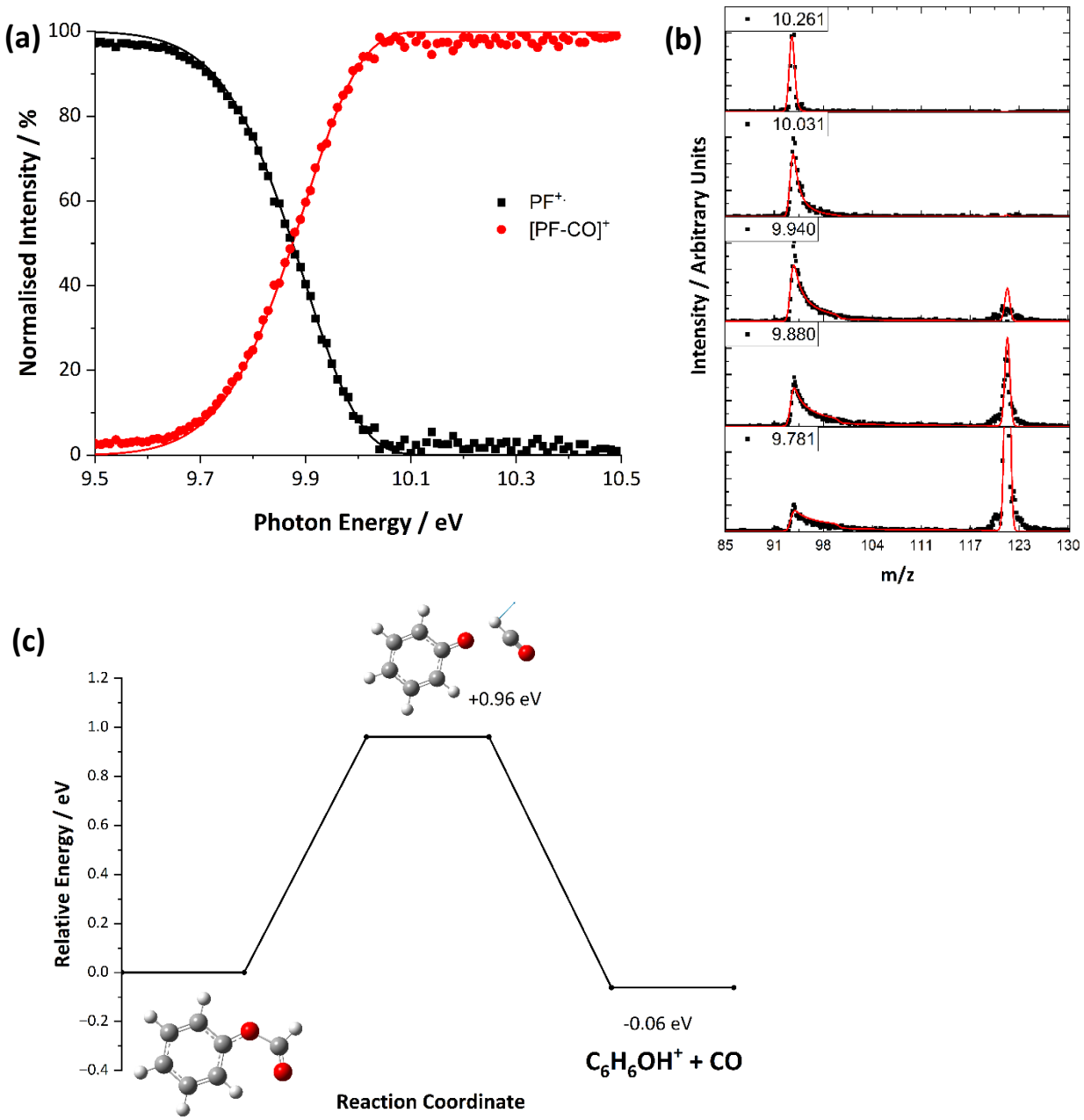

Figure 6-2: (a) Breakdown diagram of PF^+ losing CO with the statistical model overlaid as a solid line of the respective colours, **(b)** TOFs for the m/z 122 and 94 peaks for PF^+ decomposition at the indicated photon energy, with RRKM fitting overlaid in red and **(c)** Minimum energy reaction pathway calculated for loss of CO from PF^+ at B3LYP/6-311++G(d,p).

6.5.2. Phenyl Chloroformate

The TPES and ms-TPES for $PCF^{+\bullet}$ for the ground-state band are presented in Figure 6-3a and they show a similar broad, featureless band as the PF^{+} TPES, due to the analogous internal rotation upon ionisation (shown in Figure 6-3b). Here again, experimental ionisation onset is close to the CBS-QB3 value for the IE of 9.03 eV.

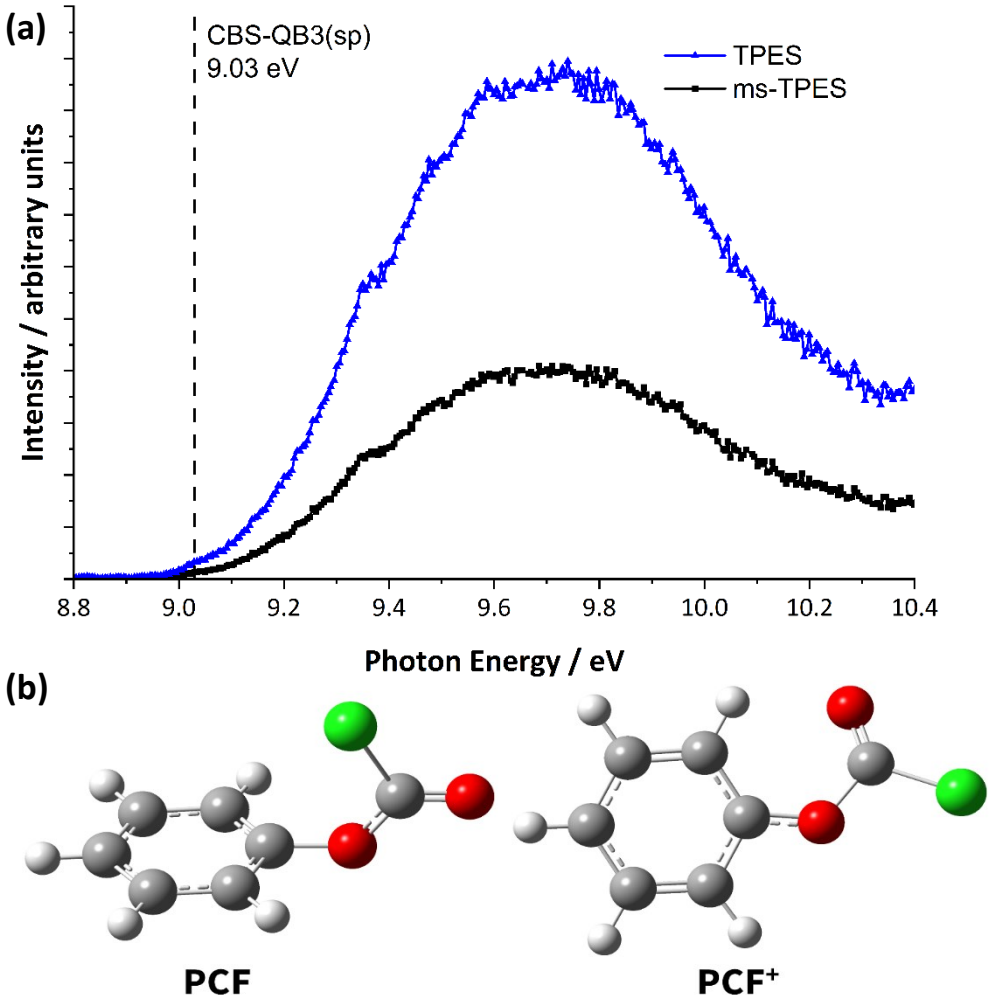

Figure 6-3: (a) TPES and ms-TPES at m/z 156 for $PCF^{+\bullet}$ **(b)** Structures of PCF and $PCF^{+\bullet}$ optimised at B3LYP/6-311++G(d,p)

However, $PCF^{+\bullet}$ shows a more complicated dissociation pattern than $PF^{+\bullet}$. The mass spectra exhibit major peaks at *m/z* 156/158 ($PCF^{+\bullet}$), 128/130 (loss of CO), 121 (loss of Cl), 112/114 (loss of CO_2), 93

(nominal loss of COCl), and 77 (nominal loss of CO_2Cl). The breakdown diagram is shown in Figure 6-4.

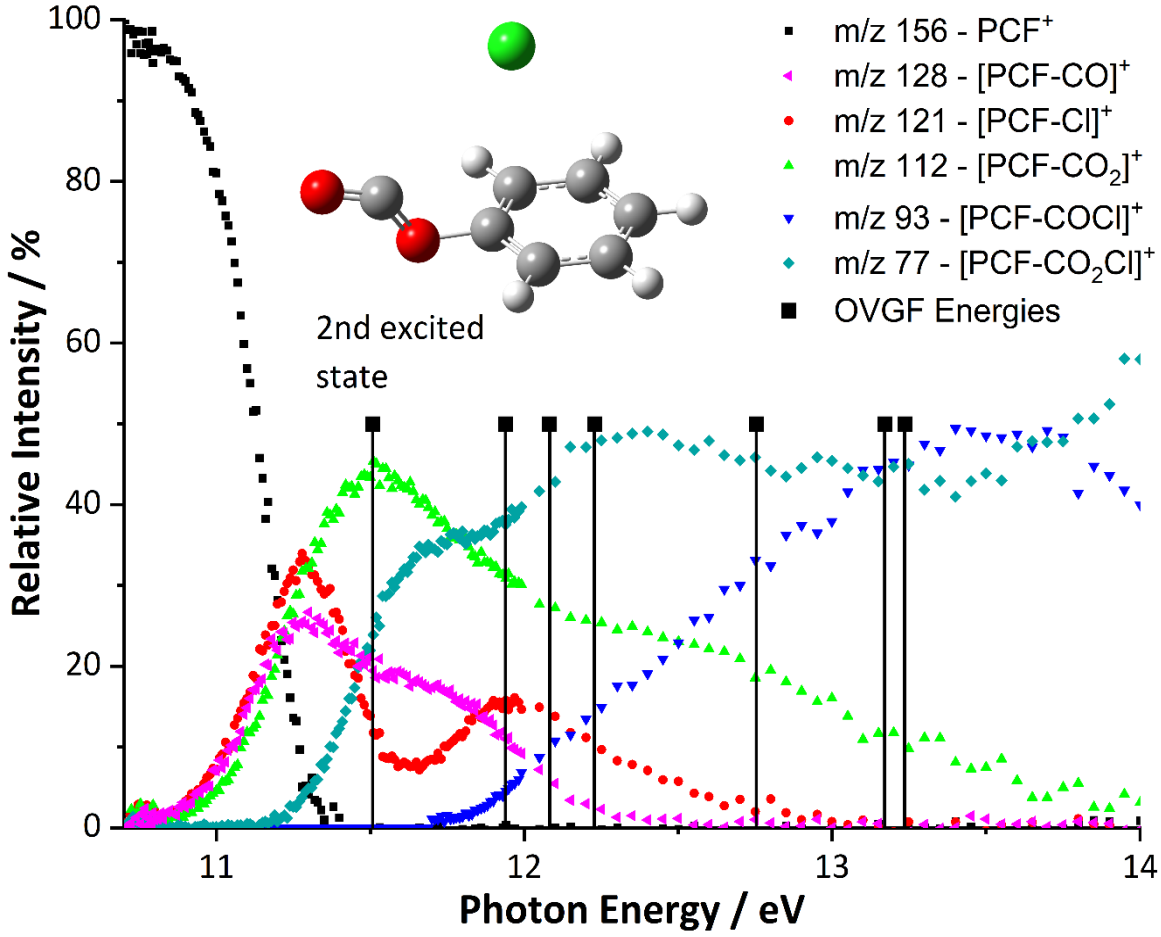

Figure 6-4: Breakdown diagram of PCF^+ with OVGF/cc-pVTZ vertical ionization energies overlaid.

The three high mass fragment ions, m/z 128, 121 and 112 can only occur directly from $PCF^{+\bullet}$ by the loss of CO, Cl and CO_2, respectively. The mass-analysed ion kinetic energy (MIKE) spectrum[56] for *m/z* 156 (the isotopically pure ^{35}Cl-containing molecular ion) is shown in Figure 6-5. The spectrum confirms the origin of these three fragment ions and shows that the peak with *m/z* 112 is dish-shaped, indicating that CO_2 loss occurs with a large kinetic energy release, and thus the reaction likely has a significant reverse energy barrier. Both *m/z* 77 and 93 ions may have resulted from different precursors.

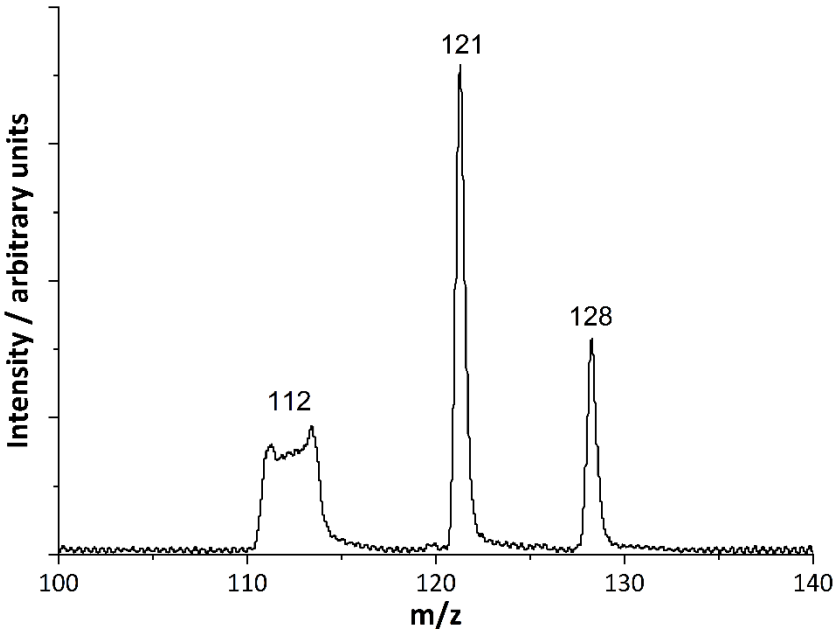

Figure 6-5: MIKES mass spectrum of $PCF^{+\bullet}$ showing a dish-shaped peak for m/z 112.

MIKES experiments were performed to confirm which pathways occur, and the results are shown in Figure A4-1 and summarised in **Error! Reference source not found.**.

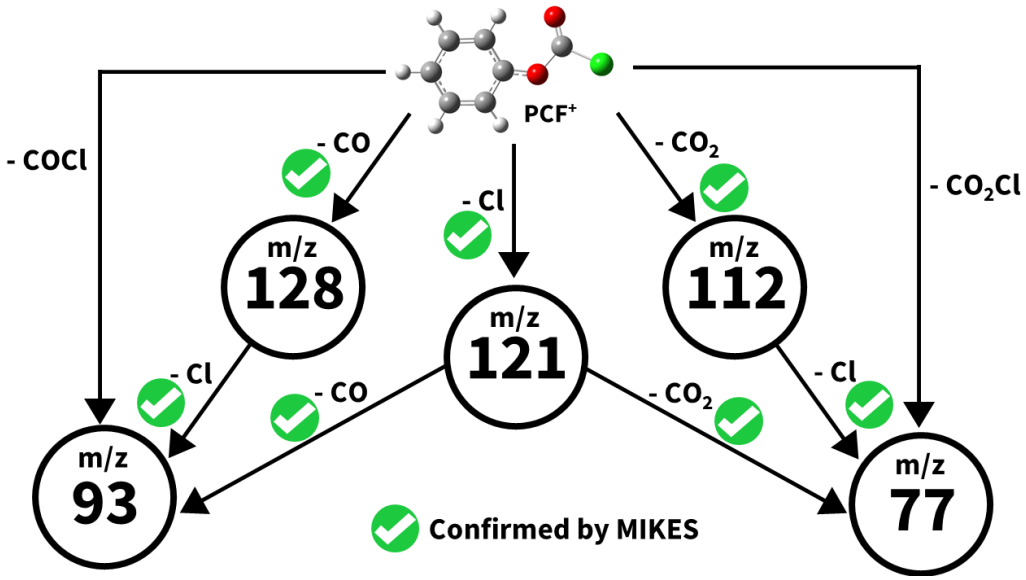

Figure 6-6: Summary of potential dissociation pathways of PCF^{+} with check marks next to the pathways that have been confirmed through MIKES

The minimum-energy reaction pathways are shown in Figure 6-7. Cl loss (red) is a dissociation without a barrier in the reverse direction leading to $C_6H_5CO_2^+$. This fragment ion at *m/z* 121 can dissociate sequentially by two competing channels, by loss of CO or CO_2, with a difference in energy of 0.51 eV favouring CO_2. As a neutral, PCF undergoes a rearrangement process to transfer the Cl to the ring to form chlorophenol.[147] However, this process does not occur in the ion as the more energetically favourable process involves the ClCO moiety pulling away from the phenoxy group after which the Cl atom hops back to the O-atom resulting in CO loss (green). This dissociation also takes place without a reverse barrier according to bond length scans at the current level of theory. Sequential Cl loss from the CO-loss daughter ion, thus, starts from an ion–molecule complex, in which the Cl is bound weakly to the π-system of the benzene ring.

CO_2 loss proceeds through a transition state (1.38 eV, mauve) leading to the low energy products ionized chlorobenzene + CO_2. The large excess product energy results in the large kinetic energy distribution of *m/z* 112 observed in the MIKE spectrum (Figure 6-5).

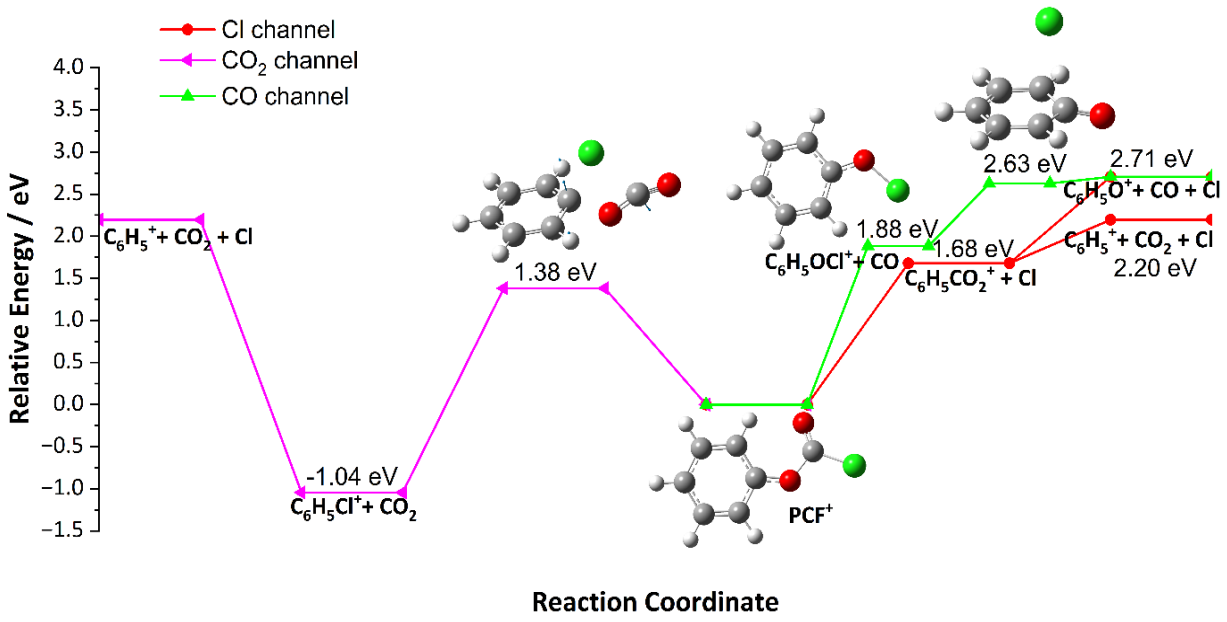

Figure 6-7: Minimum energy reaction pathway for $PCF^{+\bullet}$ dissociation at the B3LYP/6-311++G(d,p) level of theory.

In the breakdown diagram for PCF^+ (Figure 6-4) the *m*/*z* 121 breakdown curve decreases until 11.6 eV then increases up to 11.95 eV. This indicates a new, more competitive fragmentation channel opening up. In lieu of a more favourable, higher activation entropy channel on the ground potential energy surface, this alternate channel likely corresponds to a non-statistical dissociation from an excite state of the ion. The pattern is similar to that observed in CH_3Cl^+ where an excited state is responsible for a portion of the Cl loss pathway.[151] Indeed, OVGF energies for the ion states show that there is an excited state at 11.5 eV and three in close proximity between 11.9 and 12.2 eV. The TD-DFT optimized structure of the second excited state (HOMO-2, OVGF energy of 11.5 eV) has a distanced chlorine that is weakly bound and dissociates upon ionisation, Figure 6-4.

The fragment ion peaks in the mass spectra are asymmetric, as shown in Figure 6-8. Therefore, a breakdown diagram derived from a simple integration of the peaks over a time-of-flight range incorrectly estimates the contribution of each channel where overlap occurs, as it does for those between *m*/*z* 128 and 112; this gives rise to three identical breakdown channels up to ~11.2 eV in Figure 6-4. For this reason, we focussed more on the RRKM fitting of the TOFs up to 11.2 eV, Figure 6-8, which yields E_0 values of 1.60 ± 0.03, 1.49 ± 0.03 and 1.44 ± 0.04 eV for *m*/*z* 128, 121 and 112, respectively. These can be compared with the CBS-QB3//B3LYP/6-311++G(d,p) results of 1.88, 1.68, and 1.38 eV, respectively. The RRKM model appears to overextrapolate the rate constants to a lower threshold energy for reactions without a reverse barrier, which is in line with previous observations.[152] The activation entropies respectively are −8 ± 5, −14 ± 4, and −15 ± 4 J K^{-1} mol^{-1} at 1000 K.

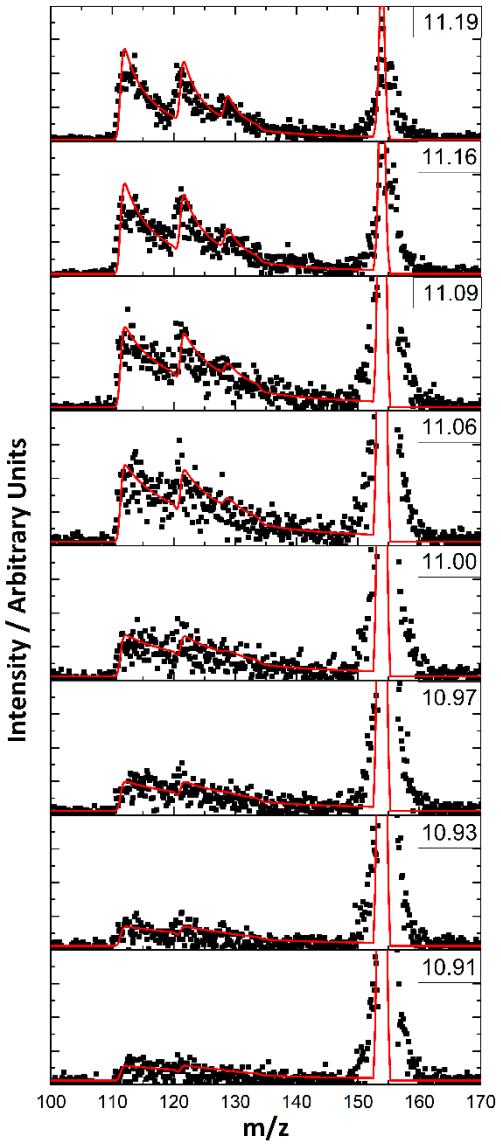

Figure 6-8: TOFs for the m/z 112–154 peaks for $PCF^{+\bullet}$ decomposition, with RRKM fitting overlaid in red.

Once the peaks become symmetric and baseline separated above 11.25 eV photon energy, they can be integrated accurately to plot the breakdown diagram. The three parallel channels reach comparable abundances at this photon energy. Afterwards, the Cl-loss signal at *m/z* 121 drops precipitously as CO_2 is lost sequentially and the phenyl cation is formed at *m/z* 77. The CO-loss abundance decays at somewhat higher energies, as it is followed by Cl loss yielding the phenoxy cation at *m/z* 93. Both the CO- and CO_2-loss branches decay above 11.7 eV photon energy, when the excited-state driven non-statistical Cl-loss gains abundance (see above).

6.6. Conclusions

The TPES and mass-selected TPES of PF and PCF were reported for the first time. Poor Franck-Condon overlap due to the rotation of the formate functional group relative to the benzene group accounts for the broad and featureless TPES. CBS-QB3//B3LYP/6-311++G (d,p) calculations yielded ionization energies of 8.88 and 9.03 eV for PF and PCF, respectively and are consistent with the reported TPES.

Ionised PF only dissociates by loss of CO via a transition state of the H-transferring to form a phenoxy radical. The energetics of this reaction are comparable to that of phenyl acetate where the H on the formate is replaced by CH_3.[146]

The ion chemistry of PCF showed 5 primary ion products, m/z 128/130 (CO loss), m/z 121 (Cl loss), m/z 112/114 (CO_2 loss), m/z 98 (COCl loss), and m/z 77 ((CO_2Cl loss). MIKES experiments determined that the primary channels for dissociation are loss of CO, Cl and CO_2, sequential loss of all of these contributes to the respective ions m/z 98 and m/z 77. The minimum energy reaction pathway confirmed these findings and showed that the CO loss is least energetically favoured, which is opposite to what is seen in the neutral chemistry of PCF, where H-transfer to form chlorophenol is favoured.[147] Cl loss was shown to also dissociate in a non-statistical process from its second excited state, where the chlorine becomes weakly bound to the ring. The MIKES of PCF^+ showed that loss of CO_2 occurs with a large reverse energy barrier, consistent with the computationally-derived minimum energy reaction pathway from B3LYP/6-311++G(d,p) calculations.

Chapter 7. Conclusions

While the chapters each have their respective conclusions, this chapter highlights any trends and particularly novel finds from throughout the chapters while considering the motivations for the study and how the chapters help to answer that.

7.1. Pyrolysis

In chapter 3, 4 and 5 the pyrolysis chemistry of methyl formate, ethyl formate and methyl chloroformate were studied, respectively. The results that were found were in agreement to prior studies using shock-tube methods and showed that utilising the micro-reactor coupled with iPEPICO helped to better account for the nuances in the reaction. For example, in chapter 3 methyl formate was confirmed to pyrolyse to CO and methanol, which is a reaction reflected in the ion chemistry, ms-TPES enabled distinction between the 2 reactions. Chapter 4 highlighted this further by distinguishing between isobaric species, for example the identification of CO and C_2H_4 at m/z 28 by using ms-TPES. Overall, this method provides a quicker, more effective means of detecting products of unimolecular pyrolysis reactions, while providing other important information about the nature of the dissociation products such as vibrational information.

An interesting finding in the pyrolysis studies was the dominance of dissociation leading to CO, CO_2 and CH_2O, all of which were exhibited by all 3 formates studied. All 3 show a similar mechanism for CO_2 loss by transferring H or Cl from the formate group onto C2. It is therefore expected that with increasing chain length, CO_2 would continue to dominate as a pyrolysis product.

On the contrary, MF and EF show similar mechanisms of dissociation for CO and CH_2O, where the hydrogen transfers from the formate group onto the oxygen for CO loss and CH_2O formation by H transfer onto the formate carbon. However, substitution of chlorine in the formate group, as in the

case of MCF, Cl-O bonds are hindered from being formed as they are weak as both species are electronegative. For MCF CO loss therefore proceeds by HCl formation, it is therefore expected that similar reactions would occur in larger chloroformates, producing RCH_2O. So as chain length increases CH_2O is expected to be a dominant pyrolysis product for formates, however, for chloroformates RCH_2O will likely dominate. Ethyl formate also shows formation of formic acid from transfer of hydrogen from C3, this is a product that would expect to continue to form as chain length increases, producing longer chain alkenes, it is also a possible product for ethyl chloroformate and longer chain chloroformates, producing chloroformic acid.

7.2. Ion Chemistry

Chapters 5 and 6 focus on the ion chemistry of MCF^+, PF^+, and PCF^+. TPES for MF and EF showed that the neutral and ion structures didn't have great differences as they had well-defined vibrational structure in the TPES and ms-TPES, however, for MCF the TPES was much more poorly defined, this is due to the ion interacting more similar to a dimer of CH_3O and ClCO. PF and PCF both showed poorly defined TPES due to π interactions causing rotation to a planar structure upon ionisation.

For the chloroformates they both exhibit similar losses, that of $Cl^\bullet$ and $ClCO^\bullet$, the latter of which differs in PCF to MCF as it occurs stepwise rather than concerted, this is likely due to the difference in ion structures, with the elongation of the CH_3O─C(O)Cl bond for MCF. Therefore, these are both expected to continue to dominate at longer chain lengths.

PF^+ and PCF^+ both exhibited CO loss which also occurs in MF^+ and EF^+ but does not occur in MCF^+ due to the O-Cl being a weak bond, as discussed earlier. It does however occur in PCF^+ due to π interactions of the ring with Cl, which cannot occur in MCF^+. $CO^\bullet$ loss may be possible in longer chain chloroformates due to the presence of a C3 enabling transfer to the carbon rather than the oxygen.

CO_2 loss is observed for PCF^+ and MCF^+ but not for PF^+. Firstly, the loss of CO_2 for PCF^+ and MCF^+ differ as the former proceeds via a substitution reaction producing $C_6H_5Cl^+$ and CO_2, while MCF^+ first loses $Cl^\bullet$ then loses CO_2. CO_2 loss is therefore possible in chloroformates for 2 reasons, (1) $Cl^\bullet$ is a good leaving group and (2) Cl is a nucleophile; however, H is neither of these so CO_2 loss cannot proceed in the ionised formates.

7.3. Ion Chemistry vs Pyrolysis Chemistry

While the ion and pyrolysis chemistry of the formates show some differences, they tended to be more similar for the formates than the chloroformates. For example, CO loss is a primary dissociation for MF, EF and PF in pyrolysis and ion chemistry. However, MF^+ loses $HCO^\bullet$ a process that does not occur in pyrolysis. Overall, pyrolysis tended not to display these bond cleavage reaction products, but rather rearranged species forming small neutral closed-shell molecules.

Ion and pyrolysis chemistry differs more greatly for the chloroformates, this is largely due to Cl loss not being as favourable as a neutral. However, for PCF the difference is only the loss of Cl, as CO_2 and CO loss both occur in both ion and pyrolysis chemistry. The mechanisms for their formation are different, however. For example, for CO loss in pyrolysis, the Cl transfers onto the ring to form chlorophenol, whereas in the ion it is more favourable for the Cl to interact with the ring in π interactions. For MCF CO_2 loss occurs in both however, in the ion it is lost in a sequential process, while in the neutral it occurs in a concerted manner.

7.4. Future Outlooks

The knowledge gained through study of the ion and pyrolysis chemistry can therefore give insights in what chemistry is expected to occur from biofuels. It also helps to shape what can be expected for coupling non-thermal plasma techniques with biofuels in cars.

Further work can include studying chloroformate ion and pyrolysis chemistry for those with a C3 carbon to see if any differences occur with the added stability provided by the extra carbon. Other work can utilise a similar experimental set up to explore the pyrolysis of other molecules such as polyfluorinated alkyl substances that are solids at room temperature so would require a change in set-up to enable them to enter into the gas-phase into the pyrolysis set-up.

References

1 J. R. Holton, in *Encyclopedia of Atmospheric Sciences: Second Edition*, Elsevier Inc., 2015, pp. 257–261.

2 J. G. Speight, in *Environmental Organic Chemistry for Engineers*, ed. J. G. Speight, Butterworth-Heinemann, 2017, pp. 1–41.

3 A. P. Showman and T. E. Dowling, in *Encyclopedia of the Solar System*, Elsevier, 2014, pp. 423–444.

4 M. L. Brusseau, A. D. Matthias, S. A. Musil and H. L. Bohn, in *Environmental and Pollution Science*, Elsevier, 2019, pp. 47–59.

5 Radiation Spectrum, http://agron-www.agron.iastate.edu/courses/Agron541/classes/541/lesson09a/9a.3.html, (accessed 14 April 2020).

6 A. C. Balachandra Swamy, *Astrophys. Space Sci.*, 1991, **178**, 71–88.

7 K.N. Liou, in *An Introduction to Atmospheric Radiation*, ed. K.N. Liou, Academic Press, 2002, vol. 84, pp. 65–115.

8 T. C. E. Marcus, M. David, M. Yaacob, M. R. Salim, M. H. Ibrahim, N. H. Ngajikin and A. I. Azmi, *J. Teknol. (Sciences Eng).*, 2013, **64**, 95–98.

9 H. Keller-Rudek, G. K. Moortgat, R. Sander and R. Sörensen, *Earth Syst. Sci. Data*, 2013, **5**, 365–373.

10 V. M. Ellsworth and J. J. Hopfield, *Phys. Rev.*, 1927, **29**, 79–84.

11 K. Yoshino, D. E. Freeman and W. H. Parkinson, *J. Phys. Chem. Ref. Data*, 1984, **13**, 207–227.

12 S. Chapman, *Q. J. R. Meteorol. Soc.*, 1932, **3**, 11–13.

13 J. T. Kiehl and T. Yamanouchi, *Tellus B*, 1985, **37B**, 1–6.

14 M. J. Molina and F. S. Rowland, *Nat. 1974 2495460*, 1974, **249**, 810–812.

15 Y. Maréchal, *Hydrog. Bond Water Mol.*, 2007, 195–213.

16 J. R. Prescott, J. R. Patterson, A. G. Gregory, P. C. Crouch, D. F. Liebing, A. A. Watson, K. J. Orford, K. E. Turver, I. Samorski, W. Astrophys, J. C. Farman, B. G. Gardiner and J. D. Shanklin, *Nature*, 1985, **315**, 207–210.

17 WMO, WMO, UNEP, NOAA, NASA, European Commission, Geneva, 2022.

18 Pollutant information - NAEI, UK, https://naei.beis.gov.uk/overview/pollutants?pollutant_id=9, (accessed 16 May 2020).

19 Volatile Organic Compounds' Impact on Indoor Air Quality | Indoor Air Quality (IAQ) | US EPA, https://www.epa.gov/indoor-air-quality-iaq/volatile-organic-compounds-impact-indoor-air-quality, (accessed 16 May 2020).

20 H. Levy, *Science.*, 1971, **173**, 141–143.

21 C. E. Reeves, S. A. Penkett, S. Bauguitte, K. S. Law, M. J. Evans, B. J. Bandy, P. S. Monks, G. D. Edwards, G. Phillips, H. Barjat, J. Kent, K. Dewey, S. Schmitgen and D. Kley, *J. Geophys. Res. Atmos.*, 2002, **107**, 1–14.

22 R. Atkinson, *Atmos. Environ.*, 2000, **34**, 2063–2101.

23 P. J. Ziemann and R. Atkinson, *Chem. Soc. Rev.*, 2012, **41**, 6582–6605.

24 R. Atkinson and J. Arey, *Chem. Rev.*, 2003, **103**, 4605–4638.

25 Screening assessment formic acid and formates substance group - Canada.ca, https://www.canada.ca/en/environment-climate-change/services/evaluating-existing-substances/screening-assessment-fa-fs-group.html, (accessed 7 June 2020).

26 G. Thiault, R. Thévenet, A. Mellouki and G. Le Bras, *Phys. Chem. Chem. Phys.*, 2002, **4**, 613–619.

27 S. Zhou, I. Barnes, T. Zhu, I. Bejan and T. Benter, *J. Phys. Chem. A*, 2006, **110**, 7386–7392.

28 H. Konishi, H. Nagase and K. Manabe, *Chem. Commun.*, 2015, **51**, 1854–1857.

29 A. Aronica, F. Ragaini, F. Ferretti and M. A. Fouad, *Catalysts*, 2023, **13**, 224.

30 R. A. L. Michael D. Larrañaga, Richard J. Lewis Sr., in *Hawley's Condensed Chemical Dictionary.*, ed. R. A. L. Michael D. Larrañaga, Richard J. Lewis Sr., Van Nostrand Reinhold Co, New York, 11`., 1987, p. 764.

31 U. EPA, in *Patty's industrial hygiene and toxicology: Volume 2A: Toxicology*, John Wiley & Sons, New York, 1981, vol. 2A, p. 2878.

32 J. M. Wieting, T. J. Fisher, A. G. Schafer, M. D. Visco, J. C. Gallucci and A. E. Mattson, *European J. Org. Chem.*, 2015, **2015**, 525–533.

33 S. H. Kwak and Y. D. Gong, *Tetrahedron*, 2013, **69**, 7107–7111.

34 J. J. Orlando, G. S. Tyndall, E. C. Apel, D. D. Riemer and S. E. Paulson, *Int. J. Chem. Kinet.*, 2003, **35**, 334–353.

35 T. Cordova, A. Rotinov and G. Chuchani, *J. Phys. Org. Chem. J. Phys. Org. Chem*, 2004, **17**, 148–

151.

36 C. K. Westbrook, C. V. Naik, O. Herbinet, W. Pitz, M. Mehl, S. M. Sarathy and H. J. Curran, *Combust. Flame*, 2011, **158**, 742–755.

37 H. Ning, J. Wu, L. Ma and W. Ren, *Combust. Flame*, 2020, **211**, 337–346.

38 M. A. González D., W. Piel, T. Asmus, W. Clark, J. Garbak, E. Liney, M. Natarajan, D. W. Naegeli, D. Yost, E. A. Frame and J. P. Wallace, *SAE Trans.*, 2001, **110**, 2246–2255.

39 R. Balla, B. Muthaiah and P. Arathala, *ChemistrySelect*, 2017, **2**, 11603–11614.

40 S. Dooley, M. P. Burke, M. Chaos, Y. Stein, F. L. Dryer, V. P. Zhukov, O. Finch, J. M. Simmie and H. J. Curran, *Int. J. Chem. Kinet.*, 2010, **42**, 527–549.

41 H. Ning, J. Wu, L. Ma, W. Ren, D. F. Davidson and R. K. Hanson, *J. Phys. Chem. A*, 2017, **121**, 6568–6579.

42 A. L. Cardona, J. Salas, L. Lesniak, A. A. Mommers, P. M. Mayer and M. A. Burgos Paci, *ChemistrySelect*, 2023, **8**, e202202897.

43 P. Hemberger, X. Wu, Z. Pan and A. Bodi, *J. Phys. Chem. A*, 2022, **126**, 2196–2210.

44 P. Hemberger, V. B. F. Custodis, A. Bodi, T. Gerber and J. A. Van Bokhoven, *Nat. Commun.*, 2017, **8**, 1–9.

45 E. Bosa, C. Paradisi and G. Scorrano, *Rapid Commun. Mass Spectrom.*, 2003, **17**, 1–8.

46 S. Mohapatro, N. Kumar Sharma and A. Madhukar, *IEEE Trans. Dielectr. Electr. Insul.*, 2017, **24**, 2738–2745.

47 K. V. S. S. Bhargavi, D. Ray, P. Chawdhury, M. Selvaraj, T. Shashidhar and C. Subrahmanyam,

IEEE Trans. Plasma Sci., 2022, **50**, 1416–1422.

48 F. Di Giacomo, *J. Chem. Educ.*, 2014, **92**, 476–481.

49 R. A. Marcus, *J. Chem. Phys.*, 1952, **20**, 359.

50 L. S. Kassel, *J. Phys. Chem.*, 1928, **32**, 225–242.

51 T. Baer and P. M. Mayer, *J. Am. Soc. Mass Spectrom.*, 1997, **8**, 103–115.

52 T. Baer, O. A. Mazyar, J. W. Keister and P. M. Mayer, *Berichte der Bunsengesellschaft für Phys. Chemie*, 1997, **101**, 478–483.

53 B. Sztáray, A. Bodi and T. Baer, *J. Mass Spectrom.*, 2010, **45**, 1233–1245.

54 T. Baer and W. L. Hase, Oxford University Press, 1996.

55 T. Beyer and D. F. Swinehart, *Commun. ACM*, 1973, **16**, 379.

56 R. G. Cooks, Elsevier Scientific Pub. Co., Amsterdam;, 1973.

57 B. West, C. Joblin, V. Blanchet, A. Bodi, B. Sztáray and P. M. Mayer, *J. Phys. Chem. A*, 2012, **116**, 10999–11007.

58 Y. Zhao and D. G. Truhlar, *Theor. Chem. Acc.*, 2008, **120**, 215–241.

59 S. Grimme, J. Antony, S. Ehrlich and H. Krieg, *J. Chem. Phys.*, 2010, **132**, 154104.

60 T. H. Dunning, *J. Chem. Phys.*, 1989, **90**, 1007–1023.

61 G. D. Purvis III and R. J. Bartlett, *J. Chem. Phys.*, 1982, **76**, 1910–1918.

62 J. A. Pople, M. Head-Gordon and K. Raghavachari, *J. Chem. Phys.*, 1987, **87**, 5968–5975.

63 J. A. Montgomery, M. J. Frisch, J. W. Ochterski and G. A. Petersson, *J. Chem. Phys.*, 2000, **112**,

6532–6542.

64 O. N. Ventura, M. Kieninger, A. Katz, M. Vega-Teijido, M. Segovia and K. Irving, *Int. J. Quantum Chem.*

65 R. Kumar, A. Katoch, A. Singhal and S. Kumar, *Energy and Fuels*, 2018, **32**, 12936–12948.

66 Y. Isayama and S. Saka, *Bioresour. Technol.*, 2008, **99**, 4775–4779.

67 J. S. Lee, J. C. Kim and Y. G. Kim, J. S. Lee, J. C. Kim and Y. G. Kim (version) Elsevier.

68 S. Dooley, F. L. Dryer, B. Yang, J. Wang, T. A. Cool, T. Kasper and N. Hansen, *Combust. Flame*, 2011, **158**, 732–741.

69 J. Wu, H. Ning, L. Ma and W. Ren, *Phys. Chem. Chem. Phys.*, 2018, **20**, 26190–26199.

70 J. S. Francisco, *J. Am. Chem. Soc.*, 2003, **125**, 10475–10480.

71 T. Nishimura, Q. Zha and G. G. Meisels, *J. Chem. Phys.*, 1987, **87**, 4589.

72 A. Bodi, P. Hemberger, T. Gerber and B. Sztáray, A. Bodi, P. Hemberger, T. Gerber and B. Sztáray (version) American Institute of Physics.

73 B. Sztáray, K. Voronova, K. G. Torma, K. J. Covert, A. Bodi, P. Hemberger, T. Gerber and D. L. Osborn, *J. Chem. Phys.*, 2017, **147**, 013944.

74 X. Tang, X. Lin, Y. Zhu, X. Wu, Z. Wen, L. Zhang, F. Liu, X. Gu and W. Zhang, *RSC Adv.*, 2017, **7**, 28746–28753.

75 B. Sztáray and T. Baer, *Rev. Sci. Instrum.*, 2003, **74**, 3763.

76 P. Hemberger, A. Bodi, T. Bierkandt, M. Köhler, D. Kaczmarek and T. Kasper, *Energy & Fuels*, 2021, **35**, 16265–16302.

77 R. M. Stephenson and S. Malanowski, Springer, Dordrecht, 1987.

78 Q. Guan, K. N. Urness, T. K. Ormond, D. E. David, G. Barney Ellison, J. W. Daily, G. B. Ellison and J. W. Daily, *Int. Rev. Phys. Chem.*, 2014, **33**, 447–487.

79 S. Grimm, S. J. Baik, P. Hemberger, A. Bodi, A. M. Kempf, T. Kasper and B. Atakan, *Phys. Chem. Chem. Phys.*, 2021, **23**, 15059–15075.

80 M. J. Frisch, G. W. Trucks, H. B. Schlegel, G. E. Scuseria, M. A. Robb, J. R. Cheeseman, G. Scalmani, V. Barone, A. Petersson, H. Nakatsuji, X. Li, M. Caricato, A. V. Marenich, J. Bloino, B. G. Janesko, R. Gomperts, B. Mennucci, H. P. Hratchian, J. V. Ortiz, A. F. Izmaylov, J. L. Sonnenberg, D. Williams-Young, F. Ding, F. Lipparini, F. Egidi, J. Goings, B. Peng, A. Petrone, T. Henderson, D. Ranasinghe, V. G. Zakrzewski, J. Gao, N. Rega, G. Zheng, W. Liang, M. Hada, M. Ehara, K. Toyota, R. Fukuda, J. Hasegawa, M. Ishida, T. Nakajima, Y. Honda, O. Kitao, H. Nakai, T. Vreven, K. Throssell, M. J. A. Jr., J. E. Peralta, F. Ogliaro, M. J. Bearpark, J. J. Heyd, E. N. Brothers, K. N. Kudin, V. N. Staroverov, T. A. Keith, R. Kobayashi, J. Normand, K. Raghavachari, A. P. Rendell, J. C. Burant, S. S. Iyengar, J. Tomasi, M. Cossi, J. M. Millam, M. Klene, C. Adamo, R. Cammi, J. W. Ochterski, R. L. Martin, K. Morokuma, O. Farkas, J. B. Foresman and D. J. Fox, M. J. Frisch, G. W. Trucks, H. B. Schlegel, G. E. Scuseria, M. A. Robb, J. R. Cheeseman, G. Scalmani, V. Barone, A. Petersson, H. Nakatsuji, X. Li, M. Caricato, A. V. Marenich, J. Bloino, B. G. Janesko, R. Gomperts, B. Mennucci, H. P. Hratchian, J. V. Ortiz, A. F. Izmaylov, J. L. Sonnenberg, D. Williams-Young, F. Ding, F. Lipparini, F. Egidi, J. Goings, B. Peng, A. Petrone, T. Henderson, D. Ranasinghe, V. G. Zakrzewski, J. Gao, N. Rega, G. Zheng, W. Liang, M. Hada, M. Ehara, K. Toyota, R. Fukuda, J. Hasegawa, M. Ishida, T. Nakajima, Y. Honda, O. Kitao, H. Nakai, T. Vreven, K. Throssell, M. J. A. Jr., J. E. Peralta, F. Ogliaro, M. J. Bearpark, J. J. Heyd, E. N.

Brothers, K. N. Kudin, V. N. Staroverov, T. A. Keith, R. Kobayashi, J. Normand, K. Raghavachari, A. P. Rendell, J. C. Burant, S. S. Iyengar, J. Tomasi, M. Cossi, J. M. Millam, M. Klene, C. Adamo, R. Cammi, J. W. Ochterski, R. L. Martin, K. Morokuma, O. Farkas, J. B. Foresman and D. J. Fox (version) Gaussian, Inc., Wallingford CT.

81 J. R. Barker, T. L. Nguyen, J. F. Stanton, C. Aieta, M. Ceotto, F. Gabas, T. J. D. Kumar, C. G. L. Li, L. L. Lohr, A. Maranzana, N. F. Ortiz, J. M. Preses, J. M. Simmie, J. A. Sonk and P. J. Stimac, J. R. Barker, T. L. Nguyen, J. F. Stanton, C. Aieta, M. Ceotto, F. Gabas, T. J. D. Kumar, C. G. L. Li, L. L. Lohr, A. Maranzana, N. F. Ortiz, J. M. Preses, J. M. Simmie, J. A. Sonk and P. J. Stimac (version) University of Michigan, Ann Arbor, Michigan, USA.

82 J. R. Barker, *Int. J. Chem. Kinet.*, 2001, **33**, 232–245.

83 J. R. Barker, *Int. J. Chem. Kinet.*, 2009, **41**, 748–763.

84 C. Eckart, *Phys. Rev.*, 1930, **35**, 1303.

85 L. Yang, J. A. Sonk and J. R. Barker, *J. Phys. Chem. A*, 2015, **119**, 5723–5731.

86 M. A. Ali, J. A. Sonk and J. R. Barker, *J. Phys. Chem. A*, 2016, **120**, 7060–7070.

87 J. R. Barker, T. L. Nguyen, J. F. Stanton, C. Aieta, M. Ceotto, F. Gabas, T. J. D. Kumar, C. G. L. Li, L. L. Lohr, A. Maranzana, N. F. Ortiz, J. M. Preses, J. M. Simmie, J. A. Sonk, P. J. Stimac and A. Arbor, 2019.

88 J. C. Ianni, *Comput. Fluid Solid Mech. 2003*, 2003, 1368–1372.

89 E. Waterstradt, R. Jung, T. Belling and K. Müller-Dethlefs, *Berichte der Bunsengesellschaft für Phys. Chemie*, 1994, **98**, 176–179.

90 Y. Nunes, G. Martins, N. J. Mason, D. Duflot, S. V. Hoffmann, J. Delwiche, M. J. Hubin-Franskin

and P. Limão-Vieira, *Phys. Chem. Chem. Phys.*, 2010, **12**, 15734–15743.

91 B. Niu, D. A. Shirley and Y. Bai, *J. Chem. Phys.*, 1993, **98**, 4377–4390.

92 T. Yu, X. Wu, X. Zhou, A. Bodi and P. Hemberger, *Combust. Flame*, 2020, **222**, 123–132.

93 R. D. Johnson and J. W. Hudgens, *J. Phys. Chem.*, 1996, **100**, 19874–19890.

94 X. Tang, X. Lin, G. A. Garcia, J. C. Loison, C. Fittschen, X. Gu, W. Zhang and L. Nahon, *J. Chem. Phys.*, 2020, **153**, 31101.

95 O. A. Mazyar and T. Baer, *J. Phys. Chem. A*, 1998, **102**, 1682–1690.

96 W. Ren, K. Y. Lam, S. H. Pyun, A. Farooq, D. F. Davidson and R. K. Hanson, *Proc. Combust. Inst.*, 2013, **34**, 453–461.

97 K. P. Somers and J. M. Simmie, *J. Phys. Chem. A*, 2015, **119**, 8922–8933.

98 A. Karton and L. Goerigk, *J. Comput. Chem.*, 2015, **36**, 622–632.

99 A. J. Ragauskas, C. K. Williams, B. H. Davison, G. Britovsek, J. Cairney, C. A. Eckert, W. J. Frederick, J. P. Hallett, D. J. Leak, C. L. Liotta, J. R. Mielenz, R. Murphy, R. Templer and T. Tschaplinski, *Science.*, 2006, **311**, 484–489.

100 K. Ishida and S. Mayama, *Theor. Chim. Acta*, 1983, **62**, 245–255.

101 J. A. Erickson and S. D. Kfthn, *J. Am. Chem. Soc.*, 1994, **116**, 6271–6276.

102 J. M. Hermida-Ramón, J. Rodríguez-Otero and E. M. Cabaleiro-Lago, *J. Phys. Chem. A*, 2003, **107**, 1651–1654.

103 Y. C. Chou, *J. Chinese Chem. Soc.*, 2012, **59**, 1528–1535.

104 Q. Zha, T. Nishimura and G. G. Meisels, *Int. J. Mass Spectrom. Ion Process.*, 1992, **120**, 85–101.

105 D. W. Kohn, H. Clauberg and P. Chen, *Rev. Sci. Instrum.*, 1998, **63**, 4003.

106 A. K. Vasiliou, J. H. Kim, T. K. Ormond, K. M. Piech, K. N. Urness, A. M. Scheer, D. J. Robichaud, C. Mukarakate, M. R. Nimlos, J. W. Daily, Q. Guan, H.-H. Carstensen and G. B. Ellison, *J. Chem. Phys.*, 2013, **139**, 104310.

107 C. O. Rogers, K. S. Lockwood, Q. L. D. Nguyen and N. J. Labbe, *Int. J. Chem. Kinet.*, 2021, **53**, 1272–1284.

108 D. P. Zaleski, R. Sivaramakrishnan, H. R. Weller, N. A. Seifert, D. H. Bross, B. Ruscic, K. B. Moore, S. N. Elliott, A. V. Copan, L. B. Harding, S. J. Klippenstein, R. W. Field and K. Prozument, *J. Am. Chem. Soc.*, 2021, **143**, 3124–3142.

109 M. A. Śmiałek, M. Łabuda, J. Guthmuller, M. J. Hubin-Franskin, J. Delwiche, D. Duflot, N. J. Mason, S. V. Hoffmann, N. C. Jones and P. Limão-Vieira, *J. Chem. Phys.*, 2014, **141**, 104311.

110 M. Łabuda and J. Guthmuller, *Eur. Phys. J. Spec. Top. 2013 2229*, 2013, **222**, 2257–2266.

111 K. Johnson, I. Powis and C. J. Danby, *Chem. Phys.*, 1982, **70**, 329.

112 L. Wang, J. E. Reutt, Y. T. Lee and D. A. Shirley, *J. Electron Spectrosc. Relat. Phenom.*, 1988, **47**, 167.

113 B. A. Williams and T. A. Cool, *J. Am. Chem. Soc.*, 1991, **94**, 6358.

114 K.-M. Weitzel, J. Mahnert and H. Baumgartel, *Ber bunsenges. Phys Chemer bunsenges. Phys Chem*, 1993, **97**, 134–139.

115 F. Giithe and K.-M. M. Weitzel, *Berichte der Bunsengesellschaft für Phys. Chemie*, 1997, **101**,

484–490.

116 S. Magne Briten, T. Helgaker, E. Uggerud and T. Vulpius, 1993, **28**, 1262–1269.

117 T. S. Venkatesan and S. Mahapatra, *J. Chem. Phys.*, 2005, **123**, 114308.

118 P. Erman, A. Karawajczyk, E. Rachlew-Kallne, C. Stromholm, J. Larsson, A. Persson and R. Zerne, *Chem. Phys. Lett.*, 1993, **215**, 173.

119 S. Bell, T. L. Ng and A. D. Walsh, *J. Chem. Soc. Faraday Trans. 2*, 1975, **71**, 393.

120 A. Bodi, M. Daniel Brannock, B. Sztáray and T. Baer, *Phys. Chem. Chem. Phys.*, 2012, **14**, 16047–16054.

121 V. K. K. Potapov and V. V. V Sorokin, *Khim. Vys. Energ.*, 1972, **6**, 387–391.

122 T. Hayaishi, S. Iwata, M. Sasanuma, E. Ishiguro, Y. Morioka, Y. Iida and M. Nakamura, *J. Phys. B*, 1982, **15**, 79.

123 R. Bombach, J. Dannacher and J.-P. Stadelmann, *Int. J. Mass Spectrom. Ion Process.*, 1984, **58**, 217.

124 M. Balaganesh, G. Sudhakar and B. Rajakumar, *29th Int. Symp. Shock Waves 1*, 2013, 233–238.

125 W. Ren, R. Mitchell Spearrin, D. F. Davidson and R. K. Hanson, *J. Phys. Chem. A*, 2014, **118**, 1785–1798.

126 P. Osswald, U. Struckmeier, T. Kasper, K. Kohse-Höinghaus, J. Wang, T. A. Cool, N. Hansen and P. R. Westmoreland, *J. Phys. Chem. A*, 2007, **111**, 4093–4101.

127 K. Saito, T. Shiose, O. Takahashi, Y. Hidaka, F. Aiba and K. Tabayashi, *J. Chem. Phys.*, 2005, **109**, 5352–5357.

128 Z. Peng, S. Shlykov, C. Van Alsenoy, H. J. Geise and B. Van der Veken, *J. Phys. Chem.*, 1995, **99**, 10201–10212.

129 Y. C. Chou, *J. Chinese Chem. Soc.*, 2013, **59**, 1528–1535.

130 W. K. Metcalfe, J. M. Simmie and H. J. Curran, *J. Phys. Chem. A*, 2010, **114**, 5478–5484.

131 B. Lowe, A. L. Cardona, J. Salas, A. Bodi, M. A. Burgos Paci and P. M. Mayer, *J. Mass Spectrom.*, 2022, **57**, e4868.

132 T. M. Pazdera, J. Wenz and M. Olzmann, *Faraday Discuss.*, 2022, **238**, 665–681.

133 M. N. McCabe, P. Hemberger, D. Campisi, J. C. Broxterman, E. Reusch, A. Bodi and J. Bouwman, *Phys. Chem. Chem. Phys.*, 2022, **24**, 1869–1876.

134 J. G. Chang, H. T. Chen, S. Xu and M. C. Lin, *J. Phys. Chem. A*, 2007, **111**, 6789–6797.

135 R. F. Makens and W. G. Eversole, *J. Am. Chem. Soc.*, 1939, **61**, 3203–3206.

136 S. Grimme, S. Ehrlich and L. Goerigk, *J. Comput. Chem.*, 2011, **32**, 1456–1465.

137 R. L. Johnson and V. Raymond Stimson, *Aust. J. Chem.*, 1977, **30**, 1917–1920.

138 R. L. Johnson and V. Raymond Stimson, *Aust. J. Chem.*, 1976, **29**, 1389–1392.

139 M. C. Blanchette, J. L. Holmes, C. E. C. A. Hop, F. P. Lossing, R. Postma, P. J. A. Ruttink and J. K. Terlouw, *J. Am. Chem. Soc.*, 1986, **108**, 7589.

140 J. L. Holmes and F. P. Lossing, *Int. J. Mass Spectrom. Ion Process.*, 1984, **58**, 113.

141 P. R. Briggs and T. W. Shannon, *J. Am. Chem. Soc.*, 1969, **91**, 4307.

142 L. R. McCunn, K. C. Lau, M. J. Krisch, L. J. Butler, J. W. Tsung and J. J. Lin, *J. Phys. Chem. A*, 2006,

110, 1625–1634.

143 B. Lowe, A. L. Cardona, J. Salas, A. Bodi, P. M. Mayer and M. A. B. Paci, *J. Mass Spectrom.*, 2023, e4901.

144 J. R. Barker, T. L. Nguyen, J. F. Stanton, C. Aieta, M. Ceotto, F. Gabas, T. J. D. Kumar, L. L. L. C.G.L.Li, A. Maranzana, N. F. Ortiz, J. M. Preses, J. M. Simmie, J. A. Sonk and P. J. Stimac, J. R. Barker, T. L. Nguyen, J. F. Stanton, C. Aieta, M. Ceotto, F. Gabas, T. J. D. Kumar, L. L. L. C.G.L.Li, A. Maranzana, N. F. Ortiz, J. M. Preses, J. M. Simmie, J. A. Sonk and P. J. Stimac (version) University of Michigan, Ann Arbor, Michigan, USA.

145 J. L. Ragle, I. A. Stenhouse, D. C. Frost and C. A. Mcuoweli, *J. Chem. Phys.*, 1970, **53**, 178.

146 G. Bouchoux, *Int. J. Mass Spectrom. Ion Phys.*, 1978, **26**, 379–394.

147 J. Lezama and G. Chuchani, *Int. J. Chem. Kinet.*, 2015, **47**, 10.

148 J. L. Holmes and P. M. Mayer, *J. Phys. Chem.*, 1995, **99**, 1366–1370.

149 J. C. Traeger and A. A. Mommers, *Org. Mass Spectrom.*, 1987, **22**, 592–596.

150 R. E. Ballard, J. Jones, D. Read, A. Inchley and M. Cranmer, *Chem. Phys. Lett.*, 1987, **137**, 125–129.

151 X. Tang, X. Lin, W. Zhang, G. A. Garcia and L. Nahon, *Phys. Chem. Chem. Phys.*, 2016, **18**, 23923–23931.

152 W. Stevens, B. Sztáray, N. Shuman, T. Baer and J. Troe, *J. Phys. Chem. A*, 2009, **113**, 573–582.

Appendix 1

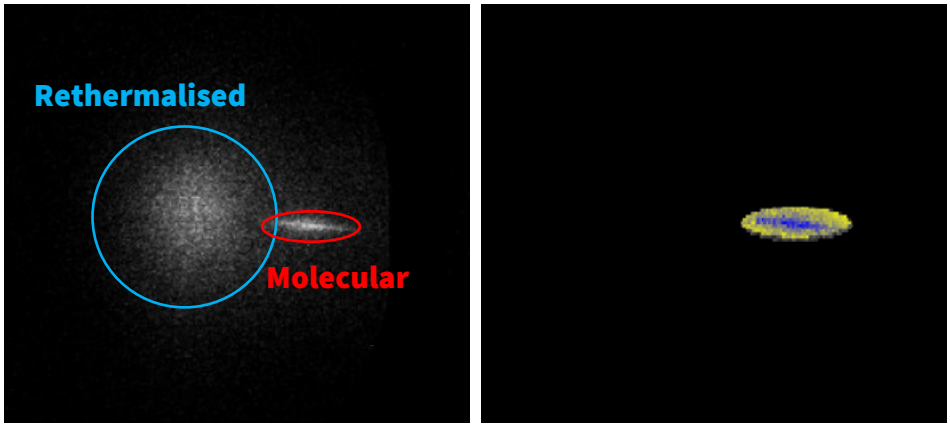

Explanatory figures about selecting the molecular beam

Figure A1-1: Ion detector signals, left shows the different signals and right shows the area selected for the molecular beam only selected mass spectra.

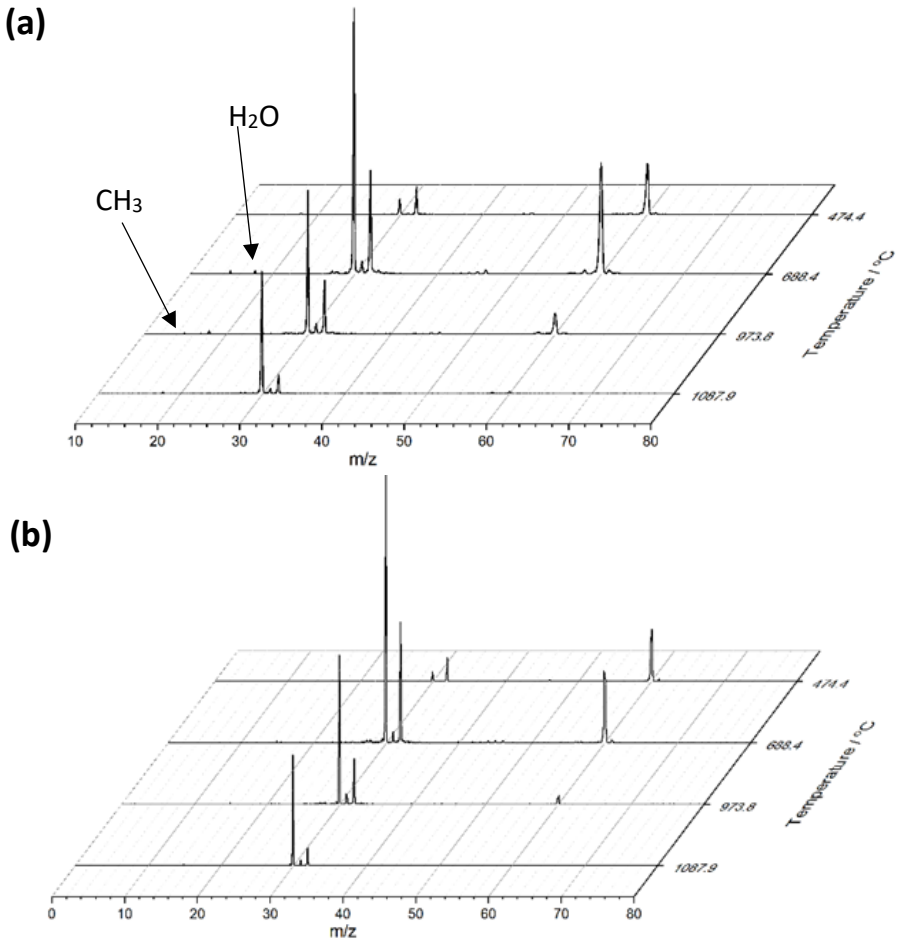

Figure A1-2: Mass spectra at a photon energy of 11 eV over varying pyrolysis temperatures, **(a)** all signal included. **(b)** molecular beam signal selected only.

Threshold Photoelectron Spectrum for CO

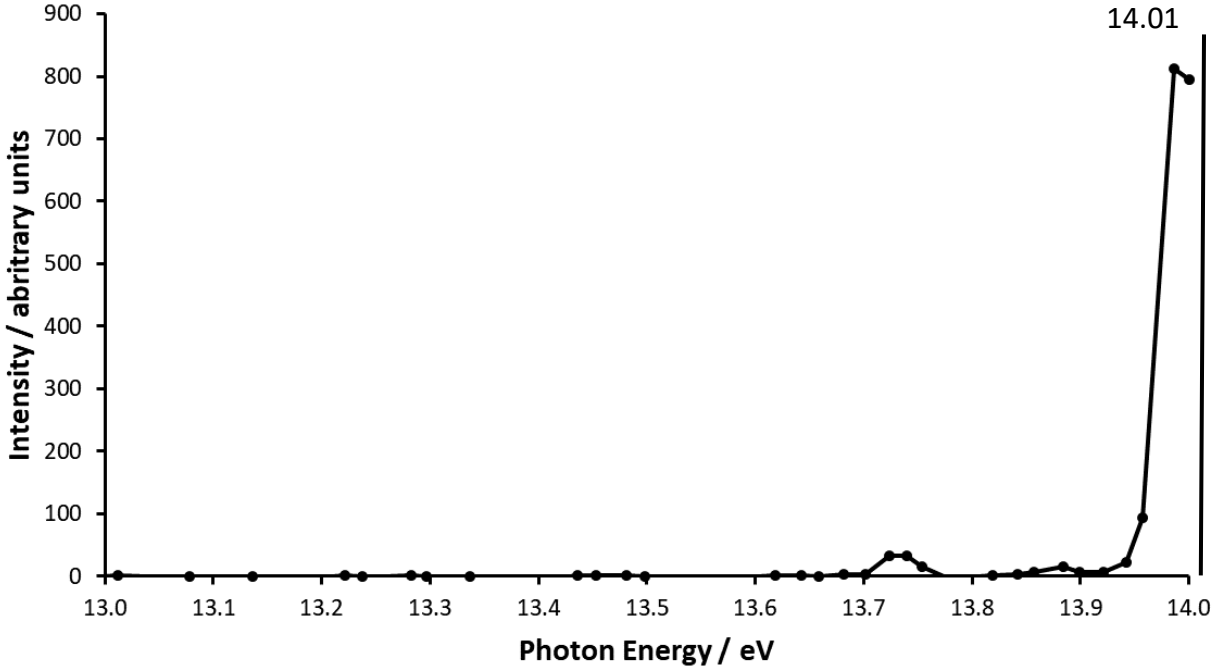

Figure A1-3: TPES of m/z 28, CO at 688 °C.

Scan of coordinates for the homolytic path analysis.

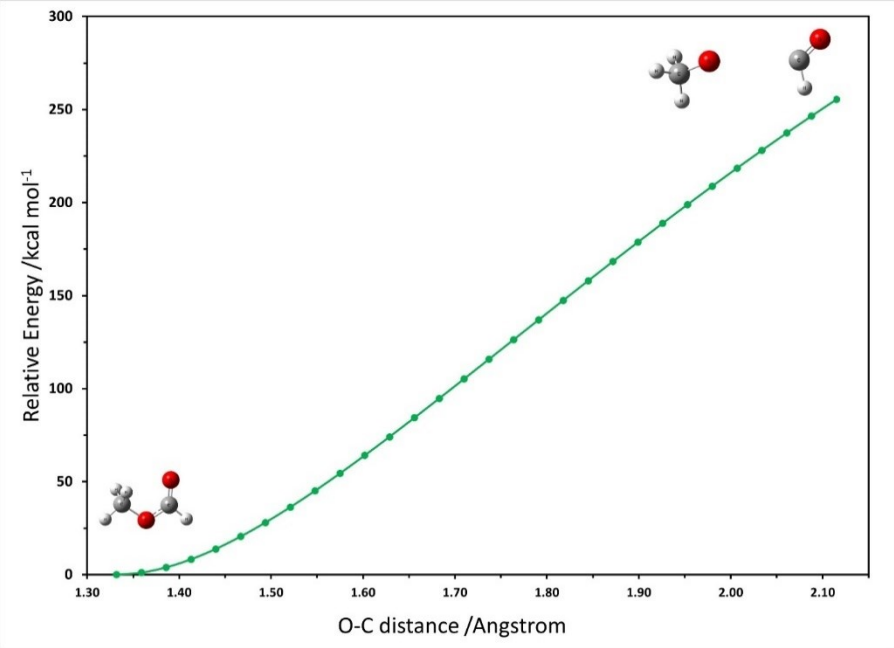

Figure A1-4: Relative energy in the O-C scan of coordinates for the methyl formate unimolecular decomposition.

O-C distance	R. Energy	O-C distance	R. Energy	O-C distance	R. Energy
1.332	0.00	1.602	64.11	1.872	168.37
1.359	1.06	1.629	74.10	1.899	178.67
1.386	3.89	1.656	84.31	1.926	188.86
1.413	8.23	1.683	94.69	1.953	198.90
1.440	13.83	1.710	105.18	1.980	208.79
1.467	20.48	1.737	115.74	2.007	218.50
1.494	28.01	1.764	126.33	2.034	228.03
1.521	36.27	1.791	136.91	2.061	237.37
1.548	45.11	1.818	147.46	2.088	246.49
1.575	54.42	1.845	157.96	2.115	255.38

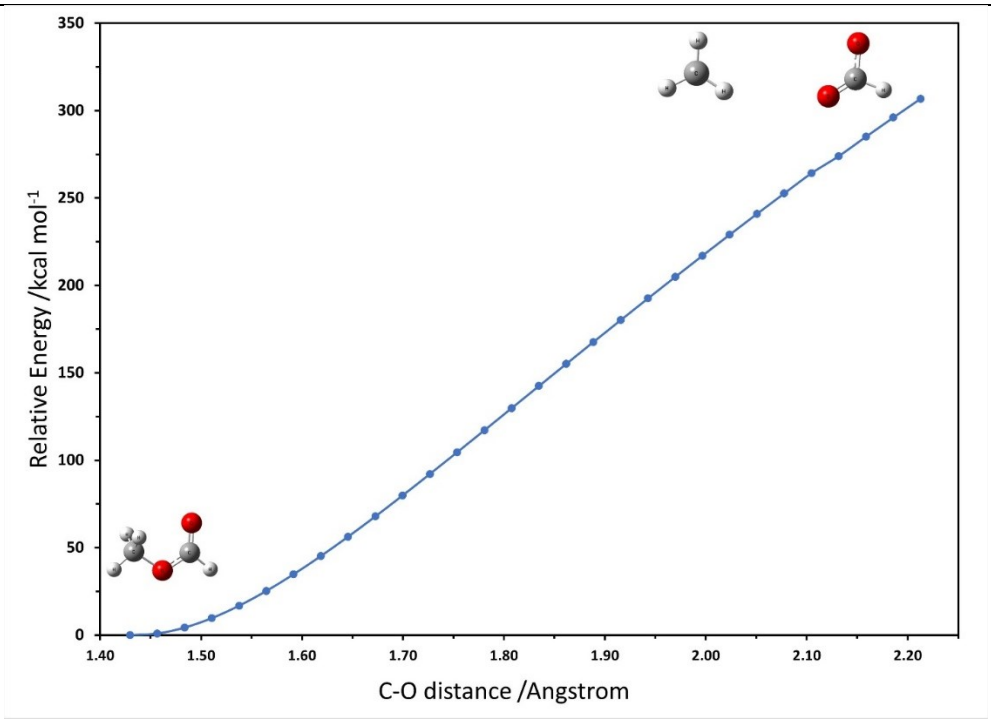

Figure A1-5: Relative energy in the C-O scan of coordinates for the methyl formate unimolecular decomposition.

C-O distance	R. Energy	C-O distance	R. Energy	C-O distance	R. Energy
1.430	0.00	1.700	79.90	1.970	204.90
1.457	0.90	1.727	92.16	1.997	217.07
1.484	4.28	1.754	104.62	2.024	229.10
1.511	9.71	1.781	117.19	2.051	240.98
1.538	16.80	1.808	129.83	2.078	252.70
1.565	25.26	1.835	142.48	2.105	264.25
1.592	34.81	1.862	155.11	2.132	274.03
1.619	45.22	1.889	167.69	2.159	285.13
1.646	56.31	1.916	180.19	2.186	296.06
1.673	67.91	1.943	192.60	2.213	306.81

Thermochemistry for Methyl Formate thermal decomposition.

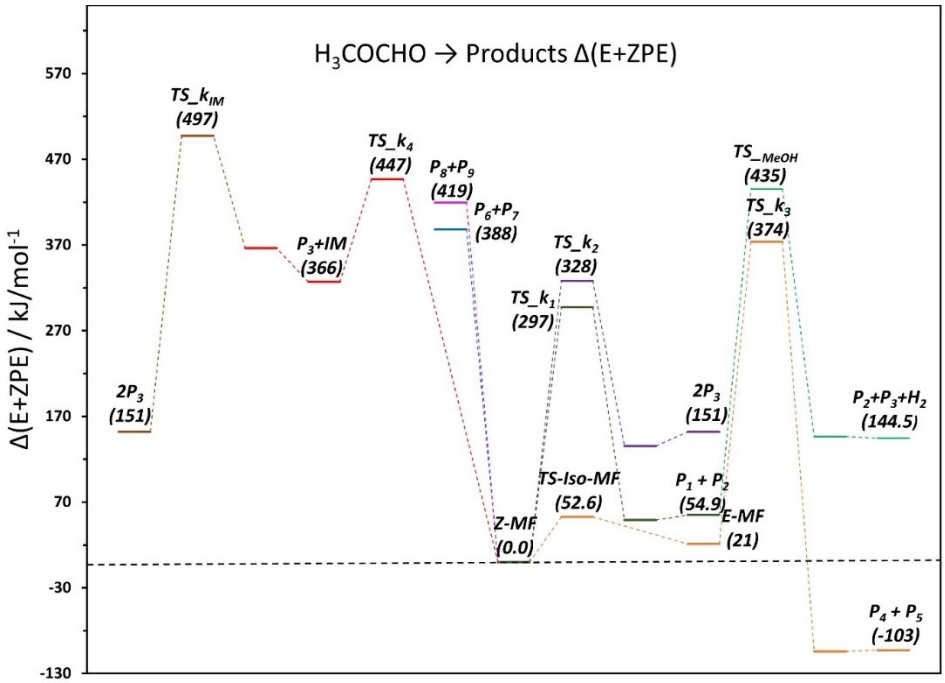

Figure A1-6: Potential Energy diagram for the Hydroxy Methylene thermal decomposition (ZPE corrected).

Optimized geometries and vibrational frequencies at the M06-2X-GD3/cc-pVTZ level of theory of Methyl Formate conformers.

Z-H_3COCHO

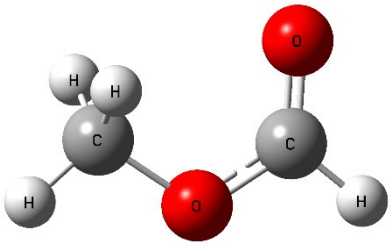

Method	Ee	E+ZPE	ΔH	ΔG
M06-2X-GD3/cc-pVTZ	-229.059914	-228.99697	-228.991582	-229.023605
CCSD(T)/cc-pVTZ	-228.726033	-228.663089	-228.657701	-228.689724
CBS-QB3	-228.800379	-228.739213	-228.733688	-228.766118

Coordinates (xyz)				Vibrations (cm^{-1})		
C	-1.350570	0.400880	0.000000	158.4674	1191.0631	3084.3196
H	-1.974188	1.288051	0.000000	351.4166	1207.6203	3093.6978
H	-1.539019	-0.202756	0.885514	156.469	1273.3393	3159.0109
H	-1.539019	-0.202756	-0.885514	319.233	1412.3654	3195.5672
C	0.927003	-0.086630	0.000000	346.2657	1481.0627	
H	1.924632	0.365989	0.000000	792.69	1496.9728	
O	0.000000	0.869711	0.000000	984.8394	1509.2319	
O	0.708625	-1.261465	0.000000	1068.7905	1856.5579	

Z ↔ E					
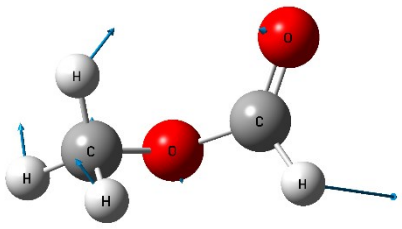					
Method	**Ee**		**E+ZPE**	**ΔH**	**ΔG**
M06-2X-GD3/cc-pVTZ	-229.038414		-228.976931	-228.97186	-229.003377
CCSD(T)/cc-pVTZ	-228.704619		-228.643136	-228.638066	-228.669583
CBS-QB3	-228.778863		-228.718779	-228.713514	-228.745701
Coordinates (xyz)				**Vibrations (cm^{-1})**	
C	1.498657	0.316423	-0.132487	*i* 240.6476	1238.9819	3118.6702
H	2.394163	0.075596	0.430858	169.1488	1403.0934	3180.5381
H	1.258177	1.373135	-0.012739	296.8958	1484.7744	
H	1.665238	0.093182	-1.189227	680.2104	1504.0503	
C	-0.738085	-0.335327	-0.236695	1002.8748	1516.0972	
H	-0.863747	-1.029710	-1.081441	1069.0901	1889.6793	
O	0.451740	-0.492561	0.399698	1174.5723	3028.7321	
O	-1.568135	0.444232	0.097042	1182.4295	3047.8617	

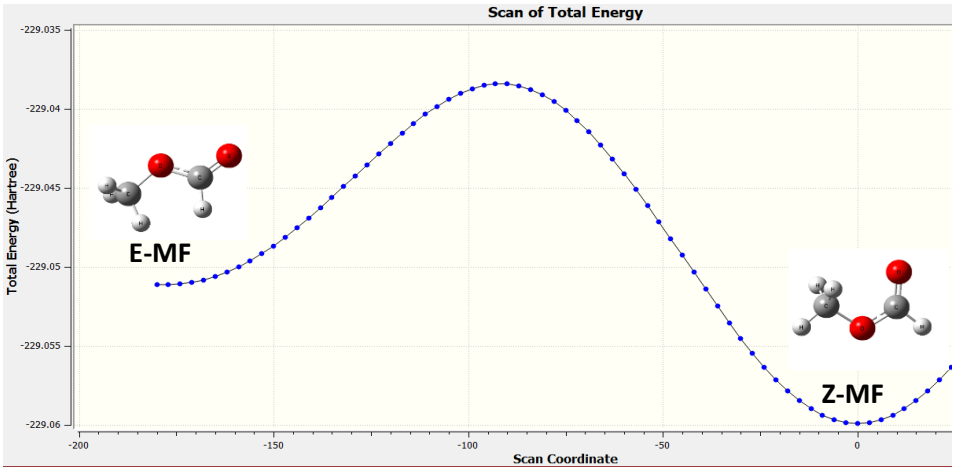

Figure A1-7: Intrinsic reaction coordinate (IRC) for the Methyl formate Isomerization.

E-H_3COCHO						
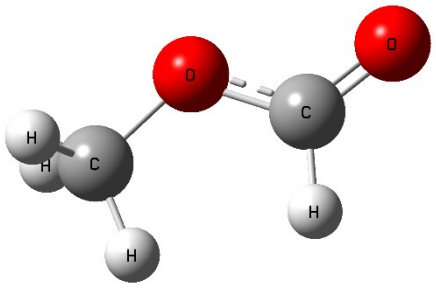						
Method	**Ee**		**E+ZPE**	**ΔH**	**ΔG**	
M06-2X-GD3/cc-pVTZ	-229.051143		-228.988971	-228.983189	-229.016674	
CCSD(T)/cc-pVTZ	-228.71762		-228.655448	-228.649666	-228.683151	
CBS-QB3	-228.791774		-228.731329	-228.725537	-228.758772	
Coordinates (xyz)				**Vibrations (cm^{-1})**		
C	1.667497	0.106368	0.000002	76.7145	1161.0023	3006.6502
H	2.201648	-0.221095	-0.888833	192.0387	1191.216	3066.2334
H	2.201603	-0.220996	0.888901	43.5476	1301.7568	3143.8189
H	1.601567	1.195487	-0.000061	187.5595	1427.9759	3161.5208
C	-0.692206	0.315565	-0.000002	391.6194	1497.2129	
H	-0.430198	1.386578	-0.000006	658.6516	1503.4179	
O	0.378271	-0.488476	-0.000003	1054.3064	1526.5641	
O	-1.806566	-0.095470	0.000002	1067.1226	1900.2229	

Optimized geometries and vibrational frequencies at the M06-2X-GD3/cc-pVTZ level of theory of MF thermal decomposition products.

P1_H_3COH

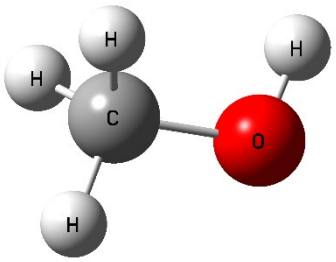

Method	Ee	E+ZPE	ΔH	ΔG
M06-2X-GD3/cc-pVTZ	-115.714123	-115.662351	-115.658051	-115.685125
CCSD(T)/cc-pVTZ	-115.550706	-115.498934	-115.494634	-115.521708
CBS-QB3	-115.590536	-115.539945	-115.535678	-115.562686

Coordinates (xyz)				Vibrations (cm^{-1})	
C	0.046447	0.659697	0.000000	291.0778	1509.0519
H	1.086424	0.978263	0.000000	1072.1235	1522.6243
H	-0.437586	1.073106	0.888918	1117.1085	3031.8771
H	-0.437586	1.073106	-0.888918	1182.6848	3083.6557
O	0.046447	-0.752830	0.000000	1375.6759	3145.1909
H	-0.861510	-1.060017	0.000000	1489.2782	3904.8309

P2_CO

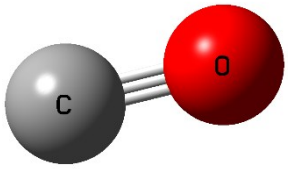

Method	Ee	E+ZPE	ΔH	ΔG
M06-2X-GD3/cc-pVTZ	-113.318864	-113.313681	-113.310377	-113.332793
CCSD(T)/cc-pVTZ	-113.155151	-113.149968	-113.146663	-113.16908
CBS-QB3	-113.186998	-113.181991	-113.178686	-113.201111

Coordinates (xyz)				Vibrations (cm^{-1})
C	0.000000	0.000000	-0.641050	2275.0612
O	0.000000	0.000000	0.480787	

P3_H_2CO

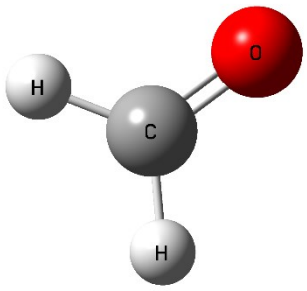

Method	Ee	E+ZPE	ΔH	ΔG
M06-2X-GD3/cc-pVTZ	-114.496616	-114.469571	-114.465762	-114.491216
CCSD(T)/cc-pVTZ	-114.333558	-114.306513	-114.302703	-114.328157
CBS-QB3	-114.370391	-114.344169	-114.340356	-114.36517

Coordinates (xyz)				Vibrations (cm^{-1})	
C	0.000000	0.524880	0.000000	1216.698	2940.9127
H	0.937529	1.107259	0.000000	1279.3426	3011.8873
H	-0.937529	1.107259	0.000000	1545.8433	
O	0.000000	-0.670475	0.000000	1876.7914	

4_CH_4

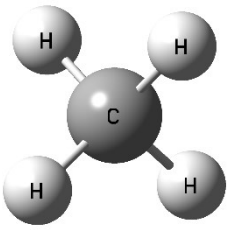

Method	Ee	E+ZPE	ΔH	ΔG
M06-2X-GD3/cc-pVTZ	-40.501416	-40.456434	-40.452622	-40.473742
CCSD(T)/cc-pVTZ	-40.4380897	-40.393108	-40.389296	-40.410416
CBS-QB3	-40.45414	-40.410008	-40.406194	-40.427326

Coordinates (xyz)				Vibrations (cm^{-1})	
C	0.000000	0.000000	0.000000	1341.6426	3061.8336
H	0.627607	0.627607	0.627607	1341.6426	3175.5036
H	-0.627607	-0.627607	0.627607	1341.6426	3175.5036
H	-0.627607	0.627607	-0.627607	1565.7156	3175.5036
H	0.627607	-0.627607	-0.627607	1565.7156	

P5_CO_2

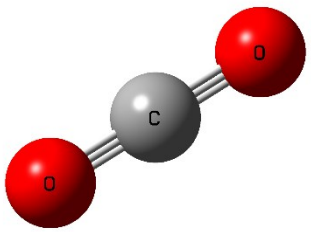

Method	Ee	E+ZPE	ΔH	ΔG
M06-2X-GD3/cc-pVTZ	-188.591597	-188.579631	-188.576087	-188.600307
CCSD(T)/cc-pVTZ	-188.326731	-188.314765	-188.311221	-188.335442
CBS-QB3	-188.383668	-188.372065	-188.368492	-188.392762

Coordinates (xyz)				Vibrations (cm^{-1})	
C	0.000000	0.000000	0.000000	691.2595	2457.3752
O	0.000000	0.000000	1.155292	691.2595	
O	0.000000	0.000000	-1.155292	1412.492	

P6_H_3CO

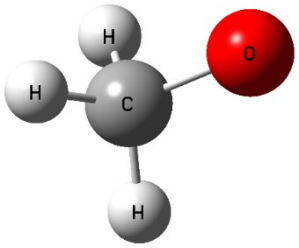

Method	Ee	E+ZPE	ΔH	ΔG
M06-2X-GD3/cc-pVTZ	-115.039488	-115.003288	-114.999124	-115.02633
CCSD(T)/cc-pVTZ	-114.874762	-114.838562	-114.834399	-114.861605
CBS-QB3	-114.910281	-114.874519	-114.870534	-114.897459

Coordinates (xyz)				Vibrations (cm^{-1})	
C	0.575862	0.000002	0.012183	405.2277	1523.164
H	0.871564	-0.000069	-1.050146	973.5631	2962.7613
H	1.000088	-0.904773	0.459552	1140.8748	3034.0137
H	1.000095	0.904826	0.459445	1386.3964	3075.861
O	-0.790865	0.000001	0.007256	1388.0461	

P7_HCO					
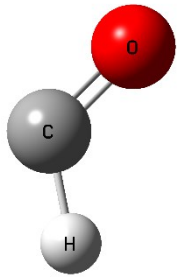					
Method			**Ee**	**E+ZPE**	**ΔH**	**ΔG**
M06-2X-GD3/cc-pVTZ			-113.847274	-113.834	-113.830198	-113.85565
CCSD(T)/cc-pVTZ			-113.683758	-113.670484	-113.666682	-113.692134
CBS-QB3			-113.717545	-113.704757	-113.700954	-113.726423
Coordinates (xyz)				**Vibrations (cm^{-1})**	
C	0.062327	0.584225	0.000000	1111.121	
H	-0.872574	1.214856	0.000000	1941.1117	
O	0.062327	-0.590026	0.000000	2617.9199	

P8_H_3C					
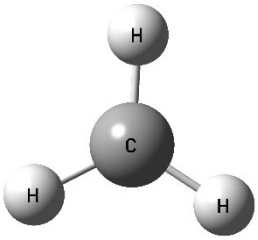					
Method			**Ee**	**E+ZPE**	**ΔH**	**ΔG**
M06-2X-GD3/cc-pVTZ			-39.824679	-39.79499	-39.790909	-39.814821
CCSD(T)/cc-pVTZ			-39.7609659	-39.731277	-39.727195	-39.751108
CBS-QB3			-39.774072	-39.744799	-39.740783	-39.764596
Coordinates (xyz)				**Vibrations (cm^{-1})**	
C	0.000000	0.000000	-0.000003	420.0955	3321.0435
H	0.000000	0.000000	1.076526	1412.498	3322.2239
H	0.932305	0.000000	-0.538261	1413.5104	
H	-0.932305	0.000000	-0.538261	3142.7821	

P9_OCHO

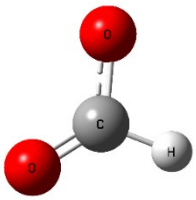

Method	Ee	E+ZPE	ΔH	ΔG
M06-2X-GD3/cc-pVTZ	-189.073639	-189.054186	-189.050007	-189.07879
CCSD(T)/cc-pVTZ	-188.810074	-188.790621	-188.786443	-188.815226
CBS-QB3	-188.869961	-188.854533	-188.849856	-188.879619

Coordinates (xyz)				Vibrations (cm^{-1})	
C	-0.038910	0.000000	-0.066752	384.4872	1824.1978
H	0.101200	0.000000	1.035241	1013.339	2925.1418
O	1.166858	0.000000	-0.599153	1035.3701	
O	-1.080537	0.000000	-0.643536	1356.1918	

H_2

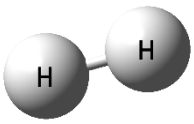

Method	Ee	E+ZPE	ΔH	ΔG
M06-2X-GD3/cc-pVTZ	-1.168867	-1.158688	-1.155383	-1.170165
CCSD(T)/cc-pVTZ	-1.17232797	-1.16214897	-1.15884397	-1.17362597
CBS-QB3	-1.176051	-1.166078	-1.162773	-1.177568

Coordinates (xyz)				Vibrations (cm^{-1})
H	0.000000	0.000000	0.369504	4468.1905
H	0.000000	0.000000	-0.369504	

IM_HC=OH

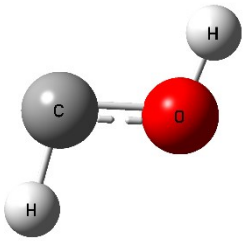

Method	Ee	E+ZPE	ΔH	ΔG
M06-2X-GD3/cc-pVTZ	-114.415051	-114.387937	-114.384107	-114.409632
CCSD(T)/cc-pVTZ	-114.251344	-114.22423	-114.220399	-114.245925
CBS-QB3	-114.286291	-114.259853	-114.256019	-114.281566

Coordinates (xyz)				Vibrations (cm^{-1})	
H	0.017503	-0.000140	0.000940	1093.3637	2899.4059
C	-0.005523	0.000105	1.857076	1227.9048	3784.5443
H	0.813167	-0.000115	2.609255	1381.1207	
O	0.651081	-0.000291	0.730307	1515.2087	

Optimized geometries and vibrational frequencies at the M06-2X-GD3/cc-pVTZ level of theory of Methyl Formate thermal decomposition transition states and products wells.

Z-H_3COCHO → H_3COH (P_1) + CO (P_2) → H_2CO (P_3) + CO (P_2) + H_2 k_1

TS_k_1						
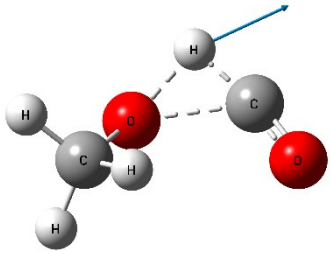						
Method			**Ee**	**E+ZPE**	**ΔH**	**ΔG**
M06-2X-GD3/cc-pVTZ			-228.938838	-228.883719	-228.877522	-228.911687
CCSD(T)/cc-pVTZ			-228.609627	-228.554508	-228.548311	-228.582476
CBS-QB3			-228.682202	-228.628303	-228.622751	-228.655485
Coordinates (xyz)				**Vibrations (cm^{-1})**		
C	-1.498959	-0.352344	-0.015109	*i* 1841.9374	1186.117	3080.495
H	-2.257826	-0.109805	0.730504	82.227	1192.9282	3111.5798
H	-0.933726	-1.227264	0.330131	156.9547	1479.1856	
H	-1.998123	-0.628224	-0.945324	259.9687	1495.2236	
C	1.088996	0.431862	-0.002385	390.0827	1516.2607	
H	0.368910	1.200290	0.529285	706.9839	1960.7042	
O	-0.652771	0.750887	-0.238270	976.0198	2507.1253	
O	1.541021	-0.545051	-0.384684	1082.8684	3009.7222	

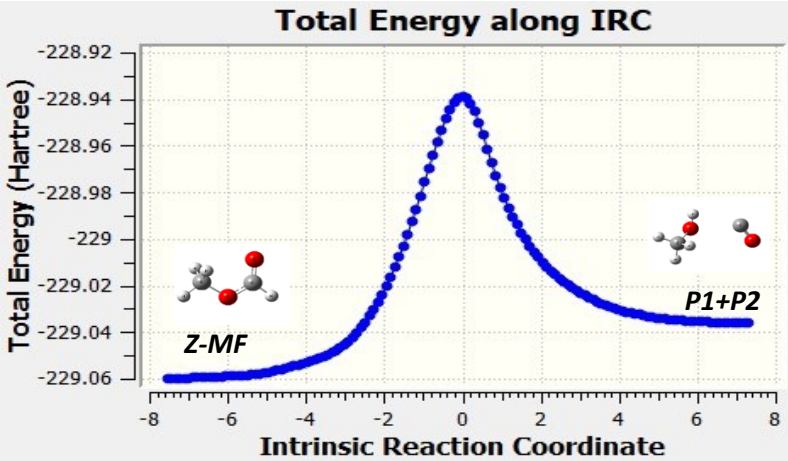

Figure A1-8: Intrinsic reaction coordinate (IRC) for the Methyl formate thermal decomposition (k_1).

PW_k_1						
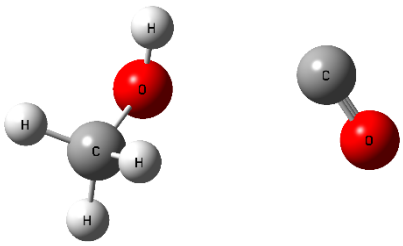						
Method			**Ee**	**E+ZPE**	**ΔH**	**ΔG**
M06-2X-GD3/cc-pVTZ			-229.036342	-228.978279	-228.970219	-229.010619
CCSD(T)/cc-pVTZ			-228.708427	-228.650364	-228.642304	-228.682704
CBS-QB3			-228.779699	-228.722936	-228.714886	-228.755365
Coordinates (xyz)				**Vibrations (cm^{-1})**		
C	-1.688873	-0.563999	0.103807	35.8933	1185.2565	3147.1448
H	-2.586033	-0.486843	0.722832	45.7634	1379.5	3893.834
H	-0.936412	-1.144664	0.646157	79.5724	1489.6291	
H	-1.944293	-1.101461	-0.806398	106.3827	1508.2812	
C	1.584079	0.267458	0.520620	157.1212	1522.0119	
H	-0.959486	1.194603	0.502200	354.5786	2276.5048	
O	-1.201338	0.703852	-0.286001	1077.02	3029.9436	
O	2.083212	-0.289151	-0.315418	1114.4978	3083.5667	

TS_MeOH					
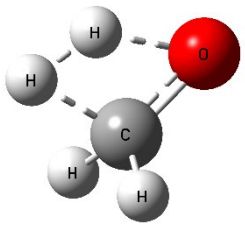					
Method			**Ee**	**E+ZPE**	**ΔH**	**ΔG**
M06-2X-GD3/cc-pVTZ			-115.560485	-115.517516	-115.513577	-115.540054
CCSD(T)/cc-pVTZ			-115.39599	-115.353036	-115.349097	-115.375574
CBS-QB3			-115.43672	-115.395241	-115.391283	-115.4178
Coordinates (xyz)				**Vibrations (cm^{-1})**	
C	0.000000	0.000000	0.000000	*i* 2243.656	1499.9448
H	0.000000	0.000000	1.099685	885.9018	1514.2133
H	1.404498	0.000000	-0.111721	932.6318	2032.3422
H	-0.120646	-1.010289	-0.417193	1167.1778	2325.7714
O	-0.469545	1.041547	-0.656422	1202.6096	2981.0441
H	0.914886	0.704984	-0.542435	1289.038	3030.5147

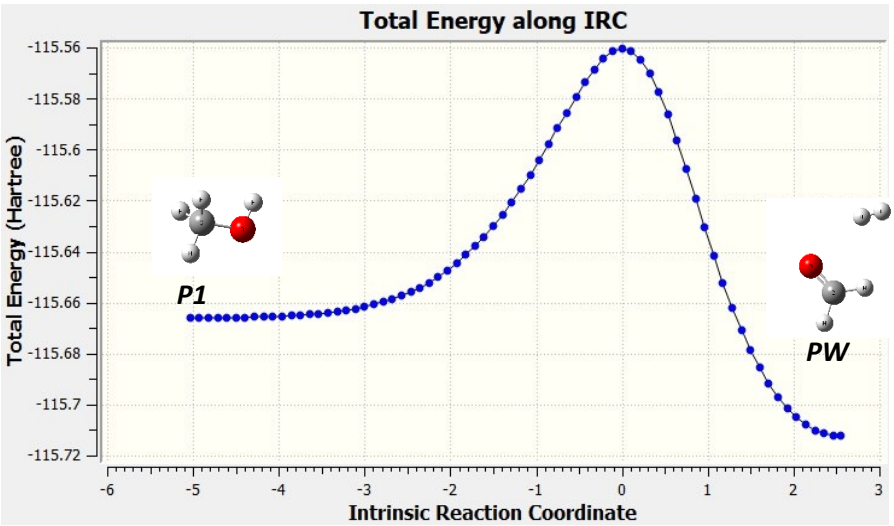

Figure A1-9: Intrinsic reaction coordinate (IRC) for the Methanol thermal decomposition (k_{MeOH}).

PW_MeOH					
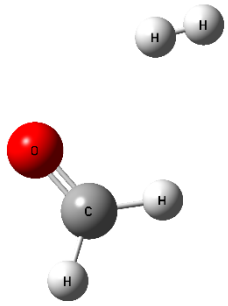					
Method			**Ee**	**E+ZPE**	**ΔH**	**ΔG**
M06-2X-GD3/cc-pVTZ			-115.667436	-115.627515	-115.62114	-115.652794
CCSD(T)/cc-pVTZ			-115.507559	-115.467638	-115.461264	-115.492918
CBS-QB3			-115.547485	-115.508663	-115.502149	-115.534741
Coordinates (xyz)				**Vibrations (cm^{-1})**	
C	0.056130	-0.152169	-0.090586	133.8211	1279.0608
H	0.699630	-0.562836	0.706261	151.7677	1541.2982
H	3.215228	0.471865	0.680635	211.4207	1873.2115
H	-0.977693	-0.533816	-0.137753	326.3263	2949.4457
O	0.460002	0.665871	-0.864150	387.3042	3022.6017
H	2.725308	0.703468	0.174833	1220.375	4426.4457

Z-$H_3COCHO \rightarrow 2H_2CO$ (P_3) k_2

TS_k_2						
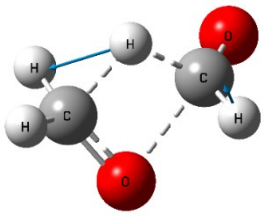						
Method			**Ee**	**E+ZPE**	**ΔH**	**ΔG**
M06-2X-GD3/cc-pVTZ			-228.928594	-228.872032	-228.866999	-228.898237
CCSD(T)/cc-pVTZ			-228.596086	-228.539524	-228.534491	-228.565729
CBS-QB3			-228.671129	-228.61593	-228.610783	-228.642226
Coordinates (xyz)				**Vibrations (cm^{-1})**		
C	1.222987	0.382271	0.073890	*i* 1144.8891	1234.8323	3085.4734
H	2.081904	0.604406	-0.572205	289.2963	1291.763	3186.8335
H	1.064076	1.088288	0.897028	380.3357	1369.668	
H	0.217079	0.967157	-0.747482	518.3145	1513.9633	
C	-0.660858	0.027206	-0.457007	680.1593	1552.1075	
H	-0.557268	-0.591506	-1.342920	850.207	1762.5231	
O	0.812346	-0.834454	0.191585	1011.1453	1883.9147	
O	-1.525668	0.288311	0.296630	1214.933	3002.3124	

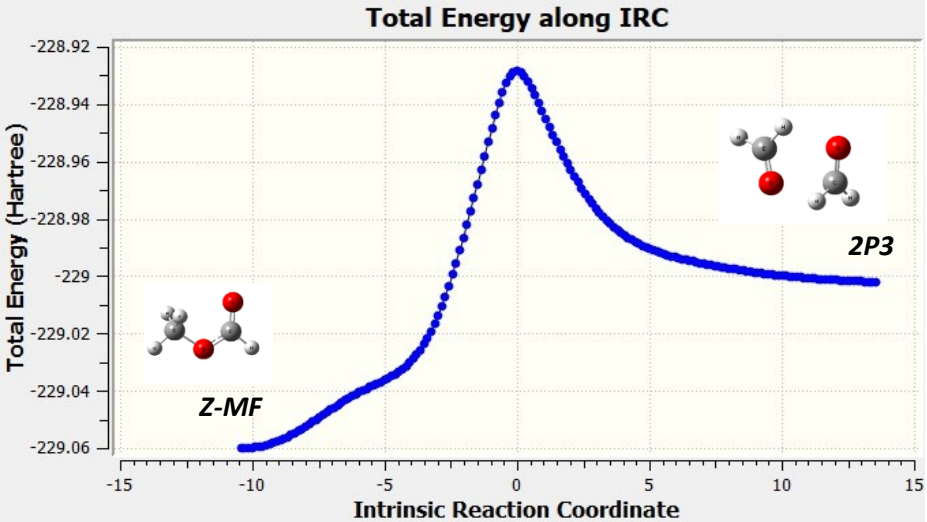

Figure A1-10: Intrinsic reaction coordinate (IRC) for the Methyl formate thermal decomposition (k_2).

PW_k_2						
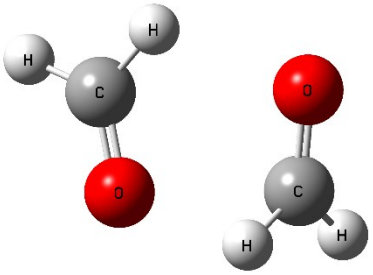						
Method			**Ee**	**E+ZPE**	**ΔH**	**ΔG**
M06-2X-GD3/cc-pVTZ			-229.002233	-228.945328	-228.938007	-228.974654
CCSD(T)/cc-pVTZ			-228.674028	-228.617123	-228.609802	-228.646449
CBS-QB3			-228.748229	-228.69326	-228.685733	-228.723052
Coordinates (xyz)				**Vibrations (cm^{-1})**		
C	-1.546575	0.502432	0.000010	84.7913	1277.6596	3040.861
H	-2.596879	0.835450	-0.000019	141.608	1286.5094	3048.0706
H	-0.764945	1.279043	0.000061	184.3866	1538.1473	
H	1.309614	-1.092895	0.934271	209.3289	1546.3872	
C	1.365628	-0.512504	0.000014	232.0382	1850.6278	
H	1.309626	-1.092946	-0.934212	306.1598	1862.6571	
O	-1.267232	-0.663912	-0.000012	1210.7036	2962.7001	
O	1.495765	0.680385	-0.000018	1228.6776	2967.2035	

E-$H_3COCHO \rightarrow H_4C$ $(P_4) + CO_2$ (P_5) k_3

TS_k_3						
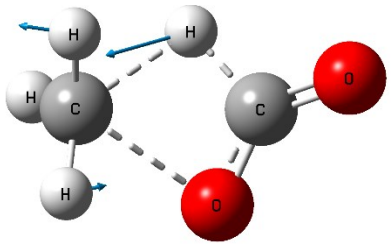						
Method			**Ee**	**E+ZPE**	**ΔH**	**ΔG**
M06-2X-GD3/cc-pVTZ			-228.911049	-228.854678	-228.84906	-228.881903
CCSD(T)/cc-pVTZ			-228.583846	-228.527475	-228.521856	-228.5547
CBS-QB3			-228.658976	-228.604072	-228.598226	-228.631947
Coordinates (xyz)				**Vibrations (cm^{-1})**		
C	1.359513	0.187972	-0.080886	-1346.545	1189.2229	3263.1863
H	1.763324	-0.761637	-0.395238	115.0643	1291.3568	3301.1604
H	1.674782	0.540724	0.889354	204.5185	1366.5878	
H	1.283282	0.928072	-0.868336	469.8397	1426.7563	
C	-0.718878	-0.299323	0.097762	711.1237	1489.5729	
H	-0.187478	0.767845	0.262569	777.0974	1904.8282	
O	-0.044525	-1.170423	0.697419	856.0576	2178.2658	
O	-1.684330	-0.271728	-0.602635	1080.719	3118.7934	

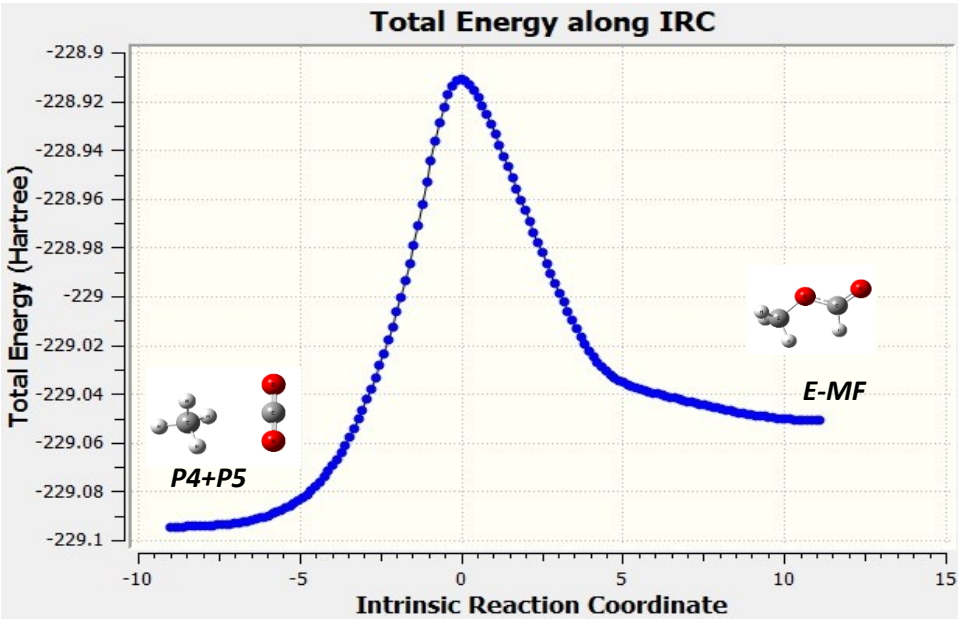

Figure A1-11: Intrinsic reaction coordinate (IRC) for the Methyl formate thermal decomposition (k_3).

E-$H_3COCHO \rightarrow HC{=}OH\ (P_8) + H_2CO\ (P_3) \rightarrow 2H_2CO\ (P_3)$ $\quad k_4$

TS_k_4						
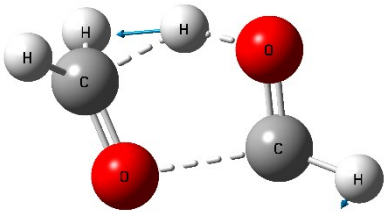						
Method			**Ee**	**E+ZPE**	**ΔH**	**ΔG**
M06-2X-GD3/cc-pVTZ			-228.880624	-228.826836	-228.821573	-228.853274
CCSD(T)/cc-pVTZ			-228.55138	-228.497592	-228.49233	-228.524031
CBS-QB3			-228.624788	-228.572875	-228.567453	-228.599472
Coordinates (xyz)				**Vibrations (cm^{-1})**		
C	-0.099996	-0.009412	-0.069700	*i* 1188.6936	1203.3321	3020.9609
H	-0.173724	-0.089438	1.021990	272.3162	1251.3089	3071.9423
H	0.898103	-0.088773	-0.518185	432.2962	1297.8371	
H	-0.502710	-1.440730	-0.350382	451.9454	1492.6502	
C	-2.032798	-1.226858	-1.415107	556.6733	1568.7482	
H	-2.849505	-1.697151	-1.983484	625.2601	1614.7893	
O	-1.043779	0.492184	-0.726231	813.8443	1882.4633	
O	-1.292292	-2.048742	-0.899910	1070.8573	2982.826	

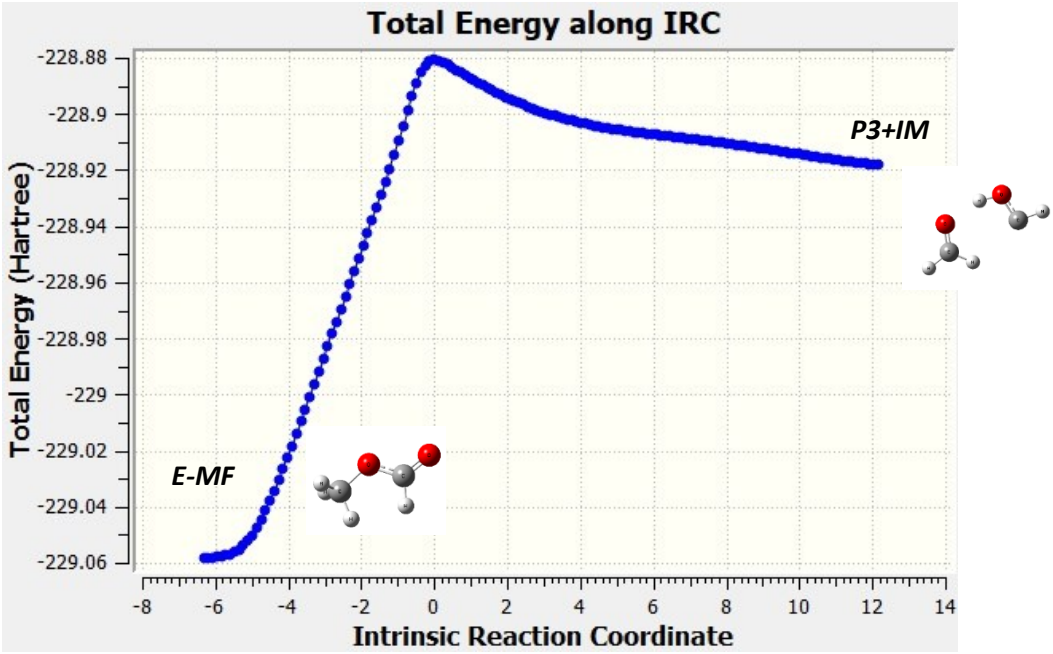

Figure A1-12: Intrinsic reaction coordinate (IRC) for the Methyl formate thermal decomposition (k_4).

PW_k_4

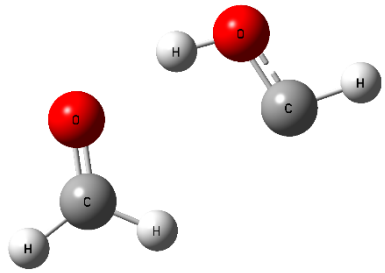

Method	Ee	E+ZPE	ΔH	ΔG
M06-2X-GD3/cc-pVTZ	-228.929777	-228.872465	-228.865399	-228.901348
CCSD(T)/cc-pVTZ	-228.601705	-228.544393	-228.537327	-228.573276
CBS-QB3	-228.672864	-228.616943	-228.609871	-228.645843

Coordinates (xyz)				Vibrations (cm^{-1})		
C	-1.688187	0.506740	-0.000005	106.6898	1288.8902	3099.7193
H	-1.000835	1.362291	-0.000024	188.5618	1304.8359	3450.7665
H	-2.773719	0.690399	0.000003	194.2697	1430.8744	
H	0.492097	-0.790702	-0.000001	200.6419	1524.6923	
C	1.549676	0.721021	0.000010	243.3692	1554.5193	
H	2.647483	0.900703	0.000001	415.9553	1831.4805	
O	-1.266230	-0.622496	0.000007	1203.8929	2887.6173	
O	1.449485	-0.568661	-0.000008	1251.0318	2979.3798	

TS_k_{IM}

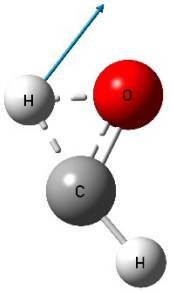

Method	Ee	E+ZPE	ΔH	ΔG
M06-2X-GD3/cc-pVTZ	-114.358842	-114.337882	-114.333985	-114.359609
CCSD(T)/cc-pVTZ	-114.19611	-114.17515	-114.171253	-114.196877
CBS-QB3	-114.231499	-114.211205	-114.207315	-114.232949

Coordinates (xyz)				Vibrations (cm^{-1})	
H	-0.176610	-0.002315	0.374091	*i* 2157.3148	2675.4779
C	0.115348	-0.019333	1.584561	714.6631	2953.1327
H	0.564971	-0.024192	2.597529	1348.6899	
O	0.966826	0.045840	0.619795	1508.3647	

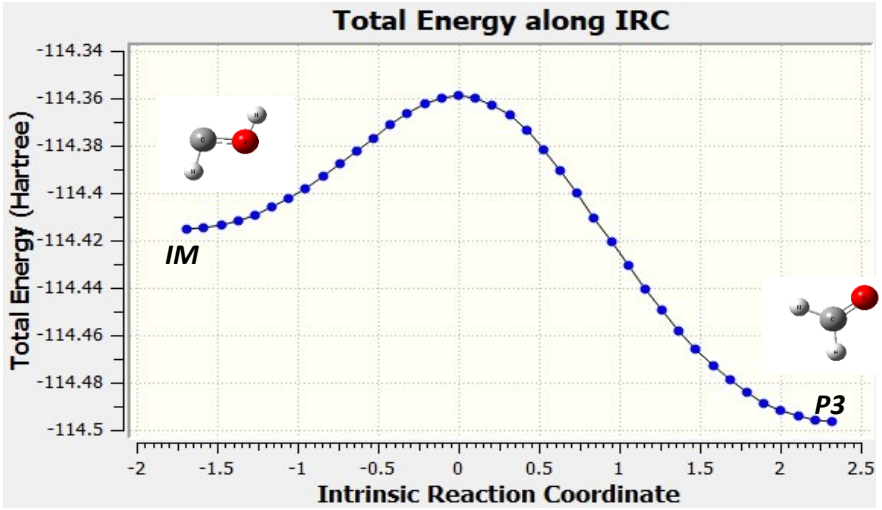

Figure A1-13: Intrinsic reaction coordinate (IRC) for the Hydroxy Methylene thermal decomposition (k_{IM}).

Kinetics

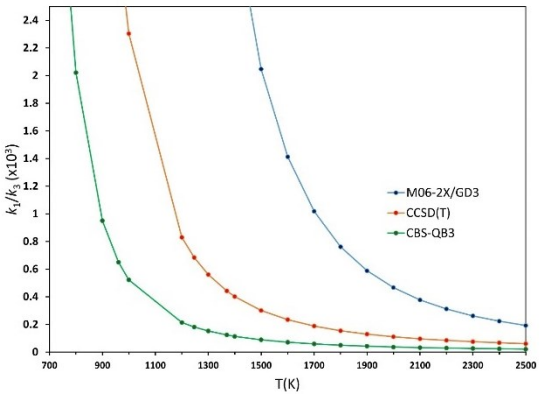

Figure A1-14: Ratio for k1 and k3 coefficient rates as function of temperature.

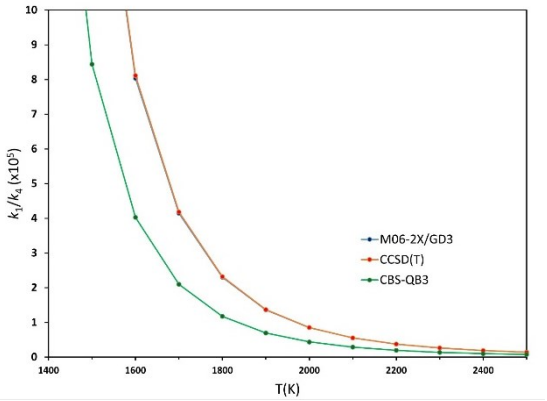

Figure A1-15: Ratio for k_1 and k_4 coefficient rates as function of temperature.

Table A1-1: Theoretical rate coefficients for the thermal decomposition of methyl formate at the M06-2X-GD3/cc-pVTZ level of theory.

M06-2X-GD3/cc-pVTZ														
T / K	k_1	k_2	k_{eq}	k_{bar}	k_3	k_4	$k_{D\_C\text{-}O}$	$k_{D\_O\text{-}C}$	k_1/k_2	k_1/k_3	k_1/k_4	$k_1/k_{D\_C\text{-}O}$	$k_1/k_{D\_O\text{-}C}$	$k_{D\_C\text{-}O}/k_{D\_O\text{-}C}$
300	6.17E-34	1.82E-44	6.86E-04	5.09E-48	3.49E-51	7.21E-65	4.17E-55	1.55E-56	3.39E+10	1.76E+17	8.55E+30	1.48E+21	3.98E+22	3.71E-02
400	1.33E-24	1.60E-30	6.28E-03	1.56E-33	9.77E-36	8.28E-46	4.94E-38	1.38E-36	8.29E+05	1.36E+11	1.61E+21	2.69E+13	9.62E+11	2.80E+01
500	2.19E-17	4.98E-22	2.39E-02	1.81E-24	4.33E-26	3.39E-34	9.41E-28	1.07E-24	4.40E+04	5.06E+08	6.45E+16	2.33E+10	2.05E+07	1.14E+03
600	2.64E-12	2.49E-16	5.83E-02	2.35E-18	1.37E-19	2.11E-26	7.05E-21	7.54E-17	1.06E+04	1.93E+07	1.25E+14	3.75E+08	3.50E+04	1.07E+04
700	1.32E-08	3.07E-12	1.10E-01	5.80E-14	6.39E-15	8.25E-21	5.92E-16	2.59E-11	4.30E+03	2.06E+06	1.60E+12	2.23E+07	5.08E+02	4.39E+04
747	3.37E-07	1.09E-10	1.40E-01	2.68E-12	3.76E-13	1.08E-18	4.31E-14	3.03E-09	3.11E+03	8.97E+05	3.12E+11	7.83E+06	1.11E+02	7.04E+04
800	8.36E-06	3.68E-09	1.78E-01	1.18E-10	2.11E-11	1.34E-16	2.97E-12	3.20E-07	2.27E+03	3.97E+05	6.25E+10	2.81E+06	2.61E+01	1.08E+05
900	1.31E-03	9.29E-07	2.59E-01	4.53E-08	1.17E-08	2.58E-13	2.27E-09	4.31E-04	1.41E+03	1.12E+05	5.08E+09	5.75E+05	3.04E+00	1.89E+05
961	1.72E-02	1.55E-05	3.13E-01	9.37E-07	2.93E-07	1.21E-11	6.66E-08	1.58E-02	1.11E+03	5.88E+04	1.42E+09	2.59E+05	1.09E+00	2.38E+05
1000	7.62E-02	7.85E-05	3.49E-01	5.36E-06	1.87E-06	1.11E-10	4.65E-07	1.23E-01	9.71E+02	4.07E+04	6.86E+08	1.64E+05	6.18E-01	2.65E+05
1200	3.50E+01	6.23E-02	5.46E-01	7.06E-03	3.86E-03	1.03E-06	1.38E-03	4.61E+02	5.62E+02	9.08E+03	3.41E+07	2.54E+04	7.59E-02	3.34E+05
1247	1.12E+02	2.20E-01	5.95E-01	2.74E-02	1.63E-02	5.76E-06	6.23E-03	2.08E+03	5.07E+02	6.85E+03	1.94E+07	1.79E+04	5.38E-02	3.33E+05
1300	3.74E+02	8.20E-01	6.49E-01	1.13E-01	7.32E-02	3.48E-05	3.00E-02	9.76E+03	4.57E+02	5.11E+03	1.08E+07	1.25E+04	3.83E-02	3.25E+05
1370	1.61E+03	3.99E+00	7.22E-01	6.18E-01	4.46E-01	3.02E-04	1.98E-01	6.09E+04	4.03E+02	3.60E+03	5.31E+06	8.09E+03	2.63E-02	3.07E+05
1400	2.87E+03	7.49E+00	7.53E-01	1.22E+00	9.16E-01	7.16E-04	4.21E-01	1.25E+05	3.83E+02	3.13E+03	4.01E+06	6.81E+03	2.29E-02	2.97E+05
1500	1.68E+04	5.11E+01	8.57E-01	9.59E+00	8.21E+00	9.88E-03	4.16E+00	1.08E+06	3.29E+02	2.05E+03	1.70E+06	4.04E+03	1.56E-02	2.59E+05
1600	7.92E+04	2.75E+02	9.59E-01	5.85E+01	5.61E+01	9.86E-02	3.09E+01	6.72E+06	2.88E+02	1.41E+03	8.03E+05	2.56E+03	1.18E-02	2.17E+05
1700	3.12E+05	1.22E+03	1.06E+00	2.89E+02	3.06E+02	7.53E-01	1.82E+02	3.23E+07	2.56E+02	1.02E+03	4.14E+05	1.72E+03	9.65E-03	1.78E+05
1800	1.06E+06	4.56E+03	1.16E+00	1.20E+03	1.38E+03	4.59E+00	8.77E+02	1.25E+08	2.31E+02	7.62E+02	2.30E+05	1.20E+03	8.45E-03	1.42E+05
1900	3.15E+06	1.49E+04	1.25E+00	4.27E+03	5.35E+03	2.32E+01	3.59E+03	4.03E+08	2.11E+02	5.88E+02	1.36E+05	8.77E+02	7.80E-03	1.12E+05
2000	8.43E+06	4.34E+04	1.35E+00	1.34E+04	1.81E+04	9.99E+01	1.28E+04	1.12E+09	1.94E+02	4.66E+02	8.44E+04	6.60E+02	7.53E-03	8.77E+04
2100	2.06E+07	1.14E+05	1.44E+00	3.80E+04	5.45E+04	3.74E+02	4.03E+04	2.73E+09	1.80E+02	3.78E+02	5.49E+04	5.11E+02	7.54E-03	6.78E+04
2200	4.63E+07	2.75E+05	1.52E+00	9.76E+04	1.48E+05	1.25E+03	1.14E+05	5.96E+09	1.68E+02	3.12E+02	3.72E+04	4.05E+02	7.78E-03	5.21E+04
2300	9.73E+07	6.15E+05	1.61E+00	2.31E+05	3.71E+05	3.74E+03	2.97E+05	1.18E+10	1.58E+02	2.62E+02	2.60E+04	3.28E+02	8.22E-03	3.99E+04
2400	1.92E+08	1.29E+06	1.69E+00	5.10E+05	8.60E+05	1.02E+04	7.11E+05	2.17E+10	1.50E+02	2.24E+02	1.88E+04	2.70E+02	8.88E-03	3.04E+04
2500	3.60E+08	2.53E+06	1.77E+00	1.06E+06	1.87E+06	2.59E+04	1.59E+06	3.69E+10	1.42E+02	1.93E+02	1.39E+04	2.26E+02	9.76E-03	2.32E+04

Table A1-2: Theoretical rate coefficients for the thermal decomposition of methyl formate at the CCSD(T)/cc-pVTZ level of theory.

CCSD(T)/M06-2X-GD3/cc-pVTZ														
T / K	k_1	k_2	k_{eq}	k_{bar}	k_3	k_4	$k_{D\_C\text{-}O}$	$k_{D\_O\text{-}C}$	k_1/k_2	k_1/k_3	k_1/k_4	$k_1/k_{D\_C\text{-}O}$	$k_1/k_{D\_O\text{-}C}$	$k_{D\_C\text{-}O}/k_{D\_O\text{-}C}$
300	7.97E-32	7.76E-44	1.00E-03	6.62E-42	6.62E-45	9.44E-63	7.14E-40	1.04E-49	1.03E+12	1.20E+13	8.45E+30	1.12E+08	7.67E+17	1.46E-10
400	5.35E-23	4.75E-30	8.34E-03	6.23E-29	5.19E-31	3.22E-44	1.31E-26	1.44E-31	1.13E+07	1.03E+08	1.66E+21	4.07E+03	3.71E+08	1.10E-05
500	4.23E-16	1.19E-21	2.99E-02	8.73E-21	2.61E-22	6.35E-33	1.30E-18	9.07E-21	3.56E+05	1.62E+06	6.67E+16	3.26E+02	4.66E+04	6.99E-03
600	3.12E-11	5.14E-16	7.04E-02	2.75E-15	1.93E-16	2.42E-25	2.92E-13	1.19E-13	6.06E+04	1.61E+05	1.29E+14	1.07E+02	2.61E+02	4.10E-01
700	1.09E-07	5.70E-12	1.30E-01	2.48E-11	3.21E-12	6.69E-20	2.00E-09	1.24E-08	1.92E+04	3.40E+04	1.64E+12	5.47E+01	8.84E+00	6.19E+00
747	2.45E-06	1.94E-10	1.63E-01	7.81E-10	1.28E-10	7.68E-18	5.65E-08	9.17E-07	1.26E+04	1.92E+04	3.19E+11	4.33E+01	2.67E+00	1.62E+01
800	5.32E-05	6.33E-09	2.05E-01	2.37E-08	4.87E-09	8.35E-16	1.53E-06	6.19E-05	8.41E+03	1.09E+04	6.38E+10	3.47E+01	8.60E-01	4.04E+01
900	6.78E-03	1.50E-06	2.93E-01	5.04E-06	1.48E-06	1.31E-12	2.72E-04	4.12E-02	4.51E+03	4.59E+03	5.17E+09	2.49E+01	1.64E-01	1.52E+02
961	8.04E-02	2.44E-05	3.52E-01	7.72E-05	2.72E-05	5.55E-11	3.79E-03	1.06E+00	3.30E+03	2.96E+03	1.45E+09	2.12E+01	7.60E-02	2.79E+02
1000	3.35E-01	1.21E-04	3.91E-01	3.72E-04	1.45E-04	4.81E-10	1.73E-02	6.71E+00	2.76E+03	2.30E+03	6.97E+08	1.94E+01	4.99E-02	3.89E+02
1200	1.20E+02	8.95E-02	6.00E-01	2.42E-01	1.45E-01	3.48E-06	8.87E+00	1.08E+04	1.34E+03	8.29E+02	3.46E+07	1.36E+01	1.12E-02	1.22E+03
1247	3.66E+02	3.12E-01	6.51E-01	8.22E-01	5.35E-01	1.86E-05	2.88E+01	4.14E+04	1.17E+03	6.84E+02	1.96E+07	1.27E+01	8.85E-03	1.44E+03
1300	1.17E+03	1.14E+00	7.08E-01	2.94E+00	2.08E+00	1.07E-04	9.83E+01	1.65E+05	1.02E+03	5.61E+02	1.09E+07	1.19E+01	7.09E-03	1.68E+03
1370	4.73E+03	5.47E+00	7.84E-01	1.37E+01	1.07E+01	8.80E-04	4.30E+02	8.43E+05	8.64E+02	4.42E+02	5.37E+06	1.10E+01	5.61E-03	1.96E+03
1400	8.25E+03	1.02E+01	8.16E-01	2.51E+01	2.05E+01	2.04E-03	7.74E+02	1.60E+06	8.08E+02	4.02E+02	4.05E+06	1.07E+01	5.16E-03	2.07E+03
1500	4.51E+04	6.82E+01	9.24E-01	1.62E+02	1.50E+02	2.62E-02	4.63E+03	1.08E+07	6.61E+02	3.02E+02	1.72E+06	9.73E+00	4.17E-03	2.33E+03
1600	2.00E+05	3.61E+02	1.03E+00	8.28E+02	8.52E+02	2.46E-01	2.22E+04	5.46E+07	5.54E+02	2.34E+02	8.11E+05	8.99E+00	3.65E-03	2.46E+03
1700	7.45E+05	1.57E+03	1.13E+00	3.50E+03	3.96E+03	1.78E+00	8.86E+04	2.18E+08	4.75E+02	1.88E+02	4.18E+05	8.41E+00	3.42E-03	2.46E+03
1800	2.40E+06	5.81E+03	1.23E+00	1.26E+04	1.55E+04	1.04E+01	3.03E+05	7.14E+08	4.14E+02	1.55E+02	2.32E+05	7.92E+00	3.36E-03	2.36E+03
1900	6.86E+06	1.88E+04	1.33E+00	3.98E+04	5.29E+04	5.02E+01	9.13E+05	1.99E+09	3.66E+02	1.30E+02	1.37E+05	7.52E+00	3.45E-03	2.18E+03
2000	1.77E+07	5.39E+04	1.42E+00	1.12E+05	1.59E+05	2.08E+02	2.46E+06	4.82E+09	3.28E+02	1.11E+02	8.51E+04	7.18E+00	3.67E-03	1.96E+03
2100	4.17E+07	1.40E+05	1.51E+00	2.86E+05	4.33E+05	7.52E+02	6.04E+06	1.04E+10	2.97E+02	9.62E+01	5.54E+04	6.90E+00	4.00E-03	1.72E+03
2200	9.08E+07	3.35E+05	1.60E+00	6.71E+05	1.07E+06	2.43E+03	1.37E+07	2.03E+10	2.71E+02	8.46E+01	3.75E+04	6.65E+00	4.47E-03	1.49E+03
2300	1.85E+08	7.42E+05	1.69E+00	1.46E+06	2.46E+06	7.07E+03	2.88E+07	3.65E+10	2.50E+02	7.52E+01	2.62E+04	6.43E+00	5.08E-03	1.27E+03
2400	3.56E+08	1.54E+06	1.77E+00	2.99E+06	5.28E+06	1.89E+04	5.71E+07	6.07E+10	2.31E+02	6.75E+01	1.89E+04	6.24E+00	5.87E-03	1.06E+03
2500	6.51E+08	3.01E+06	1.85E+00	5.76E+06	1.06E+07	4.65E+04	1.07E+08	9.46E+10	2.16E+02	6.12E+01	1.40E+04	6.08E+00	6.88E-03	8.84E+02

Table A1-3: Theoretical rate coefficients for the thermal decomposition of methyl formate at the CBS-QB3 level of theory.

	CBS-QB3													
T / K	k_1	k_2	k_{eq}	k_{bar}	k_3	k_4	$k_{D\_C\text{-}O}$	$k_{D\_O\text{-}C}$	k_1/k_2	k_1/k_3	k_1/k_4	$k_1/k_{D\_C\text{-}O}$	$k_1/k_{D\_O\text{-}C}$	$k_{D\_C\text{-}O}/k_{D\_O\text{-}C}$
300	4.98E-33	1.04E-43	7.74E-04	1.81E-41	1.40E-44	3.51E-63	1.95E-41	4.42E-51	4.77E+10	3.56E+11	1.42E+30	2.55E+08	1.13E+18	4.42E+09
400	5.87E-24	5.94E-30	6.88E-03	1.33E-28	9.15E-31	1.42E-44	1.35E-25	5.86E-33	9.89E+05	6.42E+06	4.12E+20	4.34E+01	1.00E+09	2.31E+07
500	6.46E-17	1.42E-21	2.57E-02	1.60E-20	4.12E-22	3.17E-33	3.48E-16	3.49E-22	4.56E+04	1.57E+05	2.04E+16	1.86E-01	1.85E+05	9.98E+05
600	5.91E-12	5.96E-16	6.19E-02	4.56E-15	2.82E-16	1.31E-25	5.38E-10	4.35E-15	9.90E+03	2.09E+04	4.50E+13	1.10E-02	1.36E+03	1.24E+05
700	2.41E-08	6.48E-12	1.16E-01	3.82E-11	4.44E-12	3.84E-20	1.20E-05	4.28E-10	3.71E+03	5.42E+03	6.26E+11	2.01E-03	5.62E+01	2.80E+04
747	5.69E-07	2.19E-10	1.47E-01	1.17E-09	1.73E-10	4.51E-18	4.95E-04	3.10E-08	2.60E+03	3.29E+03	1.26E+11	1.15E-03	1.84E+01	1.60E+04
800	1.31E-05	7.07E-09	1.87E-01	3.47E-08	6.46E-09	5.02E-16	1.88E-02	2.04E-06	1.85E+03	2.02E+03	2.60E+10	6.96E-04	6.40E+00	9.20E+03
900	1.81E-03	1.66E-06	2.69E-01	7.07E-06	1.90E-06	8.16E-13	5.05E+00	1.30E-03	1.09E+03	9.50E+02	2.22E+09	3.59E-04	1.39E+00	3.88E+03
961	2.24E-02	2.67E-05	3.25E-01	1.06E-04	3.44E-05	3.52E-11	8.15E+01	3.26E-02	8.37E+02	6.50E+02	6.35E+08	2.74E-04	6.85E-01	2.50E+03
1000	9.53E-02	1.32E-04	3.62E-01	5.04E-04	1.82E-04	3.08E-10	3.96E+02	2.04E-01	7.20E+02	5.22E+02	3.10E+08	2.41E-04	4.67E-01	1.94E+03
1200	3.76E+01	9.64E-02	5.63E-01	3.11E-01	1.75E-01	2.32E-06	2.09E+05	3.07E+02	3.90E+02	2.14E+02	1.62E+07	1.80E-04	1.23E-01	6.81E+02
1247	1.17E+02	3.35E-01	6.12E-01	1.05E+00	6.42E-01	1.25E-05	6.48E+05	1.16E+03	3.48E+02	1.81E+02	9.29E+06	1.80E-04	1.00E-01	5.58E+02
1300	3.79E+02	1.23E+00	6.68E-01	3.72E+00	2.48E+00	7.28E-05	2.06E+06	4.56E+03	3.09E+02	1.53E+02	5.20E+06	1.84E-04	8.30E-02	4.52E+02
1370	1.57E+03	5.84E+00	7.41E-01	1.70E+01	1.26E+01	6.04E-04	8.03E+06	2.29E+04	2.68E+02	1.24E+02	2.59E+06	1.95E-04	6.82E-02	3.50E+02
1400	2.75E+03	1.09E+01	7.73E-01	3.12E+01	2.41E+01	1.40E-03	1.36E+07	4.32E+04	2.53E+02	1.14E+02	1.96E+06	2.02E-04	6.37E-02	3.16E+02
1500	1.54E+04	7.24E+01	8.78E-01	1.98E+02	1.74E+02	1.83E-02	6.57E+07	2.86E+05	2.13E+02	8.87E+01	8.44E+05	2.35E-04	5.39E-02	2.30E+02
1600	6.98E+04	3.81E+02	9.81E-01	1.00E+03	9.82E+02	1.74E-01	2.45E+08	1.42E+06	1.83E+02	7.11E+01	4.02E+05	2.85E-04	4.91E-02	1.72E+02
1700	2.65E+05	1.65E+03	1.08E+00	4.18E+03	4.53E+03	1.27E+00	7.42E+08	5.60E+06	1.60E+02	5.86E+01	2.09E+05	3.57E-04	4.74E-02	1.33E+02
1800	8.70E+05	6.10E+03	1.18E+00	1.49E+04	1.76E+04	7.43E+00	1.89E+09	1.81E+07	1.43E+02	4.94E+01	1.17E+05	4.60E-04	4.79E-02	1.04E+02
1900	2.52E+06	1.97E+04	1.28E+00	4.67E+04	5.96E+04	3.63E+01	4.17E+09	5.02E+07	1.28E+02	4.23E+01	6.96E+04	6.05E-04	5.03E-02	8.31E+01
2000	6.58E+06	5.64E+04	1.37E+00	1.30E+05	1.79E+05	1.51E+02	8.15E+09	1.21E+08	1.17E+02	3.69E+01	4.35E+04	8.07E-04	5.43E-02	6.72E+01
2100	1.57E+07	1.46E+05	1.46E+00	3.30E+05	4.82E+05	5.51E+02	1.44E+10	2.62E+08	1.07E+02	3.25E+01	2.85E+04	1.09E-03	5.99E-02	5.51E+01
2200	3.46E+07	3.49E+05	1.55E+00	7.70E+05	1.19E+06	1.79E+03	2.34E+10	5.14E+08	9.91E+01	2.90E+01	1.93E+04	1.48E-03	6.73E-02	4.56E+01
2300	7.12E+07	7.72E+05	1.63E+00	1.67E+06	2.72E+06	5.24E+03	3.54E+10	9.29E+08	9.22E+01	2.62E+01	1.36E+04	2.01E-03	7.66E-02	3.81E+01
2400	1.38E+08	1.60E+06	1.71E+00	3.39E+06	5.80E+06	1.40E+04	5.03E+10	1.57E+09	8.64E+01	2.38E+01	9.84E+03	2.75E-03	8.81E-02	3.21E+01
2500	2.54E+08	3.12E+06	1.79E+00	6.51E+06	1.16E+07	3.48E+04	6.79E+10	2.49E+09	8.14E+01	2.18E+01	7.30E+03	3.74E-03	1.02E-01	2.73E+01

Arrhenius plots for the different pathways in the thermal decomposition of Methyl Formate

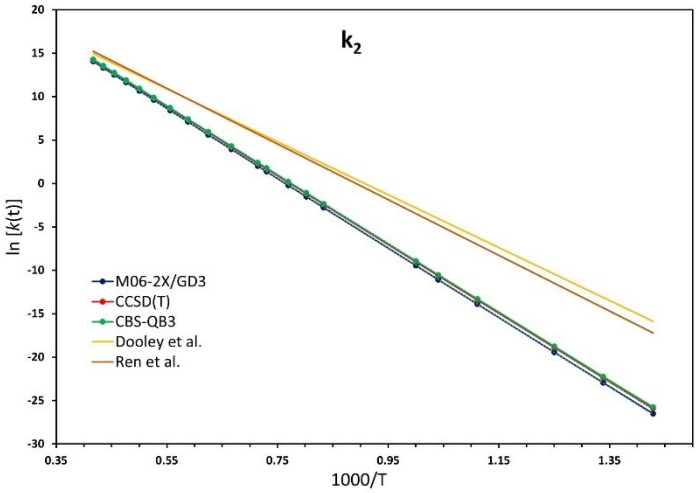

Figure A1-16: Comparison of Arrhenius plots for methyl formate decomposition (k_2) with previous rate values.[40,96]

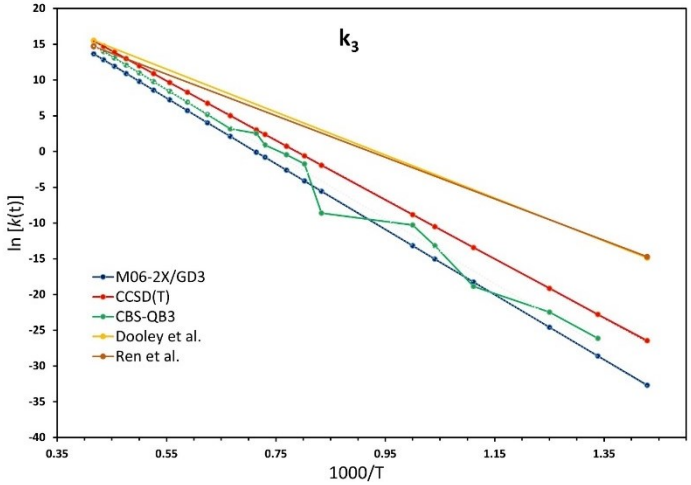

Figure A1-17: Comparison of Arrhenius plots for methyl formate decomposition (k_3) with previous rate values.[40,96]

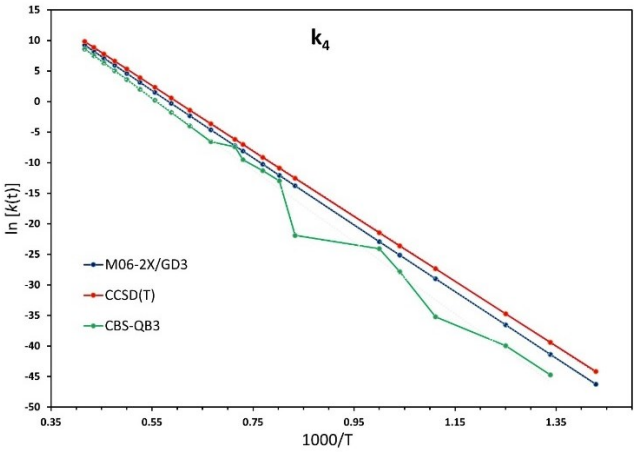

Figure A1-18: Comparison of Arrhenius plots for methyl formate decomposition (k_4).

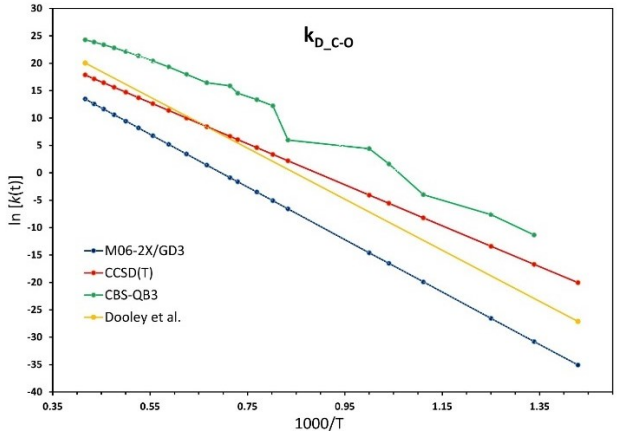

Figure A1-19: Comparison of Arrhenius plots for methyl formate decomposition ($k_{(C\text{-}O)}$) with previous rate values.[40,96]

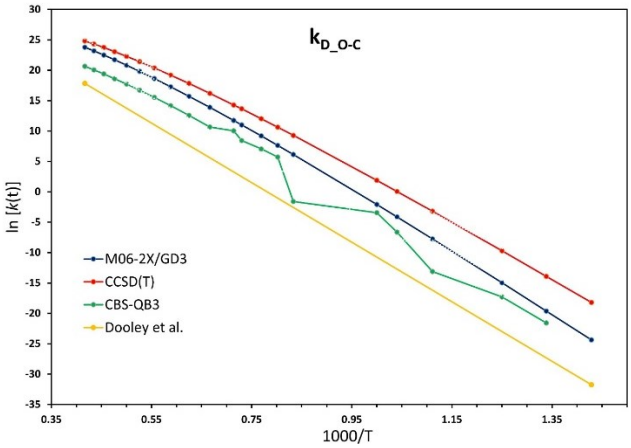

Figure A1-20: Comparison of Arrhenius plots for methyl formate decomposition ($k_{(O\text{-}C)}$) with previous rate values.[40,96]

Formaldehyde branching ratio

To calculate the ratio of CH_2O coming directly from methyl formate (path 2) vs that coming from methanol (path 1) it is necessary to obtain kinetic information all the path to formaldehyde formation.

$$H_3COCHO \rightarrow CH_2O\ (P3) + H_2 + CO(P2) \qquad k_1 \qquad (1)$$

$$H_3COCHO \rightarrow 2\ CH_2O(P3) \qquad k_2 \qquad (2)$$

As can see in Figure S20, comparing paths 1 and 2 taking into account only TS1 and TS2 has as a consequence an overestimation of the yield of formaldehyde formation in path 1. Since although the barrier for TS1 is smaller, the path 1 goes through two transitions states (TS1 and TS_MeOH) and the barrier for the second TS is even higher than TS2 barrier.

The formaldehyde formation from path 1 goes through by three steps, the P1 and P2 formations with rate constant k_1,

$$H_3COCHO \rightarrow H_3COH(P1) + CO(P2) \qquad k_1 \qquad (1a)$$

reverse reaction with rate constant k_{-1},

$$H_3COH(P1) + CO(P2) \rightarrow H_3COCHO \qquad k_{-1} \qquad (1b)$$

and CH_2O formation from methanol (P1) with the rate constant k_{MeOH}, that competes with (1b),

$$H_3COH(P1) + CO(P2) \rightarrow CH_2O(P3) + H_2 + CO(P2)\ k_{\_MeOH} \qquad (1c)$$

the overall rate for (k_{1corr}) can be written as

$$k_{1corr} = k_1 \left[\frac{k_{MeOH}}{k_{-1}+k_{MeOH}}\right]$$

Where the bracket denotes that fraction which completes the reaction via (1c) rather than (1b). Assuming additive rate constants, we can calculate the global constant.

$$k_{tot}=k_1\left[\frac{k_{MeOH}}{k_{-1}+k_{MeOH}}\right]+k_2$$

Figure S21 show the branching ratio k_1/k_2 as function of temperature, it can be seen that initially the reaction goes mainly through path 2 and as the temperature increases, path 1 becomes increasingly important, since there is enough energy to overcome the TS_MeOH barrier.

To obtain the branching ratio of formaldehyde formation, it must be considered that in path 1, for each MF, one molecule of formaldehyde is produced while two molecules of formaldehyde are produced in path 2.

$$Y_{tot}= k_{1corr}/k_{tot} +2(k_2/k_{tot})$$

At 747K, 99.96% of the formed formaldehyde come from R2, when temperature raise to 1247K the ratio for R2 drops to 71.45%. At 1370K, the ratio of the mechanisms is almost the same, 48.99 and 51.01 for R2 and R1 respectively (Figure S22). At higher temperatures it is seen how the proportion of R1 continues to increase until it reaches levels above 97% at 2500 K. Although the TS1 barrier is lower, it is notable that at low temperatures the energy of the system is not enough to overcome the TS_MeOH barrier and the formation of formaldehyde via pathway 2 is favoured. As the temperature increases, the system has more energy and finally the ratio changes and the reaction goes almost exclusively by path 1.

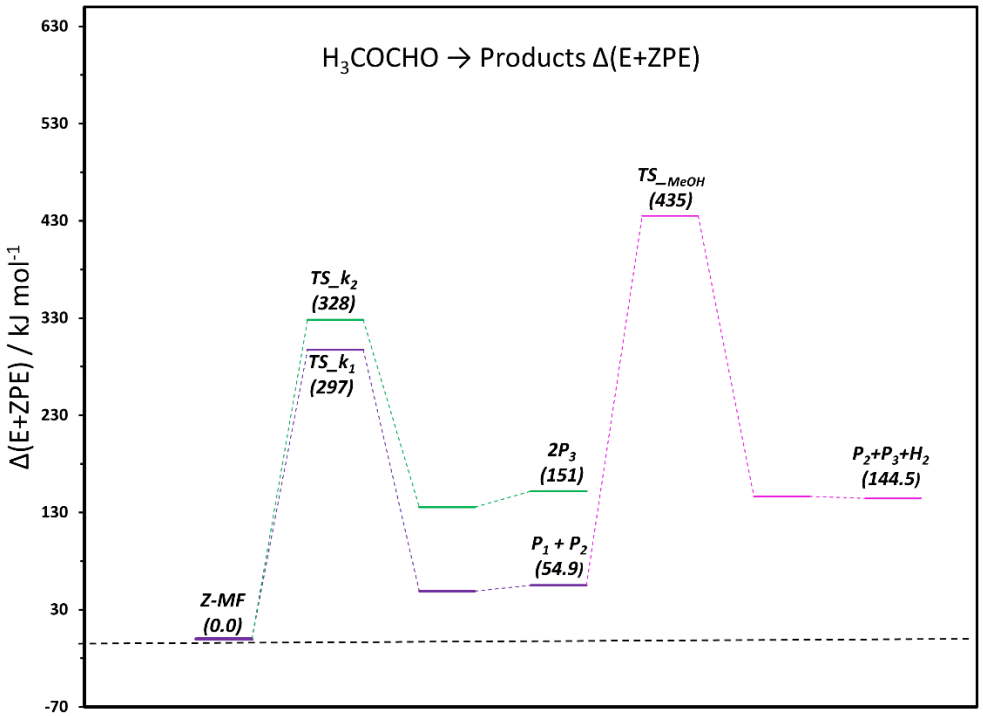

Figure A1-21: Relative potential energy diagram (kJ/mol) for paths 1 and 2 of MF thermal decomposition calculated at M06-2X/GD3/cc-pVTZ level of theory.

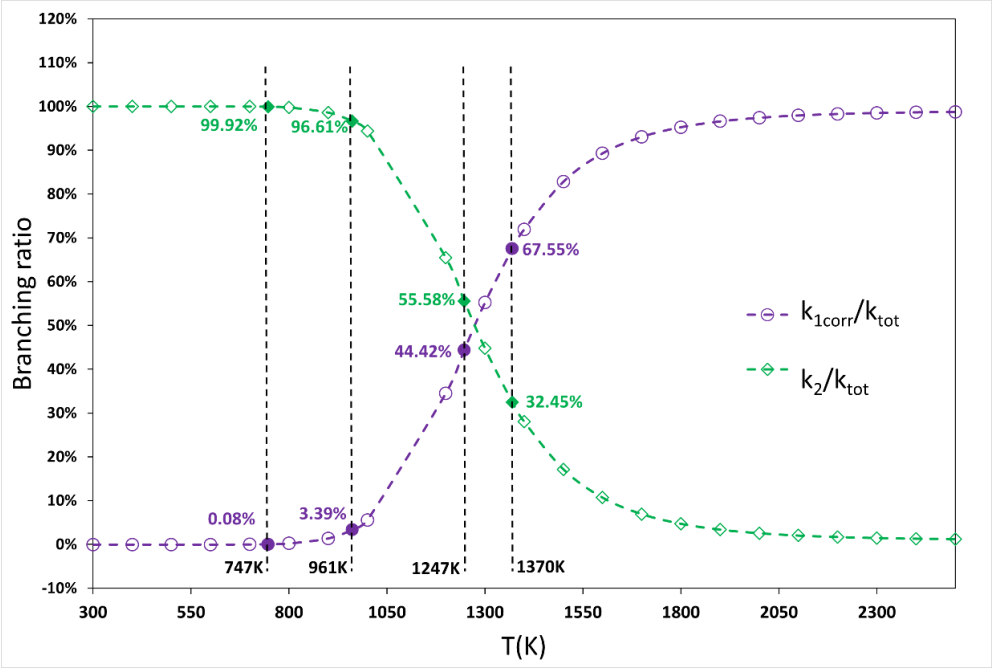

Figure A1-22: Branching ratio for k1(purple) and k2(green) rate constants (kn/ktot) as function of temperature in the MF thermal decomposition calculated at M06-2X/GD3/cc-pVTZ level of theory.

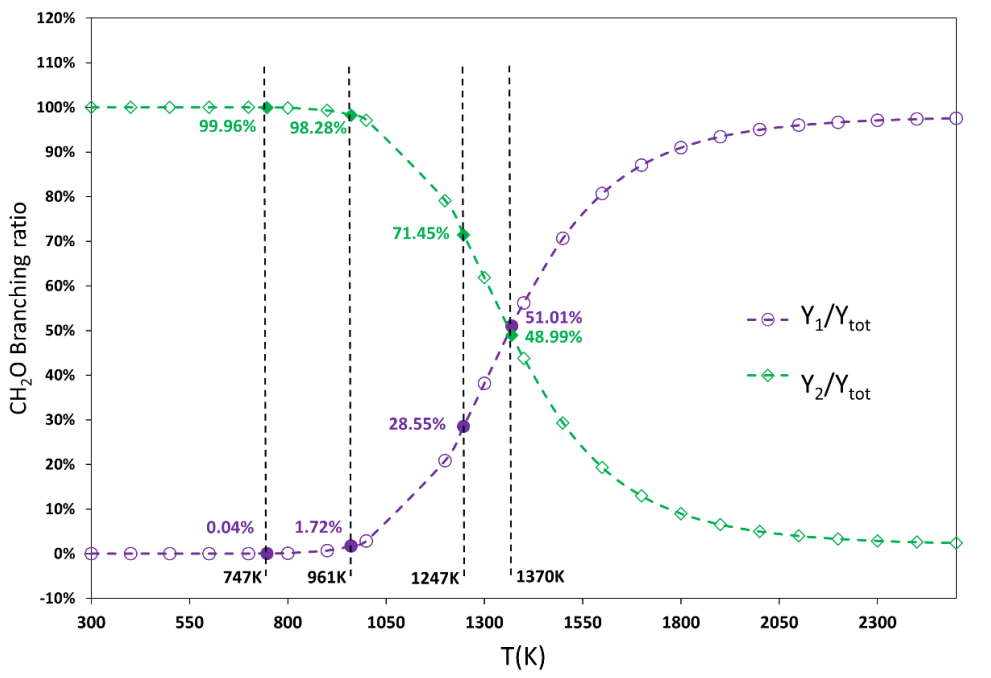

Figure A1-23: Branching ratio for formaldehyde formation of R1(purple) and R2 (green) pathways as function of temperature in the MF thermal decomposition. Calculated at M06-2X/GD3/cc-pVTZ level of theory.

Table A1-4: Kinetic data and branching ratios for paths 1 and 2 calculated at M06-2X/GD3/cc-pVTZ level of theory.

T(K)	k_1	k_{-1}	k_{MeOH}	k_{1cor}	k_2	k_{tot}	k_{1corr}/k_{tot}	k_2/k_{tot}	Y_1/Y_{tot}	Y_2/Y_{tot}
300	6.17E-34	5.22E-28	3.21E-43	3.79E-49	1.82E-44	1.82E-44	0.00%	100.00%	0.00%	100.00%
400	1.33E-24	3.60E-21	4.15E-34	1.53E-37	1.60E-30	1.60E-30	0.00%	100.00%	0.00%	100.00%
500	2.19E-17	1.70E-15	2.45E-26	3.16E-28	4.98E-22	4.98E-22	0.00%	100.00%	0.00%	100.00%
600	2.64E-12	1.83E-11	2.96E-20	4.27E-21	2.49E-16	2.49E-16	0.00%	100.00%	0.00%	100.00%
700	1.32E-08	1.58E-08	1.00E-15	8.35E-16	3.07E-12	3.07E-12	0.03%	99.97%	0.01%	99.99%
747	3.37E-07	2.08E-07	5.44E-14	8.83E-14	1.09E-10	1.09E-10	0.08%	99.92%	0.04%	99.96%
800	8.36E-06	2.66E-06	2.86E-12	9.00E-12	3.68E-09	3.69E-09	0.24%	99.76%	0.12%	99.88%
900	1.31E-03	1.47E-04	1.48E-09	1.32E-08	9.29E-07	9.42E-07	1.40%	98.60%	0.70%	99.30%
961	1.72E-02	1.14E-03	3.58E-08	5.43E-07	1.55E-05	1.60E-05	3.39%	96.61%	1.72%	98.28%
1000	7.62E-02	3.69E-03	2.26E-07	4.65E-06	7.85E-05	8.31E-05	5.60%	94.40%	2.88%	97.12%
1200	3.50E+01	4.79E-01	4.50E-04	3.29E-02	6.23E-02	9.52E-02	34.52%	65.48%	20.86%	79.14%
1247	1.12E+02	1.20E+00	1.90E-03	1.76E-01	2.20E-01	3.96E-01	44.42%	55.58%	28.55%	71.45%
1300	3.74E+02	3.14E+00	8.51E-03	1.01E+00	8.20E-01	1.83E+00	55.23%	44.77%	38.15%	61.85%
1370	1.61E+03	9.97E+00	5.18E-02	8.30E+00	3.99E+00	1.23E+01	67.55%	32.45%	51.01%	48.99%
1400	2.87E+03	1.58E+01	1.07E-01	1.92E+01	7.49E+00	2.67E+01	71.95%	28.05%	56.19%	43.81%
1500	1.68E+04	6.44E+01	9.59E-01	2.47E+02	5.11E+01	2.98E+02	82.84%	17.16%	70.71%	29.29%
1600	7.92E+04	2.21E+02	6.59E+00	2.30E+03	2.75E+02	2.57E+03	89.31%	10.69%	80.69%	19.31%
1700	3.12E+05	6.56E+02	3.63E+01	1.63E+04	1.22E+03	1.75E+04	93.07%	6.93%	87.05%	12.95%
1800	1.06E+06	1.73E+03	1.66E+02	9.22E+04	4.56E+03	9.67E+04	95.28%	4.72%	90.99%	9.01%
1900	3.15E+06	4.12E+03	6.46E+02	4.26E+05	1.49E+04	4.41E+05	96.62%	3.38%	93.45%	6.55%
2000	8.43E+06	9.03E+03	2.20E+03	1.65E+06	4.34E+04	1.70E+06	97.44%	2.56%	95.01%	4.99%
2100	2.06E+07	1.84E+04	6.70E+03	5.50E+06	1.14E+05	5.61E+06	97.97%	2.03%	96.01%	3.99%
2200	4.63E+07	3.51E+04	1.85E+04	1.60E+07	2.75E+05	1.63E+07	98.31%	1.69%	96.67%	3.33%
2300	9.73E+07	6.33E+04	4.66E+04	4.13E+07	6.15E+05	4.19E+07	98.53%	1.47%	97.11%	2.89%
2400	1.92E+08	1.09E+05	1.09E+05	9.62E+07	1.29E+06	9.75E+07	98.68%	1.32%	97.40%	2.60%
2500	3.60E+08	1.80E+05	2.39E+05	2.05E+08	2.53E+06	2.08E+08	98.78%	1.22%	97.59%	2.41%

Table A1-5: Kinetic data and branching ratios for paths 1 and 2 calculated at CCSD(T)/cc-pVTZ level of theory.

T(K)	k_1	k_{-1}	k_{OH}	k_{1cor}	k_2	$k_{\_tot}$	k_{1corr}/k_{tot}	k_2/k_{tot}	Y_{1corr}/Y_{tot}	Y_2/Y_{tot}
300	7.97E-32	1.23E-28	2.21E-43	1.43E-46	7.76E-44	7.77E-44	0.18%	99.82%	0.09%	99.91%
400	5.35E-23	1.28E-21	2.12E-34	8.88E-36	4.75E-30	4.75E-30	0.00%	100.00%	0.00%	100.00%
500	4.23E-16	7.48E-16	1.29E-26	7.29E-27	1.19E-21	1.19E-21	0.00%	100.00%	0.00%	100.00%
600	3.12E-11	9.24E-12	1.71E-20	5.76E-20	5.14E-16	5.14E-16	0.01%	99.99%	0.01%	99.99%
700	1.09E-07	8.81E-09	6.26E-16	7.76E-15	5.70E-12	5.71E-12	0.14%	99.86%	0.07%	99.93%
747	2.45E-06	1.20E-07	3.49E-14	7.13E-13	1.94E-10	1.95E-10	0.37%	99.63%	0.18%	99.82%
800	5.32E-05	1.59E-06	1.89E-12	6.32E-11	6.33E-09	6.39E-09	0.99%	99.01%	0.50%	99.50%
900	6.78E-03	9.30E-05	1.02E-09	7.44E-08	1.50E-06	1.58E-06	4.72%	95.28%	2.41%	97.59%
961	8.04E-02	7.40E-04	2.53E-08	2.75E-06	2.44E-05	2.71E-05	10.16%	89.84%	5.35%	94.65%
1000	3.35E-01	2.45E-03	1.62E-07	2.21E-05	1.21E-04	1.43E-04	15.45%	84.55%	8.37%	91.63%
1200	1.20E+02	3.40E-01	3.41E-04	1.21E-01	8.95E-02	2.10E-01	57.39%	42.61%	40.24%	59.76%
1247	3.66E+02	8.65E-01	1.45E-03	6.14E-01	3.12E-01	9.26E-01	66.33%	33.67%	49.63%	50.37%
1300	1.17E+03	2.29E+00	6.59E-03	3.36E+00	1.14E+00	4.50E+00	74.58%	25.42%	59.46%	40.54%
1370	4.73E+03	7.39E+00	4.07E-02	2.59E+01	5.47E+00	3.14E+01	82.56%	17.44%	70.29%	29.71%
1400	8.25E+03	1.18E+01	8.40E-02	5.84E+01	1.02E+01	6.86E+01	85.12%	14.88%	74.10%	25.90%
1500	4.51E+04	4.90E+01	7.69E-01	6.97E+02	6.82E+01	7.65E+02	91.08%	8.92%	83.62%	16.38%
1600	2.00E+05	1.71E+02	5.36E+00	6.08E+03	3.61E+02	6.44E+03	94.40%	5.60%	89.39%	10.61%
1700	7.45E+05	5.15E+02	2.98E+01	4.08E+04	1.57E+03	4.23E+04	96.29%	3.71%	92.85%	7.15%
1800	2.40E+06	1.38E+03	1.38E+02	2.18E+05	5.81E+03	2.24E+05	97.41%	2.59%	94.95%	5.05%
1900	6.86E+06	3.32E+03	5.42E+02	9.63E+05	1.88E+04	9.82E+05	98.09%	1.91%	96.25%	3.75%
2000	1.77E+07	7.35E+03	1.87E+03	3.58E+06	5.39E+04	3.63E+06	98.52%	1.48%	97.07%	2.93%
2100	4.17E+07	1.51E+04	5.72E+03	1.14E+07	1.40E+05	1.16E+07	98.79%	1.21%	97.61%	2.39%
2200	9.08E+07	2.91E+04	1.59E+04	3.21E+07	3.35E+05	3.24E+07	98.97%	1.03%	97.95%	2.05%
2300	1.85E+08	5.30E+04	4.03E+04	8.01E+07	7.42E+05	8.08E+07	99.08%	0.92%	98.18%	1.82%
2400	3.56E+08	9.18E+04	9.49E+04	1.81E+08	1.54E+06	1.83E+08	99.16%	0.84%	98.33%	1.67%
2500	6.51E+08	1.52E+05	2.09E+05	3.76E+08	3.01E+06	3.79E+08	99.21%	0.79%	98.42%	1.58%

Table A1-6: Kinetic data and branching ratios for paths 1 and 2 calculated at CBS-QB3 level of theory.

T(K)	k_1	k_{-1}	k_{OH}	k_{1cor}	k_2	$k_{\_tot}$	k_{1corr}/k_{tot}	k_2/k_{tot}	Y_{1corr}/Y_{tot}	Y_2/Y_{tot}
300	4.98E-33	1.48E-25	2.01E-43	6.77E-51	1.04E-43	1.04E-43	0.00%	100.00%	0.00%	100.00%
400	5.87E-24	2.36E-18	3.01E-34	7.49E-40	5.94E-30	5.94E-30	0.00%	100.00%	0.00%	100.00%
500	6.46E-17	1.97E-12	2.44E-26	8.02E-31	1.42E-21	1.42E-21	0.00%	100.00%	0.00%	100.00%
600	5.91E-12	3.21E-08	3.25E-20	5.98E-24	5.96E-16	5.96E-16	0.00%	100.00%	0.00%	100.00%
700	2.41E-08	3.83E-05	1.14E-15	7.17E-19	6.48E-12	6.48E-12	0.00%	100.00%	0.00%	100.00%
747	5.69E-07	5.70E-04	6.24E-14	6.23E-17	2.19E-10	2.19E-10	0.00%	100.00%	0.00%	100.00%
800	1.31E-05	8.28E-03	3.31E-12	5.22E-15	7.07E-09	7.07E-09	0.00%	100.00%	0.00%	100.00%
900	1.81E-03	5.60E-01	1.72E-09	5.57E-12	1.66E-06	1.66E-06	0.00%	100.00%	0.00%	100.00%
961	2.24E-02	4.81E+00	4.21E-08	1.96E-10	2.67E-05	2.67E-05	0.00%	100.00%	0.00%	100.00%
1000	9.53E-02	1.66E+01	2.66E-07	1.52E-09	1.32E-04	1.32E-04	0.00%	100.00%	0.00%	100.00%
1200	3.76E+01	2.77E+03	5.36E-04	7.27E-06	9.64E-02	9.64E-02	0.01%	99.99%	0.00%	100.00%
1247	1.17E+02	7.31E+03	2.27E-03	3.61E-05	3.35E-01	3.35E-01	0.01%	99.99%	0.01%	99.99%
1300	3.79E+02	2.01E+04	1.02E-02	1.92E-04	1.23E+00	1.23E+00	0.02%	99.98%	0.01%	99.99%
1370	1.57E+03	6.77E+04	6.23E-02	1.44E-03	5.84E+00	5.84E+00	0.02%	99.98%	0.01%	99.99%
1400	2.75E+03	1.10E+05	1.28E-01	3.21E-03	1.09E+01	1.09E+01	0.03%	99.97%	0.01%	99.99%
1500	1.54E+04	4.81E+05	1.16E+00	3.71E-02	7.24E+01	7.24E+01	0.05%	99.95%	0.03%	99.97%
1600	6.98E+04	1.76E+06	7.98E+00	3.17E-01	3.81E+02	3.81E+02	0.08%	99.92%	0.04%	99.96%
1700	2.65E+05	5.52E+06	4.40E+01	2.11E+00	1.65E+03	1.66E+03	0.13%	99.87%	0.06%	99.94%
1800	8.70E+05	1.53E+07	2.01E+02	1.14E+01	6.10E+03	6.11E+03	0.19%	99.81%	0.09%	99.91%
1900	2.52E+06	3.82E+07	7.88E+02	5.21E+01	1.97E+04	1.97E+04	0.26%	99.74%	0.13%	99.87%
2000	6.58E+06	8.69E+07	2.69E+03	2.04E+02	5.64E+04	5.66E+04	0.36%	99.64%	0.18%	99.82%
2100	1.57E+07	1.83E+08	8.21E+03	7.03E+02	1.46E+05	1.47E+05	0.48%	99.52%	0.24%	99.76%
2200	3.46E+07	3.61E+08	2.26E+04	2.17E+03	3.49E+05	3.51E+05	0.62%	99.38%	0.31%	99.69%
2300	7.12E+07	6.71E+08	5.72E+04	6.07E+03	7.72E+05	7.78E+05	0.78%	99.22%	0.39%	99.61%
2400	1.38E+08	1.19E+09	1.34E+05	1.56E+04	1.60E+06	1.61E+06	0.97%	99.03%	0.49%	99.51%
2500	2.54E+08	2.00E+09	2.94E+05	3.73E+04	3.12E+06	3.16E+06	1.18%	98.82%	0.59%	99.41%

Appendix 2

Conformational analysis for Ethyl Formate

Scan of coordinates of internal rotations of EF

Two relaxed and one rigid scans of redundant internal coordinates in the dihedral angles O1-C1–O2–C2 and C1–O2–C2–C3 (**O1**=**C1**(H)–**O2**–**C2**(H_2)–**C3**H_3) were performed to search the local minimum energy conformations of EF Using the Zhao´s and Truhlar´s M06-2X functional with the cc-pVDZ basis sets of Dunning. [58,60]

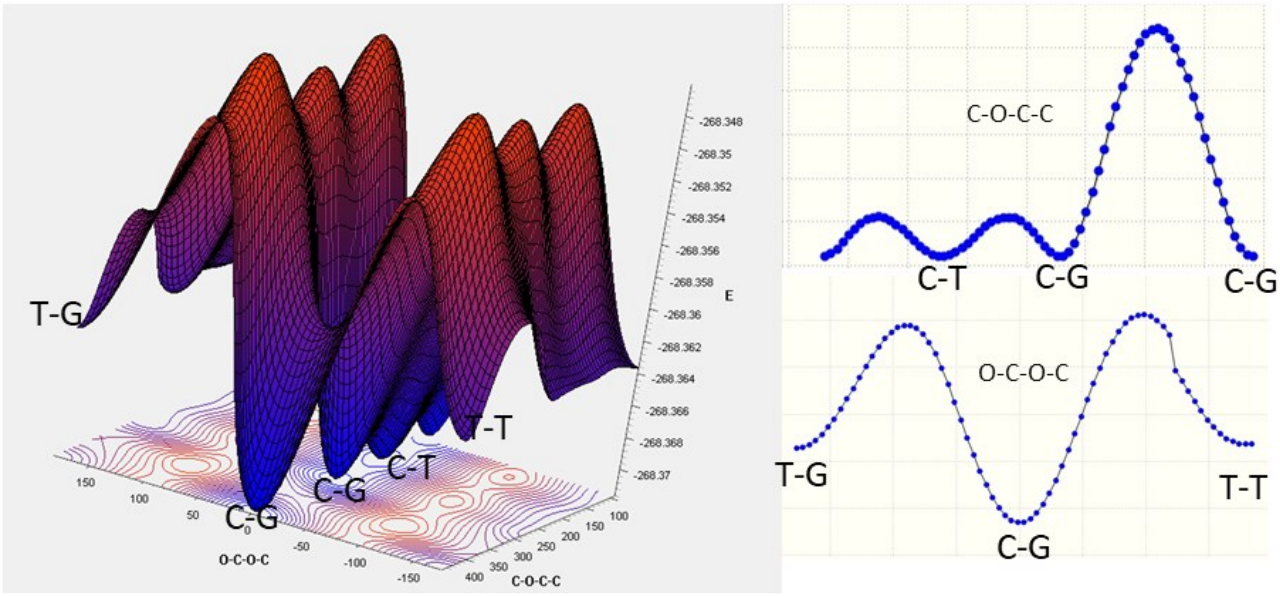

Figure A2-1: Potential energy surface for the ethyl formate isomerization.

Once the local minima configurations were determined, they were reoptimized using M06-2X functional including Grimme´s empirical dispersion correction (GD3) and the cc-pVTZ and aug-cc-pVTZ basis sets of Dunning. [58–60]

Section **I-B** includes the optimized geometries in xyz format and vibrational frequencies at the M06-2X-GD3/aug-cc-pVTZ level of theory. Calculated energies for all methods used are also included.

Optimized geometries and vibrational frequencies at the M06-2X-GD3/aug-cc-pVTZ level of theory of EF conformers

(I) T-G_CH_3CH_2OCHO					
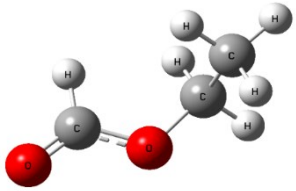					
Method		**Ee**	**E+ZPE**	**ΔH**	**ΔG**
M06-2X-GD3/cc-pVTZ		-268.363642	-268.272629	-268.265905	-268.301819
CCSD(T)/cc-pVTZ		-267.96273	-267.871720	-267.864995	-267.900909
CBS-QB3		-268.05085	-267.962140	-267.955273	-267.991772
M06-2X-GD3/aug-cc-pVTZ		-268.36785	-268.276915	-268.270190	-268.306084
SVECV-f12		-268.33580	-268.244867	-268.238142	-268.274037
Coordinates (xyz)			**Vibrations (cm^{-1})**		
C	0.0009	0.0057	-0.0035	81.493	1163.144	3068.380
O	-0.0008	0.0036	1.1858	157.404	1242.753	3069.129
O	1.1222	-0.0126	-0.7316	231.261	1346.711	3131.561
C	0.9767	0.0820	-2.1518	382.570	1400.744	3149.219
C	0.9693	1.5276	-2.5980	421.903	1421.584	
H	-0.9166	0.0124	-0.6162	645.143	1438.346	
H	0.0646	-0.4346	-2.4599	803.653	1489.905	
H	1.8243	-0.4586	-2.5653	933.359	1500.544	
H	0.9160	1.5859	-3.6846	1056.543	1527.294	
H	0.1108	2.0558	-2.1828	1085.693	1886.211	
H	1.8757	2.0293	-2.2643	1124.949	3000.040	

(II) C-G_CH_3CH_2OCHO						
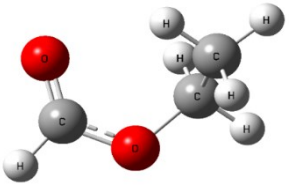						
Method			**Ee**	**E+ZPE**	**ΔH**	**ΔG**
M06-2X-GD3/cc-pVTZ			-268.371611	-268.279910	-268.273441	-268.308515
CCSD(T)/cc-pVTZ			-267.97014	-267.878440	-267.871971	-267.907045
CBS-QB3			-268.05845	-267.969013	-267.962386	-267.998026
M06-2X-GD3/aug-cc-pVTZ			-268.37559	-268.283972	-268.277498	-268.312584
SVECV-f12			-268.34342	-268.251797	-268.245323	-268.280409
Coordinates (xyz)				Vibrations (cm^{-1})		
C	-0.001272	0.001321	0.000591	112.499	1195.0091	3087.3171
O	-0.000945	0.004085	1.197188	227.4687	1249.8702	3102.5939
O	1.07701	-7.10E-05	-0.779322	262.6517	1342.226	3143.8224
C	2.35041	-0.010737	-0.107181	340.866	1398.0139	3150.0677
C	2.717212	-1.408333	0.341417	467.3128	1414.6367	3168.377
H	-0.904484	0.004577	-0.619648	764.4103	1428.2274	
H	2.304764	0.676265	0.735891	830.971	1491.2912	
H	3.050679	0.369341	-0.84629	874.8258	1502.166	
H	3.710141	-1.400765	0.789888	1039.8117	1513.626	
H	2.007306	-1.769866	1.0824	1067.2562	1838.6194	
H	2.727285	-2.090374	-0.507457	1127.8066	3074.5881	

(III) C-T_CH_3CH_2OCHO						
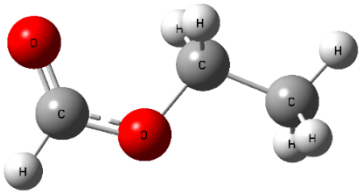						
Method			**Ee**	**E+ZPE**	**ΔH**	**ΔG**
M06-2X-GD3/cc-pVTZ			-268.371637	-268.280226	-268.273609	-268.309154
CCSD(T)/cc-pVTZ			-267.97025	-267.878837	-267.872220	-267.907766
CBS-QB3			-268.05879	-267.969599	-267.962856	-267.998904
M06-2X-GD3/aug-cc-pVTZ			-268.37571	-268.284384	-268.277763	-268.313304
SVECV-f12			-268.34357	-268.252239	-268.245618	-268.281159
Coordinates (xyz)				**Vibrations (cm^{-1})**		
C	-0.001087	-0.003707	4.90E-05	79.1274	1185.5833	3082.9891
O	-0.000845	-0.020668	1.196118	235.0127	1260.367	3086.1546
O	1.082039	0.014069	-0.772361	236.1835	1310.3622	3124.1171
C	2.342021	0.012157	-0.078047	344.4428	1398.9953	3151.1841
C	3.434262	0.033781	-1.117765	388.7608	1410.4432	3156.9037
H	-0.902396	-0.000548	-0.622962	804.1964	1433.4511	
H	2.38866	-0.876845	0.550367	813.0338	1490.6776	
H	2.377573	0.883499	0.575331	881.497	1503.1362	
H	4.407412	0.032978	-0.628999	1061.2312	1525.427	
H	3.369381	-0.841427	-1.761925	1062.9442	1840.6729	
H	3.35825	0.926016	-1.73686	1145.1539	3075.6576	

(IV) T-T_CH_3CH_2OCHO					
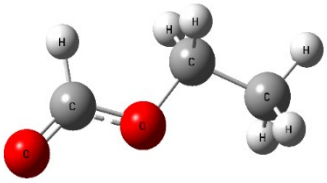					
Method		**Ee**	**E+ZPE**	**ΔH**	**ΔG**
M06-2X-GD3/cc-pVTZ		-268.363257	-268.272474	-268.265522	-268.302426
CCSD(T)/cc-pVTZ		-267.96235	-267.871565	-267.864613	-267.901517
CBS-QB3		-268.05066	-267.962146	-267.955996	-267.990370
M06-2X-GD3/aug-cc-pVTZ		-268.36750	-268.276774	-268.269846	-268.306473
SVECV-f12		-268.33545	-268.244722	-268.237794	-268.274421
Coordinates (xyz)			**Vibrations (cm^{-1})**		
C	-0.000502	-0.007493	-0.000269	44.9744	1185.8163	3058.0754
O	-0.001955	0.013237	1.189192	154.0112	1238.5816	3078.5423
O	1.121136	0.020924	-0.72715	229.5614	1318.9247	3100.392
C	0.960485	-0.009857	-2.151724	260.8722	1398.2648	3155.4631
C	2.336402	0.0298	-2.768902	442.3016	1421.8919	3159.6723
H	-0.917766	-0.051789	-0.611012	635.5937	1449.1585	
H	0.364725	0.850161	-2.46395	820.8728	1488.6537	
H	0.429675	-0.921546	-2.432993	949.0864	1504.2621	
H	2.257345	0.007929	-3.854691	1060.851	1528.4077	
H	2.857862	0.938253	-2.473642	1091.7239	1887.8085	
H	2.922583	-0.82719	-2.442794	1156.6108	3003.8731	

Thermochemistry for Ethyl Formate thermal decomposition

In this section the paths determined for unimolecular decomposition of EF are presented. Six molecular paths (1-6) with a well-define transition state (TS), for which the optimized structures of the TS, postreaction well (PW) and the intrinsic reaction coordinate (IRC) were determined. And two homolytic bond rupture for paths (7) and (8) for which scans of redundant coordinates increasing the C1-O2 or O2-C2 bond length was performed. Optimized structures for final products and paths for secondary products were also determined.

All tables include the optimized geometries in xyz format and vibrational frequencies at the M06-2X-GD3/aug-cc-pVTZ level of theory. Calculated energies for all methods used are also included.

Optimized geometries and vibrational frequencies at the M06-2X-GD3/aug-cc-pVTZ level of theory of Ethyl Formate thermal decomposition paths 1-6: transition states and postreaction wells.

$H_3CCH_2OCHO \rightarrow H_2C{=}CH_2$ (P1) + HOCOH (P2) k1

TS_1

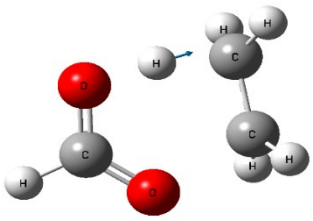

Method	Ee	E+ZPE	ΔH	ΔG
M06-2X-GD3/cc-pVTZ	-268.283950	-268.199722	-268.193408	-268.228218
CCSD(T)/cc-pVTZ	-267.88249	-267.798258	-267.791944	-267.826754
CBS-QB3	-267.96964	-267.887781	-267.881073	-267.918547
M06-2X-GD3/aug-cc-pVTZ	-268.28833	-268.204217	-268.197910	-268.232675
SVECV-f12	-268.25649	-268.172371	-268.166064	-268.200829

Coordinates (xyz)			Vibrations (cm^{-1})		
C -0.0589	0.0160	-0.0628	-1522.62	1088.12	3024.84
O 0.0157	-0.3800	1.1323	131.38	1185.81	3145.58
O 0.8606	-0.0991	-0.9020	170.96	1230.09	3182.41
C 2.6403	-0.0967	-0.1282	419.56	1271.13	3233.34
C 2.5986	-0.1264	1.2670	473.23	1315.07	3271.56
H -0.9863	0.5176	-0.3786	563.66	1395.84	
H 2.8171	0.8267	-0.6603	573.09	1424.61	
H 2.8784	-0.9911	-0.6844	795.33	1467.90	
H 2.7731	0.7990	1.7997	809.04	1517.86	
H 1.2686	-0.3217	1.3448	905.54	1576.07	
H 2.9423	-1.0312	1.7539	1021.31	1729.90	

PW_1					
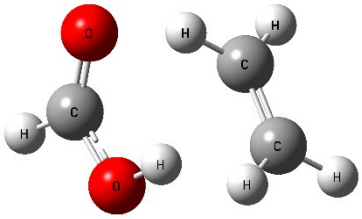					
Method		**Ee**	**E+ZPE**	**ΔH**	**ΔG**
M06-2X-GD3/cc-pVTZ		-268.345505	-268.258142	-268.249575	-268.291190
CCSD(T)/cc-pVTZ		-267.94670	-267.859335	-267.850768	-267.892383
CBS-QB3		-268.03432	-267.949187	-267.941284	-267.981196
M06-2X-GD3/aug-cc-pVTZ		-268.34971	-268.262473	-268.253879	-268.295642
SVECV-f12		-268.31977	-268.232537	-268.223943	-268.265706
Coordinates (xyz)			**Vibrations (cm^{-1})**		
C	-0.0171	-0.0528	-0.0204	33.55	1078.18	3156.34
O	0.0092	0.0769	1.3043	84.28	1083.25	3171.93
O	0.9452	-0.0761	-0.7311	99.33	1192.73	3233.18
C	3.2525	0.2512	1.5212	105.12	1241.90	3259.52
C	3.0256	0.3665	2.8218	146.42	1347.01	3644.46
H	-1.0501	-0.1360	-0.3759	174.37	1385.34	
H	3.3013	1.1150	0.8710	665.93	1423.09	
H	3.3878	-0.7126	1.0481	775.22	1477.43	
H	2.8895	1.3331	3.2900	827.29	1704.88	
H	0.9385	0.1486	1.5916	1009.99	1852.53	
H	2.9762	-0.5008	3.4677	1027.50	3089.77	

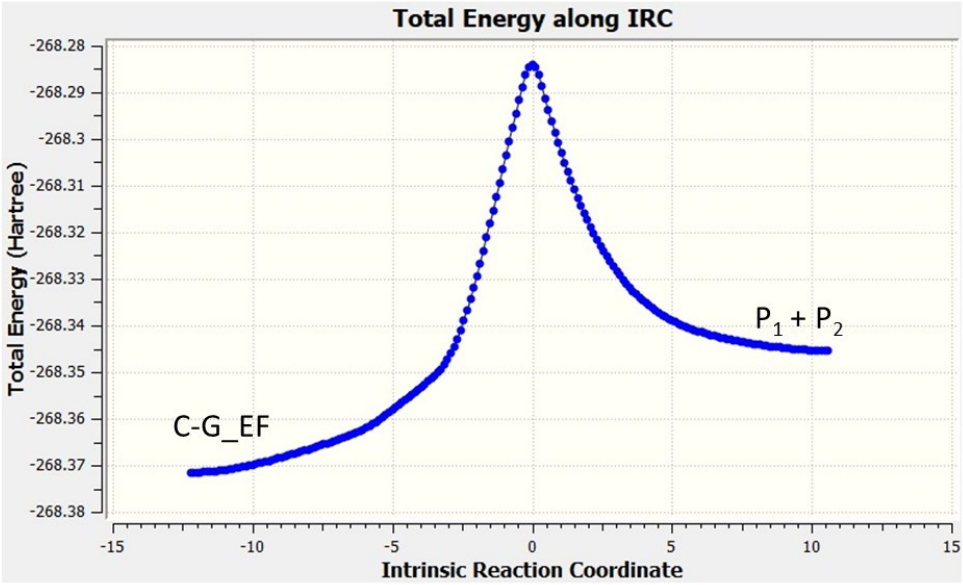

Figure A2-2: Intrinsic reaction coordinate (IRC) for the ethyl formate thermal decomposition (k_1).

$H_3CCH_2OCHO \rightarrow H_3CCH_2OH\ (P_3) + CO\ (P_4)$ k_2

TS_2						
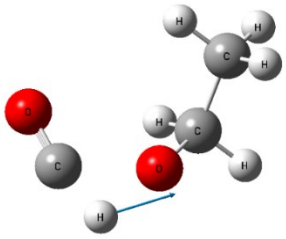						
Method			**Ee**	**E+ZPE**	**ΔH**	**ΔG**
M06-2X-GD3/cc-pVTZ			-268.250819	-268.166977	-268.159681	-268.197178
CCSD(T)/cc-pVTZ			-267.85457	-267.770700	-267.763412	-267.800856
CBS-QB3			-267.94146	-267.859300	-267.851912	-267.889845
M06-2X-GD3/aug-cc-pVTZ			-268.25505	-268.171329	-268.164003	-268.201591
SVECV-f12			-268.22707	-268.143349	-268.136023	-268.173611
Coordinates (xyz)				**Vibrations (cm^{-1})**		
C	-0.1783	0.1544	0.1053	i1835.10	1085.97	2992.06
O	-0.1307	-0.1448	1.2058	49.82	1140.35	3065.27
O	1.1581	-0.2941	-1.0055	123.83	1178.96	3066.34
C	2.4529	-0.0910	-0.4755	206.31	1318.50	3139.47
C	3.0645	-1.4130	-0.0519	257.46	1393.20	3146.93
H	0.1000	0.5618	-0.9658	384.05	1415.78	
H	2.4058	0.5852	0.3896	427.39	1487.52	
H	3.0707	0.3934	-1.2352	696.54	1498.09	
H	4.0702	-1.2631	0.3418	806.00	1517.12	
H	2.4538	-1.8791	0.7203	913.64	1957.87	
H	3.1186	-2.0905	-0.9028	983.53	2497.83	

PW_2					
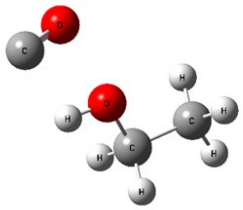					
Method		**Ee**	**E+ZPE**	**ΔH**	**ΔG**
M06-2X-GD3/cc-pVTZ		-268.348904	-268.261983	-268.253014	-268.295437
CCSD(T)/cc-pVTZ		-267.95302	-267.866102	-267.857132	-267.899555
CBS-QB3		-268.03835	-267.953362	-267.944212	-267.988442
M06-2X-GD3/aug-cc-pVTZ		-268.35309	-268.266265	-268.257276	-268.299742
SVECV-f12		-268.32379	-268.236961	-268.227972	-268.270437
Coordinates (xyz)			**Vibrations (cm^{-1})**		
C	0.0772	0.2929	0.2477	34.53	1132.60	3055.01
O	-0.0332	-0.3675	1.1477	64.10	1186.71	3071.54
O	2.9623	-0.0027	-0.2677	88.90	1271.63	3147.66
C	3.2519	0.9294	0.7640	119.16	1307.58	3148.66
C	3.5277	0.1475	2.0271	142.47	1402.99	3887.70
H	2.7361	0.4727	-1.0701	251.37	1456.74	
H	2.4040	1.6067	0.9154	306.14	1487.04	
H	4.1200	1.5384	0.4949	424.31	1504.92	
H	3.7657	0.8208	2.8496	818.97	1538.62	
H	2.6558	-0.4456	2.3004	918.23	2268.70	
H	4.3676	-0.5285	1.8733	1052.76	3022.53	

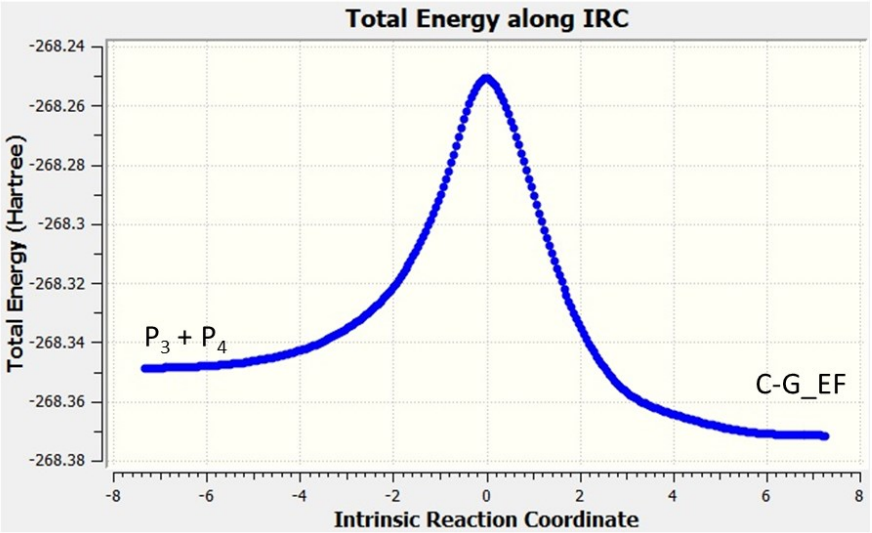

Figure A2-3: Intrinsic reaction coordinate (IRC) for the ethyl formate thermal decomposition (k_2).

$H_3CCH_2OCHO \rightarrow H_2CO\ (P_5) + H_3CCHO\ (P_5)$ k_3

TS_3					
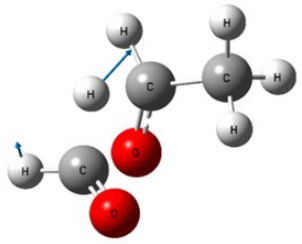					
Method		**Ee**	**E+ZPE**	**ΔH**	**ΔG**
M06-2X-GD3/cc-pVTZ		-268.248861	-268.163781	-268.157544	-268.191930
CCSD(T)/cc-pVTZ		-267.84782	-267.762745	-267.756508	-267.790894
CBS-QB3		-267.93731	-267.854802	-267.848394	-267.883141
M06-2X-GD3/aug-cc-pVTZ		-268.25397	-268.168975	-268.162723	-268.197144
SVECV-f12		-268.22180	-268.136812	-268.130560	-268.164981
Coordinates (xyz)			**Vibrations (cm^{-1})**		
C	-0.0282	-0.0363	-0.0568	-1118.53	1136.05	3024.91
O	-0.1268	-0.0651	1.1258	180.42	1180.22	3065.12
O	1.6066	0.0141	-0.7383	213.23	1288.23	3137.48
C	1.2356	1.2502	-0.8897	355.09	1357.51	3163.83
C	1.5897	2.2685	0.1497	463.80	1387.34	3167.30
H	-0.3603	-0.7000	-0.8501	512.45	1422.39	
H	-0.1873	1.1093	-0.6332	565.75	1465.67	
H	1.0998	1.6222	-1.9142	696.26	1484.27	
H	1.1079	3.2251	-0.0418	867.99	1517.43	
H	1.3262	1.8896	1.1370	966.74	1770.02	
H	2.6726	2.3994	0.1161	1048.12	1869.35	

PW_3					
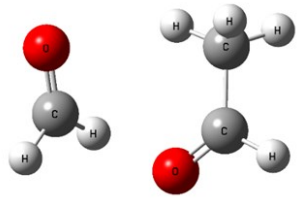					
Method		**Ee**	**E+ZPE**	**ΔH**	**ΔG**
M06-2X-GD3/cc-pVTZ		-268.322446	-268.237585	-268.228505	-268.271325
CCSD(T)/cc-pVTZ		-267.92576	-267.840904	-267.831824	-267.874644
CBS-QB3		-268.01411	-267.931661	-267.922342	-267.965831
M06-2X-GD3/aug-cc-pVTZ		-268.32737	-268.242354	-268.233501	-268.274801
SVECV-f12		-268.29811	-268.213097	-268.204244	-268.245544
Coordinates (xyz)			**Vibrations (cm^{-1})**		
C	0.2279	-0.1855	0.0895	61.38	1147.51	2968.88
O	0.5841	-0.5450	1.1770	92.78	1216.18	3043.20
O	2.5221	0.5192	-1.1986	111.72	1272.67	3062.01
C	3.3643	0.4212	-0.3441	120.30	1383.48	3127.26
C	3.2607	1.0200	1.0208	164.28	1432.52	3181.20
H	0.2113	-0.8691	-0.7731	194.34	1457.98	
H	-0.1024	0.8478	-0.1019	263.84	1469.67	
H	4.2846	-0.1569	-0.5480	521.07	1542.29	
H	4.1862	1.5415	1.2672	767.99	1845.97	
H	2.4068	1.6879	1.0881	911.90	1858.08	
H	3.1340	0.2093	1.7425	1140.99	2958.44	

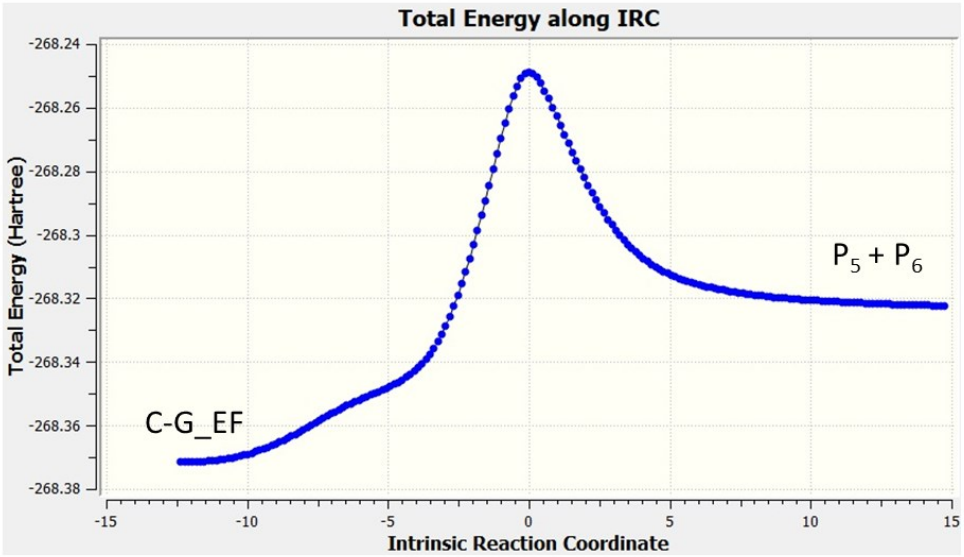

Figure A2-4: Intrinsic reaction coordinate (IRC) for the ethyl formate thermal decomposition (k_3).

$H_3CCH_2OCHO \rightarrow C_2H_6$ (P7) + CO_2 (P8) k4

TS_4					
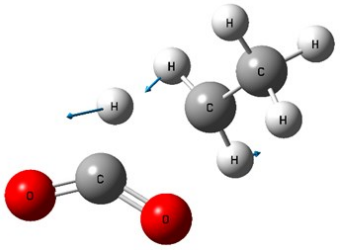					
Method		**Ee**	**E+ZPE**	**ΔH**	**ΔG**
M06-2X-GD3/cc-pVTZ		-268.230359	-268.145657	-268.138551	-268.175711
CCSD(T)/cc-pVTZ		-267.83425	-267.749550	-267.742443	-267.779603
CBS-QB3		-267.92473	-267.843013	-267.835739	-267.873163
M06-2X-GD3/aug-cc-pVTZ		-268.23581	-268.151202	-268.144075	-268.181296
SVECV-f12		-268.20850	-268.123892	-268.116765	-268.153986
Coordinates (xyz)			**Vibrations (cm^{-1})**		
C	0.0547	-0.0116	0.0848	-1181.02	1119.10	3018.20
O	0.0941	-0.0740	1.2832	69.61	1189.54	3139.19
O	0.9009	0.0210	-0.8392	91.81	1223.92	3166.27
C	-0.7237	-1.2553	-1.6393	201.36	1248.55	3195.34
C	-1.1285	-0.4115	-2.7747	242.52	1358.67	3272.01
H	-1.0405	-0.0247	-0.3666	417.91	1380.71	
H	-1.4889	-1.7285	-1.0356	728.45	1443.90	
H	0.1852	-1.8291	-1.7343	775.34	1494.33	
H	-1.3872	-1.1137	-3.5797	815.03	1526.23	
H	-2.0011	0.1990	-2.5623	882.43	1852.23	
H	-0.3000	0.2014	-3.1149	1017.25	2266.52	

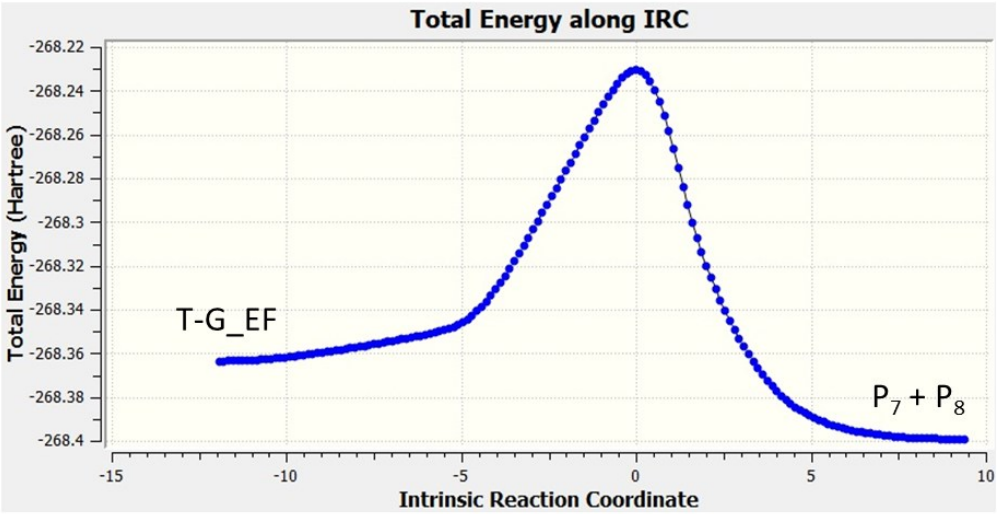

Figure A2-5: Intrinsic reaction coordinate (IRC) for the ethyl formate thermal decomposition (k_4).

$H_3CCH_2OCHO \rightarrow CH_3CHO\ (P_6) + HCOH\ (IM) \quad k_5$

TS_5

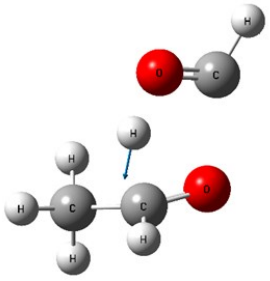

Method	**Ee**	**E+ZPE**	**ΔH**	**ΔG**
M06-2X-GD3/cc-pVTZ	-268.194069	-268.112107	-268.105345	-268.141011
CCSD(T)/cc-pVTZ	-267.79787	-267.715911	-267.709149	-267.744815
CBS-QB3	-267.88599	-267.806409	-267.799479	-267.835466
M06-2X-GD3/aug-cc-pVTZ	-268.19865	-268.116748	-268.109976	-268.145668
SVECV-f12	-268.17031	-268.088406	-268.081634	-268.117326

Coordinates (xyz)			**Vibrations (cm^{-1})**		
C 0.0006	-0.0002	-0.0014	-1336.27	1096.28	2992.96
O 0.0002	-0.0033	1.2135	135.14	1114.29	3030.31
O 2.0911	0.0049	-0.2534	171.16	1238.93	3053.13
C 2.4764	-0.1070	0.9395	213.26	1275.61	3117.34
C 2.9116	-1.4539	1.4790	451.10	1362.18	3142.39
H -1.0092	0.0220	-0.4369	491.01	1401.42	
H 1.1270	-0.0177	1.5118	522.70	1477.00	
H 2.8339	0.7966	1.4552	621.80	1487.84	
H 2.9752	-1.4505	2.5663	685.34	1557.83	
H 2.2071	-2.2239	1.1615	896.65	1611.80	
H 3.8918	-1.7179	1.0776	951.33	1851.08	

PW_5				
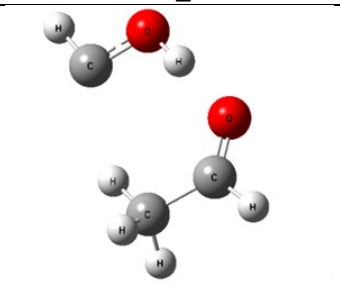				
Method	**Ee**	**E+ZPE**	**ΔH**	**ΔG**
M06-2X-GD3/cc-pVTZ	-268.252458	-268.166784	-268.158432	-268.198371
CCSD(T)/cc-pVTZ	-267.85553	-267.769853	-267.761501	-267.801440
CBS-QB3	-267.94120	-267.857254	-267.848959	-267.888640
M06-2X-GD3/aug-cc-pVTZ	-268.25725	-268.171619	-268.163263	-268.203200
SVECV-f12	-268.22696	-268.141333	-268.132977	-268.172915
Coordinates (xyz)			**Vibrations (cm^{-1})**	
C -0.1127	-0.7052	0.6370	66.43	1168.52	2994.12
O 0.3611	0.4868	0.7783	124.52	1218.69	3041.01
O 2.2085	0.3804	2.7488	129.15	1319.93	3115.58
C 2.5288	-0.6012	3.3781	173.48	1388.31	3142.75
C 1.9580	-1.9617	3.1855	181.66	1434.35	3353.90
H -0.8605	-0.6008	-0.1789	236.50	1440.31	
H 1.0414	0.4830	1.4932	430.93	1466.99	
H 3.3020	-0.4945	4.1577	540.75	1484.25	
H 1.5310	-2.2979	4.1331	789.54	1550.86	
H 1.2063	-1.9621	2.3966	913.45	1831.23	
H 2.7721	-2.6512	2.9506	1159.33	2889.17	

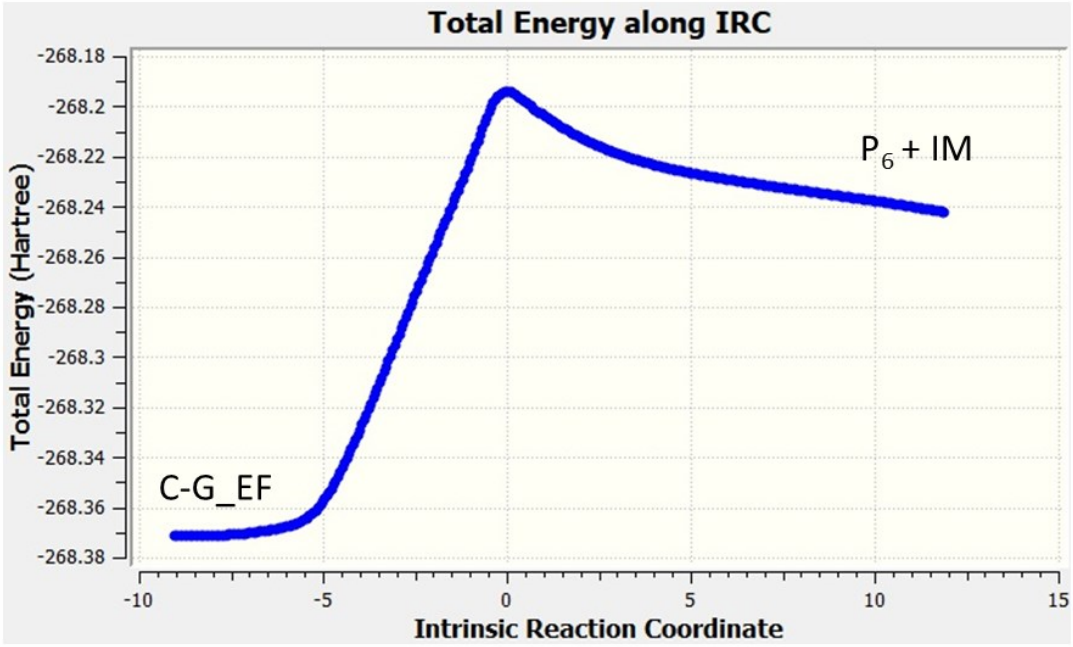

Figure A2-6: Intrinsic reaction coordinate (IRC) for the ethyl formate thermal decomposition (k_5).

$H_3CCH_2OCHO \rightarrow H_2C{=}CH_2$ (P_1) + CO_2 (P_8) + H_2 (P_9) k_6

TS_6

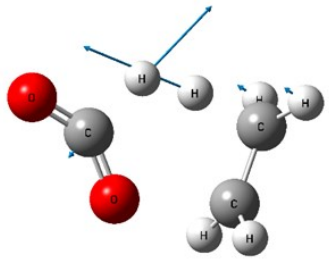

Method	**Ee**	**E+ZPE**	**ΔH**	**ΔG**
M06-2X-GD3/cc-pVTZ	-268.242722	-268.162286	-268.155709	-268.191080
CCSD(T)/cc-pVTZ	-267.84337	-267.762930	-267.756354	-267.791724
CBS-QB3	-267.93302	-267.854365	-267.847674	-267.883276
M06-2X-GD3/aug-cc-pVTZ	-268.24752	-268.167272	-268.160662	-268.196104
SVECV-f12	-268.21779	-268.137546	-268.130936	-268.166378

Coordinates (xyz)			**Vibrations (cm^{-1})**		
C 0.0144	-0.0632	0.2666	-1290.45	940.72	1999.96
O -0.3986	0.0298	1.3857	119.06	1069.98	3150.73
O 0.9848	-0.3966	-0.3841	240.30	1187.41	3202.30
C 0.7715	-0.1874	-2.5755	334.67	1202.30	3238.85
C -0.4826	0.3076	-2.8360	367.39	1260.58	3298.57
H -0.9409	0.3497	-0.5494	418.92	1337.99	
H 0.9722	-1.2472	-2.5814	540.80	1382.26	
H 1.6266	0.4634	-2.4818	799.30	1474.27	
H -1.2536	-0.3635	-3.1934	802.98	1589.60	
H -0.8382	0.3684	-1.5448	852.30	1647.08	
H -0.5967	1.3531	-3.0934	905.91	1860.39	

PW_6					
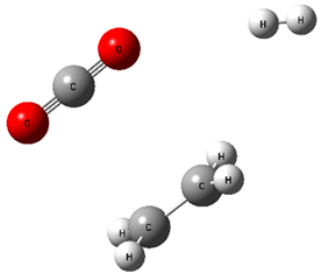					
Method		**Ee**	**E+ZPE**	**ΔH**	**ΔG**
M06-2X-GD3/cc-pVTZ		-268.337080	-268.261411	-268.249701	-268.300629
CCSD(T)/cc-pVTZ		-267.94104	-267.865373	-267.853662	-267.904590
CBS-QB3		-268.03019	-267.956403	-267.945341	-267.995637
M06-2X-GD3/aug-cc-pVTZ		-268.34017	-268.264419	-268.252832	-268.303108
SVECV-f12		-268.31287	-268.248825	-268.237115	-268.275804
Coordinates (xyz)			**Vibrations (cm^{-1})**		
C	-0.3487	0.0115	-0.4918	11.91	694.67	3156.50
O	-0.9020	0.0600	0.5215	46.11	827.87	3172.10
O	0.2225	-0.0367	-1.4947	59.79	999.38	3232.01
C	-2.7906	-0.0180	-2.6051	71.06	1009.91	3258.12
C	-3.4420	-0.0158	-1.4536	82.38	1071.55	4455.46
H	-4.1061	-0.0644	2.3210	95.87	1241.80	
H	-2.5040	-0.9400	-3.0939	109.11	1386.84	
H	-2.5148	0.9024	-3.1033	113.86	1410.18	
H	-3.7156	-0.9359	-0.9535	202.29	1475.93	
H	-3.4258	-0.0035	2.0375	236.12	1712.33	
H	-3.7256	0.9060	-0.9625	679.59	2439.27	

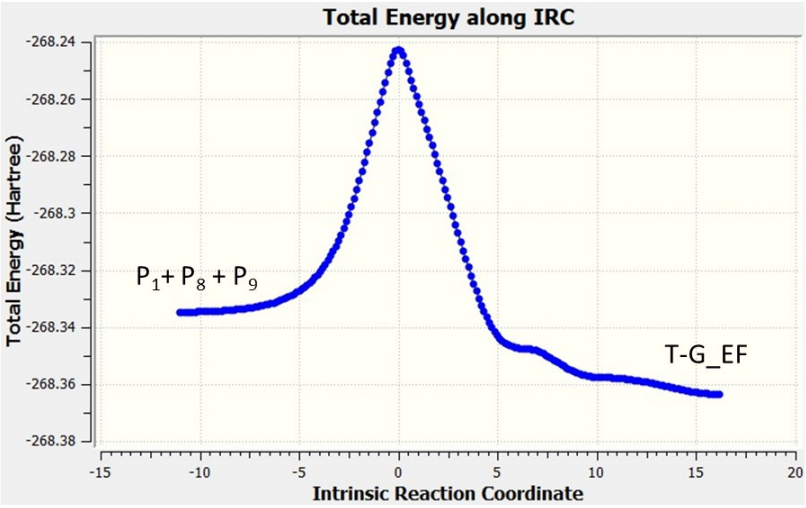

Figure A2-7: Intrinsic reaction coordinate (IRC) for the ethyl formate thermal decomposition (k_6).

Plots of scan of redundant coordinates for the homolytic paths (7) and (8)

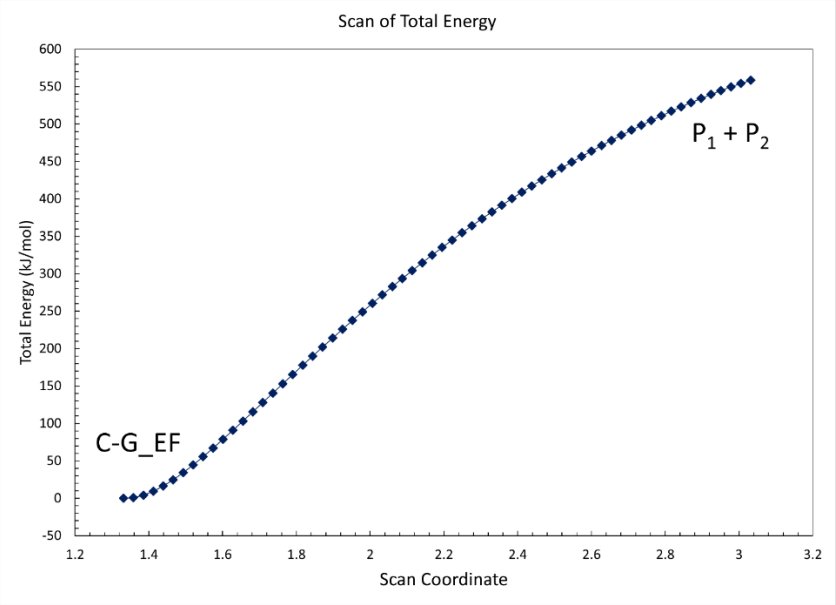

Figure A2-8: Relative energy in the O-C scan of coordinates for the ethyl formate unimolecular decomposition.

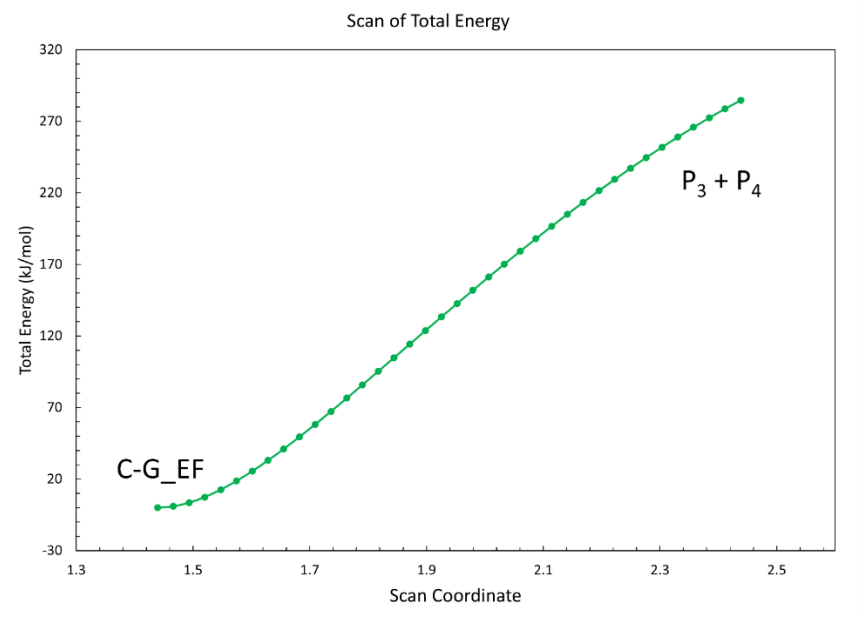

Figure A2-9: Relative energy in the C-O scan of coordinates for the ethyl formate unimolecular decomposition.

Optimized geometries and vibrational frequencies at the M06-2X-GD3/aug-cc-pVTZ level of theory for secondary reactions of Ethyl Formate thermal decomposition: transition states and postreaction wells

CH_3CH_2OH $(P_3) \rightarrow CH_3CHO$ $(P_6) + H_2$ (P_7) k_{2a}

TS_2a					
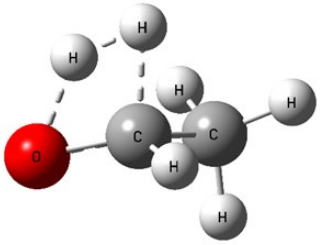					
Method		**Ee**	**E+ZPE**	**ΔH**	**ΔG**
M06-2X-GD3/cc-pVTZ		-154.879863	-154.808426	-154.803500	-154.833545
CCSD(T)/cc-pVTZ		-154.64773	-154.576289	-154.571363	-154.601409
CBS-QB3		-154.70221	-154.632705	-154.627729	-154.657863
M06-2X-GD3/aug-cc-pVTZ		-154.88425	-154.812818	-154.807892	-154.837939
SVECV-f12		-154.87120	-154.799772	-154.794846	-154.824893
Coordinates (xyz)				**Vibrations (cm^{-1})**	
C	0.0144	-0.0372	-0.0328	-2214.38	1272.61	3066.20
H	-0.0783	0.0163	1.0619	253.51	1371.62	3141.50
H	1.4359	0.0611	-0.0166	443.88	1394.20	3176.54
O	-0.4146	0.9937	-0.7423	627.77	1446.14	
H	0.9480	0.7546	-0.4739	860.06	1474.98	
C	-0.1547	-1.4255	-0.5864	910.52	1492.92	
H	0.3838	-2.1738	-0.0068	965.96	2007.88	
H	-1.2257	-1.6306	-0.5296	1045.47	2251.78	
H	0.1424	-1.4534	-1.6312	1154.27	2995.86	

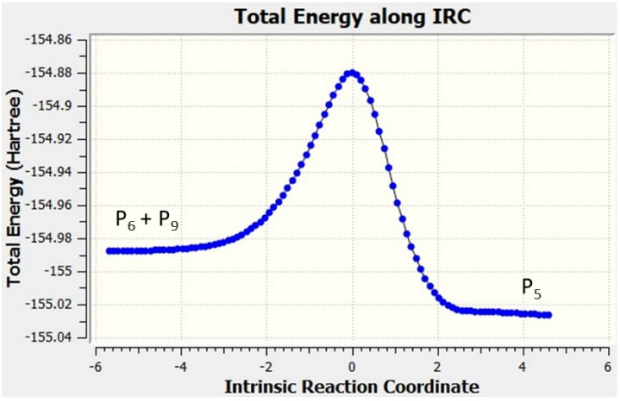

Figure A2-10: Intrinsic reaction coordinate (IRC) for the ethanol thermal decomposition (k_{2a}).

$H_2C{=}CH_2$ $(P_1) \rightarrow C_2H_2$ (P_{15}) + H_2 (P_9) k_{1b}

TS_k_{1b_1}				
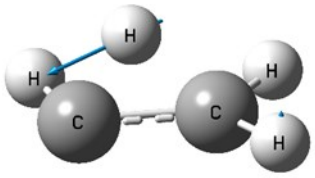				
Method	**Ee**	**E+ZPE**	**ΔH**	**ΔG**
M06-2X-GD3/cc-pVTZ	-78.449224	-78.403337	-78.399422	-78.425548
CCSD(T)/cc-pVTZ	-78.31397	-78.268079	-78.264164	-78.290290
CBS-QB3	-78.34032	-78.295528	-78.291612	-78.317740
M06-2X-GD3/aug-cc-pVTZ	-78.45094	-78.405069	-78.401153	-78.427278
SVECV-f12	-78.44259	-78.396719	-78.392803	-78.418928
Coordinates (xyz)			**Vibrations (cm^{-1})**	
C -0.0246	0.0302	0.0013	-291.70	1368.36
C -0.0081	-0.0844	1.4033	950.45	1525.24
H 0.9192	0.0377	-0.5396	1032.83	2410.31
H -0.9111	-0.0666	-0.6298	1124.87	3002.25
H 0.0044	1.0813	0.5784	1250.59	3053.91
H -1.0583	-0.1043	1.7329	1269.40	3148.03

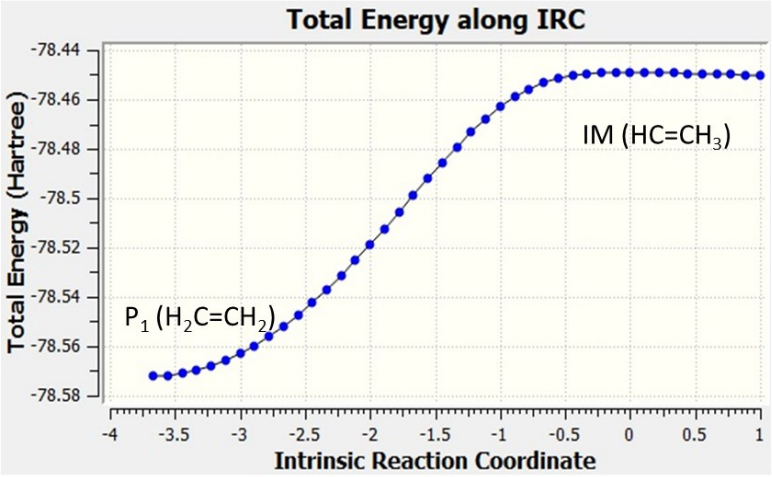

Figure A2-11: Intrinsic reaction coordinate (IRC) for the ethylene thermal decomposition (k_{1b}).

TS_k_{1b_2}				
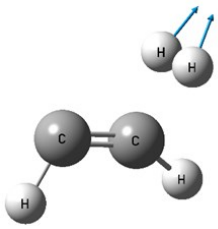				
Method	**Ee**	**E+ZPE**	**ΔH**	**ΔG**
M06-2X-GD3/cc-pVTZ	-78.390016	-78.348154	-78.343967	-78.370486
CCSD(T)/cc-pVTZ	-78.25082	-78.208958	-78.204771	-78.231289
CBS-QB3	-78.27935	-78.238905	-78.234693	-78.261252
M06-2X-GD3/aug-cc-pVTZ	-78.39192	-78.350098	-78.345906	-78.372431
SVECV-f12	-78.38110	-78.339276	-78.335084	-78.361609
Coordinates (xyz)			**Vibrations (cm^{-1})**	
C -0.116248	-0.12335	-0.11207	-1321.215	1358.8157
C 0.162475	0.149156	1.122092	592.3606	1574.2296
H 1.5328	0.2268	1.2901	756.80	1685.29
H -1.1382	0.1097	-0.4080	878.91	3150.89
H 1.2913	-0.5459	1.5153	933.18	3200.64
H -0.1620	0.5290	2.0779	990.12	3235.45

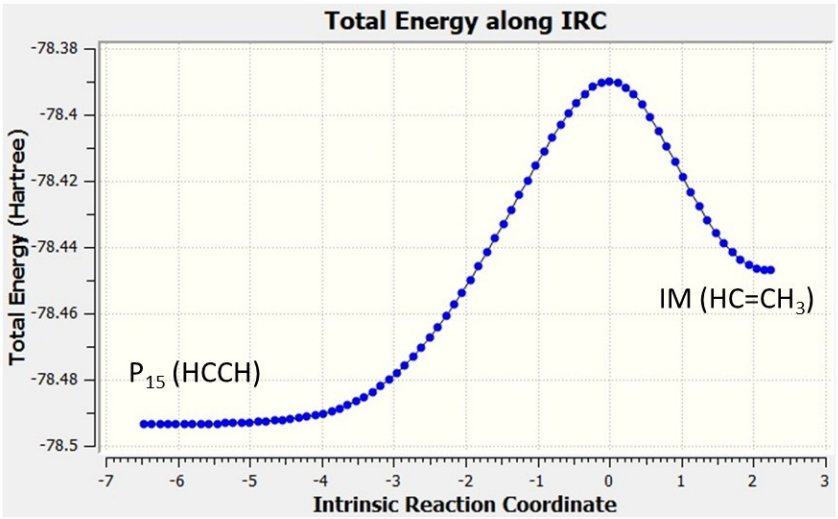

Figure A2-12: Intrinsic reaction coordinate (IRC) for the ethylene thermal decomposition (k_{1b_2}).

trans-HOCHO (P_2) → H_2O (P_{14}) + CO (P_4) k_{1a}

TS_k_{1a}				
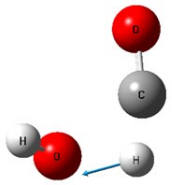				
Method	**Ee**	**E+ZPE**	**ΔH**	**ΔG**
M06-2X-GD3/cc-pVTZ	-189.645227	-189.619106	-189.614309	-189.643822
CCSD(T)/cc-pVTZ	-189.38491	-189.358789	-189.353992	-189.383505
CBS-QB3	-189.44397	-189.418162	-189.413376	-189.442918
M06-2X-GD3/aug-cc-pVTZ	-189.65059	-189.624579	-189.619744	-189.649336
SVECV-f12	-189.63015	-189.604136	-189.599301	-189.628893
Coordinates (xyz)			**Vibrations (cm^{-1})**	
C -0.0207	-0.0299	-0.1685	-1825.62	1056.28
O 0.0883	0.3722	1.6094	316.72	1985.76
O 0.8910	0.0122	-0.8462	368.93	2566.26
H -0.8061	-0.1525	0.6883	545.99	3832.94
H 0.6892	-0.2021	2.1002	745.86	

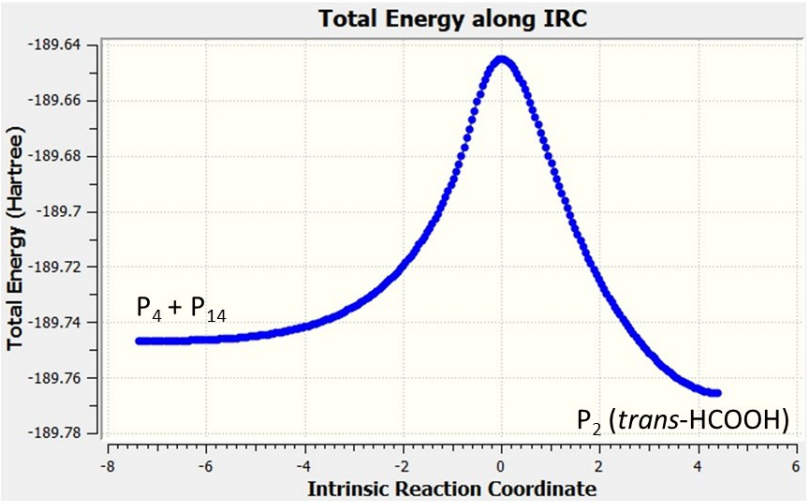

Figure A2-13: Intrinsic reaction coordinate (IRC) for the trans-formic acid thermal decomposition (k_{1a}).

cis-HOCHO (P_2) → CO2 (P_8) + H_2 (P_9) k_{1c}

TS_k_{1c}				
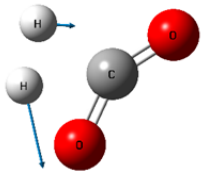				
Method	**Ee**	**E+ZPE**	**ΔH**	**ΔG**
M06-2X-GD3/cc-pVTZ	-189.644510	-189.619763	-189.615653	-189.643749
CCSD(T)/cc-pVTZ	-189.38146	-189.356709	-189.352599	-189.380694
CBS-QB3	-189.43957	-189.415838	-189.411695	-189.439851
M06-2X-GD3/aug-cc-pVTZ	-189.64808	-189.623404	-189.619293	-189.647391
SVECV-f12	-189.62491	-189.600234	-189.596123	-189.624221
Coordinates (xyz)			**Vibrations (cm^{-1})**	
C 0.2189	-0.0012	0.2435	-2254.89	1379.29
O 0.1853	-0.0218	1.4922	619.79	1853.49
O 0.8738	0.0091	-0.7177	751.05	2100.79
H -1.1835	0.0162	-0.0431	917.61	2167.71
H -1.0059	-0.0023	0.9655	1039.85	

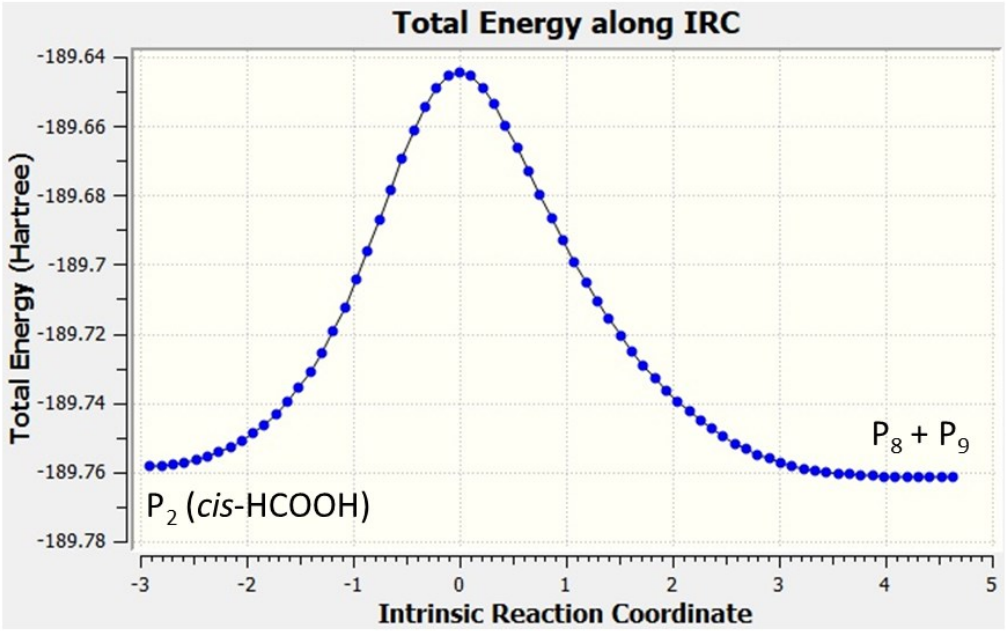

Figure A2-14: Intrinsic reaction coordinate (IRC) for the cis-formic acid thermal decomposition (k_{1c}).

Optimized geometries and vibrational frequencies at the M06-2X-GD3/aug-cc-pVTZ level of theory of Ethyl Formate thermal decomposition products

P1_$H_2C=CH_2$

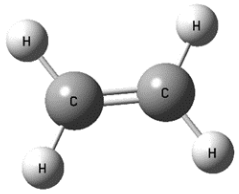

Method	Ee	E+ZPE	ΔH	ΔG
M06-2X-GD3/cc-pVTZ	-78.572077	-78.520705	-78.516726	-78.542871
CCSD(T)/cc-pVTZ	-78.43853	-78.387161	-78.383182	-78.409327
CBS-QB3	-78.46694	-78.416642	-78.412647	-78.438821
M06-2X-GD3/aug-cc-pVTZ	-78.57285	-78.521541	-78.517560	-78.543054
SVECV-f12	-78.56748	-78.516172	-78.512191	-78.537686

Coordinates (xyz)			Vibrations (cm^{-1})	
C 0.0000	0.0010	0.0005	825.74	1473.48
C 0.0000	0.0006	1.3225	989.46	1714.69
H 0.9219	-0.0004	-0.5661	1002.71	3159.20
H -0.9219	0.0028	-0.5661	1059.67	3175.17
H 0.9219	-0.0012	1.8892	1241.53	3234.20
H -0.9219	0.0020	1.8892	1386.36	3260.68

P2_trans-HOCHO

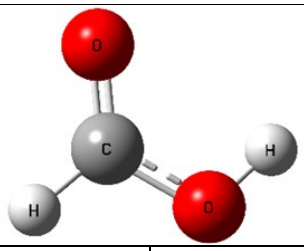

Method	Ee	E+ZPE	ΔH	ΔG
M06-2X-GD3/cc-pVTZ	-189.765786	-189.731407	-189.727309	-189.755468
CCSD(T)/cc-pVTZ	-189.50165	-189.467269	-189.463172	-189.491330
CBS-QB3	-189.56095	-189.527435	-189.523324	-189.551512
M06-2X-GD3/aug-cc-pVTZ	-189.76957	-189.735285	-189.731182	-189.759348
SVECV-f12	-189.74579	-189.711504	-189.707401	-189.735567

Coordinates (xyz)			Vibrations (cm^{-1})	
C -0.0005	0.0000	-0.0030	644.51	1414.04
O 0.0011	0.0000	1.3348	674.24	1868.38
O 0.9785	0.0000	-0.6852	1076.06	3101.23
H -1.0286	0.0000	-0.3792	1161.99	3791.04
H 0.9233	0.0000	1.6294	1317.41	

P2_cis-HOCHO

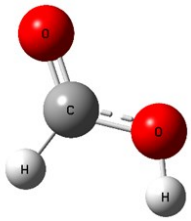

Method	Ee	E+ZPE	ΔH	ΔG
M06-2X-GD3/cc-pVTZ	-189.758341	-189.724279	-189.720099	-189.748345
CCSD(T)/cc-pVTZ	-189.49450	-189.460441	-189.456261	-189.484507
CBS-QB3	-189.55406	-189.520988	-189.516792	-189.545073
M06-2X-GD3/aug-cc-pVTZ	-189.76258	-189.728600	-189.724420	-189.752668
SVECV-f12	-189.73898	-189.704997	-189.700817	-189.729066

Coordinates (xyz)			Vibrations (cm^{-1})	
C -0.0180	0.0000	-0.0094	519.04	1431.38
O -0.0015	0.0000	1.3351	673.82	1911.41
O 0.9758	0.0000	-0.6579	1058.09	3026.86
H -1.0306	0.0000	-0.4408	1140.68	3865.77
H -0.8987	0.0000	1.6833	1288.14	

P3_CH_3CH_2OH

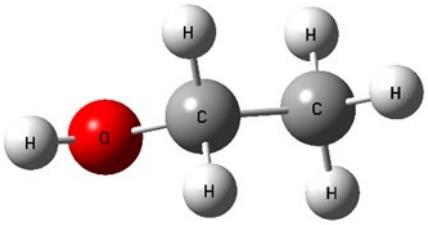

Method	Ee	E+ZPE	ΔH	ΔG
M06-2X-GD3/cc-pVTZ	-155.026326	-154.945732	-154.940458	-154.971165
CCSD(T)/cc-pVTZ	-154.79524	-154.714643	-154.709369	-154.740076
CBS-QB3	-154.84910	-154.770146	-154.764892	-154.795541
M06-2X-GD3/aug-cc-pVTZ	-155.02999	-154.949475	-154.944191	-154.974920
SVECV-f12	-155.01748	-154.936968	-154.931684	-154.962413

Coordinates (xyz)			Vibrations (cm^{-1})		
O -0.0031	-0.0202	-0.0001	228.37	1308.57	3146.41
C 0.0003	-0.0051	1.4196	272.04	1402.13	3148.49
C 1.4406	0.0007	1.8768	421.15	1456.77	3898.20
H -0.9087	-0.0241	-0.3157	823.12	1487.24	
H -0.5168	-0.8861	1.8122	917.73	1504.47	
H -0.5180	0.8834	1.7934	1050.14	1534.77	
H 1.4969	0.0123	2.9647	1134.21	3026.41	
H 1.9549	-0.8860	1.5090	1184.90	3056.50	
H 1.9538	0.8800	1.4902	1268.4106	3070.7859	

P4_CO

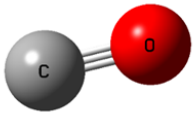

Method	Ee	E+ZPE	ΔH	ΔG
M06-2X-GD3/cc-pVTZ	-113.318864	-113.313681	-113.310377	-113.332793
CCSD(T)/cc-pVTZ	-113.15515	-113.149968	-113.146663	-113.169080
CBS-QB3	-113.18700	-113.181991	-113.178686	-113.201111
M06-2X-GD3/aug-cc-pVTZ	-113.32024	-113.315064	-113.311760	-113.334175
SVECV-f12	-113.30409	-113.298910	-113.295606	-113.318021

Coordinates (xyz)			Vibrations (cm^{-1})
C -0.7296	0.3460	0.0000	2272.16
O 0.3918	0.3460	0.0000	

P5_H_2CO

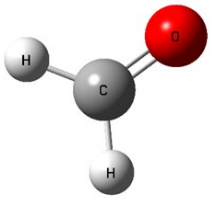

Method	Ee	E+ZPE	ΔH	ΔG
M06-2X-GD3/cc-pVTZ	-114.496616	-114.469571	-114.465762	-114.491216
CCSD(T)/cc-pVTZ	-114.33356	-114.306513	-114.302703	-114.328157
CBS-QB3	-114.37039	-114.344169	-114.340356	-114.365170
M06-2X-GD3/aug-cc-pVTZ	-114.49897	-114.471958	-114.468148	-114.492949
SVECV-f12	-114.48693	-114.459918	-114.456108	-114.480909

Coordinates (xyz)			Vibrations (cm^{-1})	
C -0.7259	-0.0881	0.0000	1213.56	2945.47
H -0.2031	-1.0595	0.0000	1273.49	3015.72
H -1.8285	-0.1214	0.0000	1539.88	
O -0.1280	0.9478	0.0000	1869.11	

P6_H_3CCHO

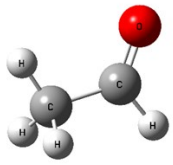

Method	Ee	E+ZPE	ΔH	ΔG
M06-2X-GD3/cc-pVTZ	-153.818126	-153.762145	-153.757316	-153.787070
CCSD(T)/cc-pVTZ	-153.58605	-153.530071	-153.525241	-153.554996
CBS-QB3	-153.63711	-153.582461	-153.577612	-153.607404
M06-2X-GD3/aug-cc-pVTZ	-153.82081	-153.764850	-153.760020	-153.789775
SVECV-f12	-153.80480	-153.748849	-153.744019	-153.773774

Coordinates (xyz)			Vibrations (cm^{-1})		
O 0.0093	0.0169	0.0022	157.71	1430.11	3179.89
C -0.0031	-0.0009	1.2019	513.53	1464.92	
C 1.2246	0.0000	2.0615	775.75	1474.84	
H -0.9671	-0.0194	1.7459	900.89	1866.02	
H 1.2202	-0.8864	2.6983	1138.36	2944.78	
H 2.1206	0.0188	1.4476	1145.76	3062.97	
H 1.2010	0.8670	2.7240	1380.55	3125.20	

P7_CH_3CH_3

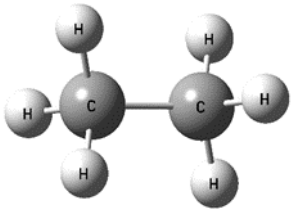

Method	Ee	E+ZPE	ΔH	ΔG
M06-2X-GD3/cc-pVTZ	-79.805555	-79.730457	-79.726029	-79.753562
CCSD(T)/cc-pVTZ	-79.67441	-79.599314	-79.594886	-79.622419
CBS-QB3	-79.70420	-79.630569	-79.626126	-79.653692
M06-2X-GD3/aug-cc-pVTZ	-79.80614	-79.731096	-79.726665	-79.754203
SVECV-f12	-79.80495	-79.729908	-79.725477	-79.753014

Coordinates (xyz)			Vibrations (cm^{-1})		
C -0.0008	-0.0014	-0.0022	306.77	1507.76	3143.38
C -0.0005	-0.0008	1.5215	822.00	1507.90	3143.80
H 1.0147	0.0046	-0.3970	823.33	1509.72	
H -0.5032	-0.8841	-0.3964	1019.82	1510.11	
H -0.5139	0.8748	-0.3971	1221.15	3065.97	
H -1.0160	-0.0068	1.9163	1221.53	3067.57	
H 0.5126	-0.8770	1.9164	1405.75	3120.02	
H 0.5019	0.8819	1.9158	1424.03	3120.56	

P8_CO_2					
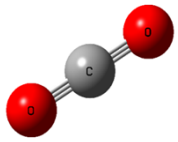					
Method		**Ee**	**E+ZPE**	**ΔH**	**ΔG**
M06-2X-GD3/cc-pVTZ		-188.591597	-188.579631	-188.576087	-188.600307
CCSD(T)/cc-pVTZ		-188.32673	-188.314765	-188.311221	-188.335442
CBS-QB3		-188.38367	-188.372065	-188.368492	-188.392762
M06-2X-GD3/aug-cc-pVTZ		-188.59421	-188.582263	-188.578721	-188.602938
SVECV-f12		-188.56753	-188.555590	-188.552048	-188.576265
Coordinates (xyz)			**Vibrations (cm^{-1})**		
C	-0.5363	0.3979 0.0000	694.18	2443.53	
O	-1.6915	0.3979 0.0000	694.18		
O	0.6189	0.3979 0.0000	1410.90		
P9_H_2					
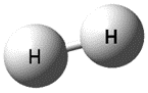					
Method		**Ee**	**E+ZPE**	**ΔH**	**ΔG**
M06-2X-GD3/cc-pVTZ		-1.168867	-1.158688	-1.155383	-1.170165
CCSD(T)/cc-pVTZ		-1.17233	-1.162149	-1.158844	-1.173626
CBS-QB3		-1.17605	-1.166078	-1.162773	-1.177568
M06-2X-GD3/aug-cc-pVTZ		-1.16888	-1.158706	-1.155402	-1.170184
SVECV-f12		-1.17417	-1.163997	-1.160693	-1.175475
Coordinates (xyz)			**Vibrations (cm^{-1})**		
H	0.0000	0.0000 0.0003	4467.08		
H	0.0000	0.0000 0.7393			

P10_H_3CCH_2O

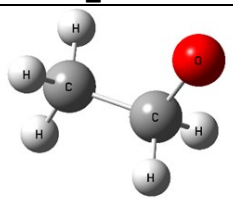

Method	Ee	E+ZPE	ΔH	ΔG
M06-2X-GD3/cc-pVTZ	-154.351415	-154.286239	-154.280925	-154.312377
CCSD(T)/cc-pVTZ	-154.11896	-154.053786	-154.048472	-154.079924
CBS-QB3	-154.16847	-154.105003	-154.099582	-154.131348
M06-2X-GD3/aug-cc-pVTZ	-154.35434	-154.288907	-154.283766	-154.314787
SVECV-f12	-154.33788	-154.272448	-154.267307	-154.298327

Coordinates (xyz)			Vibrations (cm^{-1})		
O -0.0031	-0.0202	-0.0001	228.37	1308.57	3146.41
C 0.0003	-0.0051	1.4196	272.04	1402.13	3148.49
C 1.4406	0.0007	1.8768	421.15	1456.77	3898.20
H -0.9087	-0.0241	-0.3157	823.12	1487.24	
H -0.5168	-0.8861	1.8122	917.73	1504.47	
H -0.5180	0.8834	1.7934	1050.14	1534.77	
H 1.4969	0.0123	2.9647	1134.21	3026.41	
H 1.9549	-0.8860	1.5090	1184.90	3056.50	
H 1.9538	0.8800	1.4902	1268.4106	3070.7859	

P11_HCO

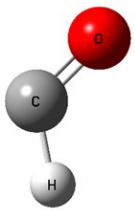

Method	Ee	E+ZPE	ΔH	ΔG
M06-2X-GD3/cc-pVTZ	-113.847274	-113.834000	-113.830198	-113.855650
CCSD(T)/cc-pVTZ	-113.68376	-113.670484	-113.666682	-113.692134
CBS-QB3	-113.71755	-113.704757	-113.700954	-113.726423
M06-2X-GD3/aug-cc-pVTZ	-113.84942	-113.836155	-113.832353	-113.857801
SVECV-f12	-113.83571	-113.822442	-113.818640	-113.844089

Coordinates (xyz)			Vibrations (cm^{-1})
C -0.4198	0.0140	0.0000	1101.68
H 0.0810	-0.9881	0.0000	1993.52
O 0.1495	1.0337	0.0000	2728.52

P12_H_3CCH_2

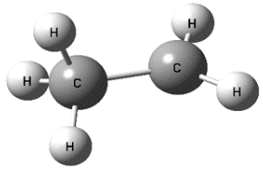

Method	**Ee**	**E+ZPE**	**ΔH**	**ΔG**
M06-2X-GD3/cc-pVTZ	-79.135332	-79.075732	-79.070817	-79.099850
CCSD(T)/cc-pVTZ	-79.00246	-78.942857	-78.931981	-78.960523
CBS-QB3	-79.02996	-78.971547	-78.966622	-78.995735
M06-2X-GD3/aug-cc-pVTZ	-79.13627	-79.076695	-79.071775	-79.100824
SVECV-f12	-79.13176	-79.072180	-79.067260	-79.096309

Coordinates (xyz)			**Vibrations (cm^{-1})**		
C 0.0000	0.0457	0.0175	122.32	1471.37	3274.91
C 0.0000	0.0137	1.5013	445.97	1487.41	
H 0.9231	-0.0243	-0.5364	808.39	1488.78	
H -0.9231	-0.0243	-0.5364	982.08	3004.73	
H 0.0000	-1.0138	1.8868	1080.76	3084.41	
H 0.8833	0.5015	1.9136	1194.61	3127.54	
H -0.8833	0.5015	1.9136	1402.98	3175.95	

P13_OCHO

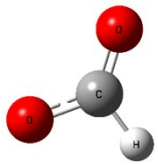

Method	**Ee**	**E+ZPE**	**ΔH**	**ΔG**
M06-2X-GD3/cc-pVTZ	-189.073639	-189.054186	-189.050007	-189.078790
CCSD(T)/cc-pVTZ	-188.81007	-188.790621	-188.786443	-188.815226
CBS-QB3	-188.86996	-188.854533	-188.849856	-188.879619
M06-2X-GD3/aug-cc-pVTZ	-189.07690	-189.057451	-189.053277	-189.082054
SVECV-f12	-189.05067	-189.031224	-189.027050	-189.055827

Coordinates (xyz)			**Vibrations (cm^{-1})**	
C -0.0380	0.0000	-0.0641	390.20	1811.98
H 0.0991	0.0000	1.0372	1013.02	2934.52
O 1.1659	0.0000	-0.6027	1036.52	
O -1.0784	0.0000	-0.6445	1351.63	

P14_H_2O

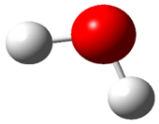

Method	**Ee**	**E+ZPE**	**ΔH**	**ΔG**
M06-2X-GD3/cc-pVTZ	-76.425276	-76.403683	-76.399904	-76.421317
CCSD(T)/cc-pVTZ	-76.33218	-76.310584	-76.306805	-76.333475
CBS-QB3	-76.35858	-76.337480	-76.333700	-76.355127
M06-2X-GD3/aug-cc-pVTZ	-76.43011	-76.408556	-76.404776	-76.426189
SVECV-f12	-76.42668	-76.405126	-76.401346	-76.422759

Coordinates (xyz)			**Vibrations (cm^{-1})**
O 0.0000	0.0000	0.1121	1619.68
H 0.0000	0.7626	-0.4699	3868.51
H 0.0000	-0.7626	-0.4699	3971.49

P15_HC=CH

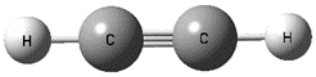

Method	**Ee**	**E+ZPE**	**ΔH**	**ΔG**
M06-2X-GD3/cc-pVTZ	-77.324507	-77.298820	-77.294740	-77.314330
CCSD(T)/cc-pVTZ	-77.18717	-77.161483	-77.157403	-77.176993
CBS-QB3	-77.21414	-77.189173	-77.185023	-77.204697
M06-2X-GD3/aug-cc-pVTZ	-77.32531	-77.299646	-77.295568	-77.314498
SVECV-f12	-77.31462	-77.288958	-77.284880	-77.303810

Coordinates (xyz)			**Vibrations (cm^{-1})**	
C 0.0007	0.0001	0.0000	707.93	3422.24
C -0.0007	-0.0001	1.1939	707.93	3535.49
H 0.0003	0.0000	-1.0629	790.48	
H -0.0036	-0.0004	2.2568	2102.67	

Table A2-1: Calculated relative energies (kJ mol-1) for the EF thermal decomposition

ROUTE	REACTION	ENERGY	M06-2X-GD3/TZ		CCSD(T)/TZ		CBS-QB3	
			TS	Products	TS	Products	TS	Products
k_{O-C} (7)	$H_3CCH_2OCHO \rightarrow H_3CCH_2O + HCO$	**ΔE**	-	454.01	-	439.56	-	452.71
		Δ(E+ZPE)	-	419.22	-	404.77	-	418.12
		ΔH	-	426.17	-	411.72	-	424.94
		ΔG	-	368.85	-	354.41	-	368.24
k_{C-O} (8)	$H_3CCH_2OCHO \rightarrow H_3CCH_2 + OCHO$	**ΔE**	-	427.01	-	413.80	-	416.22
		Δ(E+ZPE)	-	393.80	-	380.60	-	375.27
		ΔH	-	400.70	-	403.14	-	383.08
		ΔG	-	340.99	-	344.72	-	322.08
k_1	$H_3CCH_2OCHO \rightarrow H_2C=CH_2 + HOCHO$	**ΔE**	230.15	88.61	230.14	78.66	233.17	80.24
		Δ(E+ZPE)	210.53	72.98	210.52	63.04	213.27	65.47
		ΔH	210.13	77.21	210.11	67.26	213.49	69.35
		ΔG	210.82	26.72	210.80	16.77	208.67	20.20
	$H_2C=CH_2 + HOCHO \rightarrow H_2C=CH_2 + H_2O + CO$	**ΔE**	405.13	145.44	385.15	116.25	387.37	120.59
		Δ(E+ZPE)	367.83	109.85	347.85	80.67	352.37	86.38
		ΔH	373.89	121.91	353.91	92.73	358.02	98.07
		ΔG	319.84	30.28	299.87	-12.70	305.31	7.79
	$H_2C=CH_2 + HOCHO \rightarrow H_2C=CH_2 + H_2 + CO_2$	**ΔE**	407.02	102.58	394.22	85.45	398.91	83.46
		Δ(E+ZPE)	366.10	54.84	353.31	37.72	358.47	37.36
		ΔH	370.36	66.28	357.57	49.16	362.43	48.50
		ΔG	320.04	-12.68	307.25	-29.80	313.36	-29.21

ROUTE	REACTION	ENERGY	M06-2X-GD3/TZ		CCSD(T)/TZ		CBS-QB3	
			TS	Products	TS	Products	TS	Products
k_2	$H_3CCH_2OCHO \rightarrow H_3CCH_2OH + CO$	**ΔE**	317.14	69.37	303.44	51.86	307.14	58.69
		Δ(E+ZPE)	296.51	53.81	282.87	36.31	288.05	44.31
		ΔH	298.68	59.35	285.02	41.85	290.05	49.38
		ΔG	292.32	11.96	278.80	-5.54	284.03	3.61
	$H_3CCH_2OH + CO \rightarrow H_3CCHO + H_2 + CO$	**ΔE**	453.91	172.64	439.15	148.63	444.33	153.02
		Δ(E+ZPE)	414.31	119.19	399.56	95.18	405.16	101.04
		ΔH	418.94	132.23	404.18	108.23	409.50	113.72
		ΔG	373.29	48.54	358.53	24.53	365.08	31.36
k_3	$H_3CCH_2OCHO \rightarrow H_2CO + H_3CCHO$	**ΔE**	322.28	149.31	321.14	132.67	318.06	133.75
		Δ(E+ZPE)	304.90	126.53	303.76	109.89	299.86	111.28
		ΔH	304.29	132.23	303.15	115.59	299.29	116.62
		ΔG	306.09	79.37	304.95	62.73	301.63	66.82
k_4	$H_3CCH_2OCHO \rightarrow H_3CCH_3 + CO_2$	**ΔE**	370.86	-67.06	356.78	-81.40	351.07	-77.25
		Δ(E+ZPE)	352.48	-79.23	338.40	109.89	330.81	-88.27
		ΔH	354.15	-75.29	340.08	115.59	332.51	-84.63
		ΔG	348.68	-119.08	334.60	62.73	327.83	-127.15

ROUTE	REACTION	ENERGY	M06-2X-GD3/TZ		CCSD(T)/TZ		CBS-QB3	
			TS	Products	TS	Products	TS	Products
k_5	$H_3CCH_2OCHO \rightarrow H_3CCHO + HC{=}OH$	**ΔE**	466.14	363.46	452.29	348.52	452.79	354.55
		Δ(E+ZPE)	440.57	340.86	426.72	325.93	426.92	332.65
		ΔH	441.34	346.61	427.49	331.68	427.71	338.05
		ΔG	439.78	293.57	425.93	278.63	426.80	286.33
	$H_3CCHO + HC{=}OH \rightarrow H_3CCHO + H_2CO$	**ΔE**	511.04	149.31	493.54	132.67	498.41	133.75
		Δ(E+ZPE)	472.28	126.53	454.79	109.89	460.37	111.28
		ΔH	478.21	132.23	460.71	115.59	465.92	116.62
		ΔG	424.90	79.37	407.40	62.73	413.97	66.82
k_6	$H_3CCH_2OCHO \rightarrow H_2C{=}CH_2 + H_2 + CO_2$	**ΔE**	338.40	102.58	332.85	85.45	329.32	83.46
		Δ(E+ZPE)	308.82	54.84	303.27	37.72	301.01	37.36
		ΔH	309.11	66.28	303.55	49.16	301.18	48.50
		ΔG	308.33	-12.68	302.78	-29.80	301.28	-29.21
	$H_2C{=}CH_2 + H_2 + CO_2 \rightarrow HC{=}CH + 2H_2 + CO_2$	**ΔE**	580.58	309.21	578.30	292.96	575.98	284.96
		Δ(E+ZPE)	507.87	220.76	505.59	204.51	504.00	198.54
		ΔH	519.86	241.15	517.58	224.90	515.72	218.77
		ΔG	439.92	140.59	437.64	124.34	437.00	119.28

ROUTE	REACTION	ENERGY	M06-2X-GD3/a-Tz		SVECV-f12	
			TS	Products	TS	Products
k_{O-C} (7)	$H_3CCH_2OCHO \rightarrow H_3CCH_2O + HCO$	**ΔE**	-	451.13	-	445.87
		Δ(E+ZPE)	-	417.22	-	411.96
		ΔH	-	423.70	-	418.44
		ΔG	-	367.56	-	362.30
k_{C-O} (8)	$H_3CCH_2OCHO \rightarrow H_3CCH_2 + OCHO$	**ΔE**	-	426.42	-	422.66
		Δ(E+ZPE)	-	393.37	-	389.61
		ΔH	-	400.25	-	396.48
		ΔG	-	340.54	-	336.78
k_1	$H_3CCH_2OCHO \rightarrow H_2C=CH_2 + HOCHO$	**ΔE**	229.10	87.09	228.23	79.15
		Δ(E+ZPE)	209.40	71.27	208.53	63.33
		ΔH	208.96	75.50	208.09	67.56
		ΔG	209.80	26.73	208.94	18.79
	$H_2C=CH_2 + HOCHO \rightarrow H_2C=CH_2 + H_2O + CO$	**ΔE**	399.46	137.56	382.75	118.60
		Δ(E+ZPE)	361.93	101.90	345.23	82.94
		ΔH	368.08	113.95	351.37	94.99
		ΔG	315.57	24.07	298.86	5.10
	$H_2C=CH_2 + HOCHO \rightarrow H_2C=CH_2 + H_2 + CO_2$	**ΔE**	406.07	104.10	396.52	89.86
		Δ(E+ZPE)	365.02	56.35	355.47	42.11
		ΔH	369.26	67.78	359.72	53.54
		ΔG	320.68	-9.43	311.13	-23.67

ROUTE	REACTION	ENERGY	M06-2X-GD3/a-Tz		SVECV-f12	
			TS	Products	TS	Products
k_2	$H_3CCH_2OCHO \rightarrow H_3CCH_2OH + CO$	**ΔE**	316.48	66.60	305.47	57.37
		Δ(E+ZPE)	295.74	51.02	284.73	41.80
		ΔH	297.98	56.57	286.97	47.35
		ΔG	291.41	9.16	280.40	-0.06
	$H_3CCH_2OH + CO \rightarrow H_3CCHO + H_2 + CO$	**ΔE**	449.24	172.40	441.42	158.46
		Δ(E+ZPE)	409.81	119.07	402.00	105.13
		ΔH	414.42	132.10	406.61	118.16
		ΔG	368.80	48.44	360.99	34.50
k_3	$H_3CCH_2OCHO \rightarrow H_2CO + H_3CCHO$	**ΔE**	319.33	146.54	319.29	135.69
		Δ(E+ZPE)	301.92	123.83	301.89	112.98
		ΔH	301.34	129.52	301.31	118.66
		ΔG	303.09	78.40	303.06	67.54
k_4	$H_3CCH_2OCHO \rightarrow H_3CCH_3 + CO_2$	**ΔE**	367.01	-65.00	354.24	-76.33
		Δ(E+ZPE)	348.59	-77.16	335.81	-88.48
		ΔH	350.30	-73.22	337.53	-84.55
		ΔG	344.70	-116.98	331.92	-128.31

ROUTE	REACTION	ENERGY	M06-2X-GD3/a-Tz		SVECV-f12	
			TS	Products	TS	Products
k_5	$H_3CCH_2OCHO \rightarrow H_3CCHO + HC{=}OH$	**ΔE**	464.57	359.10	454.50	353.30
		Δ(E+ZPE)	439.05	336.57	428.98	330.77
		ΔH	439.83	342.32	429.77	336.52
		ΔG	438.24	289.30	428.18	283.50
	$H_3CCHO + HC{=}OH \rightarrow H_3CCHO + H_2CO$	**ΔE**	506.67	146.54	497.25	135.69
		Δ(E+ZPE)	467.85	123.83	458.43	112.98
		ΔH	473.78	129.52	464.36	118.66
		ΔG	420.48	78.40	411.06	67.54
k_6	$H_3CCH_2OCHO \rightarrow H_2C{=}CH_2 + H_2 + CO_2$	**ΔE**	336.25	104.10	329.83	89.86
		Δ(E+ZPE)	306.40	56.35	299.97	42.11
		ΔH	306.75	67.78	300.32	53.54
		ΔG	305.82	-9.43	299.39	-23.67
	$H_2C{=}CH_2 + H_2 + CO_2 \rightarrow HC{=}CH + 2H_2 + CO_2$	**ΔE**	579.14	310.61	579.22	296.45
		Δ(E+ZPE)	506.47	222.25	506.55	208.09
		ΔH	518.45	242.61	518.53	228.44
		ΔG	438.54	143.82	438.62	129.66

Proposed mechanism and schematic potential energy surfaces at the M06-2X-GD3/aug-cc-pVTZ level of theory for of Ethyl Formate thermal decomposition

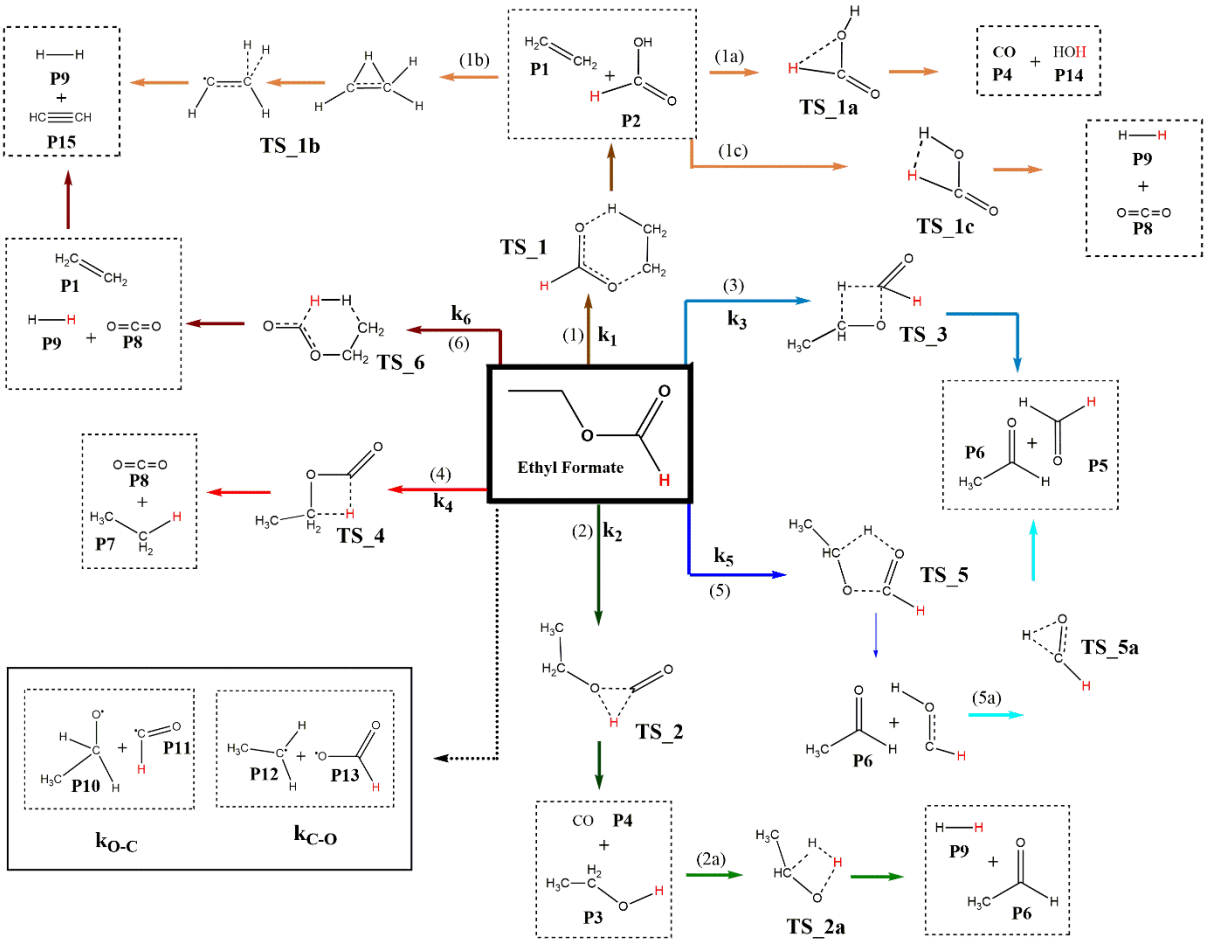

Figure A2-15: Theoretical mechanism for the unimolecular decomposition of EF. The formyl hydrogen is shown in red.

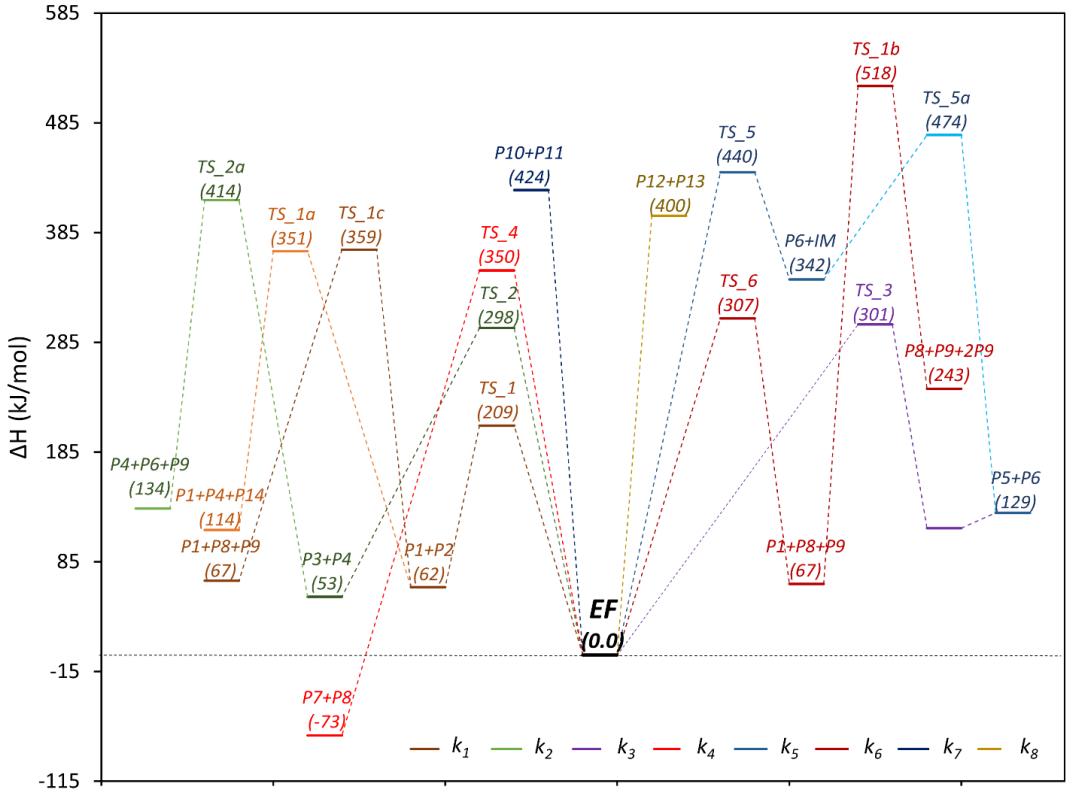

Figure A2-16: Enthalpy diagram (298 K) for the unimolecular decomposition of EF at the M06-2X-GD3/aug-cc-pVTZ level of theory.

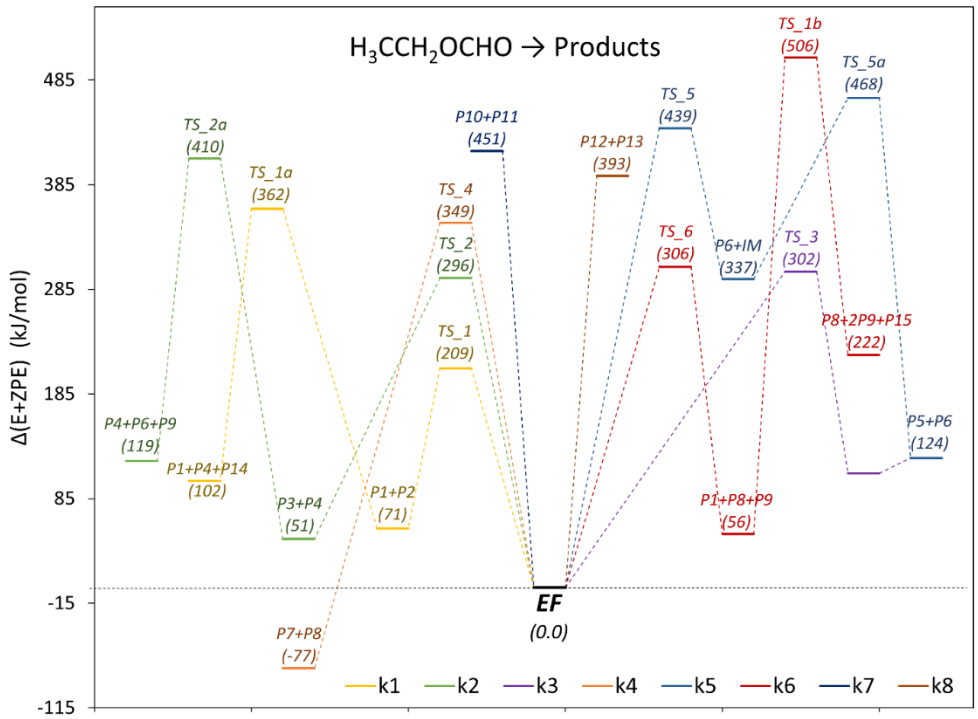

Figure A2-17: Potential Energy diagram for the ethyl formate thermal decomposition at the M06-2X-GD3/aug-cc-pVTZ level of theory. (ZPE corrected)

Kinetics

Calculated temperature dependent rate coefficients for the unimolecular decomposition of ethyl formate over the 300–2500 K temperature range.

Canonical transition state theory (CTST) with Eckart asymmetric tunnelling correction[84] for molecular pathways R1-R6.

The high-pressure rate constant is the average rate constant at pressures high enough so that differences of the actual population distribution from the thermal Boltzmann distribution are negligible. The resulting expression for k∞ is the same as canonical TST. The rate coefficients for molecular pathways were calculated using the thermochemical parameters obtained for the transition state determined for each path.

Canonical variational transition state theory (CVTST) for barrierless pathways R7 and R8.

Rate constants in canonical variational transition state theory are calculated via RRKM theory. Constrained geometry optimizations were carried out at fixed C–O and O–C bond distances depending on the case (see figures S8 and S9), starting with 30 points with a step size of 0.03 Å. The optimized geometries were used at each point to obtain the rotational constants, the vibrational ZPE corrections and frequencies orthogonal to the reaction path. The CVTST rate constant for each temperature is identified as the minimum "trial" CTST rate constant as a function of distance along the reaction coordinate.[85–87]

Values for temperature dependent rate coefficients over the 300–2500 K temperature range.

Table A2-2: M06-2X-GD3/cc-pVTZ

T	k_1	k_2	k_3	k_4	k_5	k_6	k_7	k_8
300	3.16E-22	4.11E-33	4.14E-40	2.65E-47	1.23E-59	5.72E-40	4.08E-57	3.88E-56
400	3.60E-14	8.92E-24	4.96E-27	3.45E-32	9.88E-43	4.89E-27	9.16E-39	8.30E-39
500	7.73E-09	1.54E-16	4.81E-19	6.42E-23	1.30E-31	5.65E-19	9.56E-28	2.24E-28
600	3.54E-05	1.98E-11	1.15E-13	1.12E-16	5.58E-24	1.62E-13	2.13E-20	2.10E-21
700	1.62E-02	1.06E-07	8.46E-10	3.48E-12	1.86E-18	1.41E-09	3.76E-15	2.06E-16
800	1.70E+00	7.13E-05	7.01E-07	8.48E-09	2.78E-14	1.35E-06	3.23E-11	1.16E-12
818	3.61E+00	2.05E-04	2.08E-06	2.99E-08	1.32E-13	4.11E-06	1.39E-10	4.66E-12
900	6.57E+01	1.18E-02	1.34E-04	3.76E-06	5.13E-11	2.93E-04	3.69E-08	9.66E-10
990	9.58E+02	4.99E-01	6.23E-03	3.22E-04	1.25E-08	1.50E-02	6.15E-06	1.30E-07
1000	1.25E+03	7.27E-01	9.16E-03	5.03E-04	2.16E-08	2.23E-02	1.03E-05	2.12E-07
1200	1.10E+05	3.67E+02	5.35E+00	8.06E-01	1.97E-04	1.56E+01	4.70E-02	6.94E-04
1250	2.70E+05	1.29E+03	1.93E+01	3.55E+00	1.23E-03	5.82E+01	2.53E-01	3.51E-03
1300	6.21E+05	4.09E+03	6.29E+01	1.40E+01	6.66E-03	1.97E+02	1.19E+00	1.57E-02
1347	1.29E+06	1.13E+04	1.77E+02	4.61E+01	2.92E-02	5.72E+02	4.62E+00	5.79E-02
1400	2.77E+06	3.26E+04	5.23E+02	1.62E+02	1.37E-01	1.75E+03	1.91E+01	2.28E-01
1500	1.02E+07	1.98E+05	3.30E+03	1.36E+03	1.90E+00	1.17E+04	2.10E+02	2.31E+00
1600	3.19E+07	9.64E+05	1.66E+04	8.78E+03	1.91E+01	6.21E+04	1.70E+03	1.76E+01
1700	8.79E+07	3.92E+06	6.92E+04	4.58E+04	1.47E+02	2.72E+05	1.08E+04	1.06E+02
1800	2.17E+08	1.37E+07	2.47E+05	1.99E+05	9.00E+02	1.02E+06	5.56E+04	5.21E+02
1900	4.89E+08	4.18E+07	7.74E+05	7.42E+05	4.58E+03	3.31E+06	2.41E+05	2.17E+03
2000	1.02E+09	1.15E+08	2.17E+06	2.43E+06	1.98E+04	9.62E+06	8.97E+05	7.84E+03
2100	1.98E+09	2.87E+08	5.51E+06	7.14E+06	7.49E+04	2.53E+07	2.95E+06	2.50E+04
2200	3.62E+09	6.61E+08	1.29E+07	1.90E+07	2.51E+05	6.11E+07	8.67E+06	7.19E+04
2300	6.30E+09	1.42E+09	2.80E+07	4.65E+07	7.58E+05	1.37E+08	2.32E+07	1.88E+05
2400	1.05E+10	2.86E+09	5.72E+07	1.06E+08	2.09E+06	2.87E+08	5.71E+07	4.52E+05
2500	1.68E+10	5.45E+09	1.10E+08	2.26E+08	5.32E+06	5.67E+08	1.31E+08	1.01E+06

Table A2-3: CCSD(T)/cc-pVTZ

T	k_1	k_2	k_3	k_4	k_5	k_6	k_7	k_8
300	5.95E-23	8.39E-31	6.57E-40	7.49E-45	2.90E-57	5.33E-39	1.56E-54	2.57E-29
400	3.30E-14	5.30E-22	6.98E-27	2.38E-30	6.28E-41	2.60E-26	8.45E-37	1.08E-18
500	1.05E-08	4.08E-15	6.33E-19	1.90E-21	3.63E-30	2.15E-18	3.77E-26	2.76E-12
600	5.86E-05	3.04E-10	1.44E-13	1.89E-15	8.95E-23	4.93E-13	4.76E-19	5.39E-08
700	3.06E-02	1.10E-06	1.03E-09	3.91E-11	2.01E-17	3.67E-09	5.62E-14	6.42E-05
800	3.55E+00	5.53E-04	8.32E-07	7.04E-08	2.23E-13	3.12E-06	3.56E-10	1.32E-02
818	7.68E+00	1.52E-03	2.46E-06	2.37E-07	1.01E-12	9.30E-06	1.46E-09	3.12E-02
900	1.49E+02	7.32E-02	1.56E-04	2.47E-05	3.27E-10	6.16E-04	3.22E-07	8.41E-01
990	2.31E+03	2.62E+00	7.16E-03	1.78E-03	6.71E-08	2.95E-02	4.52E-05	1.74E+01
1000	3.04E+03	3.75E+00	1.05E-02	2.74E-03	1.14E-07	4.34E-02	7.41E-05	2.35E+01
1200	2.96E+05	1.44E+03	6.00E+00	3.31E+00	7.88E-04	2.72E+01	2.56E-01	3.52E+03
1250	7.47E+05	4.77E+03	2.15E+01	1.38E+01	4.65E-03	9.92E+01	1.30E+00	9.60E+03
1300	1.76E+06	1.45E+04	6.99E+01	5.13E+01	2.40E-02	3.29E+02	5.83E+00	2.43E+04
1347	3.72E+06	3.81E+04	1.96E+02	1.62E+02	1.00E-01	9.39E+02	2.16E+01	5.45E+04
1400	8.15E+06	1.05E+05	5.77E+02	5.42E+02	4.51E-01	2.82E+03	8.48E+01	1.27E+05
1500	3.11E+07	5.91E+05	3.61E+03	4.20E+03	5.78E+00	1.83E+04	8.61E+02	5.35E+05
1600	1.01E+08	2.69E+06	1.81E+04	2.53E+04	5.41E+01	9.43E+04	6.52E+03	1.88E+06
1700	2.86E+08	1.03E+07	7.50E+04	1.24E+05	3.90E+02	4.03E+05	3.88E+04	5.72E+06
1800	7.24E+08	3.39E+07	2.67E+05	5.10E+05	2.27E+03	1.47E+06	1.89E+05	1.54E+07
1900	1.67E+09	9.91E+07	8.32E+05	1.81E+06	1.10E+04	4.71E+06	7.79E+05	3.73E+07
2000	3.56E+09	2.61E+08	2.32E+06	5.68E+06	4.56E+04	1.34E+07	2.78E+06	8.27E+07
2100	7.06E+09	6.27E+08	5.88E+06	1.60E+07	1.66E+05	3.48E+07	8.76E+06	1.70E+08
2200	1.32E+10	1.39E+09	1.37E+07	4.10E+07	5.35E+05	8.27E+07	2.49E+07	3.27E+08
2300	2.34E+10	2.89E+09	2.97E+07	9.71E+07	1.56E+06	1.83E+08	6.43E+07	5.92E+08
2400	3.96E+10	5.66E+09	6.05E+07	2.14E+08	4.18E+06	3.79E+08	1.54E+08	1.02E+09
2500	6.43E+10	1.05E+10	1.17E+08	4.44E+08	1.04E+07	7.41E+08	3.42E+08	1.66E+09

Table A2-4: CBS-QB3

T	k_1	k_2	k_3	k_4	k_5	k_6	k_7	k_8
300	1.98E-23	1.04E-31	3.13E-39	1.56E-43	1.86E-57	1.32E-38	3.91E-53	7.57E-45
400	1.44E-14	1.12E-22	2.25E-26	2.33E-29	5.65E-41	5.13E-26	1.52E-36	2.58E-30
500	5.40E-09	1.18E-15	1.62E-18	1.18E-20	3.43E-30	3.70E-18	1.48E-26	1.45E-21
600	3.37E-05	1.08E-10	3.14E-13	8.64E-15	8.58E-23	7.77E-13	7.00E-20	1.22E-15
700	1.91E-02	4.51E-07	2.01E-09	1.44E-10	1.94E-17	5.41E-09	4.21E-15	1.42E-10
800	2.35E+00	2.54E-04	1.50E-06	2.20E-07	2.16E-13	4.38E-06	1.64E-11	2.27E-06
818	5.12E+00	7.09E-04	4.36E-06	7.22E-07	9.78E-13	1.30E-05	6.24E-11	1.07E-05
900	1.03E+02	3.66E-02	2.63E-04	6.81E-05	3.18E-10	8.33E-04	1.03E-08	3.59E-03
990	1.65E+03	1.39E+00	1.15E-02	4.48E-03	6.55E-08	3.88E-02	1.12E-06	6.39E-01
1000	2.19E+03	2.01E+00	1.68E-02	6.81E-03	1.12E-07	5.70E-02	1.79E-06	1.06E+00
1200	2.25E+05	8.57E+02	8.87E+00	7.07E+00	7.72E-04	3.41E+01	4.17E-03	3.34E+03
1250	5.73E+05	2.90E+03	3.13E+01	2.85E+01	4.56E-03	1.23E+02	1.97E-02	1.53E+04
1300	1.36E+06	8.95E+03	1.00E+02	1.04E+02	2.35E-02	4.06E+02	8.26E-02	6.00E+04
1347	2.90E+06	2.40E+04	2.77E+02	3.20E+02	9.87E-02	1.15E+03	2.89E-01	1.92E+05
1400	6.43E+06	6.74E+04	8.06E+02	1.04E+03	4.44E-01	3.42E+03	1.07E+00	6.31E+05
1500	2.49E+07	3.90E+05	4.94E+03	7.72E+03	5.69E+00	2.19E+04	9.86E+00	4.35E+06
1600	8.18E+07	1.82E+06	2.42E+04	4.48E+04	5.33E+01	1.12E+05	6.89E+01	2.13E+07
1700	2.35E+08	7.12E+06	9.88E+04	2.12E+05	3.85E+02	4.73E+05	3.84E+02	7.96E+07
1800	6.03E+08	2.40E+07	3.46E+05	8.46E+05	2.24E+03	1.71E+06	1.77E+03	2.37E+08
1900	1.40E+09	7.14E+07	1.06E+06	2.93E+06	1.09E+04	5.43E+06	6.93E+03	5.85E+08
2000	3.01E+09	1.91E+08	2.93E+06	8.96E+06	4.51E+04	1.54E+07	2.37E+04	1.24E+09
2100	6.03E+09	4.66E+08	7.35E+06	2.47E+07	1.64E+05	3.96E+07	7.21E+04	2.29E+09
2200	1.13E+10	1.05E+09	1.70E+07	6.21E+07	5.29E+05	9.36E+07	1.98E+05	3.79E+09
2300	2.02E+10	2.21E+09	3.64E+07	1.45E+08	1.55E+06	2.06E+08	4.96E+05	5.71E+09
2400	3.45E+10	4.36E+09	7.36E+07	3.13E+08	4.14E+06	4.24E+08	1.15E+06	7.94E+09
2500	5.63E+10	8.18E+09	1.41E+08	6.40E+08	1.03E+07	8.26E+08	2.47E+06	1.03E+10

Table A2-5: M06-2X-GD3/aug-cc-pVTZ

T	k_1	k_2	k_3	k_4	k_5	k_6	k_7	k_8
300	5.19E-22	5.06E-33	1.33E-39	1.07E-46	1.33E-62	1.31E-39	3.89E-60	4.68E-56
400	5.45E-14	1.19E-23	1.22E-26	1.09E-31	5.97E-44	1.01E-26	8.79E-42	9.65E-39
500	1.11E-08	2.05E-16	9.95E-19	1.65E-22	1.76E-32	1.04E-18	9.78E-31	2.54E-28
600	4.92E-05	2.59E-11	2.11E-13	2.51E-16	9.38E-25	2.75E-13	2.36E-23	2.35E-21
700	2.20E-02	1.36E-07	1.44E-09	7.01E-12	3.39E-19	2.25E-09	4.55E-18	2.29E-16
800	2.26E+00	9.08E-05	1.12E-06	1.58E-08	5.27E-15	2.06E-06	4.25E-14	1.28E-12
818	4.79E+00	2.61E-04	3.29E-06	5.51E-08	2.51E-14	6.22E-06	1.86E-13	5.14E-12
900	8.62E+01	1.49E-02	2.04E-04	6.59E-06	9.95E-12	4.31E-04	5.25E-11	1.06E-09
990	1.24E+03	6.26E-01	9.15E-03	5.40E-04	2.45E-09	2.15E-02	9.37E-09	1.42E-07
1000	1.63E+03	9.11E-01	1.34E-02	8.39E-04	4.26E-09	3.18E-02	1.57E-08	2.31E-07
1200	1.40E+05	4.55E+02	7.39E+00	1.25E+00	3.95E-05	2.13E+01	8.28E-05	7.55E-04
1250	3.43E+05	1.59E+03	2.63E+01	5.41E+00	2.48E-04	7.88E+01	4.60E-04	3.81E-03
1300	7.87E+05	5.05E+03	8.49E+01	2.10E+01	1.35E-03	2.65E+02	2.24E-03	1.70E-02
1347	1.63E+06	1.39E+04	2.36E+02	6.86E+01	5.93E-03	7.63E+02	8.93E-03	6.28E-02
1400	3.49E+06	4.00E+04	6.92E+02	2.37E+02	2.80E-02	2.32E+03	3.80E-02	2.46E-01
1500	1.28E+07	2.42E+05	4.29E+03	1.95E+03	3.91E-01	1.53E+04	4.42E-01	2.50E+00
1600	3.99E+07	1.18E+06	2.13E+04	1.24E+04	3.95E+00	8.04E+04	3.79E+00	1.90E+01
1700	1.10E+08	4.77E+06	8.76E+04	6.34E+04	3.05E+01	3.49E+05	2.52E+01	1.14E+02
1800	2.70E+08	1.66E+07	3.09E+05	2.72E+05	1.88E+02	1.29E+06	1.36E+02	5.61E+02
1900	6.06E+08	5.07E+07	9.59E+05	1.00E+06	9.63E+02	4.18E+06	6.16E+02	2.33E+03
2000	1.26E+09	1.39E+08	2.66E+06	3.24E+06	4.19E+03	1.21E+07	2.40E+03	8.42E+03
2100	2.44E+09	3.47E+08	6.70E+06	9.41E+06	1.59E+04	3.15E+07	8.20E+03	2.69E+04
2200	4.46E+09	7.97E+08	1.56E+07	2.48E+07	5.35E+04	7.56E+07	2.50E+04	7.71E+04
2300	7.75E+09	1.71E+09	3.36E+07	6.02E+07	1.62E+05	1.69E+08	6.92E+04	2.01E+05
2400	1.29E+10	3.44E+09	6.81E+07	1.36E+08	4.49E+05	3.52E+08	1.75E+05	4.84E+05
2500	2.06E+10	6.54E+09	1.31E+08	2.87E+08	1.15E+06	6.93E+08	4.09E+05	1.08E+06

Table A2-6: SVECV-F12

T	k_1	k_2	k_3	k_4	k_5	k_6	k_7	k_8
300	7.67E-22	3.39E-31	1.36E-39	1.79E-44	7.35E-61	1.77E-38	3.20E-59	2.06E-55
400	7.09E-14	3.20E-22	1.23E-26	5.05E-30	1.23E-42	7.00E-26	4.23E-41	2.88E-38
500	1.37E-08	2.89E-15	1.00E-18	3.57E-21	1.98E-31	4.88E-18	3.41E-30	6.02E-28
600	5.85E-05	2.36E-10	2.13E-13	3.25E-15	7.05E-24	9.96E-13	6.64E-23	4.76E-21
700	2.55E-02	9.03E-07	1.44E-09	6.29E-11	1.91E-18	6.80E-09	1.10E-17	4.13E-16
800	2.57E+00	4.76E-04	1.13E-06	1.08E-07	2.39E-14	5.41E-06	9.13E-14	2.12E-12
818	5.44E+00	1.31E-03	3.30E-06	3.60E-07	1.10E-13	1.60E-05	3.92E-13	8.42E-12
900	9.67E+01	6.51E-02	2.05E-04	3.64E-05	3.82E-11	1.02E-03	1.03E-10	1.65E-09
990	1.38E+03	2.39E+00	9.19E-03	2.55E-03	8.33E-09	4.69E-02	1.73E-08	2.10E-07
1000	1.81E+03	3.43E+00	1.35E-02	3.90E-03	1.43E-08	6.89E-02	2.88E-08	3.41E-07
1200	1.52E+05	1.37E+03	7.41E+00	4.49E+00	1.08E-04	4.05E+01	1.36E-04	1.03E-03
1250	3.73E+05	4.59E+03	2.63E+01	1.85E+01	6.52E-04	1.46E+02	7.40E-04	5.11E-03
1300	8.53E+05	1.40E+04	8.51E+01	6.85E+01	3.42E-03	4.80E+02	3.54E-03	2.25E-02
1347	1.76E+06	3.71E+04	2.37E+02	2.15E+02	1.46E-02	1.36E+03	1.38E-02	8.19E-02
1400	3.76E+06	1.03E+05	6.94E+02	7.11E+02	6.66E-02	4.03E+03	5.78E-02	3.17E-01
1500	1.37E+07	5.86E+05	4.30E+03	5.44E+03	8.77E-01	2.57E+04	6.52E-01	3.15E+00
1600	4.26E+07	2.70E+06	2.13E+04	3.24E+04	8.41E+00	1.30E+05	5.44E+00	2.35E+01
1700	1.17E+08	1.04E+07	8.78E+04	1.57E+05	6.22E+01	5.50E+05	3.54E+01	1.38E+02
1800	2.86E+08	3.46E+07	3.10E+05	6.38E+05	3.69E+02	1.98E+06	1.87E+02	6.70E+02
1900	6.40E+08	1.02E+08	9.61E+05	2.25E+06	1.82E+03	6.28E+06	8.32E+02	2.75E+03
2000	1.32E+09	2.70E+08	2.66E+06	6.99E+06	7.68E+03	1.77E+07	3.18E+03	9.79E+03
2100	2.56E+09	6.51E+08	6.71E+06	1.96E+07	2.83E+04	4.55E+07	1.07E+04	3.09E+04
2200	4.68E+09	1.46E+09	1.56E+07	4.99E+07	9.28E+04	1.08E+08	3.22E+04	8.77E+04
2300	8.11E+09	3.04E+09	3.37E+07	1.17E+08	2.75E+05	2.36E+08	8.80E+04	2.27E+05
2400	1.35E+10	5.97E+09	6.82E+07	2.57E+08	7.44E+05	4.85E+08	2.20E+05	5.40E+05
2500	2.14E+10	1.11E+10	1.31E+08	5.31E+08	1.86E+06	9.44E+08	5.08E+05	1.19E+06

Arrhenius plots for temperature dependent rate coefficients over the 300–2500 K temperature range.

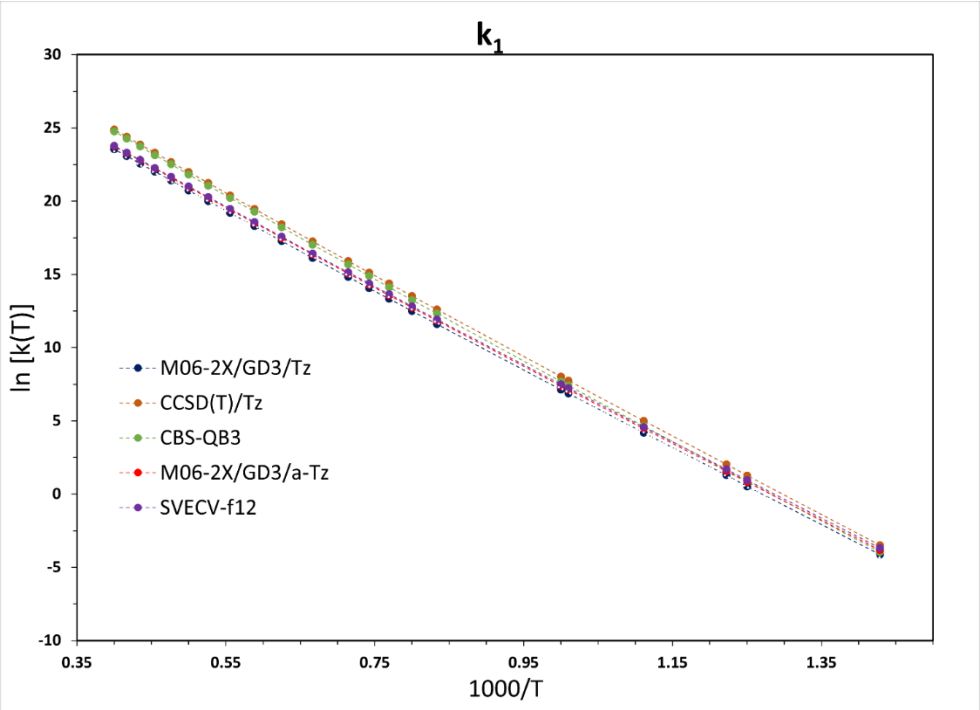

Figure A2-18: ln(k_1) vs 1000/T plot of EF decomposition in the range of 300 to 2500 K.

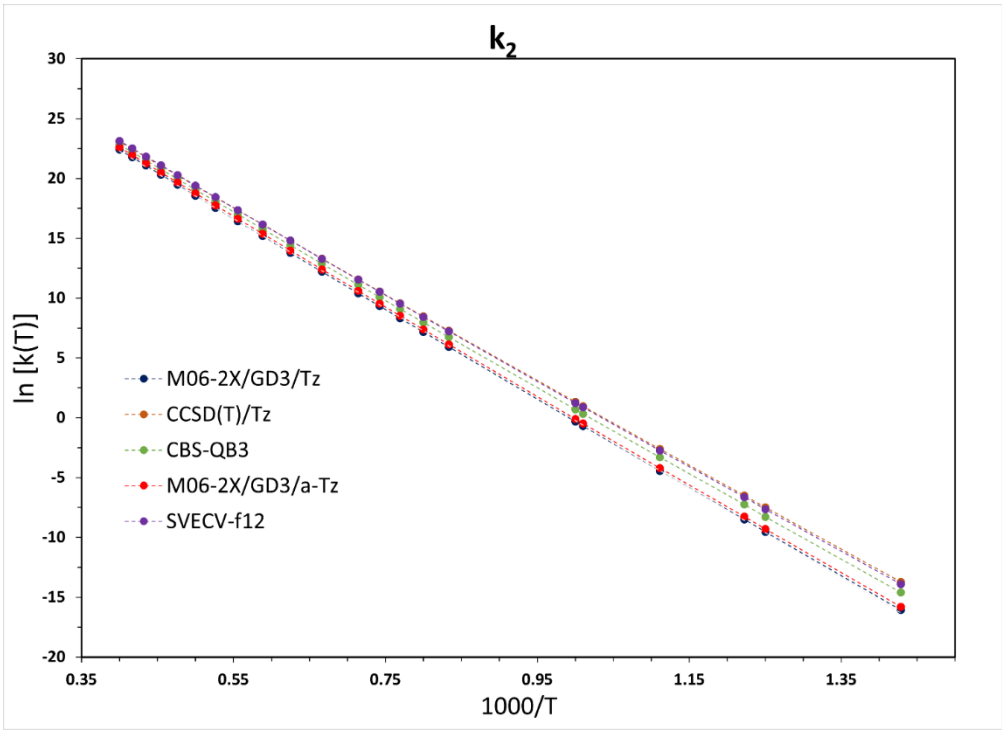

Figure A2-19: ln(k_2) vs 1000/T plot of EF decomposition in the range of 300 to 2500 K.

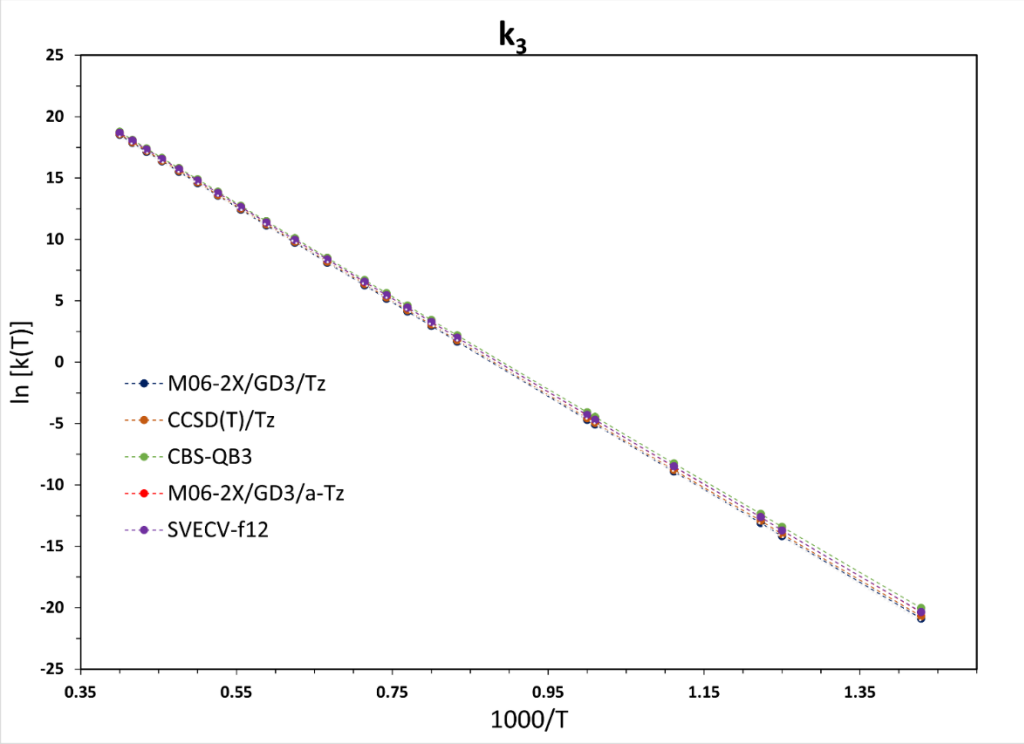

Figure A2-20: ln(k_3) vs 1000/T plot of EF decomposition in the range of 300 to 2500 K.

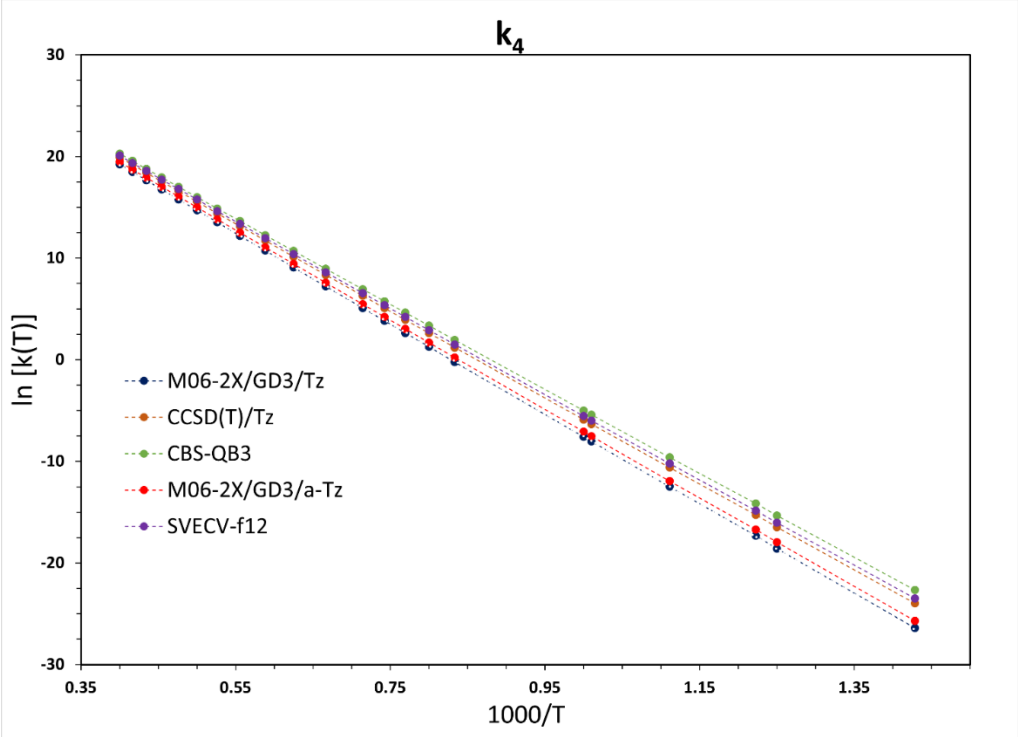

Figure A2-21: ln(k_4) vs 1000/T plot of EF decomposition in the range of 300 to 2500 K.

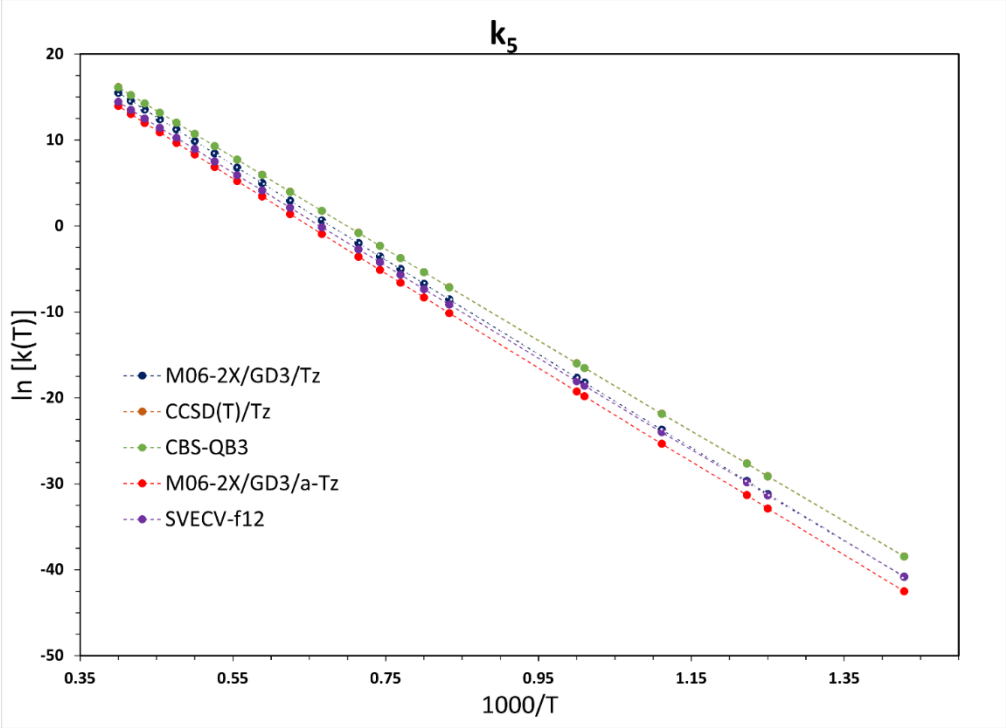

Figure A2-22: ln(k_5) vs 1000/T plot of EF decomposition in the range of 300 to 2500 K.

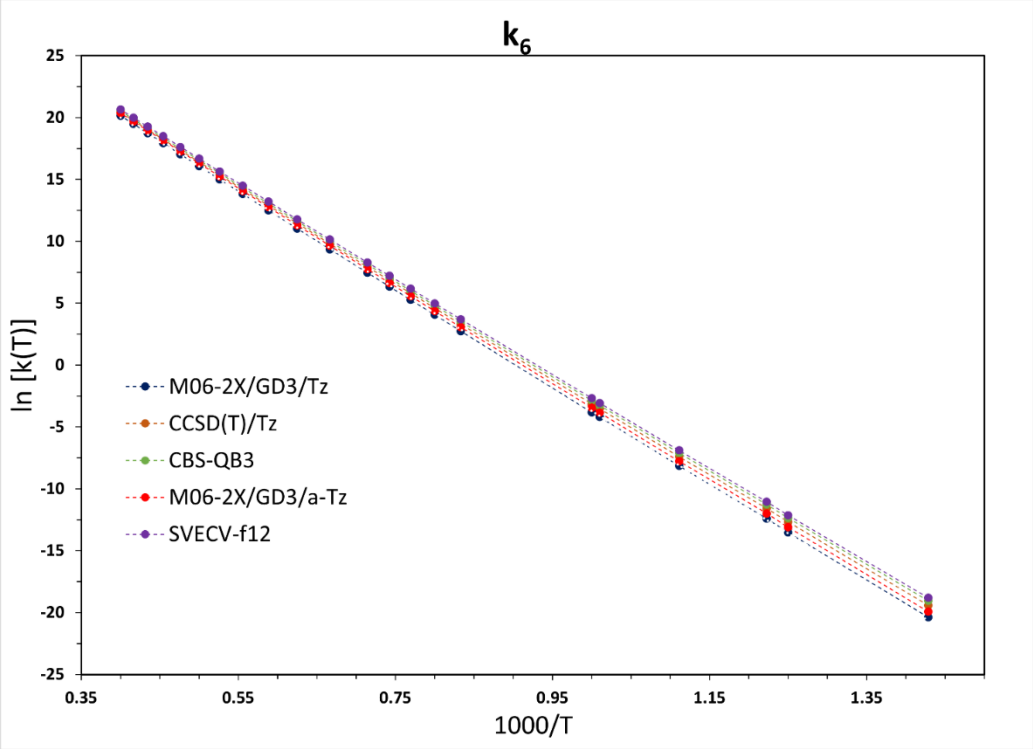

Figure A2-23: ln(k_6) vs 1000/T plot of EF decomposition in the range of 300 to 2500 K.

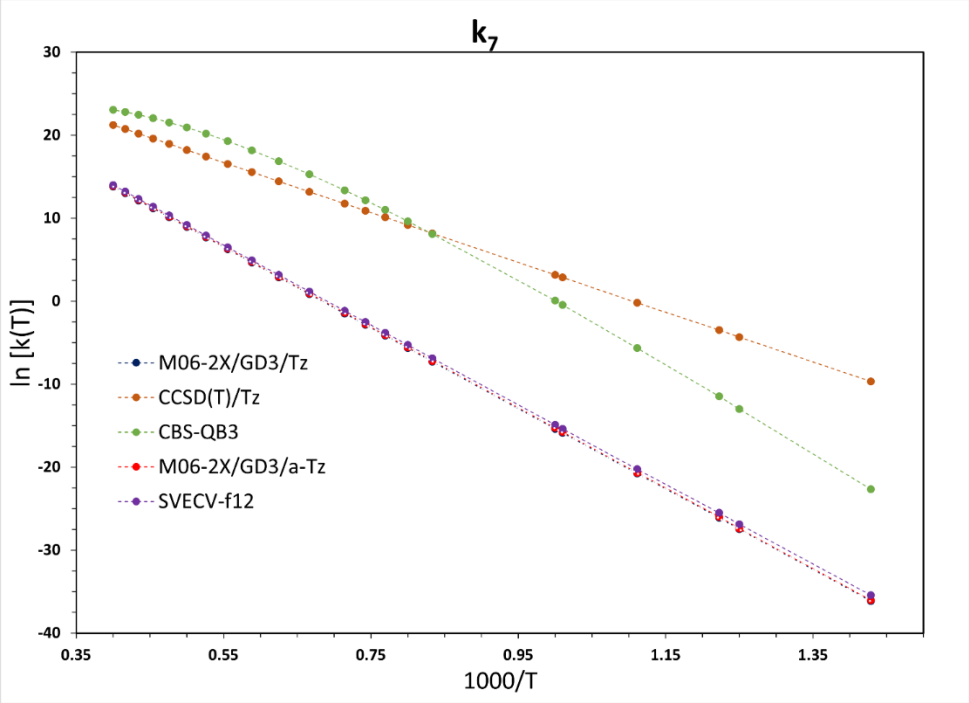

Figure A2-24: ln(k_7) vs 1000/T plot of EF decomposition in the range of 300 to 2500 K.

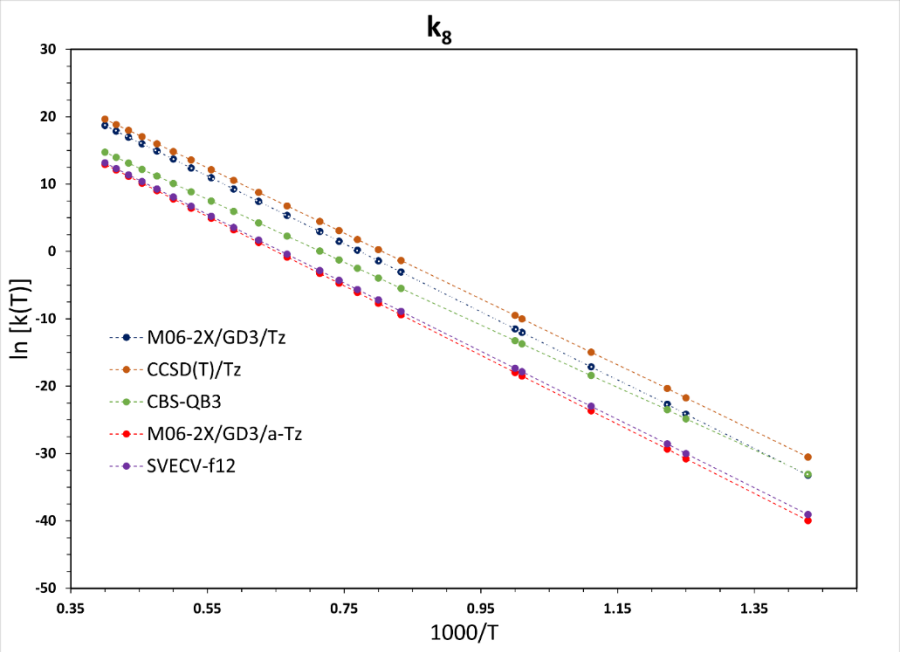

Figure A2-25: ln(k_8) vs 1000/T plot of EF decomposition in the range of 300 to 2500 K.

Calculated Rate coefficients ratios $k_2/k_3/k_4/k_5/k_6/k_7/k_8/k_1$

Table A2-7: M06-2X-GD3/cc-pVTZ

T	k_2/k_1	k_3/k_1	k_4/k_1	k_5/k_1	k_6/k_1	k_7/k_1	K_8/k_1
300	1.30E-11	1.31E-18	8.40E-26	3.89E-38	1.81E-18	1.29E-35	1.23E-34
400	2.48E-10	1.38E-13	9.57E-19	2.74E-29	1.36E-13	2.54E-25	2.31E-25
500	1.99E-08	6.22E-11	8.30E-15	1.68E-23	7.31E-11	1.24E-19	2.89E-20
600	5.59E-07	3.23E-09	3.17E-12	1.58E-19	4.58E-09	6.01E-16	5.92E-17
700	6.51E-06	5.22E-08	2.15E-10	1.15E-16	8.73E-08	2.32E-13	1.27E-14
800	4.19E-05	4.13E-07	4.99E-09	1.64E-14	7.96E-07	1.90E-11	6.81E-13
818	5.67E-05	5.76E-07	8.28E-09	3.65E-14	1.14E-06	3.85E-11	1.29E-12
900	1.80E-04	2.04E-06	5.73E-08	7.81E-13	4.46E-06	5.62E-10	1.47E-11
990	5.21E-04	6.51E-06	3.36E-07	1.30E-11	1.57E-05	6.42E-09	1.35E-10
1000	5.79E-04	7.30E-06	4.01E-07	1.73E-11	1.78E-05	8.18E-09	1.69E-10
1200	3.35E-03	4.89E-05	7.36E-06	1.80E-09	1.42E-04	4.29E-07	6.34E-09
1250	4.77E-03	7.15E-05	1.32E-05	4.55E-09	2.16E-04	9.38E-07	1.30E-08
1300	6.60E-03	1.01E-04	2.25E-05	1.07E-08	3.17E-04	1.92E-06	2.53E-08
1347	8.76E-03	1.37E-04	3.59E-05	2.27E-08	4.44E-04	3.59E-06	4.50E-08
1400	1.18E-02	1.89E-04	5.84E-05	4.96E-08	6.32E-04	6.89E-06	8.22E-08
1500	1.95E-02	3.24E-04	1.34E-04	1.87E-07	1.15E-03	2.06E-05	2.28E-07
1600	3.02E-02	5.20E-04	2.75E-04	5.98E-07	1.95E-03	5.34E-05	5.53E-07
1700	4.45E-02	7.87E-04	5.20E-04	1.67E-06	3.10E-03	1.23E-04	1.20E-06
1800	6.29E-02	1.14E-03	9.17E-04	4.15E-06	4.68E-03	2.56E-04	2.40E-06
1900	8.56E-02	1.58E-03	1.52E-03	9.37E-06	6.78E-03	4.92E-04	4.44E-06
2000	1.13E-01	2.13E-03	2.39E-03	1.95E-05	9.47E-03	8.83E-04	7.72E-06
2100	1.45E-01	2.79E-03	3.61E-03	3.79E-05	1.28E-02	1.49E-03	1.27E-05
2200	1.82E-01	3.56E-03	5.25E-03	6.93E-05	1.69E-02	2.39E-03	1.99E-05
2300	2.25E-01	4.44E-03	7.38E-03	1.20E-04	2.17E-02	3.68E-03	2.98E-05
2400	2.72E-01	5.45E-03	1.01E-02	1.99E-04	2.73E-02	5.44E-03	4.30E-05
2500	3.24E-01	6.57E-03	1.34E-02	3.17E-04	3.38E-02	7.79E-03	6.00E-05

Table A2-8: CCSD(T)/cc-pVTZ

T	k_2/k_1	k_3/k_1	k_4/k_1	k_5/k_1	k_6/k_1	k_7/k_1	K_8/k_1
300	1.41E-08	1.11E-17	1.26E-22	4.88E-35	8.97E-17	2.62E-32	4.32E-07
400	1.61E-08	2.12E-13	7.21E-17	1.91E-27	7.88E-13	2.56E-23	3.28E-05
500	3.90E-07	6.04E-11	1.81E-13	3.47E-22	2.05E-10	3.60E-18	2.64E-04
600	5.20E-06	2.46E-09	3.22E-11	1.53E-18	8.42E-09	8.12E-15	9.20E-04
700	3.58E-05	3.36E-08	1.28E-09	6.55E-16	1.20E-07	1.83E-12	2.09E-03
800	1.56E-04	2.34E-07	1.98E-08	6.28E-14	8.78E-07	1.00E-10	3.72E-03
818	1.98E-04	3.20E-07	3.08E-08	1.31E-13	1.21E-06	1.90E-10	4.07E-03
900	4.91E-04	1.05E-06	1.66E-07	2.19E-12	4.13E-06	2.16E-09	5.65E-03
990	1.13E-03	3.10E-06	7.71E-07	2.90E-11	1.28E-05	1.95E-08	7.52E-03
1000	1.23E-03	3.45E-06	8.98E-07	3.76E-11	1.43E-05	2.43E-08	7.73E-03
1200	4.86E-03	2.02E-05	1.12E-05	2.66E-09	9.16E-05	8.62E-07	1.19E-02
1250	6.39E-03	2.88E-05	1.84E-05	6.22E-09	1.33E-04	1.74E-06	1.29E-02
1300	8.23E-03	3.98E-05	2.92E-05	1.36E-08	1.87E-04	3.32E-06	1.38E-02
1347	1.02E-02	5.27E-05	4.37E-05	2.70E-08	2.53E-04	5.81E-06	1.47E-02
1400	1.29E-02	7.07E-05	6.65E-05	5.53E-08	3.46E-04	1.04E-05	1.56E-02
1500	1.90E-02	1.16E-04	1.35E-04	1.86E-07	5.88E-04	2.77E-05	1.72E-02
1600	2.67E-02	1.79E-04	2.51E-04	5.37E-07	9.36E-04	6.47E-05	1.87E-02
1700	3.60E-02	2.63E-04	4.34E-04	1.37E-06	1.41E-03	1.36E-04	2.00E-02
1800	4.69E-02	3.68E-04	7.03E-04	3.13E-06	2.03E-03	2.61E-04	2.12E-02
1900	5.93E-02	4.98E-04	1.08E-03	6.58E-06	2.82E-03	4.66E-04	2.23E-02
2000	7.33E-02	6.52E-04	1.60E-03	1.28E-05	3.78E-03	7.81E-04	2.32E-02
2100	8.88E-02	8.33E-04	2.26E-03	2.34E-05	4.93E-03	1.24E-03	2.41E-02
2200	1.06E-01	1.04E-03	3.11E-03	4.06E-05	6.27E-03	1.88E-03	2.48E-02
2300	1.24E-01	1.27E-03	4.15E-03	6.69E-05	7.82E-03	2.75E-03	2.53E-02
2400	1.43E-01	1.53E-03	5.42E-03	1.06E-04	9.57E-03	3.88E-03	2.57E-02
2500	1.63E-01	1.81E-03	6.91E-03	1.61E-04	1.15E-02	5.31E-03	2.59E-02

Table A2-9: CBS-QB3

T	k_2/k_1	k_3/k_1	k_4/k_1	k_5/k_1	k_6/k_1	k_7/k_1	K_8/k_1
300	5.25E-09	1.58E-16	7.88E-21	9.39E-35	6.66E-16	1.98E-30	3.83E-22
400	7.76E-09	1.57E-12	1.62E-15	3.92E-27	3.56E-12	1.06E-22	1.79E-16
500	2.18E-07	2.99E-10	2.18E-12	6.35E-22	6.86E-10	2.73E-18	2.69E-13
600	3.20E-06	9.32E-09	2.56E-10	2.54E-18	2.30E-08	2.08E-15	3.63E-11
700	2.36E-05	1.05E-07	7.55E-09	1.02E-15	2.84E-07	2.21E-13	7.47E-09
800	1.08E-04	6.37E-07	9.39E-08	9.22E-14	1.87E-06	7.00E-12	9.68E-07
818	1.38E-04	8.51E-07	1.41E-07	1.91E-13	2.53E-06	1.22E-11	2.08E-06
900	3.55E-04	2.55E-06	6.60E-07	3.08E-12	8.08E-06	9.99E-11	3.48E-05
990	8.43E-04	6.95E-06	2.71E-06	3.96E-11	2.35E-05	6.79E-10	3.87E-04
1000	9.19E-04	7.68E-06	3.12E-06	5.11E-11	2.61E-05	8.21E-10	4.86E-04
1200	3.81E-03	3.94E-05	3.15E-05	3.44E-09	1.52E-04	1.86E-08	1.49E-02
1250	5.06E-03	5.46E-05	4.98E-05	7.96E-09	2.15E-04	3.44E-08	2.67E-02
1300	6.58E-03	7.36E-05	7.61E-05	1.73E-08	2.98E-04	6.07E-08	4.41E-02
1347	8.26E-03	9.55E-05	1.10E-04	3.40E-08	3.96E-04	9.94E-08	6.62E-02
1400	1.05E-02	1.25E-04	1.62E-04	6.90E-08	5.32E-04	1.66E-07	9.80E-02
1500	1.57E-02	1.98E-04	3.10E-04	2.28E-07	8.80E-04	3.96E-07	1.75E-01
1600	2.23E-02	2.96E-04	5.47E-04	6.51E-07	1.37E-03	8.42E-07	2.61E-01
1700	3.03E-02	4.21E-04	9.02E-04	1.64E-06	2.01E-03	1.63E-06	3.39E-01
1800	3.99E-02	5.74E-04	1.40E-03	3.72E-06	2.84E-03	2.93E-06	3.93E-01
1900	5.09E-02	7.58E-04	2.08E-03	7.74E-06	3.87E-03	4.93E-06	4.17E-01
2000	6.34E-02	9.73E-04	2.97E-03	1.50E-05	5.11E-03	7.87E-06	4.10E-01
2100	7.73E-02	1.22E-03	4.09E-03	2.71E-05	6.57E-03	1.20E-05	3.80E-01
2200	9.25E-02	1.50E-03	5.48E-03	4.67E-05	8.25E-03	1.74E-05	3.34E-01
2300	1.09E-01	1.80E-03	7.14E-03	7.64E-05	1.02E-02	2.45E-05	2.82E-01
2400	1.27E-01	2.13E-03	9.09E-03	1.20E-04	1.23E-02	3.34E-05	2.30E-01
2500	1.45E-01	2.50E-03	1.14E-02	1.82E-04	1.47E-02	4.39E-05	1.83E-01

Table A2-10: M06-2X-GD3/aug-cc-pVTZ

T	k_2/k_1	k_3/k_1	k_4/k_1	k_5/k_1	k_6/k_1	k_7/k_1	K_8/k_1
300	9.75E-12	2.57E-18	2.06E-25	2.56E-41	2.51E-18	7.49E-39	9.01E-35
400	2.18E-10	2.23E-13	1.99E-18	1.10E-30	1.85E-13	1.61E-28	1.77E-25
500	1.85E-08	8.97E-11	1.49E-14	1.59E-24	9.37E-11	8.81E-23	2.29E-20
600	5.27E-07	4.29E-09	5.10E-12	1.91E-20	5.58E-09	4.80E-19	4.79E-17
700	6.20E-06	6.54E-08	3.19E-10	1.54E-17	1.03E-07	2.07E-16	1.04E-14
800	4.02E-05	4.95E-07	6.99E-09	2.33E-15	9.12E-07	1.88E-14	5.66E-13
818	5.44E-05	6.86E-07	1.15E-08	5.24E-15	1.30E-06	3.87E-14	1.07E-12
900	1.73E-04	2.37E-06	7.65E-08	1.15E-13	5.00E-06	6.10E-13	1.23E-11
990	5.03E-04	7.36E-06	4.34E-07	1.97E-12	1.73E-05	7.54E-12	1.14E-10
1000	5.60E-04	8.24E-06	5.16E-07	2.62E-12	1.95E-05	9.68E-12	1.42E-10
1200	3.26E-03	5.29E-05	8.93E-06	2.83E-10	1.52E-04	5.92E-10	5.40E-09
1250	4.64E-03	7.66E-05	1.58E-05	7.22E-10	2.30E-04	1.34E-09	1.11E-08
1300	6.42E-03	1.08E-04	2.67E-05	1.71E-09	3.36E-04	2.85E-09	2.16E-08
1347	8.52E-03	1.45E-04	4.21E-05	3.64E-09	4.69E-04	5.48E-09	3.86E-08
1400	1.15E-02	1.98E-04	6.80E-05	8.03E-09	6.64E-04	1.09E-08	7.06E-08
1500	1.90E-02	3.36E-04	1.53E-04	3.06E-08	1.20E-03	3.46E-08	1.96E-07
1600	2.95E-02	5.33E-04	3.10E-04	9.89E-08	2.01E-03	9.49E-08	4.77E-07
1700	4.35E-02	7.99E-04	5.79E-04	2.78E-07	3.18E-03	2.30E-07	1.04E-06
1800	6.15E-02	1.15E-03	1.01E-03	6.98E-07	4.79E-03	5.05E-07	2.08E-06
1900	8.37E-02	1.58E-03	1.65E-03	1.59E-06	6.90E-03	1.02E-06	3.86E-06
2000	1.11E-01	2.12E-03	2.58E-03	3.33E-06	9.59E-03	1.91E-06	6.70E-06
2100	1.42E-01	2.75E-03	3.86E-03	6.52E-06	1.29E-02	3.36E-06	1.10E-05
2200	1.79E-01	3.49E-03	5.56E-03	1.20E-05	1.70E-02	5.61E-06	1.73E-05
2300	2.20E-01	4.33E-03	7.76E-03	2.09E-05	2.17E-02	8.92E-06	2.60E-05
2400	2.67E-01	5.29E-03	1.05E-02	3.49E-05	2.73E-02	1.36E-05	3.76E-05
2500	3.18E-01	6.35E-03	1.40E-02	5.58E-05	3.37E-02	1.99E-05	5.24E-05

Table A2-11: SVECV-F12

T	k_2/k_1	k_3/k_1	k_4/k_1	k_5/k_1	k_6/k_1	k_7/k_1	K_8/k_1
300	4.41E-10	1.77E-18	2.33E-23	9.58E-40	2.30E-17	4.17E-38	2.68E-34
400	4.51E-09	1.73E-13	7.12E-17	1.73E-29	9.86E-13	5.97E-28	4.06E-25
500	2.11E-07	7.33E-11	2.61E-13	1.45E-23	3.57E-10	2.49E-22	4.40E-20
600	4.03E-06	3.63E-09	5.55E-11	1.20E-19	1.70E-08	1.14E-18	8.14E-17
700	3.54E-05	5.67E-08	2.47E-09	7.50E-17	2.67E-07	4.31E-16	1.62E-14
800	1.85E-04	4.37E-07	4.19E-08	9.30E-15	2.10E-06	3.55E-14	8.24E-13
818	2.41E-04	6.07E-07	6.61E-08	2.02E-14	2.94E-06	7.20E-14	1.55E-12
900	6.73E-04	2.12E-06	3.76E-07	3.95E-13	1.05E-05	1.07E-12	1.71E-11
990	1.73E-03	6.65E-06	1.84E-06	6.03E-12	3.39E-05	1.25E-11	1.52E-10
1000	1.90E-03	7.45E-06	2.16E-06	7.92E-12	3.82E-05	1.60E-11	1.89E-10
1200	9.02E-03	4.87E-05	2.95E-05	7.11E-10	2.66E-04	8.93E-10	6.75E-09
1250	1.23E-02	7.07E-05	4.97E-05	1.75E-09	3.93E-04	1.99E-09	1.37E-08
1300	1.64E-02	9.98E-05	8.03E-05	4.01E-09	5.63E-04	4.15E-09	2.64E-08
1347	2.11E-02	1.35E-04	1.22E-04	8.29E-09	7.71E-04	7.87E-09	4.66E-08
1400	2.74E-02	1.85E-04	1.89E-04	1.77E-08	1.07E-03	1.54E-08	8.44E-08
1500	4.28E-02	3.14E-04	3.97E-04	6.41E-08	1.87E-03	4.77E-08	2.30E-07
1600	6.33E-02	5.00E-04	7.60E-04	1.98E-07	3.06E-03	1.28E-07	5.51E-07
1700	8.92E-02	7.54E-04	1.34E-03	5.33E-07	4.72E-03	3.04E-07	1.19E-06
1800	1.21E-01	1.08E-03	2.23E-03	1.29E-06	6.94E-03	6.55E-07	2.34E-06
1900	1.59E-01	1.50E-03	3.51E-03	2.85E-06	9.81E-03	1.30E-06	4.29E-06
2000	2.04E-01	2.01E-03	5.28E-03	5.80E-06	1.34E-02	2.40E-06	7.39E-06
2100	2.54E-01	2.62E-03	7.63E-03	1.10E-05	1.78E-02	4.18E-06	1.21E-05
2200	3.11E-01	3.33E-03	1.07E-02	1.98E-05	2.30E-02	6.89E-06	1.88E-05
2300	3.74E-01	4.15E-03	1.45E-02	3.39E-05	2.91E-02	1.08E-05	2.80E-05
2400	4.43E-01	5.07E-03	1.91E-02	5.53E-05	3.61E-02	1.63E-05	4.02E-05
2500	5.18E-01	6.11E-03	2.48E-02	8.69E-05	4.40E-02	2.37E-05	5.57E-05

Calculated Branching ratios k_i/k_{EF}

Table A2-12: M06-2X-GD3/cc-pVTZ

T	k_1/k_{EF}	k_2/k_{EF}	k_3/k_{EF}	k_4/k_{EF}	k_5/k_{EF}	k_6/k_{EF}	k_7/k_{EF}	k_8/k_{EF}
300	100.00%	0.00%	0.00%	0.00%	0.00%	0.00%	0.00%	0.00%
400	100.00%	0.00%	0.00%	0.00%	0.00%	0.00%	0.00%	0.00%
500	100.00%	0.00%	0.00%	0.00%	0.00%	0.00%	0.00%	0.00%
600	100.00%	0.00%	0.00%	0.00%	0.00%	0.00%	0.00%	0.00%
700	100.00%	0.00%	0.00%	0.00%	0.00%	0.00%	0.00%	0.00%
800	100.00%	0.00%	0.00%	0.00%	0.00%	0.00%	0.00%	0.00%
818	99.99%	0.01%	0.00%	0.00%	0.00%	0.00%	0.00%	0.00%
900	99.98%	0.02%	0.00%	0.00%	0.00%	0.00%	0.00%	0.00%
990	99.95%	0.05%	0.00%	0.00%	0.00%	0.00%	0.00%	0.00%
1000	99.94%	0.06%	0.00%	0.00%	0.00%	0.00%	0.00%	0.00%
1200	99.65%	0.33%	0.00%	0.00%	0.00%	0.01%	0.00%	0.00%
1250	99.50%	0.47%	0.01%	0.00%	0.00%	0.02%	0.00%	0.00%
1300	99.30%	0.66%	0.01%	0.00%	0.00%	0.03%	0.00%	0.00%
1347	99.07%	0.87%	0.01%	0.00%	0.00%	0.04%	0.00%	0.00%
1400	98.75%	1.16%	0.02%	0.01%	0.00%	0.06%	0.00%	0.00%
1500	97.93%	1.91%	0.03%	0.01%	0.00%	0.11%	0.00%	0.00%
1600	96.80%	2.93%	0.05%	0.03%	0.00%	0.19%	0.01%	0.00%
1700	95.32%	4.25%	0.08%	0.05%	0.00%	0.30%	0.01%	0.00%
1800	93.47%	5.88%	0.11%	0.09%	0.00%	0.44%	0.02%	0.00%
1900	91.24%	7.81%	0.14%	0.14%	0.00%	0.62%	0.04%	0.00%
2000	88.66%	10.02%	0.19%	0.21%	0.00%	0.84%	0.08%	0.00%
2100	85.77%	12.45%	0.24%	0.31%	0.00%	1.10%	0.13%	0.00%
2200	82.60%	15.07%	0.29%	0.43%	0.01%	1.39%	0.20%	0.00%
2300	79.23%	17.81%	0.35%	0.58%	0.01%	1.72%	0.29%	0.00%
2400	75.72%	20.61%	0.41%	0.76%	0.02%	2.07%	0.41%	0.00%
2500	72.13%	23.40%	0.47%	0.97%	0.02%	2.44%	0.56%	0.00%

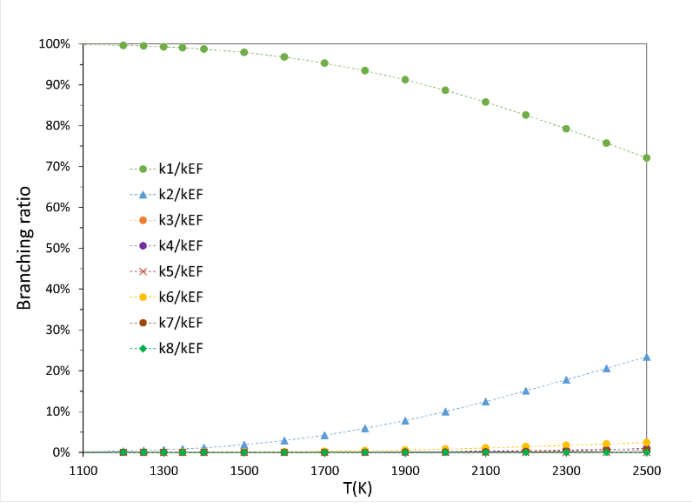

Figure A2-26: Branching ratios for the unimolecular decomposition of EF in the range of 300 to 2500 K. Calculated at M062X-GD3/cc-pVTZ level of theory

Table A2-13: CCSD(T)/cc-pVTZ.

T	k_1/k_{EF}	k_2/k_{EF}	k_3/k_{EF}	k_4/k_{EF}	k_5/k_{EF}	k_6/k_{EF}	k_7/k_{EF}	k_8/k_{EF}
300	100.00%	0.00%	0.00%	0.00%	0.00%	0.00%	0.00%	0.00%
400	100.00%	0.00%	0.00%	0.00%	0.00%	0.00%	0.00%	0.00%
500	99.97%	0.00%	0.00%	0.00%	0.00%	0.00%	0.00%	0.03%
600	99.91%	0.00%	0.00%	0.00%	0.00%	0.00%	0.00%	0.09%
700	99.79%	0.00%	0.00%	0.00%	0.00%	0.00%	0.00%	0.21%
800	99.61%	0.02%	0.00%	0.00%	0.00%	0.00%	0.00%	0.37%
818	99.58%	0.02%	0.00%	0.00%	0.00%	0.00%	0.00%	0.40%
900	99.39%	0.05%	0.00%	0.00%	0.00%	0.00%	0.00%	0.56%
990	99.14%	0.11%	0.00%	0.00%	0.00%	0.00%	0.00%	0.75%
1000	99.11%	0.12%	0.00%	0.00%	0.00%	0.00%	0.00%	0.77%
1200	98.34%	0.48%	0.00%	0.00%	0.00%	0.01%	0.00%	1.17%
1250	98.09%	0.63%	0.00%	0.00%	0.00%	0.01%	0.00%	1.26%
1300	97.82%	0.81%	0.00%	0.00%	0.00%	0.02%	0.00%	1.35%
1347	97.54%	1.00%	0.01%	0.00%	0.00%	0.02%	0.00%	1.43%
1400	97.18%	1.25%	0.01%	0.01%	0.00%	0.03%	0.00%	1.52%
1500	96.42%	1.83%	0.01%	0.01%	0.00%	0.06%	0.00%	1.66%
1600	95.53%	2.55%	0.02%	0.02%	0.00%	0.09%	0.01%	1.79%
1700	94.50%	3.40%	0.02%	0.04%	0.00%	0.13%	0.01%	1.89%
1800	93.33%	4.37%	0.03%	0.07%	0.00%	0.19%	0.02%	1.98%
1900	92.04%	5.46%	0.05%	0.10%	0.00%	0.26%	0.04%	2.05%
2000	90.63%	6.64%	0.06%	0.14%	0.00%	0.34%	0.07%	2.11%
2100	89.12%	7.91%	0.07%	0.20%	0.00%	0.44%	0.11%	2.14%
2200	87.51%	9.24%	0.09%	0.27%	0.00%	0.55%	0.16%	2.17%
2300	85.84%	10.61%	0.11%	0.36%	0.01%	0.67%	0.24%	2.17%
2400	84.10%	12.02%	0.13%	0.46%	0.01%	0.80%	0.33%	2.16%
2500	82.32%	13.43%	0.15%	0.57%	0.01%	0.95%	0.44%	2.13%

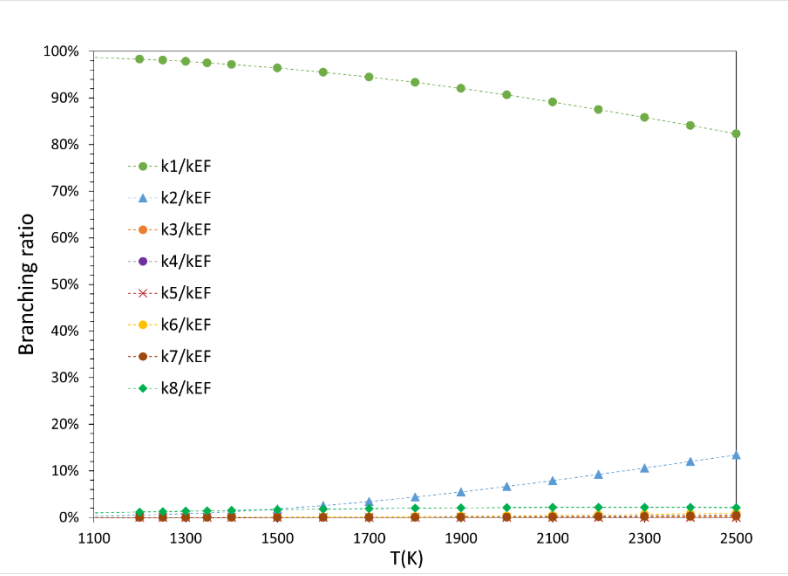

Figure A2-27: Branching ratios for the unimolecular decomposition of EF in the range of 300 to 2500 K. Calculated at CCSD(T)/cc-pVTZ level of theory

Table A2-14: CBS-QB3

T	k_1/k_{EF}	k_2/k_{EF}	k_3/k_{EF}	k_4/k_{EF}	k_5/k_{EF}	k_6/k_{EF}	k_7/k_{EF}	k_8/k_{EF}
300	100.00%	0.00%	0.00%	0.00%	0.00%	0.00%	0.00%	0.00%
400	100.00%	0.00%	0.00%	0.00%	0.00%	0.00%	0.00%	0.00%
500	100.00%	0.00%	0.00%	0.00%	0.00%	0.00%	0.00%	0.00%
600	100.00%	0.00%	0.00%	0.00%	0.00%	0.00%	0.00%	0.00%
700	100.00%	0.00%	0.00%	0.00%	0.00%	0.00%	0.00%	0.00%
800	99.99%	0.01%	0.00%	0.00%	0.00%	0.00%	0.00%	0.00%
818	99.99%	0.01%	0.00%	0.00%	0.00%	0.00%	0.00%	0.00%
900	99.96%	0.04%	0.00%	0.00%	0.00%	0.00%	0.00%	0.00%
990	99.87%	0.08%	0.00%	0.00%	0.00%	0.00%	0.00%	0.04%
1000	99.86%	0.09%	0.00%	0.00%	0.00%	0.00%	0.00%	0.05%
1200	98.14%	0.37%	0.00%	0.00%	0.00%	0.01%	0.00%	1.46%
1250	96.90%	0.49%	0.01%	0.00%	0.00%	0.02%	0.00%	2.58%
1300	95.14%	0.63%	0.01%	0.01%	0.00%	0.03%	0.00%	4.19%
1347	93.02%	0.77%	0.01%	0.01%	0.00%	0.04%	0.00%	6.16%
1400	90.15%	0.94%	0.01%	0.01%	0.00%	0.05%	0.00%	8.84%
1500	83.92%	1.31%	0.02%	0.03%	0.00%	0.07%	0.00%	14.65%
1600	77.81%	1.73%	0.02%	0.04%	0.00%	0.11%	0.00%	20.29%
1700	72.86%	2.21%	0.03%	0.07%	0.00%	0.15%	0.00%	24.68%
1800	69.54%	2.77%	0.04%	0.10%	0.00%	0.20%	0.00%	27.35%
1900	67.83%	3.45%	0.05%	0.14%	0.00%	0.26%	0.00%	28.26%
2000	67.46%	4.27%	0.07%	0.20%	0.00%	0.34%	0.00%	27.66%
2100	68.08%	5.26%	0.08%	0.28%	0.00%	0.45%	0.00%	25.84%
2200	69.34%	6.41%	0.10%	0.38%	0.00%	0.57%	0.00%	23.18%
2300	70.90%	7.72%	0.13%	0.51%	0.01%	0.72%	0.00%	20.02%
2400	72.42%	9.17%	0.15%	0.66%	0.01%	0.89%	0.00%	16.69%
2500	73.69%	10.71%	0.18%	0.84%	0.01%	1.08%	0.00%	13.48%

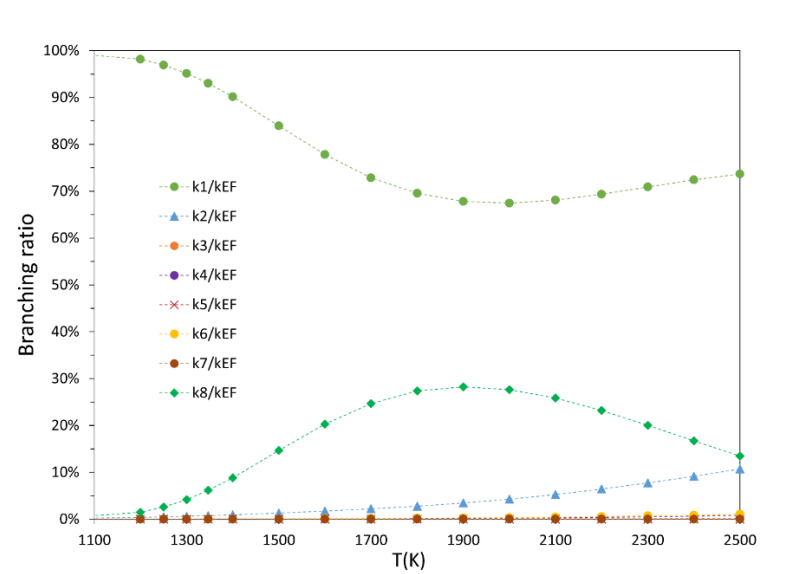

Figure A2-28: Branching ratios for the unimolecular decomposition of EF in the range of 300 to 2500 K. Calculated at CBS-QB3 level of theory

Table A2-15: M06-2X-GD3/aug-cc-pVTZ

T	k_1/k_{EF}	k_2/k_{EF}	k_3/k_{EF}	k_4/k_{EF}	k_5/k_{EF}	k_6/k_{EF}	k_7/k_{EF}	k_8/k_{EF}
300	100.00%	0.00%	0.00%	0.00%	0.00%	0.00%	0.00%	0.00%
400	100.00%	0.00%	0.00%	0.00%	0.00%	0.00%	0.00%	0.00%
500	100.00%	0.00%	0.00%	0.00%	0.00%	0.00%	0.00%	0.00%
600	100.00%	0.00%	0.00%	0.00%	0.00%	0.00%	0.00%	0.00%
700	100.00%	0.00%	0.00%	0.00%	0.00%	0.00%	0.00%	0.00%
800	100.00%	0.00%	0.00%	0.00%	0.00%	0.00%	0.00%	0.00%
818	99.99%	0.01%	0.00%	0.00%	0.00%	0.00%	0.00%	0.00%
900	99.98%	0.02%	0.00%	0.00%	0.00%	0.00%	0.00%	0.00%
990	99.95%	0.05%	0.00%	0.00%	0.00%	0.00%	0.00%	0.00%
1000	99.94%	0.06%	0.00%	0.00%	0.00%	0.00%	0.00%	0.00%
1200	99.65%	0.32%	0.01%	0.00%	0.00%	0.02%	0.00%	0.00%
1250	99.51%	0.46%	0.01%	0.00%	0.00%	0.02%	0.00%	0.00%
1300	99.32%	0.64%	0.01%	0.00%	0.00%	0.03%	0.00%	0.00%
1347	99.09%	0.84%	0.01%	0.00%	0.00%	0.05%	0.00%	0.00%
1400	98.78%	1.13%	0.02%	0.01%	0.00%	0.07%	0.00%	0.00%
1500	97.97%	1.86%	0.03%	0.01%	0.00%	0.12%	0.00%	0.00%
1600	96.87%	2.86%	0.05%	0.03%	0.00%	0.20%	0.00%	0.00%
1700	95.41%	4.15%	0.08%	0.06%	0.00%	0.30%	0.00%	0.00%
1800	93.60%	5.75%	0.11%	0.09%	0.00%	0.45%	0.00%	0.00%
1900	91.42%	7.65%	0.14%	0.15%	0.00%	0.63%	0.00%	0.00%
2000	88.91%	9.82%	0.19%	0.23%	0.00%	0.85%	0.00%	0.00%
2100	86.08%	12.24%	0.24%	0.33%	0.00%	1.11%	0.00%	0.00%
2200	83.01%	14.83%	0.29%	0.46%	0.00%	1.41%	0.00%	0.00%
2300	79.74%	17.56%	0.35%	0.62%	0.00%	1.73%	0.00%	0.00%
2400	76.34%	20.36%	0.40%	0.80%	0.00%	2.08%	0.00%	0.00%
2500	72.88%	23.18%	0.46%	1.02%	0.00%	2.45%	0.00%	0.00%

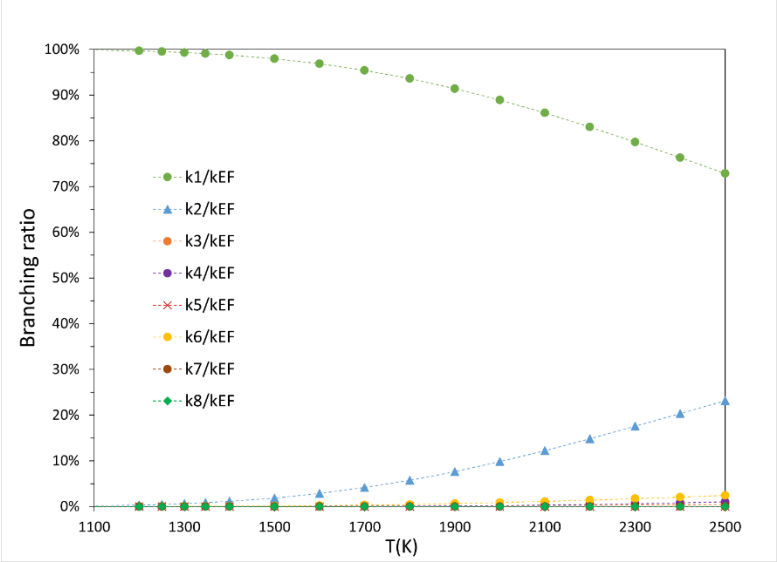

Figure A2-29: Branching ratios for the unimolecular decomposition of EF in the range of 300 to 2500 K. Calculated at M062X-GD3/aug-cc-pVTZ level of theory

Table A2-16: SVECV-F12

T	k_1/k_{EF}	k_2/k_{EF}	k_3/k_{EF}	k_4/k_{EF}	k_5/k_{EF}	k_6/k_{EF}	k_7/k_{EF}	k_8/k_{EF}
300	100.00%	0.00%	0.00%	0.00%	0.00%	0.00%	0.00%	0.00%
400	100.00%	0.00%	0.00%	0.00%	0.00%	0.00%	0.00%	0.00%
500	100.00%	0.00%	0.00%	0.00%	0.00%	0.00%	0.00%	0.00%
600	100.00%	0.00%	0.00%	0.00%	0.00%	0.00%	0.00%	0.00%
700	100.00%	0.00%	0.00%	0.00%	0.00%	0.00%	0.00%	0.00%
800	99.98%	0.02%	0.00%	0.00%	0.00%	0.00%	0.00%	0.00%
818	99.98%	0.02%	0.00%	0.00%	0.00%	0.00%	0.00%	0.00%
900	99.93%	0.07%	0.00%	0.00%	0.00%	0.00%	0.00%	0.00%
990	99.82%	0.17%	0.00%	0.00%	0.00%	0.00%	0.00%	0.00%
1000	99.81%	0.19%	0.00%	0.00%	0.00%	0.00%	0.00%	0.00%
1200	99.07%	0.89%	0.00%	0.00%	0.00%	0.03%	0.00%	0.00%
1250	98.73%	1.22%	0.01%	0.00%	0.00%	0.04%	0.00%	0.00%
1300	98.31%	1.61%	0.01%	0.01%	0.00%	0.06%	0.00%	0.00%
1347	97.84%	2.06%	0.01%	0.01%	0.00%	0.08%	0.00%	0.00%
1400	97.19%	2.67%	0.02%	0.02%	0.00%	0.10%	0.00%	0.00%
1500	95.66%	4.10%	0.03%	0.04%	0.00%	0.18%	0.00%	0.00%
1600	93.67%	5.93%	0.05%	0.07%	0.00%	0.29%	0.00%	0.00%
1700	91.24%	8.14%	0.07%	0.12%	0.00%	0.43%	0.00%	0.00%
1800	88.39%	10.70%	0.10%	0.20%	0.00%	0.61%	0.00%	0.00%
1900	85.18%	13.56%	0.13%	0.30%	0.00%	0.84%	0.00%	0.00%
2000	81.68%	16.63%	0.16%	0.43%	0.00%	1.09%	0.00%	0.00%
2100	77.98%	19.83%	0.20%	0.60%	0.00%	1.39%	0.00%	0.00%

2200	74.17%	23.08%	0.25%	0.79%	0.00%	1.71%	0.00%	0.00%
2300	70.32%	26.33%	0.29%	1.02%	0.00%	2.04%	0.00%	0.00%
2400	66.49%	29.49%	0.34%	1.27%	0.00%	2.40%	0.00%	0.00%
2500	62.77%	32.52%	0.38%	1.55%	0.01%	2.76%	0.00%	0.00%

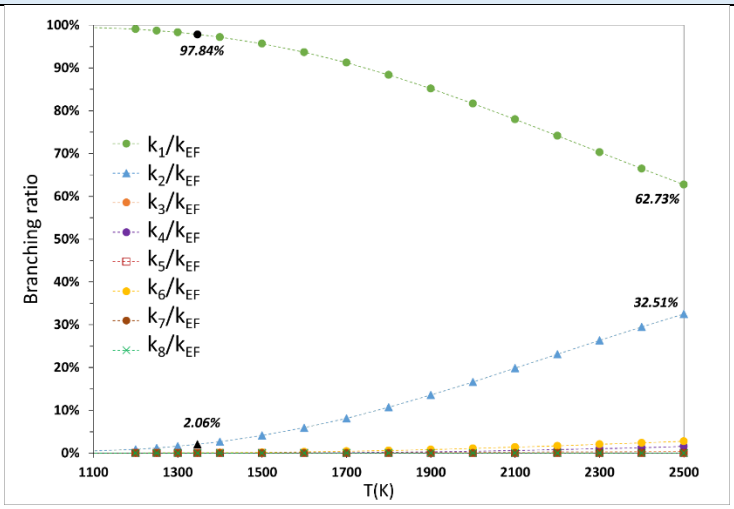

Figure A2-30: Branching ratios for the unimolecular decomposition of EF in the range of 300 to 2500 K. Calculated at SVECV-F12 level of theory

Calculated pressure dependent rate coefficients for the unimolecular decomposition of ethyl formate for temperatures above 1250 K over the pressure range 0.01–100 bar

The pressure dependent rate coefficients were calculated for unimolecular dissociation reaction of EF with RRKM theory using MultiWell program. [81–83] Argon was used as the bath gas with the Lennard-Jones (L- J) collision diameter parameter σ= 3.464 Å and well-depth ε/k = 113.5 K.[39] The L-J parameter σ= 5.12 Å and well-depth ε/k = 614.36 K were employed for EF. Energy transfer coefficients were treated by the exponential down model with an average downward transfer parameter <ΔE > down = 200 cm^{-1}.[41] The asymmetric Eckart approximation was employed to account for the tunnelling corrections.

Table A2-17: Pressure dependent rate coefficients for the path R1 in the unimolecular decomposition of EF

T(K)	k_1					
	0.01	0.1	1	10	100	HPL
990	2.08E+02	5.42E+02	8.55E+02	1.17E+03	1.13E+03	1.19E+03
1250	9.30E+03	3.43E+04	1.04E+05	2.48E+05	3.12E+05	3.29E+05
1347	2.36E+04	1.01E+05	3.47E+05	8.61E+05	1.44E+06	1.56E+06
1500	5.59E+04	3.47E+05	1.37E+06	3.81E+06	7.38E+06	1.23E+07
1700	1.43E+05	7.81E+05	4.77E+06	1.85E+07	4.38E+07	1.05E+08
1900	2.82E+05	1.86E+06	9.39E+06	4.20E+07	1.89E+08	5.81E+08
2100	4.21E+05	2.75E+06	1.75E+07	9.10E+07	3.43E+08	2.33E+09
2300	5.27E+05	4.02E+06	2.60E+07	1.59E+08	6.16E+08	7.39E+09
2500	7.60E+05	5.05E+06	3.98E+07	2.17E+08	9.94E+08	1.95E+10

Table A2-18: Pressure dependent rate coefficients for the path R2 in the unimolecular decomposition of EF

T(K)	K_2					
	0.01	0.1	1	10	100	HPL
1250	1.21E+02	3.56E+02	9.78E+02	1.29E+03	1.87E+03	1.57E+03
1347	5.39E+02	1.87E+03	4.47E+03	9.60E+03	1.46E+04	1.37E+04
1500	3.70E+03	1.43E+04	4.99E+04	8.97E+04	1.98E+05	2.40E+05
1700	1.99E+04	8.98E+04	4.24E+05	1.22E+06	2.90E+06	4.70E+06
1900	5.15E+04	3.17E+05	1.49E+06	5.85E+06	1.78E+07	4.98E+07
2100	9.73E+04	6.24E+05	3.94E+06	1.91E+07	6.47E+07	3.39E+08
2300	1.75E+05	1.19E+06	7.38E+06	4.10E+07	1.80E+08	1.66E+09
2500	2.48E+05	1.87E+06	1.24E+07	7.12E+07	3.42E+08	1.66E+09

Table A2-19: Arrhenius parameters for pressure dependent rate coefficients for the path R1 and R2 in the unimolecular decomposition of EF

	k_1			k_2		
p (bar)	A	E_a (kJ/mol)	E_a (kcal/mol)	A	E_a (kJ/mol)	E_a (kcal/mol)
0.01	6.79E+07	89.78	21.46	8.16E+08	158.11	37.79
0.10	9.38E+08	102.39	24.47	1.59E+10	177.81	42.50
1.00	1.73E+10	121.05	28.93	3.12E+11	199.33	47.64
10.00	2.84E+11	141.80	33.89	8.18E+12	229.90	54.95
100.00	5.04E+12	168.76	40.34	1.26E+14	255.14	60.98

Table A2-20: Values for log(k1/k∞) at the pressure range of 0.01-100 bar and temperature range of 990-2500K for the unimolecular decomposition of EF.

1/T(k)	$\log(k_1/k_\infty)$					
	0.01 bar	0.1 bar	1 bar	10 bar	100 bar	HPL
990.000	-0.758	-0.342	-0.143	-0.009	-0.024	0.000
1250.000	-1.549	-0.981	-0.501	-0.122	-0.022	0.000
1347.000	-1.821	-1.188	-0.652	-0.258	-0.034	0.000
1500.000	-2.342	-1.550	-0.953	-0.510	-0.222	0.000
1700.000	-2.865	-2.129	-1.343	-0.753	-0.380	0.000
1900.000	-3.314	-2.496	-1.792	-1.141	-0.488	0.000
2100.000	-3.743	-2.929	-2.124	-1.408	-0.832	0.000
2300.000	-4.147	-3.264	-2.453	-1.668	-1.079	0.000
2500.000	-4.409	-3.586	-2.690	-1.954	-1.293	0.000

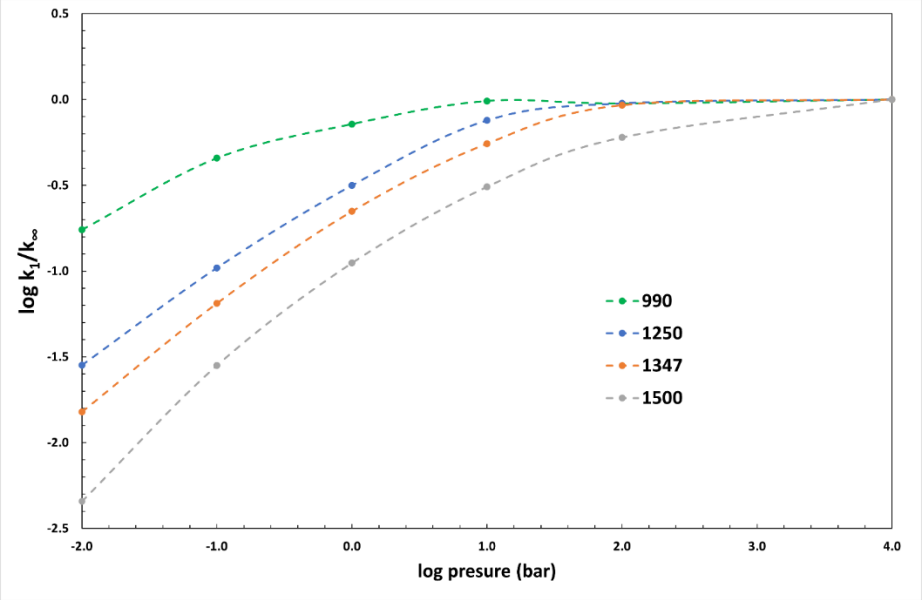

Figure A2-31: Modelled falloff curves for R1 in the unimolecular decomposition of EF. Temperature range 990-1500K.

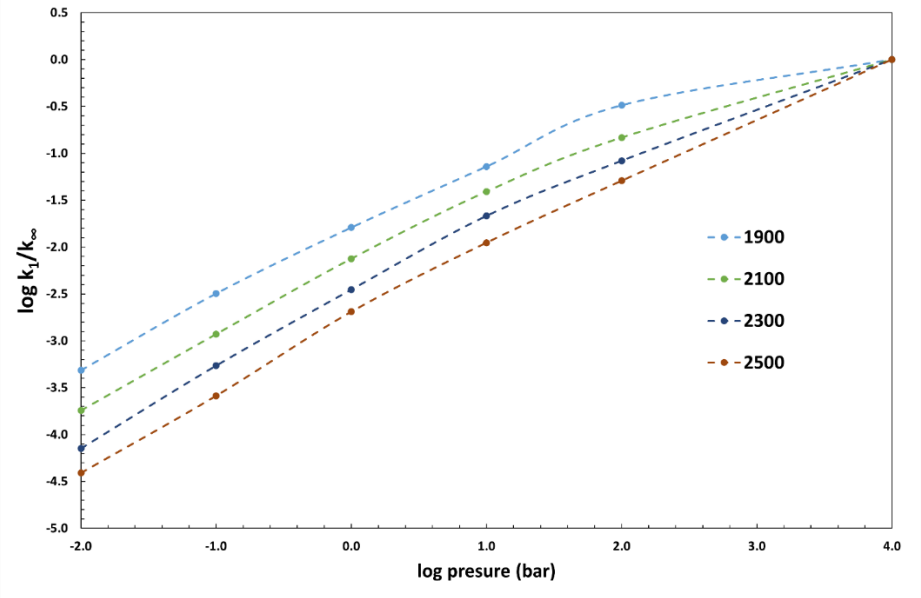

Figure A2-32: Modelled falloff curves for R1 in the unimolecular decomposition of EF. Temperature range 1700-2500K.

Arrhenius parameters, A (s^{-1}) and E_a (kJ mol^{-1}) for EF thermal decomposition in the range of 300–2500 K

Table A2-21:

	M06-2X-GD3/TZ[a]		CCSD(T)/TZ[a]		CBS-QB3		M06-2X-GD3/a-TZ[b]		SVECV-f12	
	A	E_a	A	E_a	A	E_a	A	E_a	A	E_a
k_1	2.19×10^{14}	211.3	1.23×10^{15}	218.4	1.23×10^{15}	221.2	2.57×10^{14}	210.5	2.55×10^{14}	209.5
k_2	1.52×10^{15}	286.7	1.56×10^{15}	273.3	1.56×10^{15}	278.5	1.83×10^{15}	286.4	1.89×10^{15}	275.7
k_3	2.26×10^{14}	311.2	2.26×10^{14}	310.1	2.26×10^{14}	306.2	2.34×10^{14}	308.4	2.34×10^{14}	308.4
k_4	4.85×10^{15}	360.7	4.85×10^{15}	346.6	4.85×10^{15}	339.0	5.31×10^{15}	357.3	5.31×10^{15}	344.5
K_5	2.57×10^{15}	436.7	2.61×10^{15}	422.6	2.77×10^{15}	423.4	1.32×10^{15}	446.2	1.33×10^{15}	436.2
K_6	1.19×10^{15}	316.3	1.18×10^{15}	310.8	1.19×10^{15}	308.5	1.33×10^{15}	314.4	1.33×10^{15}	307.9
K_7	2.19×10^{14}	401.4	2.19×10^{14}	247.4	6.27×10^{18}	368.5	2.31×10^{14}	401.1	2.12×10^{14}	397.2
K_8	9.38×10^{16}	421.1	1.24×10^{17}	406.9	2.38×10^{14}	384.4	2.76×10^{14}	425.0	2.66×10^{14}	419.6

[a] TZ stands for cc-pVTZ; [b] a-TZ stands for aug-cc-pVTZ

Carbon monoxide branching ratio

To calculate the ratio of CO coming directly from ethyl formate (k_2) vs that coming from formic acid (P2, k_{1a}) it is necessary to obtain kinetic information all the path to CO formation.

$$H_3CCH_2OCHO \rightarrow H_3CCH_2OH\_(P3) + CO\_(P4) \qquad k_2$$

$$trans\text{-}HOCHO\_(P2) \rightarrow H_2O\_(P14) + CO\_(P4) \qquad k_{1a}$$

The CO formation from k_1 goes through by three steps, the P1 and P2 formations with rate constant k_1, and reverse reaction with rate constant k_{-1},

$$H_3CCH_2OCHO \rightarrow H_2C{=}CH_2\_(P1) + HOCHO\_(P2) \qquad \mathbf{k_1} \qquad (1a)$$

$$H_2C{=}CH_2\_(P1) + HOCHO\_(P2) \rightarrow H_3CCH_2OCHO \qquad \mathbf{k_{-1}} \qquad (1b)$$

Once formed, formic acid could discompose in two competitive different ways depending on the cis or trans conformer,

$$trans\text{-}HOCHO\_(P2) \rightarrow H_2O\_(P14) + CO\_(P4) \qquad k_{1a} \qquad (1c)$$

$$cis\text{-}HOCHO\_(P13) \rightarrow CO_2\_(P8) + H_2\_(P9) \qquad k_{1c} \qquad (1d)$$

To obtain the branching ratio of CO, it was necessary to discount the yield for k_{1c}

$$Y_{CO\_1} = k_{1a}/(k_{1a}+k_{1c})$$

$$k_{CO} = k_{1a} * Y_{CO\_1}$$

the overall rate for (k_{1corr}) can be written as

$$k_{1corr} = k_1 \left[\frac{k_{CO}}{k_{-1}+k_{CO}}\right]$$

Where the bracket denotes that fraction which completes the reaction via (1c) rather than (1b). Assuming additive rate constants, we can calculate the global constant.

$$k_{tot}=k_1\left[\frac{k_{CO}}{k_{-1}+k_{CO}}\right]+k_2$$

The final yield for CO formation is

$$Y_{CO\_t}= k_{1corr}/k_{tot} + k_2/k_{tot}$$

Table A2-22: M06-2X-GD3/cc-pVTZ

T	k_{-1}	k_{1a}	k_{1c}	k_{1cor}	$k_{\_tot}$	k_{1corr}/k_{tot}	k_2/k_{tot}
300	1.11E-14	2.54E-33	2.64E-28	6.95E-46	4.11E-33	0.00%	100.00%
400	1.81E-09	2.20E-24	1.23E-22	7.70E-31	8.92E-24	0.00%	100.00%
500	6.71E-06	2.59E-17	4.60E-17	1.08E-20	1.54E-16	0.00%	99.99%
600	1.91E-03	2.67E-12	1.75E-12	2.99E-14	1.98E-11	0.09%	99.85%
700	1.15E-01	1.21E-08	5.04E-09	1.20E-09	1.07E-07	0.79%	98.87%
800	2.55E+00	7.16E-06	2.28E-06	3.62E-06	7.49E-05	3.67%	95.17%
818	4.21E+00	2.01E-05	6.15E-06	1.32E-05	2.18E-04	4.65%	93.93%
900	2.90E+01	1.07E-03	2.80E-04	1.92E-03	1.37E-02	11.03%	86.07%
990	1.72E+02	4.15E-02	9.58E-03	1.88E-01	6.87E-01	22.22%	72.65%
1000	2.05E+02	5.98E-02	1.37E-02	2.98E-01	1.02E+00	23.66%	70.94%
1200	3.96E+03	2.61E+01	4.91E+00	6.04E+02	9.71E+02	52.34%	37.81%
1250	7.18E+03	8.84E+01	1.61E+01	2.78E+03	4.06E+03	57.88%	31.61%
1300	1.25E+04	2.73E+02	4.80E+01	1.14E+04	1.55E+04	62.53%	26.49%
1347	2.02E+04	7.33E+02	1.25E+02	3.87E+04	5.00E+04	66.15%	22.55%
1400	3.35E+04	2.06E+03	3.42E+02	1.39E+05	1.71E+05	69.45%	19.02%
1500	7.90E+04	1.19E+04	1.89E+03	1.17E+06	1.37E+06	73.82%	14.47%
1600	1.68E+05	5.54E+04	8.46E+03	7.10E+06	8.06E+06	76.38%	11.96%
1700	3.28E+05	2.16E+05	3.19E+04	3.20E+07	3.60E+07	77.64%	10.89%
1800	5.94E+05	7.24E+05	1.04E+05	1.12E+08	1.26E+08	77.93%	10.87%
1900	1.01E+06	2.14E+06	3.01E+05	3.17E+08	3.59E+08	77.47%	11.65%
2000	1.64E+06	5.69E+06	7.83E+05	7.65E+08	8.80E+08	76.43%	13.05%
2100	2.54E+06	1.38E+07	1.86E+06	1.63E+09	1.92E+09	74.93%	14.94%
2200	3.79E+06	3.08E+07	4.11E+06	3.18E+09	3.84E+09	73.06%	17.21%
2300	5.45E+06	6.44E+07	8.47E+06	5.75E+09	7.17E+09	70.91%	19.76%
2400	7.62E+06	1.27E+08	1.64E+07	9.82E+09	1.27E+10	68.57%	22.52%
2500	1.04E+07	2.36E+08	3.03E+07	1.60E+10	2.14E+10	66.10%	25.41%

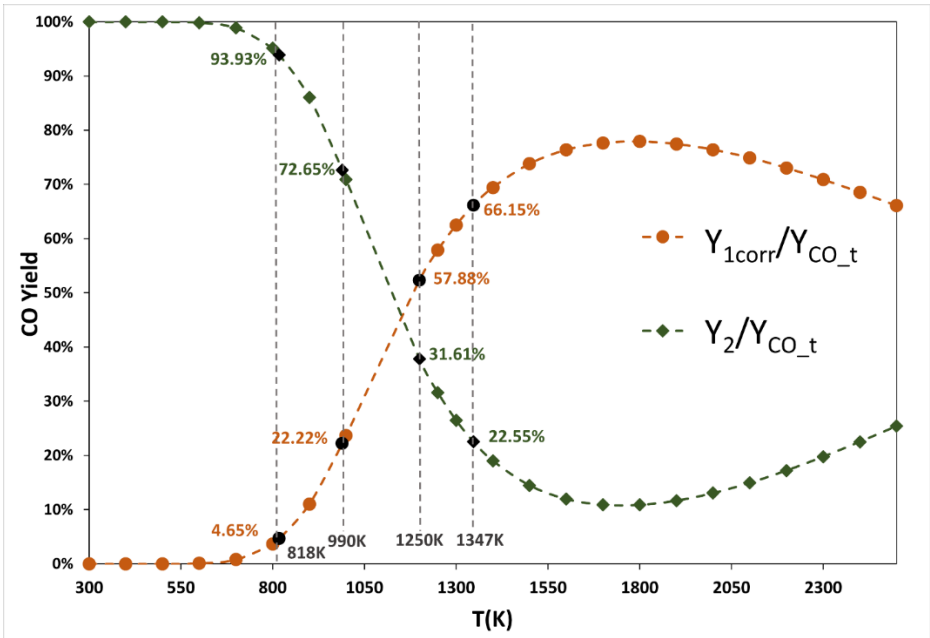

Figure A2-33: Branching ratio for carbon dioxide formation of R1 (orange) and R2 (green) pathways as function of temperature in the EF thermal decomposition. Calculated at M062X-GD3/cc-pVTZ level of theory

Table A2-23: CCSD(T)/cc-pVTZ

T	k_{-1}	k_{1a}	k_{1c}	k_{1cor}	$k_{\_tot}$	k_{1corr}/k_{tot}	k_2/k_{tot}
300	1.20E-16	1.50E-31	8.34E-28	1.34E-41	8.39E-31	0.00%	100.00%
400	1.86E-10	4.51E-23	2.90E-22	1.07E-27	5.30E-22	0.00%	100.00%
500	1.53E-06	2.90E-16	9.12E-17	1.51E-18	4.09E-15	0.03%	99.96%
600	6.95E-04	1.99E-11	3.09E-12	1.45E-12	3.06E-10	0.41%	99.52%
700	5.78E-02	6.77E-08	8.23E-09	3.20E-08	1.13E-06	2.52%	97.17%
800	1.64E+00	3.23E-05	3.49E-06	6.33E-05	6.17E-04	9.26%	89.74%
818	2.82E+00	8.79E-05	9.34E-06	2.17E-04	1.73E-03	11.29%	87.51%
900	2.26E+01	4.08E-03	4.10E-04	2.45E-02	9.76E-02	22.77%	74.94%
990	1.54E+02	1.40E-01	1.35E-02	1.92E+00	4.53E+00	38.57%	57.71%
1000	1.87E+02	2.00E-01	1.92E-02	2.97E+00	6.72E+00	40.35%	55.77%
1200	4.58E+03	7.13E+01	6.53E+00	4.16E+03	5.61E+03	68.06%	25.71%
1250	8.74E+03	2.32E+02	2.11E+01	1.78E+04	2.25E+04	72.25%	21.19%
1300	1.59E+04	6.92E+02	6.25E+01	6.75E+04	8.20E+04	75.53%	17.64%
1347	2.68E+04	1.80E+03	1.61E+02	2.15E+05	2.53E+05	77.96%	15.03%
1400	4.63E+04	4.88E+03	4.37E+02	7.18E+05	8.24E+05	80.05%	12.77%
1500	1.18E+05	2.66E+04	2.37E+03	5.34E+06	5.93E+06	82.67%	9.96%
1600	2.67E+05	1.18E+05	1.05E+04	2.90E+07	3.17E+07	84.06%	8.47%
1700	5.52E+05	4.39E+05	3.90E+04	1.21E+08	1.31E+08	84.62%	7.85%
1800	1.06E+06	1.41E+06	1.26E+05	4.00E+08	4.34E+08	84.64%	7.83%
1900	1.89E+06	4.04E+06	3.60E+05	1.11E+09	1.21E+09	84.27%	8.22%
2000	3.19E+06	1.04E+07	9.29E+05	2.66E+09	2.93E+09	83.61%	8.91%
2100	5.14E+06	2.45E+07	2.19E+06	5.74E+09	6.37E+09	82.75%	9.84%
2200	7.94E+06	5.34E+07	4.80E+06	1.14E+10	1.27E+10	81.72%	10.93%
2300	2.36E+07	1.09E+08	9.82E+06	1.11E+05	2.55E+08	0.04%	99.96%
2400	3.41E+07	2.09E+08	1.90E+07	3.06E+05	4.87E+08	0.06%	99.94%
2500	4.77E+07	3.82E+08	3.48E+07	7.67E+05	8.83E+08	0.08%	99.91%

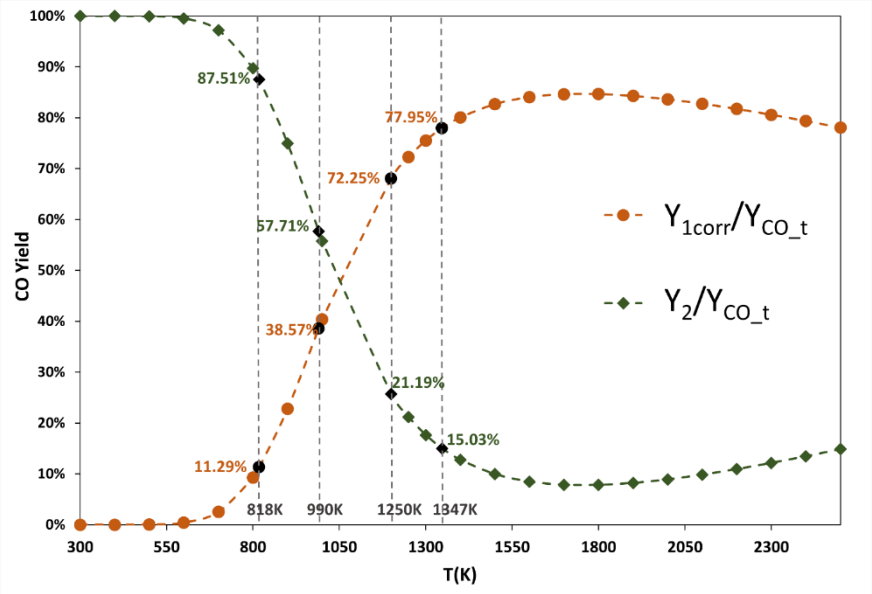

Figure A2-34: Branching ratio for carbon dioxide formation of R1 (orange) and R2 (green) pathways as function of temperature in the EF thermal decomposition. Calculated at CCSD(T)/cc-pVTZ level of theory

Table A2-24: CBS-QB3

T	k_{-1}	k_{1a}	k_{1c}	k_{1cor}	$k_{\_tot}$	k_{1corr}/k_{tot}	k_2/k_{tot}
300	3.13E-17	3.82E-34	2.39E-28	3.87E-46	1.04E-31	0.00%	100.00%
400	4.99E-11	6.70E-24	1.10E-22	1.11E-28	1.12E-22	0.00%	100.00%
500	4.15E-07	1.10E-16	4.50E-17	1.01E-18	1.18E-15	0.06%	99.91%
600	1.89E-04	1.00E-11	1.78E-12	1.51E-12	1.09E-10	1.18%	98.62%
700	1.57E-02	3.90E-08	5.22E-09	4.19E-08	4.93E-07	7.50%	91.50%
800	4.43E-01	2.03E-05	2.37E-06	9.63E-05	3.50E-04	24.62%	72.50%
818	7.62E-01	5.60E-05	6.42E-06	3.38E-04	1.05E-03	28.93%	67.75%
900	6.08E+00	2.72E-03	2.94E-04	4.16E-02	7.82E-02	47.98%	46.83%
990	4.13E+01	9.72E-02	1.01E-02	3.51E+00	4.91E+00	64.85%	28.41%
1000	5.01E+01	1.39E-01	1.44E-02	5.48E+00	7.49E+00	66.31%	26.82%
1200	1.22E+03	5.25E+01	5.21E+00	8.48E+03	9.33E+03	82.61%	9.19%
1250	2.32E+03	1.73E+02	1.71E+01	3.64E+04	3.93E+04	84.30%	7.38%
1300	4.20E+03	5.19E+02	5.11E+01	1.38E+05	1.47E+05	85.48%	6.10%
1347	7.06E+03	1.36E+03	1.34E+02	4.33E+05	4.57E+05	86.27%	5.25%
1400	1.22E+04	3.72E+03	3.65E+02	1.40E+06	1.47E+06	86.87%	4.59%
1500	3.08E+04	2.06E+04	2.02E+03	9.41E+06	9.80E+06	87.43%	3.98%
1600	6.96E+04	9.21E+04	9.06E+03	4.47E+07	4.65E+07	87.48%	3.91%
1700	1.43E+05	3.46E+05	3.42E+04	1.62E+08	1.69E+08	87.16%	4.22%
1800	2.73E+05	1.13E+06	1.12E+05	4.76E+08	5.00E+08	86.60%	4.80%
1900	4.86E+05	3.24E+06	3.24E+05	1.20E+09	1.28E+09	85.82%	5.60%
2000	8.19E+05	8.38E+06	8.44E+05	2.72E+09	2.91E+09	84.90%	6.56%
2100	1.31E+06	1.99E+07	2.01E+06	5.62E+09	6.08E+09	83.85%	7.66%
2200	2.02E+06	4.35E+07	4.44E+06	1.08E+10	1.18E+10	82.70%	8.86%
2300	3.00E+06	8.90E+07	9.15E+06	1.95E+10	2.17E+10	81.48%	10.15%
2400	4.32E+06	1.72E+08	1.78E+07	3.35E+10	3.79E+10	80.19%	11.51%
2500	6.03E+06	3.15E+08	3.28E+07	5.51E+10	6.33E+10	78.86%	12.92%

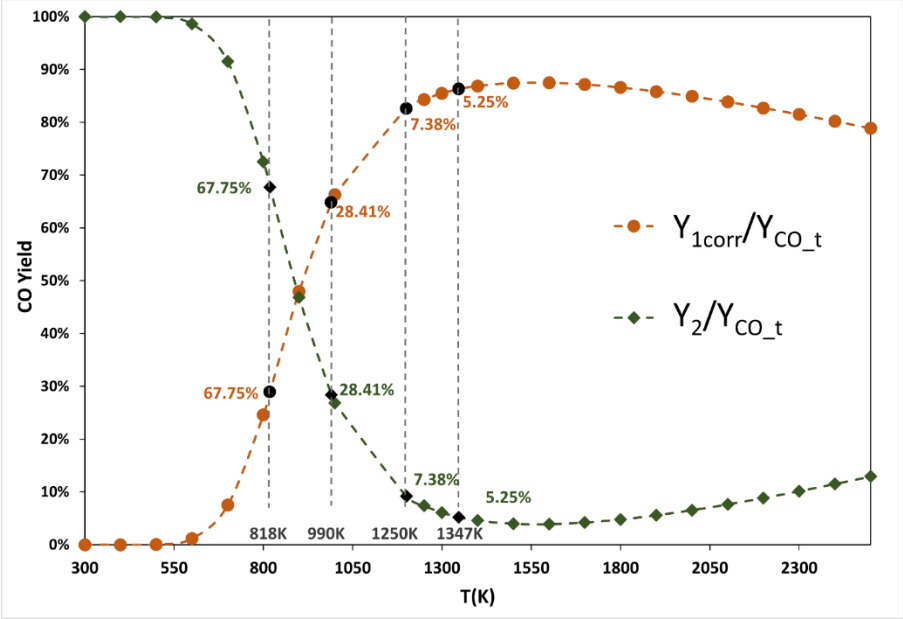

Figure A2-35: Branching ratio for carbon dioxide formation of R1 (orange) and R2 (green) pathways as function of temperature in the EF thermal decomposition. Calculated at CBS-QB3 level of theory

Table A2-25: M06-2X-GD3/aug-cc-pVTZ

T	k_{-1}	k_{1a}	k_{1c}	k_{1cor}	$k_{\_tot}$	k_{1corr}/k_{tot}	k_2/k_{tot}
300	1.15E-14	5.60E-33	1.50E-28	9.40E-45	5.06E-33	0.00%	100.00%
400	1.80E-09	6.22E-24	8.73E-23	1.26E-29	1.19E-23	0.00%	100.00%
500	6.46E-06	6.87E-17	3.76E-17	7.63E-20	2.05E-16	0.02%	99.96%
600	1.80E-03	6.28E-12	1.51E-12	1.38E-13	2.60E-11	0.43%	99.47%
700	1.07E-01	2.57E-08	4.48E-09	4.52E-09	1.41E-07	2.74%	96.79%
800	2.34E+00	1.41E-05	2.05E-06	1.19E-05	1.03E-04	10.11%	88.41%
818	3.86E+00	3.92E-05	5.57E-06	4.27E-05	3.03E-04	12.32%	85.93%
900	2.64E+01	1.98E-03	2.56E-04	5.73E-03	2.07E-02	24.54%	72.28%
990	1.55E+02	7.35E-02	8.84E-03	5.26E-01	1.15E+00	40.76%	54.34%
1000	1.85E+02	1.06E-01	1.26E-02	8.27E-01	1.74E+00	42.53%	52.39%
1200	3.53E+03	4.26E+01	4.60E+00	1.51E+03	1.96E+03	69.33%	23.20%
1250	6.39E+03	1.42E+02	1.51E+01	6.76E+03	8.35E+03	73.22%	19.02%
1300	1.11E+04	4.34E+02	4.52E+01	2.70E+04	3.20E+04	76.28%	15.77%
1347	1.79E+04	1.15E+03	1.18E+02	8.96E+04	1.03E+05	78.51%	13.41%
1400	2.96E+04	3.19E+03	3.24E+02	3.11E+05	3.51E+05	80.42%	11.41%
1500	6.96E+04	1.80E+04	1.79E+03	2.43E+06	2.67E+06	82.70%	9.07%
1600	1.48E+05	8.22E+04	8.05E+03	1.34E+07	1.46E+07	83.73%	8.06%
1700	2.87E+05	3.14E+05	3.04E+04	5.48E+07	5.95E+07	83.87%	8.01%
1800	5.19E+05	1.04E+06	9.96E+04	1.74E+08	1.91E+08	83.32%	8.69%
1900	8.84E+05	3.03E+06	2.89E+05	4.59E+08	5.10E+08	82.22%	9.95%
2000	1.43E+06	7.95E+06	7.53E+05	1.05E+09	1.19E+09	80.68%	11.68%
2100	2.21E+06	1.90E+07	1.80E+06	2.16E+09	2.51E+09	78.76%	13.81%
2200	3.28E+06	4.22E+07	3.97E+06	4.11E+09	4.91E+09	76.56%	16.24%
2300	4.72E+06	8.72E+07	8.18E+06	7.32E+09	9.02E+09	74.13%	18.91%
2400	6.59E+06	1.70E+08	1.59E+07	1.24E+10	1.58E+10	71.55%	21.75%
2500	8.96E+06	3.14E+08	2.94E+07	1.99E+10	2.65E+10	68.86%	24.70%

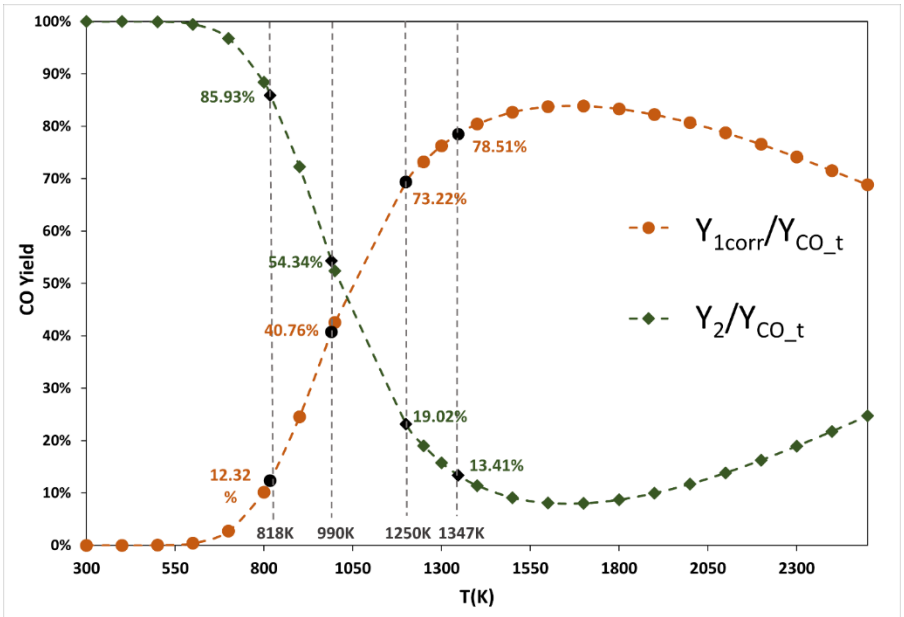

Figure A2-36: Branching ratio for carbon dioxide formation of R1 (orange) and R2 (green) pathways as function of temperature in the EF thermal decomposition. Calculated at M062X-GD3/aug-cc-pVTZ level of theory

Table A2-26: SVECV-F12

T	k_{-1}	k_{1a}	k_{1c}	k_{1cor}	$k_{\_tot}$	k_{1corr}/k_{tot}	k_2/k_{tot}
300	1.61E-15	1.74E-31	3.09E-28	4.67E-41	3.39E-31	0.00%	100.00%
400	3.99E-10	8.62E-23	1.44E-22	5.72E-27	3.20E-22	0.00%	100.00%
500	1.94E-06	5.66E-16	5.55E-17	3.64E-18	2.90E-15	0.11%	99.87%
600	6.59E-04	3.64E-11	2.08E-12	3.05E-12	2.39E-10	1.21%	98.72%
700	4.50E-02	1.16E-07	5.90E-09	6.25E-08	9.65E-07	6.16%	93.53%
800	1.10E+00	5.27E-05	2.62E-06	1.17E-04	5.93E-04	18.86%	80.20%
818	1.85E+00	1.42E-04	7.05E-06	3.99E-04	1.71E-03	22.19%	76.71%
900	1.35E+01	6.39E-03	3.18E-04	4.36E-02	1.09E-01	38.22%	59.87%
990	8.43E+01	2.13E-01	1.07E-02	3.32E+00	5.70E+00	55.38%	41.83%
1000	1.01E+02	3.03E-01	1.53E-02	5.12E+00	8.55E+00	57.05%	40.07%
1200	2.14E+03	1.03E+02	5.40E+00	6.65E+03	8.02E+03	78.74%	17.12%
1250	3.95E+03	3.31E+02	1.76E+01	2.75E+04	3.21E+04	81.37%	14.30%
1300	6.96E+03	9.76E+02	5.24E+01	1.00E+05	1.14E+05	83.27%	12.26%
1347	1.14E+04	2.51E+03	1.36E+02	3.03E+05	3.40E+05	84.51%	10.90%
1400	1.92E+04	6.76E+03	3.71E+02	9.40E+05	1.04E+06	85.42%	9.89%
1500	4.66E+04	3.63E+04	2.04E+03	5.82E+06	6.40E+06	86.02%	9.15%
1600	1.01E+05	1.59E+05	9.09E+03	2.55E+07	2.81E+07	85.53%	9.57%
1700	2.01E+05	5.85E+05	3.41E+04	8.54E+07	9.58E+07	84.24%	10.85%
1800	3.71E+05	1.87E+06	1.11E+05	2.36E+08	2.71E+08	82.32%	12.79%
1900	6.44E+05	5.28E+06	3.19E+05	5.66E+08	6.68E+08	79.93%	15.23%
2000	1.06E+06	1.35E+07	8.29E+05	1.22E+09	1.49E+09	77.18%	18.07%
2100	1.66E+06	3.15E+07	1.97E+06	2.43E+09	3.08E+09	74.19%	21.17%
2200	2.50E+06	6.81E+07	4.33E+06	4.50E+09	5.95E+09	71.05%	24.43%
2300	3.63E+06	1.38E+08	8.90E+06	7.89E+09	1.09E+10	67.83%	27.79%
2400	5.12E+06	2.64E+08	1.72E+07	1.32E+10	1.91E+10	64.61%	31.16%
2500	7.04E+06	4.79E+08	3.17E+07	2.11E+10	3.22E+10	61.44%	34.48%

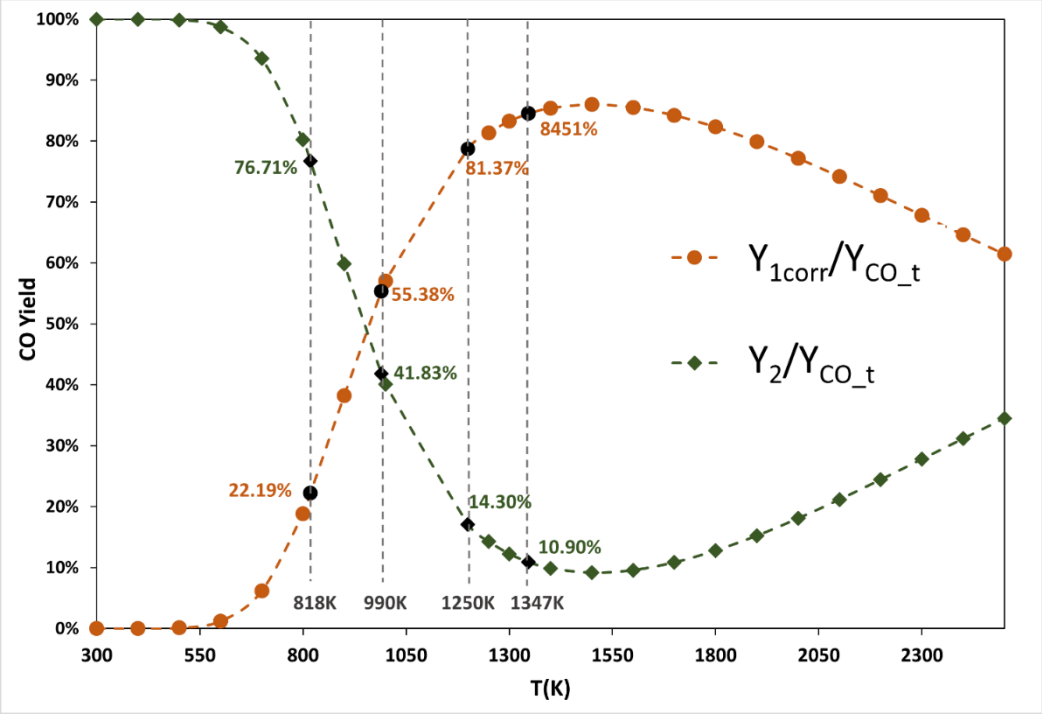

Figure A2-37: Branching ratio for carbon dioxide formation of R1 (orange) and R2 (green) pathways as function of temperature in the EF thermal decomposition. Calculated at SVECV-F12 level of theory.

Appendix 3

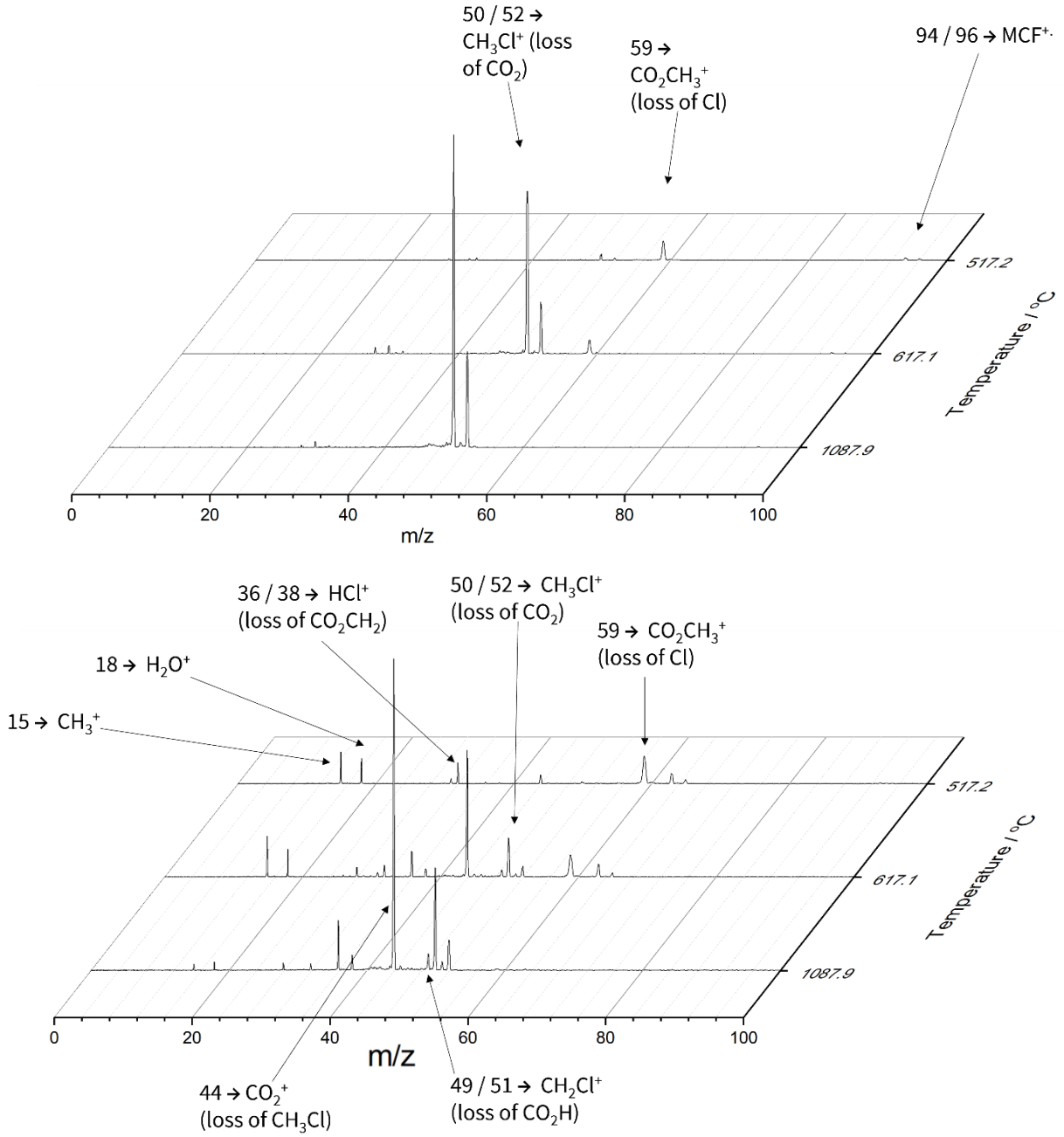

Figure A3-1: Mass spectra over varying temperatures at 11.5 eV (a) and 14.0 eV (b). MCF^+ = methyl chloroformate radical cation.

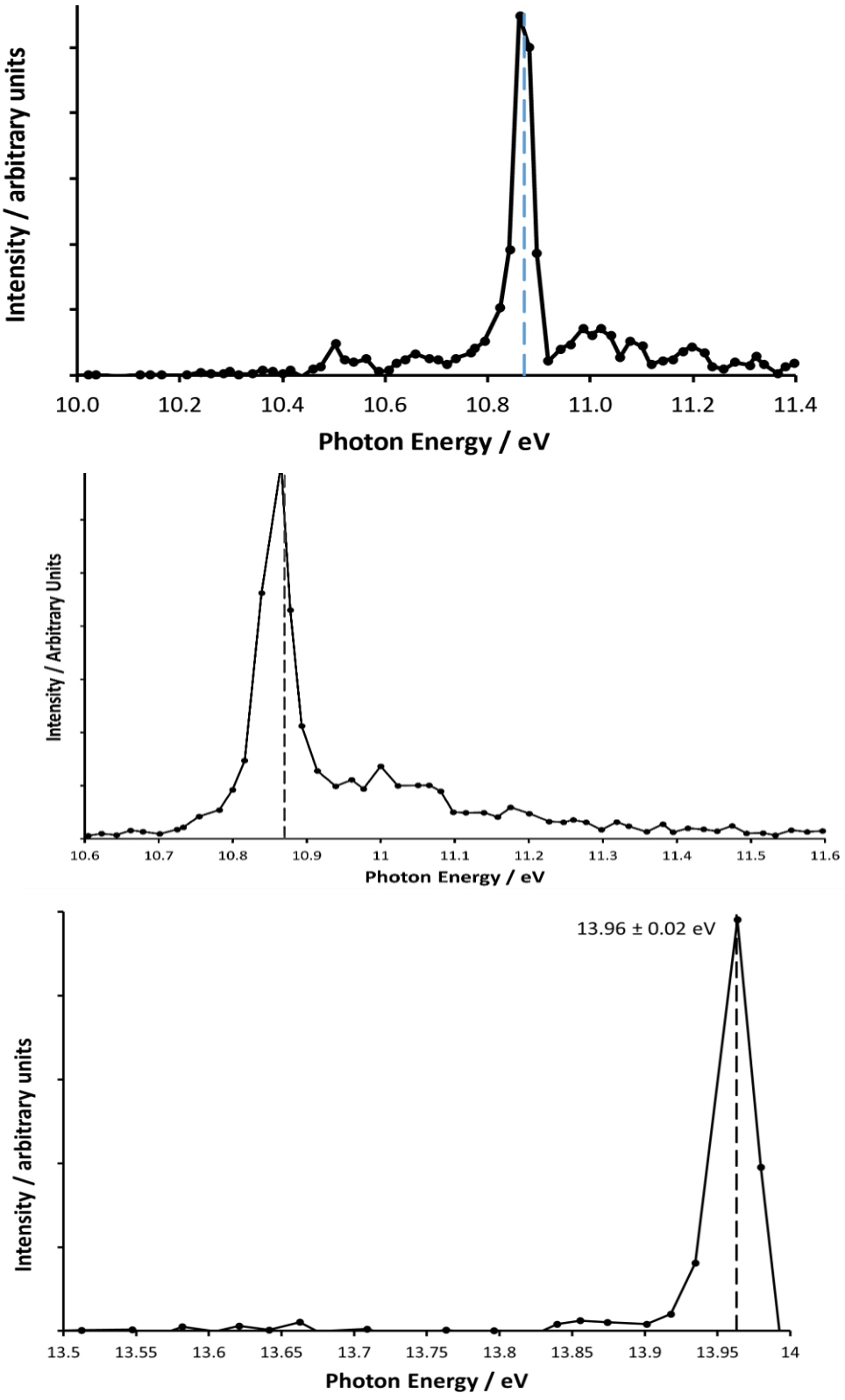

Figure A3-2: (a) [Top] ms-TPES of CO **(b)** [Middle] ms-TPES of CH_2O **(c)** [Bottom] ms-TPES of CO both obtained at 617 ^oC.

Table A3-1: Relative energies (kJ mol^{-1}) for stationary points and transitions states in the thermal decomposition of MCF. (a-Tz stands for aug-cc-pVTZ and 6-311 stands for 6-311++G(d,p)).

R	REACTION	ENERGY	M06-2X/GD3/a-Tz		B3LYP/6-311		CBS-QB3		CCSD(T)/a-Tz		SVECV-f12	
			TS	P	TS	P	TS	P	TS	P	TS	P
ISO	$Z\text{-}H_3COC(O)Cl \rightarrow E\text{-}H_3COC(O)Cl$	ΔE	43.07	15.91	42.87	16.32	44.78	17.82	43.84	16.81	44.60	16.91
		Δ(E+ZPE)	40.96	15.93	40.78	16.08	42.73	17.70	41.73	16.83	42.49	16.92
		ΔH	39.42	15.77	39.20	16.02	41.13	17.58	40.19	16.66	40.95	16.76
		ΔG	42.38	16.08	42.34	16.15	44.40	17.97	43.14	16.98	43.90	17.07
1	$E\text{-}H_3COC(O)Cl \rightarrow CH_3Cl+CO_2$	ΔE	280.31	-57.79	232.13	-84.31	270.91	-68.51	268.49	-68.02	274.69	-69.54
		Δ(E+ZPE)	265.98	-67.30	218.93	-93.04	258.06	-77.19	254.16	-77.53	260.36	-79.05
		ΔH	268.98	-64.17	221.31	-90.09	260.42	-74.33	257.16	-74.40	263.36	-75.92
		ΔG	259.24	-106.89	214.48	-134.03	253.55	-116.28	247.43	-117.13	253.63	-118.64
2	$E\text{-}H_3COC(O)Cl \rightarrow CH_2COCO+HCl$	ΔE	332.43	156.17	--	144.74	312.14	152.49	354.34	150.35	329.05	152.43
		Δ(E+ZPE)	308.13	136.45	--	124.88	289.57	133.07	342.51	130.64	304.76	132.72
		ΔH	309.99	140.18	--	128.48	290.76	136.54	344.54	134.37	306.61	136.44
		ΔG	303.83	99.46	--	88.20	287.35	96.59	338.80	93.65	300.46	95.73
2a	$CH_2COCO+HCl \rightarrow H_2CO+CO+HCl$	ΔE	292.81	137.64	261.74	109.63	278.60	117.24	271.77	110.31	279.54	119.13
		Δ(E+ZPE)	264.65	99.22	234.08	71.72	251.15	79.70	243.61	71.92	251.38	80.74
		ΔH	269.15	110.03	238.25	82.24	255.21	90.10	248.11	82.73	255.88	91.55
		ΔG	226.55	23.76	196.43	-5.09	213.71	4.83	205.51	-5.25	213.28	3.56
3	$E\text{-}H_3COC(O)Cl \rightarrow H_2CO+CO+HCl$	ΔE	386.37	137.64	343.83	109.63	367.17	117.24	366.25	110.31	376.85	119.13
		Δ(E+ZPE)	360.07	99.22	317.34	71.72	340.90	79.70	339.95	71.92	350.55	80.74
		ΔH	361.60	110.03	318.92	82.24	342.43	90.10	341.48	82.73	352.08	91.55
		ΔG	357.42	23.76	314.60	-5.09	338.27	4.83	337.29	-5.25	347.90	3.56

R	REACTION	ENERGY	M06-2X/GD3/a-Tz		B3LYP/6-311		CBS-QB3		CCSD(T)/a-Tz		SVECV-f12	
			TS	P	TS	P	TS	P	TS	P	TS	P
4	E-$H_3COC(O)Cl$ → CH_3CO+HC(O)Cl	ΔE	387.20	135.38	374.67	101.57	386.26	121.96	383.13	120.71	389.99	119.13
		Δ(E+ZPE)	371.15	116.44	357.05	82.85	368.84	103.27	367.08	101.80	373.94	80.74
		ΔH	370.28	120.85	356.41	87.05	368.12	107.41	366.21	106.21	373.07	91.55
		ΔG	372.50	71.97	358.42	36.97	370.40	59.26	368.43	55.61	375.29	3.56
4a	CH_3CO+HC(O)Cl → H_2CO+CO+HCl	ΔE	303.40	137.64	256.58	109.63	289.13	117.24	284.48	110.31	290.42	119.13
		Δ(E+ZPE)	272.41	99.22	225.98	71.72	259.03	79.70	253.52	71.92	259.46	80.74
		ΔH	277.63	110.03	231.10	82.24	264.00	90.10	258.74	82.73	264.68	91.55
		ΔG	226.48	23.76	178.57	-5.09	213.55	4.83	205.88	-5.25	211.82	3.56
5	E-$H_3COC(O)Cl$ → H_3COCl+CO	ΔE	406.23	248.76	344.33	250.03	364.74	241.42	354.34	234.61	371.02	241.67
		Δ(E+ZPE)	394.40	233.07	332.53	233.99	353.19	225.75	342.51	218.92	359.20	225.98
		ΔH	396.43	237.70	334.55	238.54	355.13	230.22	344.54	223.55	361.23	230.61
		ΔG	390.69	191.69	329.27	192.77	350.08	184.51	338.80	177.54	355.49	184.59
5a	H_3COCl+CO → H_2CO+CO+HCl	ΔE	537.20	137.64	470.65	109.63	473.09	117.24	479.92	110.31	493.34	119.13
		Δ(E+ZPE)	499.93	99.22	434.67	71.72	437.56	79.70	442.65	71.92	456.07	80.74
		ΔH	504.56	110.03	439.24	82.24	442.00	90.10	447.27	82.73	460.69	91.55
		ΔG	457.97	23.76	392.66	-5.09	395.78	4.83	400.69	-5.25	414.11	3.56
6	Z-$H_3COC(O)Cl$ → $H_3COC•(O)$+•Cl	ΔE	--	369.11	--	336.60	--	374.92	--	357.37	--	353.63
		Δ(E+ZPE)	--	359.44	--	326.70	--	365.32	--	347.70	--	343.97
		ΔH	--	363.28	--	330.62	--	369.12	--	351.53	--	347.80
		ΔG	--	323.43	--	290.26	--	329.03	--	311.69	--	307.96

Table A3-2: Thermal Boltzmann energy distribution population for MCF conformers. (a-Tz stands for aug-cc-pVTZ and 6-311 stands for 6-311++G(d,p)).

T (K)	M06-2X/GD3/a-Tz		CCSD(T)/a-Tz		SVECV-f12	
	E-MCF	Z-MCF	E-MCF	Z-MCF	E-MCF	Z-MCF
790.35	0.084	0.916	0.074	0.926	0.073	0.927
890.25	0.108	0.892	0.097	0.903	0.096	0.904
1000	0.133	0.867	0.121	0.879	0.120	0.880
1200	0.175	0.825	0.162	0.838	0.161	0.839
1361.05	0.204	0.796	0.192	0.808	0.190	0.810
1500	0.226	0.774	0.214	0.786	0.213	0.787
1700	0.254	0.746	0.242	0.758	0.241	0.759
1900	0.277	0.723	0.266	0.734	0.265	0.735
2100	0.297	0.703	0.287	0.713	0.285	0.715
2300	0.314	0.686	0.304	0.696	0.303	0.697
2500	0.329	0.671	0.319	0.681	0.318	0.682

Table A3-3: Values for temperature-dependent rate coefficients over the 790–2500 K temperature range at the high-pressure limit (HPL).

M06-2X/GD3/aug-cc-pVTZ

T	k_1c	k_2c	k_2/k_1	k_{MCF}	k_1/k_{MCF}	k_2/k_{MCF}
790.35	3.13E-03	2.03E-06	6.48E-04	3.13E-03	99.94%	0.06%
890.25	4.96E-01	6.60E-04	1.33E-03	4.97E-01	99.87%	0.13%
1000	4.01E+01	1.00E-01	2.50E-03	4.02E+01	99.75%	0.25%
1200	1.46E+04	8.54E+01	5.85E-03	1.47E+04	99.42%	0.58%
1361.05	4.60E+05	4.45E+03	9.68E-03	4.65E+05	99.04%	0.96%
1500	4.86E+06	6.70E+04	1.38E-02	4.92E+06	98.64%	1.36%
1700	7.25E+07	1.49E+06	2.06E-02	7.40E+07	97.98%	2.02%
1900	6.01E+08	1.70E+07	2.83E-02	6.18E+08	97.24%	2.76%
2100	3.32E+09	1.21E+08	3.65E-02	3.44E+09	96.48%	3.52%
2300	1.35E+10	6.08E+08	4.50E-02	1.41E+10	95.70%	4.30%
2500	4.38E+10	2.36E+09	5.38E-02	4.62E+10	94.90%	5.10%

CCSD(T)/M06-2X/GD3/aug-cc-pVTZ

T	k_1	k_2	k_2/k_1	k_{MCF}	k_1/k_{MCF}	k_2/k_{MCF}
790.35	1.81E-02	1.04E-08	5.75E-07	1.81E-02	0.9999994	5.752E-07
890.25	2.35E+00	6.12E-06	2.60E-06	2.35E+00	0.9999974	2.599E-06
1000	1.61E+02	1.55E-03	9.64E-06	1.61E+02	0.9999904	9.645E-06
1200	4.65E+04	2.66E+00	5.72E-05	4.65E+04	0.9999428	5.722E-05
1361.05	1.28E+06	2.09E+02	1.64E-04	1.28E+06	0.9998364	0.0001636
1500	1.23E+07	4.17E+03	3.39E-04	1.23E+07	0.9996607	0.0003393
1700	1.64E+08	1.28E+05	7.82E-04	1.64E+08	0.9992182	0.0007818
1900	1.25E+09	1.90E+06	1.52E-03	1.26E+09	0.9984866	0.0015134
2100	6.42E+09	1.67E+07	2.59E-03	6.44E+09	0.9974146	0.0025854
2300	2.47E+10	9.97E+07	4.03E-03	2.48E+10	0.9959836	0.0040164
2500	7.63E+10	4.45E+08	5.83E-03	7.68E+10	0.9941995	0.0058005

SVECV-f12

T	k_1	k_2	k_2/k_1	k_{MCF}	k_1/k_{MCF}	k_2/k_{MCF}
790.35	7.01E-03	3.24E-06	4.62E-04	7.01E-03	99.95%	0.05%
890.25	1.02E+00	1.00E-03	9.85E-04	1.02E+00	99.90%	0.10%
1000	7.59E+01	1.45E-01	1.91E-03	7.60E+01	99.81%	0.19%
1200	2.48E+04	1.16E+02	4.69E-03	2.49E+04	99.53%	0.47%
1361.05	7.34E+05	5.87E+03	7.99E-03	7.40E+05	99.21%	0.79%
1500	7.48E+06	8.60E+04	1.15E-02	7.56E+06	98.86%	1.14%
1700	1.06E+08	1.86E+06	1.75E-02	1.08E+08	98.28%	1.72%
1900	8.46E+08	2.07E+07	2.45E-02	8.67E+08	97.61%	2.39%
2100	4.52E+09	1.44E+08	3.20E-02	4.66E+09	96.90%	3.10%
2300	1.79E+10	7.15E+08	4.00E-02	1.86E+10	96.15%	3.85%
2500	5.66E+10	2.74E+09	4.83E-02	5.93E+10	95.39%	4.61%

Table A3-4: The Arrhenius parameters A (s^{-1}) and Ea (kJ mol^{-1}) for thermal unimolecular decomposition of MCF at the high-pressure limit (a-Tz stands for aug-cc-pVTZ and 6-311 stands for 6-311++G(d,p)).

	M06-2X/GD3/a-Tz		CCSD(T)/a-Tz		SVECV-f12	
	$A(x10^{16})$	E_a	$A(x10^{16})$	E_a	$A(x10^{16})$	E_a
k_1	5.902	290.751	5.925	279.250	5.938	285.500
k_2	2.456	333.269	2.463	367.938	2.461	330.208

Appendix 4

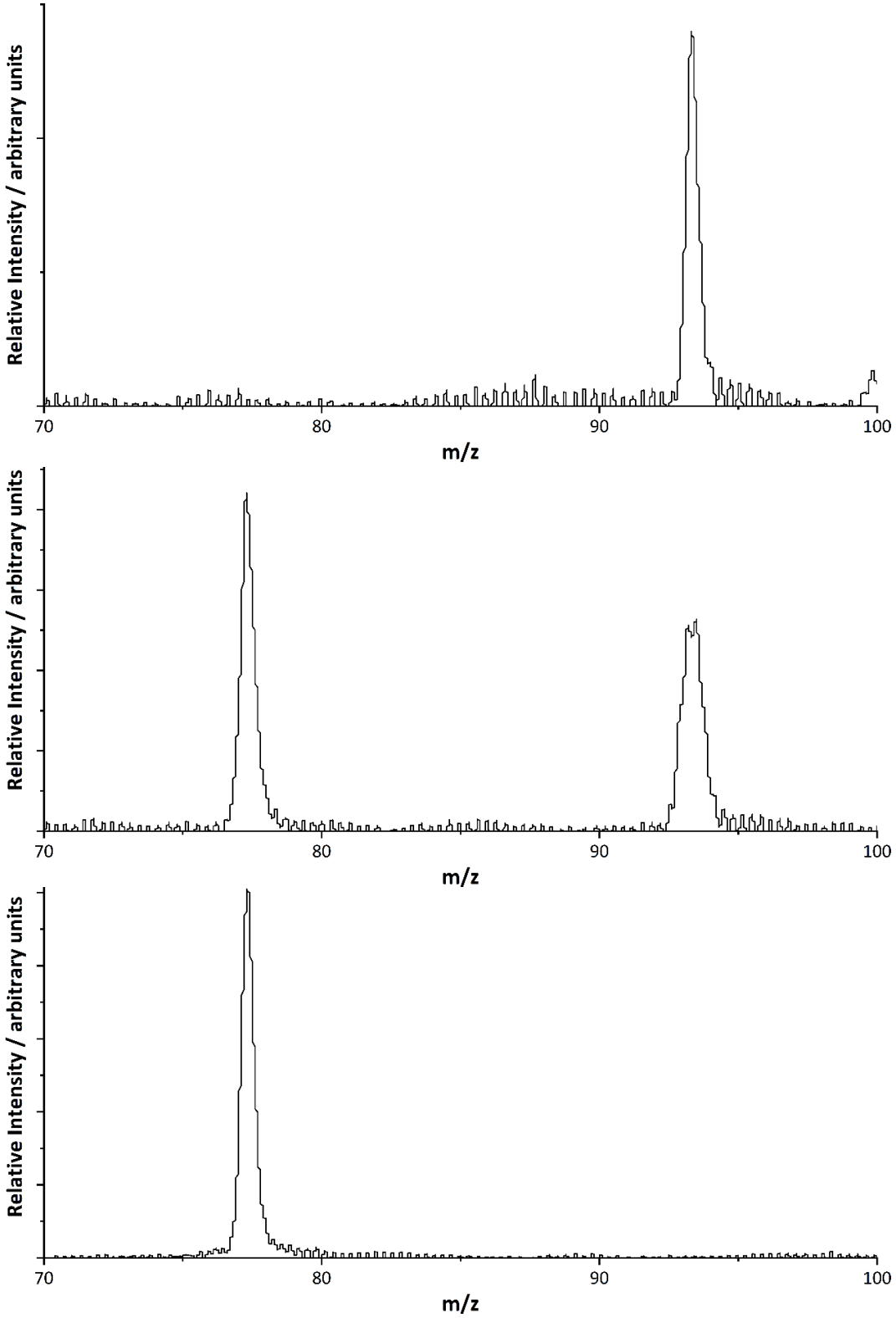

Figure A4-1: MIKES mass spectra from [top] m/z 128 showing m/z 93, [middle] m/z 121 showing both m/z 77 and 93, [bottom] m/z 112 showing m/z 77. The reader is referred to West et al[1] for typical operating conditions for this experiment.